Novel Bioinspired Pumping Models for Microscale Flow Transport

Yasser Aboelkassem

Dissertation submitted to the Faculty of the
Virginia Polytechnic Institute and State University
in partial fulfillment of the requirements for the degree of

Doctor of Philosophy
in
Engineering Mechanics

Anne E. Staples, Chair
John J. Socha
Mark A. Stremler
Raffaella De Vita
Rafael V. Davalos
Sunny Jung

August 1st, 2012
Blacksburg, Virginia

Keywords: Bioinspiration, Biomimetics, Physiological System in Insects, Stokeslets, Meshfree, Microscale Flow Transport, Collapsible Tubes, Microfluidics

Novel Bioinspired Pumping Models for Microscale Flow Transport

Yasser Aboelkassem

ABSTRACT

Bioinspiration and biomimetics are two increasingly important fields in applied science and mechanics that seek to imitate systems or processes in nature to design improved engineering devices. Here, we are inspired and motivated by microscale internal flow transport phenomena in insect tracheal networks, which are observed to be induced by the rhythmic tracheal wall contractions. These networks have been shown to mange fluid very efficiently compared to current state-of-the-art microfluidic devises.

This dissertation presents two versions of a novel bioinspired pumping mechanism "ghost-valve pumping principle" that is neither peristaltic nor belongs to impedance mismatch class of pumping mechanisms. The insect-inspired pumping models presented here are expected to function efficiently in the microscale flow regime in a simple channel/tube geometries or a complex network of channels. The first pumping approach shows the ability of inducing a unidirectional net flow by using an inelastic tube or channel with at least two moving contractions. The second pumping approach presents a new concept for directional pumping, namely "selective pumping in a network.". The results presented here might help in mimicking features of physiological systems in insects and guide efforts to fabricate novel microfluidic devices with improved efficiency.

In this study, both theoretical analysis and Stokeslets-meshfree computational methods are used to solve for the 2D and 3D viscous flow transport in several micro-geometries (tubes, channels and networks) with prescribed moving wall contractions. The derived theoretical analysis is based on both lubrication theory and quasi-steady approximations at low Reynolds numbers. The meshfree numerical method is based on the method of fundamental solutions (MFS) that uses a set of singularized force elements "Stokeslets" to induce the flow motions. Moreover, the passive particle tracking simulation approach in the Lagrangian frame of reference is also used to strengthen and support our pumping paradigm developed in this dissertation.

Dedication

Dedicated to my parents, my wife “Nehal” and my cute kids “Abdelrhman and Alia”

Acknowledgments

Firstly, I would like state my special thanks and express my gratitude to my advisor, Professor Anne E. Staples. I'm extremely grateful for your patience, your knowledge and expertise in various scientific and technical areas and for the chance you gave me to explore many horizons of the beautiful world of fluid dynamics.

Secondly, I'm also very grateful for the help and constructive comments I received from my research committee members professors John J. Socha, Mark A. Stremler, Raffaella De Vita and Rafael V. Davalos. I would like also to acknowledge Professor Sunny Jung for accepting to serve in my Ph.D. committee members and for his help and constructive comments and advices that I always receive from him. I would like also to thank all faculty and staff members of the Engineering Science and Mechanics department. Special thanks for the graduate enrolment specialist, "Ms. Lisa Smith" for her help and academic advices through out my enrolment.

My deepest gratitude goes to my parents, wife "Nehal" , and kids "Abdelrhman and Alia" for their patience and encouragement over the years. I would like also to thank all of my friends,lab mates "Omer" and "Leila" for the time we spent together.

Many Thanks goes ASME 2011 Pressure Vessels and Piping Conference organizing committee and referees members of student paper symposium and competition for selecting my paper to be among the best top 10 articles. The Honorable Mention certificate and financial travel awards are highly appreciated. Finally, I would like also gratefully acknowledge the financial support provided by the National Science Foundation Emerging Frontiers in Research and Innovation program under Grant No. 0938047 and by the Institute for Critical Technology and Applied Science at Virginia Tech.

Contents

List of Figures

List of Tables

Chapter 1

Introduction

A brief introduction about our biologically inspiration model "insects physiological system", more specifically about the insect's tracheal network of tubes and their rhythmic wall contraction patterns is given. Discussions related to various transporting flow mechanisms that are possibly exist in these physiological systems are also given. Previous researches that are directly related and form basis to our theoretical analysis and meshfree numerical computations used in this dissertation will be also included.

1.1 Preface

Biomimetic microfluid devices that are inspired by physiological systems in biological organisms (in particular, insects) have started to gain attention. In recent years, there have been several efforts to fabricate devices that mimic these systems in the guise of simple channels with membranes attached at different locations along their length to act as pumping actuators. These devices with the attached membranes are often fabricated using multilayer soft lithography (MSL) techniques Pandolfi and Ortiz (2007). The membranes on these fabricated devices are then actuated so they move in the lateral direction, as a result of these wall motions, a net momentum injection into the system occurs, and a unidirectional net flow is produced. This approach is particularly attractive because is achieved without making use of valves or other mechanical components.

In general, controlled pumping of microliters of fluid in microgeometries is a challenging problem. Valveless pumping techniques are generally preferred, since they have the advantage of requiring fewer moving parts and therefore lower maintenance. Several valveless pumping techniques have been developed including electroosmotic and peristaltic pumping, among other, and are currently used in most microfluidic systems. Electroosmotic pumping requires the patching and doping of electrodes along the tube or channel walls, while peristaltic pumping and other valveless pumping techniques rely on wave dynamics induced by elasticity in the channel walls, which is difficult to manufacture with current microfabrication methods.

This dissertation presents an alternative method that might be useful for pumping fluids in a controlled manner at the microscale that requires neither electrode manipulation nor hard-to-manufacture elastic channels. The approach is inspired by the respiratory system networks found in insects, and the rhythmic tracheal compression observed in these systems that induces multiple contractions along the tracheal tubes constituting the network to pump fluid and possibly promote enhanced mixing in certain pumping regimes.

The introduction is organized into two parts: In the first part, a brief introduction to the insect respiratory system, tracheal networks, and their rhythmic contractions which are believed to be the main driving force behind transporting fluid in these networks is given in section1.2. The second part summarize some of the previous theoretical and numerical investigations that form basis for our mathematical analysis efforts in modelling fluid-filled tubes and channels with moving wall contractions,as it will be given in section 1.4.

1.2 Insects Respiration as a Bioinspiration Model

Bioinspiration and biomimetics are an increasingly multi-disciplinary field that seek to imitate systems and processes from the life sciences to design improved engineering devices. For example, insects respiration is a natural process that have shown to mange airflow distributions within their tracheal networks very efficiently compared to current state-of-the-art microfluidic devises, and therefore it can be used as an inspiration model for mimicking novel micropumping devices.

This dissertation proposes a bioinspired pumping model that relies on tube wall collapses in inelastic tubes, rather than wave propagation dynamics in elastic tubes, and seeks to establish a third pumping paradigm found in nature, in addition to the much-studied peristaltic and valveless impedance pumping mechanisms. The present study introduces this new pumping paradigm, and an analytical model for it. It is hoped that the model for this valveless pumping mechanism will lead to the development of novel biomimetic microfluidic devices for transporting fluids in a controlled manner at the microscale regime.

In other words, this study is inspired and motivated by microscale internal flow transport phenomena in insect respiration networks and proposes novel micropumping mechanism that is expected to work efficiently at the microscale. More specifically, the approach is mainly inspired by the tracheal networks found in these physiological networks, and the multiple rhythmic tracheal contractions (RTC) regime causing the tracheal network to pump fluid in an efficient manner Westneat et al. (2003). In addition, the present study is motivated by the discussion raised by Chu (2004), which relates the transport of fluid flow within a microtube to the contractions found in the insect physiological system.

The details about the structure of the insect respiration process, structures of the tracheal network, and the rhythmic tracheal compressions found in these systems can be found in Harrison (2003a,b); Westneat et al. (2003);Socha et al. (2008); Westneat et al. (2008); Socha et al. (2010) and explained in the follwoing subsections 1.2.1 and .

1.2.1 Insect breathing via Tracheal Networks

Insects use a complex physiological network to deliver sufficient fresh oxygen to their body cells and to remove out carbon dioxide. The respiration system in most insects composed of a network of tubes called tracheal system, which composed of a complex network of tubes called tracheae (a few μm in size). The network branches again into smaller tubes known as tracheoles which is ($\sim 1\mu m$) in size. The structure of the tracheal tubes have reinforcement windings called taenidia, which might have a role of in preventing tracheal tubes from any failure due to the periodic wall compressions-inflations motions. This respiration network is responsible of carrying air directly

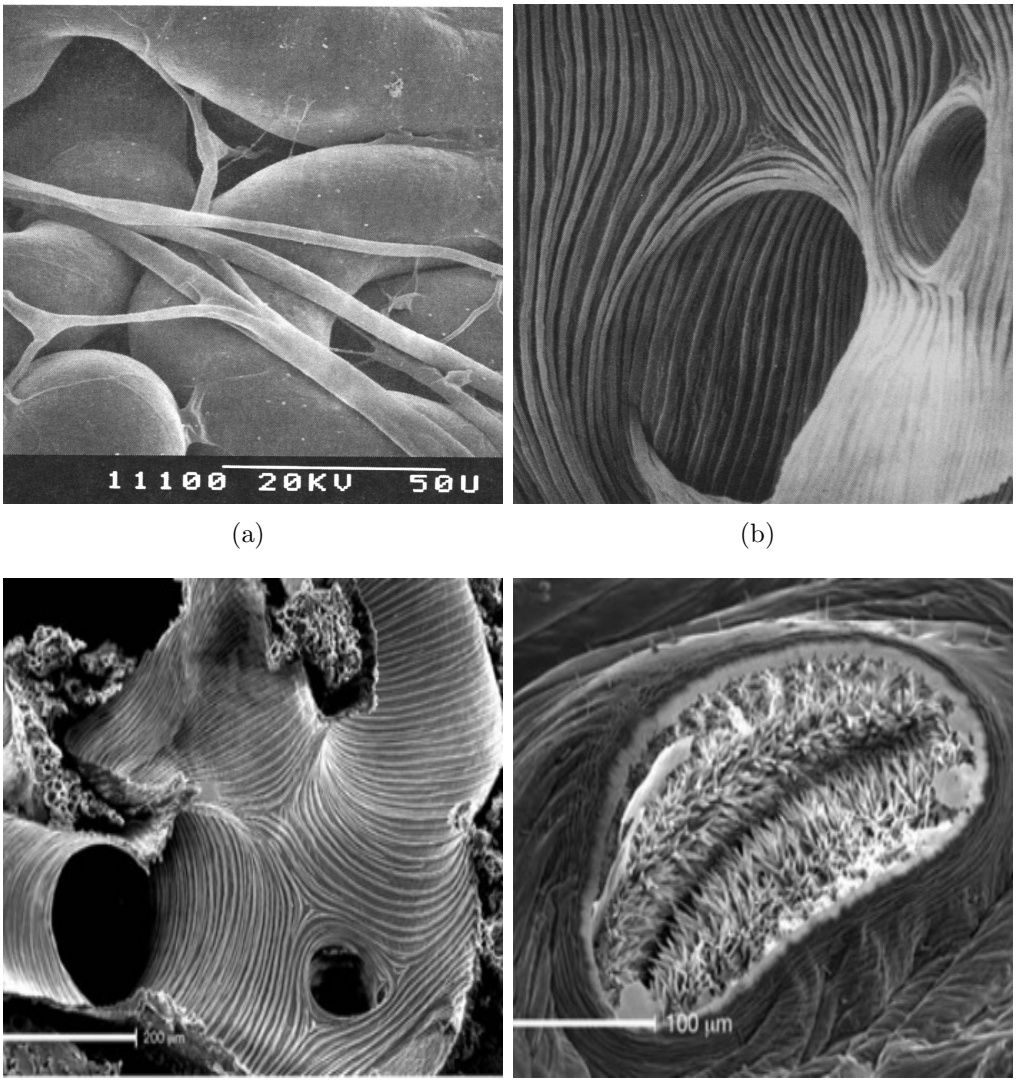

(a) (b)

(c) (d)

Figure 1.1: A Scanning electron microscope (SEM) of a tracheal tube of a Caribbean fruit fly: (a)View of tracheal branching into many fine tracheoles, (b) A cut-away view inside of a large trachea showing the onset of two smaller tracheae and taenidial windings, (c) Complex tracheal system cut and (d) Spiracle. Figures (a-b) are reprinted by permission from CRC Press: Nation, J. L., Insect Physiology and Biochemistry. Copyright (2008). Figures (c-d) are reprinted by permission from Macmillan Publishers Ltd: [Nature]. Burmester, T., A welcome shortage of breath. vol. 433, pp. 471–472. Copyright (2005)

to cells tissue for various gas exchanges. The tracheae tubes receive the fresh air via a valve-like opening called spiracles, which are openings at the body surface and distributed along their extraskelton, see Nation (2008); Burmester (2005). A scanning electron microscope (SEM) of a tracheal tube that shows branching, taenidia reinforcements and spiracles are shown in Fig.1.1.

More details about the insect respiratory system, the tracheal tube network and its structures are given in book chapters by Harrison (2003b,a); Nation (2008). These book chapters explain how airflow transported along the tracheal system by both diffusion and convection respiration. In addition, it covers the mechanics of each component of the tracheal tube functions such as spiracles openings and closed valve-like mechanisms.

In general, the insect breathing process relies on transporting a small amount of airflow along their tracheal system by mainly diffusion and possibly convection modes at the microscales. The airflow inside these insect network might be tidal or directed, depending on the insect class and their physiological systems. Since, the flow transport process within these tracheal networks is important phenomena, insects use their body movements and/or multiple wall contractions along the tracheal network to enhancing the convected airflow and producing tidal or directed airflow. Therefore, the observed rhythmic wall contractions along the tracheal network are believed to be the main deriving force for internal flow pumping in these physiological networks Westneat et al. (2003). The former will be discussed in the next subsection 1.2.2.

1.2.2 Rhythmic Wall Contractions

Rhythmic wall contractions are observed at multiple locations in insect tracheal tubes Westneat et al. (2003). They are believed to be the main deriving mechanism or the main gears to a natural pumping mechanism that efficiently deliver and transport fresh air to every cell Westneat et al. (2003); Harrison (2003b); Socha et al. (2008). Contractions exist in sequences (series) with different patterns along the tracheal network and are naturally set to move in the tube lateral direction. The motions of contractions is induced as a result of internal pressure variations or alternations that might be produced by the entire body movements action or by the hemolymph circulations Westneat et al. (2003). The observed patterns due to the rhythmic contractions in the tracheal

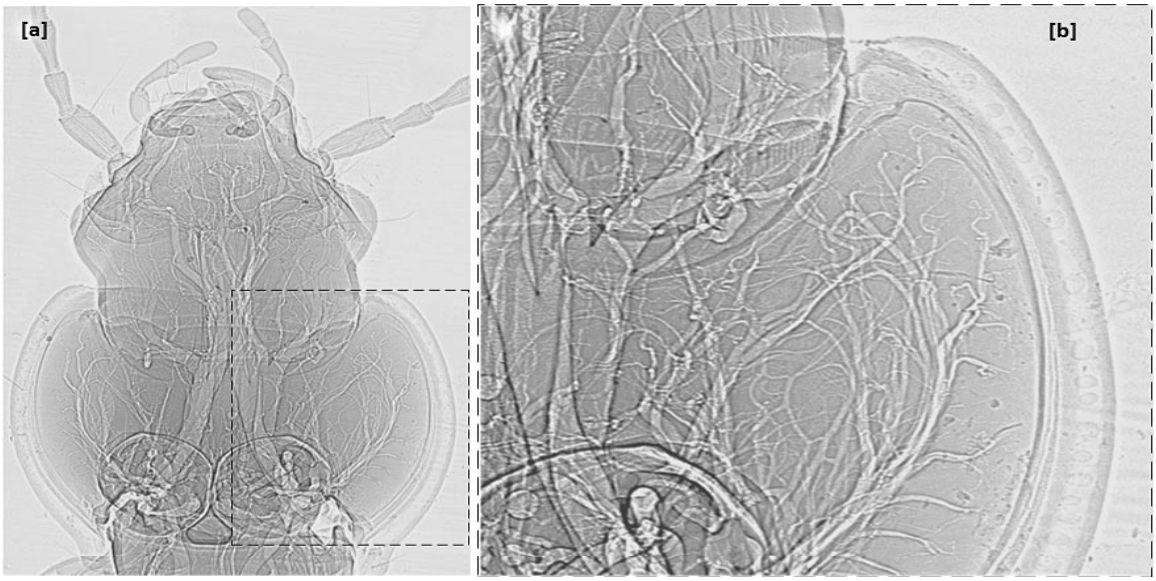

Figure 1.2: Synchrotron phase-contrast X-ray image of the tracheal system of the carabid beetle. (a) Head and prothorax view. (b) Zoom-in view of prothoracic tracheae (from the red box in panel a),illustrating the complex branching patterns of tracheae. Image is taken from Westneat et al. (2008)

system in insects attract many researchers for further investigations. For instance, visualizations using synchrotron X-ray are used to monitor the patterns of the body motion in three different living insects. Results have shown that, the insects tracheal tubes exhibit rabid cycles of compression and expansions which are believed to be the main driving force for transporting the airflow. The kinematics of the tracheal compressions is characterized by further investigation using X-ray videos on several beetles that have different masses Socha et al. (2008). Results have shown that, the compression pattern of the tracheal tube is characterized by three main phases namely, collapse region followed by a static compression and ended by re-inflation region. In this study, we propose a theoretical study that describes the airflow motions induced by these periodic form of the rhythmic tracheal collapses and re-inflations found in insects. An image experimented by X-ray technique is given in Fig.1.2 to show the tracheal network complexity and the associated rhythmic collapses.

To further understand the contraction patterns, visualizations using synchrotron X-rays are used to record videos that monitor the patterns of the body motion in three different living insects. Results have shown that insects exhibit rabid cycles of tracheal compression and expansions which

is somehow analogous to inflation and deflation of lung system. The kinematics of tracheal compression is characterized by further investigation using X-ray videos on two beetles having different masses, Socha et al. (2008). It have been found that, the compression pattern of the tracheal tube is characterized by three phases namely, collapse region followed by a static compression and ended by reinflation region. Furthermore, in a recent article by Socha et al. (2010) a summary of the tracheal architecture in insects that use convection is laid out to confirm the previous work by Westneat et al. (2003). The periodic form of tracheal collapse and reinflation which is now known as rhythmic tracheal compression according to Westneat et al. (2003) was clearly explained. However, the relationship between the airflow transport and the wall contraction is not yet fully determined. Possible connections between physiological wall movements or contractions and the induced flow transport in these systems are introduced by Macagno and Christensen (1980) and will be given in the next subsection 1.3.

1.3 Flow Transport by Wall Contractions

Although, the shape, mechanics, dynamics of the rhythmic tracheal compressions as well as their effect on the induced flow transport process in physiological networks are still not fully understood. Several theoretical and experimental research attempts are proposed in the past aiming to find this connection/relationship. For examples, Macagno and Christensen (1980); Macagno et al. (1982) have proposed two possible scenarios that might explain the link between inter flow transport and wall actions in physiological systems, which can be summarized as follows

1.3.1 Peristaltic (Propagative) Transport

Fluid transport in flexible tubes/channels can be induced by longitudinal travelling waves generated by wall contractions and expansions motions, which known as the phenomenon of peristaltic flows. For instance, within physiological systems, the peristaltic motion is observed in both locally (local peristalsis)or globally (along whole skeleton material length) format as a result of smooth progressive muscle contractions-expansions. Peristalsis mechanism has found to imitate several naturally

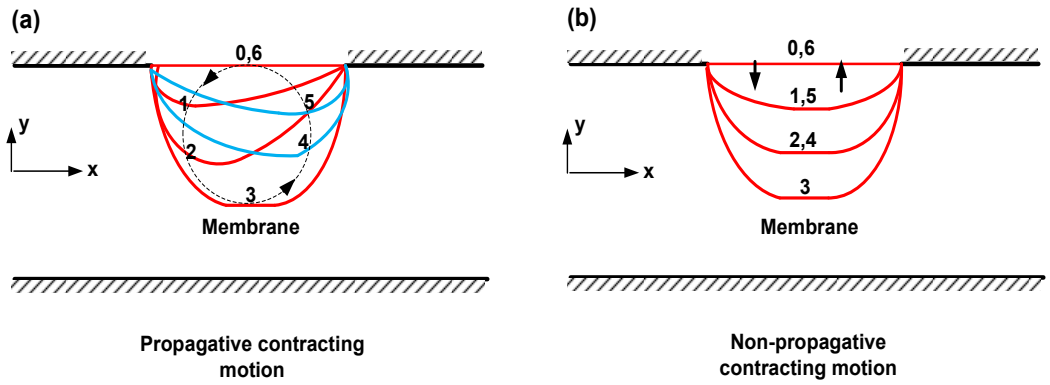

Figure 1.3: Non-propagative and propagative contractions. Numbers indicate sucessive positions of the peak profile.

occurrence biological flows such as, blood pumping and transporting urine from kidneys through the ureters into the bladder and in several other examples. The phenomenon is well addressed in the literature and has gained much attention in the past, see Jaffrin and Shapiro (1971). There are several models are proposed to explain the peristaltic pumping by assuming series of successive sinusoidal waves in two dimensional channels or axisymmetric tubes with infinite length, see Shapiro and Jaffrin (1969), Fung and Yih (1968) and several other. These mathematical models assume infinite tube length, long wavelength, small wave amplitudes and low Reynolds number approximations. A generalization to the above models that accounts for finite length tubing, arbitrary wave shape and wavenumber is given by Li and Brasseur (1993).

Although, the shape of the wave that propagates in the wall of flexible tube such as the one belongs to biological systems is not known apriori. Several mathematical modeling is used to explain the peristalsis mechanism based on harmonic wave forms with small amplitudes and large wavelengths. Further studies have looked at the effect of using different wave shapes on the peristaltic pumping characteristics, Hariharan et al. (2008) and Hayat et al. (2009). Results obtained suggest that maximum pressure gradient is obtained when rectangular wave form is used as the flow exciter and hence it has the best pumping characteristics while the triangular wave form has the worst performance. Since the pumping efficiency depend strongly on the wave forms, a complete wave shape optimization code is developed to study peristaltic pumping by Walker and Shelley (2010). Wave shapes that are not obvious and not reported before in the literature are found to be optimum

for peristaltic pumping. These waves are far from being sinusoidal and they are asymmetric in shapes. The main point in here is; the shape of the wave plays an important role for efficient peristalsis transport. It should be mentioned that, most analyses in the literature are given to model a class of peristaltic flow problems induced by infinite wall lengths, except the pioneered work by Li and Brasseur (1993) of modeling progressive contractions over a finite length tube for an arbitrary wave shape and wavenumber was first given in using the lubrication theory approach Batchelor (1967). Moreover, finite element simulations are given by (Thien and Low, 1989) to study the flow induced by contractions of localized progressive wall motions of a triangular wave-like that belongs to class of problems as shown schematically in Fig.1.3(a).

1.3.2 Non-Peristaltic (Non-Propagative) Transport

There is another class of wall motions namely, non-peristaltic, stationary and/or non-propagative contractions as the one shown schematically in Fig.1.3(b) are also observed in many of physiological systems. According to a review article by Macagno and Christensen (1980), the flow transport by this class of wall motions are not fully investigated. Although, this class of contractions are believed to be of importance in many physiological systems and seems to be relevant to our study of modeling the flow transport by rhythmic tracheal collapses found in insect's respiratory systems. This non-propagative wall contractions could result from a thin annular bundle of muscle cells that move simultaneously and dragging passive cells over a certain length from both sides see Macagno and Christensen (1980) for more details. This class of non-propagative contractions assumes that, all wall successive movements take place in the lateral directions over a finite length and normal to the plane axis of symmetry as shown in Fig.1.3(b). Although, these classes of contractions might yield an important physical explanation for how flow is transported within many of biological systems at the microscale flow regime.

Although, there is no deep theoretical analysis available to treat flow induced by this type of contractions shown in Fig. 1.3. This dissertation attempts to study the non-propagative class of contractions using both theoretically and meshfree computational methods. In the next section 1.4, we list previous researches that have been attempted to model flow transport by moving wall actions. Those citations are chosen carefully and we believe in, they are directly related to the

work presented in this dissertation and form a basis to our theoretical analysis and numerical computations efforts.

1.4 Literature Reviews

Flow motions in physiological systems that suffer from wall contractions are considered to be unsteady because of their Pulsatile wall motions. As a results, These physiological flows are hard to model analytically and challenging to simulate numerically. However, there exist several theoretical and numerical studies that have been used to model induced flow motions and sequencing flow problems in a confined domain with moving boundaries. These attempts along with the numerical tools used in, can be adopted and become useful to the study conducted in this dissertation. A summary of those previous researches is given in following subsections 1.4.1 and 1.4.2,

1.4.1 Theoretical Modelling Review

Although the induced flow motions and fluid transport within collapsible tubes and channels are complex and unsteady because of the tube-channel dynamical wall motions, several simplified analysis have been developed to understand these types of flows. For instance, a similarity solution for the unsteady viscous flow in a semi-infinite pipe with either contractions or expansions is given in Uchida and Aoki (1977)[2]. In that study, the radius of the pipe is uniformly collapsed, and the problem of the non-linearity is retained in full. The solution obtained is general and valid even when the pipe is fully collapsed. The two-dimensional flow field for incompressible viscous flows in an infinitely long channel induced by prescribed pulsatile and sinusoidal wall motions with small amplitudes is given in Secomb (1978).

The unsteady squeezing of a viscous fluid from a shrinking or expanding tube is given analytically in Skalak and Wang (1978). In that study, the full Navier-Stokes equations are reduced to a single non-linear ordinary differential equation that is a function of a squeezing parameter that marks the relative importance of unsteadiness and viscous effects. The equation is solved for the case where the unsteady effect is dominant using asymptotic expansions. A subsequent article by the same group

using the same mathematical approach investigates the squeezing of a viscous fluid from a tube at an arbitrary rate, which is characterized by a dimensionless squeezing number. The solution is restricted to low squeezing numbers, a regime in which the viscous effects dominate the unsteadiness induced by the wall motions Wang (1980). A generic approach to studying the squeezing flow problem between parallel plates (rectangular or circular) using a similarity transformation to reduce the Navier-Stokes equations to a non-linear ordinary differential equation which can then easily be solved numerically is presented in Singh et al. (1990).

Theoretical models for channel flows in which the channel wall undergoes localized contractions are somewhat more involved and have greater relevance to what has been observed in physiological systems and to subsequent bio-inspired microfluidic fabrication efforts. For example, in a review article by Macagno and Christensen (1980), two main types of localized muscle contractions, stationary and progressive (local peristalsis), have been observed in the human duodenum. These contractions produce fluid transport in the human intestine. An important conclusion from this review article supported by a basic theoretical analysis is that at least two stationary contractions operating with slightly time lag (phase lag) are needed in order to produce a net flow. Moreover, the characteristics of the phase lag between the wall contractions have been found to affect the laminar mixing in the human intestine Macagno et al. (1982). Other examples of physiological systems with localized wall contractions are given in Westneat et al. (2003); Socha et al. (2008). It has been discovered that in ground beetle respiratory systems, the tracheal tubing network undergoes periodic localized collapses and re-inflations. These motions are known as rhythmic tracheal compressions Westneat et al. (2003). The kinematics of these contractions were characterized using X-ray synchrotron imaging to visualize the respiratory systems in different ground beetles species Socha et al. (2008).

The problem of flow induced in an enclosed conduit due to localized wall contractions is more closely related to the work we present here than the previous examples cited. Several theoretical, experimental, and computational studies have been carried out to model this particular problem. In Pedley and Stephanoff (1985), the flow along a channel with a time-dependent indentation assigned to one wall is explored. In Ralph and Pedley (1988), a theoretical analysis of the same system combined with experimental studies is given for different values of observed Reynolds num-

ber and Strouhal number. Detailed flow structures, including the generation of vorticity waves downstream of the contraction region, are observed and are confirmed by numerical simulations using the vorticity-stream function formulation of the governing equations. In Mahmood and Merkin (1990), a simplified analysis of the flow in a narrow duct with an indentation on one side wall is given. The wall deformation is kept fixed in time, and an explicit expression for the flow stream function at low Reynolds number is derived.

At this point, we should mentioned that, an important distinction between the problems investigated in Uchida and Aoki (1977); Secomb (1978); Skalak and Wang (1978); Wang (1980); Singh et al. (1990) and the work present in this dissertation is that the channel walls in Uchida and Aoki (1977); Secomb (1978); Skalak and Wang (1978); Wang (1980); Singh et al. (1990) analyses undergoing rigid body motion wherein a uniform wall collapse is introduced, rather than the independent, localized wall motions that are the focus of this dissertation. Moreover, in this dissertation, the peristaltic flow modelling of progressive wavy contractions and expansions over a finite length tube by Li and Brasseur (1993) using the lubrication theory approach Batchelor (1967) is adopted inhere to model the flow in a channel with wall contractions that move in a non-peristaltic fashion. Moreover, this work is motivated by the work presented in Chu (2004) and Aboelkassem and Staples (2012a,b); Aboelkassem et al. (2011), which relate the transport of fluid flow within microtubes or microchannels to vessels with moving wall contractions found in the insect physiological system Westneat et al. (2003); Socha et al. (2008).

The main goal of this study is to explore the idea of using a channel with two collapsing sites that move with time (phase) lags with respect to each other as a pumping mechanism. As a first attempt towards the solution of this problem that have been encountered in many of insects physiological systems, a quasi-steady model is derived by reducing the unsteady Navier-Stokes equations to a steady counterpart that are then solved analytically. The theoretical derivations relies mainly on the assumptions of using slow contractions movements where the wall motion history is neglected and the unsteadiness effect is omitted from the governing equations. The time dependence effects is introduced via a series of steady wall motions as it is given in details in chapter 2. In other words, the wall contractions are assumed to move in a slow fashion, and hence, the flow field is assumed to not depend on the wall motion history and behaves as series of steady states. Although,

the quasi-steady approximations are employed in this dissertation, the reader should be aware that there might be an accumulation of errors due to the use of these assumptions, but the qualitative nature of the flow behaviour will not be altered according Feng and Josepf (1995). Furthermore, the derived analytical solution is then validated numerically using Stokeslets-MFS to the steady Stokes equations with time-dependent Stokeslets strength coefficients. More details about the numerical method used in this dissertation will be given in section 1.4.2 and in chapter 4.

1.4.2 Stokeslets-Meshfree Method Review

On the computational side, meshfree computations and more specifically on the method of fundamental solutions (MFS) is considered to be an efficient numerical technique for solving elliptic class of boundary value problems (BVP) with moving boundaries. The development of this method over the past decades a combined with supported examples for solving Stokes flow problems in confined and unconfined domains can be found Smyrlis (2009). In general, the MFS is used to construct or to approximate the stokes flow regime by using a set of fundamental solutions based on point force singularities called Stokeslets, details are given in Pozrikids (1992).

Basically, there are two available techniques for implementing the MFS, both techniques require of introducing the Stokeslets with unknown force coefficients. The unknown coefficients are then evaluated by satisfying the proper boundary conditions and solving the emerging linear system of equations. In the first approach, the Stokeslets are usually collocated at locations outside the domain of interest with a specific distance. This distance can be then optimized iteratively for better performance and solutions convergence of the emerging linear system of equations. This approach was sucessfully implemented to several problems Young et al. (2006, 2005); Tsai et al. (2006b,a); Hu et al. (2005); Chen et al. (2005). In the second approach, the classical Stokeslet velocity expression given in Pozrikids (1992)) is modified to derive a regularized version of Stokeslets Cortez (2001). This method have been used extensively to solve the Stokes flow in the presence of immersed boundaries and obstacles and three dimensional Stokes problem as well Cortez et al. (2005). Moreover, the method of regularized Stokeslets Cortez (2001) is then developed by using image methods in order to impose zero-flow boundary conditions for for plane wall problems Ainley et al. (2008). Furthermore, the (MFS) has been applied successfully to variety of Stokes flow

problems for various microfluidics applications Zhao and Povitsky (2009, 2011).

It should be mentioned here that although the MFS is relatively easy to implement and does not require any computational grid, it still suffers from some issues related to non-invertible or ill-conditioning matrix problem associated with finding the force-coefficients. This drawback can lead to inaccurate force coefficients and consequently wrong flow field. A solution to non-invertible matrix problem is found by either collocating the Stokeslets sources a distance away from the domain boundaries as given in (Young et al., 2006, 2005) or by using regularized Stokeslets expressions as derived by Cortez (2001). However, still the ill-conditioning matrix issue represents a challenging problem for the MFS to be correctly implemented. An efficient numerical algorithm by Neumaier (1998) to solve ill-conditioned linear system of equations, can be coupled with the MFS to predict accurate Stokeslets force strengths.

1.5 Dissertation Statement and Outline

Transporting small amount of fluids within network of channels by using an efficient means is a challenging problem and of importance in many of scientific applications. For example, microfluidic devices are normally composed of multiple branches that usually used used for mixing purposes, cell manipulations, drug delivery via transporting microliters of fluid from one site to another in a controlled and directional manner.

The work presented in this dissertation is inspired by the rhythmic tracheal compressions phenomena found in insects and the hypothesis of using these contractions as natural pumping mechanism. This study proposes a novel pumping paradigm via two versions of a novel bioinspired fluid flow transporting mechanism that is neither peristaltic nor belongs to impedance mismatch class of pumping mechanisms. This insect-inspired pumping models presented here are expected to function efficiently in the microscale flow regime in a simple channel/tube geometries or a complex network of channels. Both theoretical analysis and Stokeslets-meshfree computational methods are used to conduct the results presented throughout this work. The dissertation contents are organized in separate chapters and summarized in these outline as follows:

- In chapter 1, A brief introduction about our biologically inspiration model, discussions related to various transporting flow mechanisms, list of previous researches that are directly related to work conducted in this dissertation are given.

- In chapter2, a novel bioinspired pumping paradigm "ghost-valve pumping principle" is derived via solving the induced flow motions in confined domains namely tubes and channels with moving non-propagative, non-peristaltic wall contractions.

- In chapter 3, the constrained optimization technique based on the global minima approach is used to optimize our derived bioinspired pumping models for efficient net flow production.

  This chapter gives the optimum spatial and temporal parameters used to The optimization results are given for both tubes and channels models with moving wall contractions as explained previously in chapter 2.

- In chapter 4, the Stokeslets-meshfree computational method are used to validate our derived bioinspired pumping theory given previously in chapter 2. The numerical validation process covers both tube and channel pumping models.

- In chapter 5, a new pumping protocol "selective-pumping-in-a-network" for selectively transport fluids at microscale in complex network of channels is presented. The concept enables fluids to be transported, controlled and properly directed to chose a specific branch in the network and avoid other without the use of any mechanical valves.

- In chapter 6, three-dimensional meshfree simulations are given for both tubes and channels. The 3D Stokeslets MFS approach are also used to compare and validate the 3D results with our 2D theoretical analysis derived previously in chapter 2. The effect of using non-symmetrical collapses on the time averaged net flow is also investigated. These 3D results will be also used to confirm our pumping hypothesis claimed throughout this dissertation.

- In chapter 7, Conclusions that summarize the findings from this dissertation is give.

Chapter 2

Bioinspired Pumping Models via Theoretical Analysis: A Ghost-Valve Principle

Novel bioinspired pumping models are given in this chapter. The present analysis develops a new concept of using wall contractions to induce a moving stagnation line/plane across the tube or channel, which act as a "ghost-valve" and is capable of producing a unidirectional net flow. The bases of the derived mathematical modelling and analysis presented here are the lubrication theory at low Reynolds flow regime and the quasi-steady approximations. The presented models are given to solve the induced flow motions in confined domains namely tubes and channels with moving non-propagative, non-peristaltic wall contractions.

2.1 Bioinspired Tube Pumping Model

Inspired by respiratory systems in insects, in particular the nonpropagative, rhythmic wall contractions found in insect tracheal tubes, we propose a novel bioinspired, non-peristaltic model for fluid pumping that can work particularly well at the low Reynolds number flow regime. Incompressible,

viscous flow transport in a fluid-filled axisymmetric, inelastic tube is modelled using lubrication theory. The wall contractions are prescribed via a tube wall profile that includes multiple wall indentation sites. These wall contractions can move with or without phase(time) lags with respect to each other. The results demonstrate that, using an inelastic tube with at least two collapsing sites can produce a unidirectional flow. The flow field, pressure distributions, wall shear stress, and the time averaged net flow rate induced by a complete wall collapsing cycle are calculated analytically. The effects of the wall contraction parameters on the pumping efficiency are also studied. The present insect-inspired pumping model will be validated using the method of fundamental solutions, Stokeslets-based meshfree computational method in chapter 4.

2.1.1 Problem Formulation

Consider the motion of an incompressible viscous flow inside a single tracheal tube segment that belongs to the respiratory network of an insect, shown schematically in Fig. 2.1 (a). The tube is assumed to have a uniform circular cross-section of radius R and a finite length L as shown in Fig. 2.1 (b). We define the tube aspect ratio as $1/\delta$ which is assumed to be a very large, i.e., $\delta = R/L << 1$. The tube wall is assumed to suffer from a single or multiple localized contractions. The kinematics and the geometry of these contractions are governed by a generic tube wall profile $H(x,t)$, which will given in details in the result section. The wall profile allows each contraction to move independently along the lateral direction with or without phase lags θ_{12} with respect to each other as shown in Fig. 2.2. A zero pressure drop $\Delta p = 0$ is assumed along the channel length, and only two moving contractions with phase lag are actuated. In other words, we study the flow induced by the wall contractions rather than pressure driven flow. The velocity field, pressure gradient, wall shear stress, and the net flow rate induced by the movements of the wall contraction-expansion protocols are predicted. The effects of the contraction parameters such as, the collapse amplitudes and the phase lags on the net flow produced by these wall contractions are given. The main objective of this work is to investigate the ability of using a tube as described above with local contractions as a pumping mechanism at microscale without using any pressure drop or any mechanical valves.

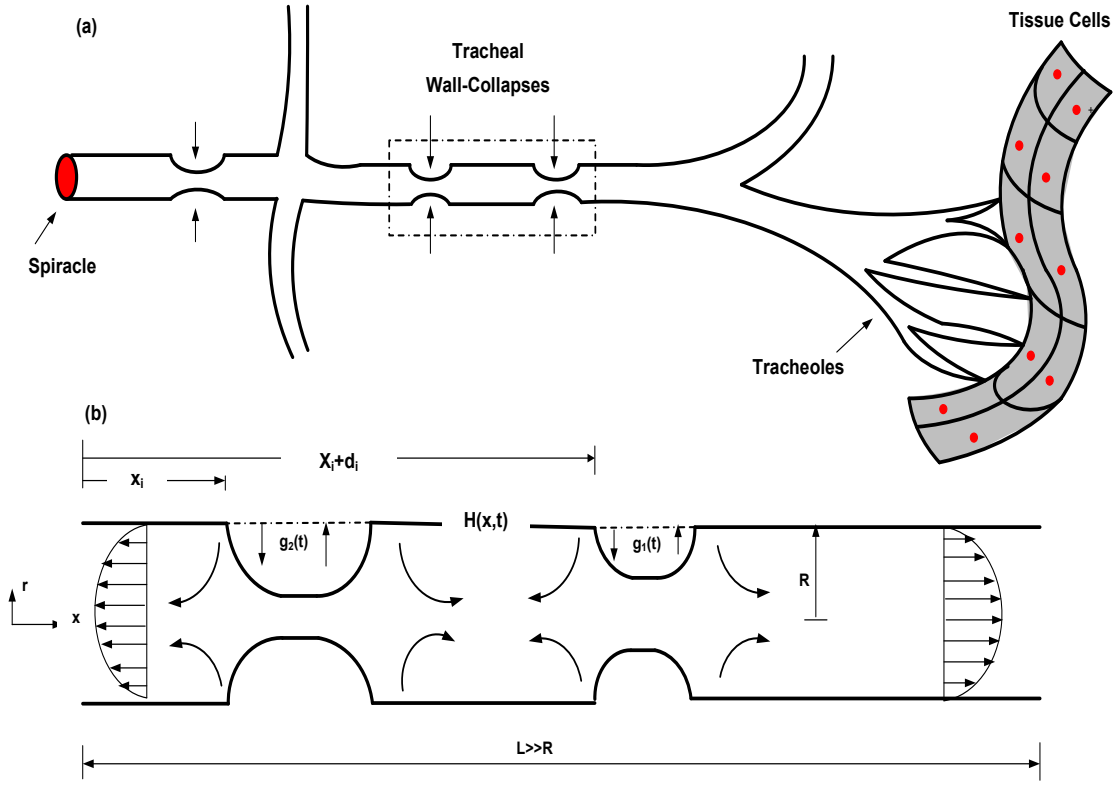

Figure 2.1: The Problem formulation:(a)Schmatic to simplified insect physiological network.(b)Schmatic to a single tracheal tube shape as prescribed by wall expression $H(x,t)$.

2.1.2 Mathematical Modeling

In this section, a simplified mathematical model that can describes the induced flow motions due to the rhythmic wall contractions is derived based on the the lubrication theory. The tube is assumed to be a 2-D axisymmetric with a very high aspect ratio i.e., $\delta = R/L << 1$. The flow is assumed to be Newtonian, incompressible, and isothermal with constant viscosity μ and having a velocity field $\mathbf{V} = (V_r, 0, V_x)$. Let us introduce the following non-dimensional parameters: $x = x^*/L$, $r = r^*/R$, $H = H^*/R$, $t = t^*/(L/u_o)$, $V_x = {V_x}^*/u_o$, $V_r = {V_r}^*/\delta u_o$, $p = p^*R^2/(\mu u_o L)$, $\tau_{rx} = {\tau_{rx}}^*/(\mu u_o/R)$, $Q = Q^*/(u_o \pi R^2)$, $S_t = fL/u_o$, $R_e = \rho u_o R/\mu$. where, V_x and V_r are the velocity components along axial x and vertical y direction respectively. p is the static pressure,τ_{xy} is the shear stress, and Q is the volumetric flow rate. S_t, R_e is the Strouhal and Reynolds numbers respectively. f is

the frequency at which the contractions move and t is the time scale involved in the problem. u_o is an arbitrary reference velocity. Now, if we recall the Navier-Stokes equations in the Cartesian coordinate system and substituted back using the above non-dimensional parameters, the governing equations reduces to

$$\frac{1}{r}\frac{\partial}{\partial r}(rV_r) + \frac{\partial V_x}{\partial x} = 0 \tag{2.1}$$

$R_e\delta^3\left[\frac{\partial V_r}{\partial t} + V_r\frac{\partial V_r}{\partial r} + V_x\frac{\partial V_r}{\partial x}\right] =$

$$-\frac{\partial p}{\partial r} + \delta^2\left[\frac{\partial^2 V_r}{\partial r^2} + \frac{1}{r}\frac{\partial V_r}{\partial r} - \frac{V_r}{r^2} + \delta^2\frac{\partial^2 V_r}{\partial x^2}\right] \tag{2.2}$$

$R_e\delta\left[\frac{\partial V_x}{\partial t} + V_r\frac{\partial V_x}{\partial r} + V_x\frac{\partial V_x}{\partial x}\right] =$

$$-\frac{\partial p}{\partial x} + \left[\frac{\partial^2 V_x}{\partial r^2} + \frac{1}{r}\frac{\partial V_x}{\partial r} + \delta^2\frac{\partial^2 V_x}{\partial x^2}\right] \tag{2.3}$$

Here, we are interested in solving the above equations analytically by making use of the following facts. The flow is at the microscale, where the viscous effects is dominant i.e., we deal with a low Reynolds number flow regime $R_e \in [0, \delta]$. In addition, the channel geometry is restricted to a very high aspect ratio i.e., ($\delta << 1$) which means that, the classical lubrication theory is applicable. Therefore, the above system of equations along with the above mentioned flow regime can be further simplified by neglecting all terms that of order δ^2 and higher,

$$\frac{1}{r}\frac{\partial}{\partial r}(rV_r) + \frac{\partial V_x}{\partial x} = 0 \tag{2.4}$$

$$\frac{\partial p}{\partial r} = 0 \tag{2.5}$$

$$\frac{1}{r}\frac{\partial}{\partial r}(r\frac{\partial V_x}{\partial r}) = \frac{\partial p}{\partial x} \tag{2.6}$$

subjected to the following boundary conditions,

(i) at $r = 0$, $V_r = 0, \frac{\partial V_x}{\partial r} = 0$

(ii) at $r = H(x,t)$,$V_r = \frac{\partial H}{\partial t}$,$V_x = 0$

(iii) at $x = 0$, $p = p_o(t)$

(iv) at $x = 1$, $p = p_L(t)$

Since equation2.5 conclude that, the static pressure is uniform along the radial direction and varies only along the axial direction, i.e., $p = p(x,t)$. Therefore, equation 2.6 can be integrated twice with respect to r and by applying the related boundary conditions, an explicit formula that can explain how the axial velocity component V_x varies

$$V_x(r,x,t) = \frac{1}{4}\frac{\partial p}{\partial x}\left(r^2 - H^2\right) \tag{2.7}$$

Also, by using equation 2.4 and satisfying the related boundary conditions, the radial velocity component V_r is given as,

$$V_r(r,x,t) = \frac{r}{4}\left[H\frac{\partial H}{\partial x}\frac{\partial p}{\partial x} - \frac{1}{4}\frac{\partial^2 p}{\partial x^2}\left(r^2 - 2H^2\right)\right] \tag{2.8}$$

Applying equation 2.8 with the boundary condition at $r = H$, where $V_r = \frac{\partial H}{\partial t}$, a relationship between and the axial pressure gradient $\frac{\partial p}{\partial x}$ and the time rate at which the tube wall moves $\frac{\partial H}{\partial t}$ can be found as,

$$\frac{\partial H}{\partial t} = \frac{H^3}{16}\frac{\partial^2 p}{\partial x^2} + \frac{H^2}{4}\frac{\partial H}{\partial x}\frac{\partial p}{\partial x} \tag{2.9}$$

An expression for the pressure gradient $\frac{\partial p}{\partial x}$ along the axial direction is derived by multiplying both sides in equation 2.9 by $16H$ and integrating once with respect to x yields

$$\frac{\partial p}{\partial x} = \frac{1}{H^4(x,t)}\left(G(t) + 16\int_0^x H(s,t)\frac{\partial H(s,t)}{\partial t}ds\right) \tag{2.10}$$

where, $G(t)$ is a function of integration that depends only on time t and to be determined after integrating equation 2.10 with respect to x where an expression for the pressure can be found as,

$$p(x,t) = p_o(t) + \int_0^x \frac{\partial p(s,t)}{\partial x}ds \tag{2.11}$$

Now, by evaluating equation 2.11 at $x^* = Li.e., x = 1$ where $P = P_L(t)$,an expression to $G(t)$ can be found be as,

$$G(t) = \frac{\Delta p - 16 \int_0^1 H^{-4}(s,t) \left(\int_0^s H(s_1,t) \frac{\partial H(s_1,t)}{\partial t} ds_1 \right) ds}{\int_0^1 H^{-4}(s,t) ds} \tag{2.12}$$

where,$\Delta p(t) = p_L(t) - p_o(t)$. Also, it should be noted that $\frac{\partial^2 p}{\partial x^2}$ term is needed to find the radial velocity V_r component as shown in equation 2.8. The is can be evaluated from equation 2.9 once the pressure gradient is determined. An expression for $\frac{\partial^2 p}{\partial x^2}$ can be given a,

$$\frac{\partial^2 p}{\partial x^2} = \frac{16}{H^3} \frac{\partial H}{\partial t} - \frac{4}{H} \frac{\partial p}{\partial x} \frac{\partial H}{\partial x} \tag{2.13}$$

Using the non-dimensional parameters as before, a non-dimensional shear stress τ_{rx} in $(r-x)$ plane can be derived and given as,

$$\tau_{rx}(x,t) = \delta^2 \frac{\partial V_r}{\partial x} + \frac{\partial V_x}{\partial r} \tag{2.14}$$

by neglecting all terms that of order δ^2, a simple expression for the shear stress can be given as,

$$\tau_{rx}(x,t) = \frac{\partial V_x}{\partial r} = \frac{r}{2} \frac{\partial p}{\partial x} \tag{2.15}$$

The wall shear stress can be evaluated by setting $r = H$ in the previous equation,

$$\tau_{rx}(x,t) \downarrow_{r=H} = \frac{H}{2} \frac{\partial p}{\partial x} \tag{2.16}$$

similarly, an expression for the volumetric flow rate $Q(x,t)$ induced by the tube wall motion can be given as,

$$Q(x,t) = \int_0^{H(x,t)} V_x(x,r,t) r dr \tag{2.17}$$

using equation 2.10 and perform the integration yield,

$$Q(x,t) = \frac{-1}{8} \frac{\partial p}{\partial x} H(x,t)^4 \tag{2.18}$$

It should be noted that once the tube wall profile $H(x,t)$ is prescribed, the static pressure can be evaluated using equation 2.10 and all the other flow variables can be simply determined. Moreover,

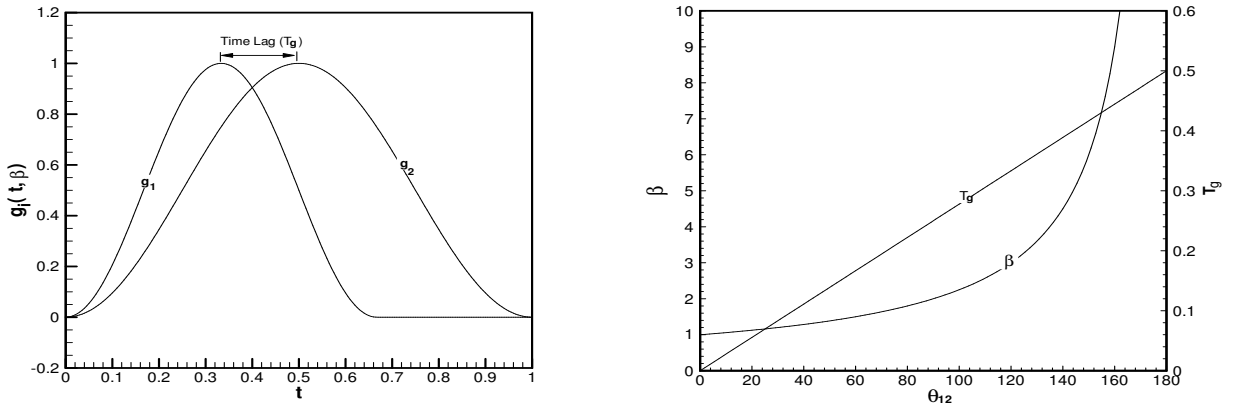

(a) $(g(t,\beta)\text{-}t)$ plane (b) $(\beta\text{-}\theta_{12})$ plane

Figure 2.2: Contraction motion protocol relationships

the above analysis is kept general and the derived equations depends on the prescribed tube wall profile $H(x,t)$, which can accommodate a single and multiple tube contractions. However, we restricted our solution to include only two collapses that moves with phase lag θ_{12} as it will be explained in the next section.

2.1.3 Results and Discussions

The result section is organized as follows: A generic tube wall profile $H(x,t)$ that describes the kinematics, geometry, and the number of local contractions is given at the beginning. This wall profile allows the contractions to move with same or different amplitudes and with or without phase lags relative to each other. The flow filed development structure induced by the wall compressions and expansions motions at specific time snapshots are given in the second subsection. In the last subsection, we show the effect of the contraction parameters such as, amplitudes and the phase lags on the pumping net flow. Moreover, the time averaged volumetric flow rate Q_T over a complete contraction-expansion cycle is studied to explore which contraction setting can produce unidirectional flows. The detailed results are summarized below in the following subsections,

A. Tube Wall Profile $H(x,t)$

Let the mathematical model that describes the kinematics and the geometry of the contractions of the tracheal tube wall be given as,

$$H(x,t) = 1 + \sum_{i=1}^{N} A_i f_i(x) g_i(t) \tag{2.19}$$

where, $f_i(x) \in C^r\,[0,1]$ and $g_i(t) \in C^r\,[0, T = 1/S_t]$ represents the spatial and the temporal distribution of the tube wall shape respectively. N defines the number of contractions used and A_i is the amplitude assigned to each contraction. The spatial form of the above equation imitates the geometry of the tube wall contractions as,

$$f_i(x) = \tanh(\alpha(x - x_i)) - \tanh(\alpha(x - (x_i + d_i))) \tag{2.20}$$

where, $\alpha = 2\pi/\delta$,x_i defines the beginning of each collapse region and $d_i \in (0, 1 - x_i]$ marks its end as shown in figure 1(b). In this paper, we only consider two contractions i.e., $N = 2$, located at $x_1 = 0.25, d_1 = 0.1$ and $x_2 = 0.65, d_2 = 0.1$ respectively. The first contraction moves in time according to the following profile,

$$g_1(t) = \begin{cases} \frac{1}{2}\left(1 - \cos(2\pi\beta S_t t)\right), & 0 \le t \le 1/\beta S_t \\ 0 & 1/\beta S_t < t \le 1/S_t \end{cases} \tag{2.21}$$

while the second contraction moves according to,

$$g_2(t) = \frac{1}{2}\left(1 - \cos(2\pi S_t t)\right), 0 \le t \le 1/S_t \tag{2.22}$$

where, the non-dimensional parameter β is related to the phase lag between the first and the second contractions according to the following assigned motion protocol, which is shown in Fig.2.2. Initially, during the compression phase we let both contractions start to move together. However, we let the first contraction reaches the maximum specified channel travel collapse (TC) distance faster than the second contraction. In other words, there will be a time-lag $T_g = (1 - 1/\beta)/(2S_t)$

between these two collapse motions which is equal to phase lag $\theta_{12} = \pi(1 - 1/\beta)$.

Moreover, during the expansion phase, the first contraction returns back to the nominal original position and continues its period with zero amplitude until the second contraction completes its own cycle, then both contractions start together the second cycle with the same explained protocol shown in Fig.2.2. It should be noted that both contractions have same time period $T = 1/S_t$, and if $\beta = 1$, there will be no phase lag and both contractions move in the same manner with time. The above motion protocol is intentionally proposed to grantee that after one cycle, the channel geometry has returned to the initial position, and does not suffer from any contractions, i.e., there will be no net flow due to volume deformation.

B. Flow Field Induced by Wall Contractions

The flow field induced by the motions of wall contractions in a tube with zero pressure drop $\Delta p(t) = 0$ is given in detail in this section. The tube wall profile as described previously by equations (2.19)-(2.22) with only two contractions, i.e., $N = 2$, located at $x_1 = 0.25, d_1 = 0.1$ and $x_2 = 0.65, d_2 = 0.1$ are considered. The kinematical motion protocol shown in Fig.2.2 is used to actuate both contractions accordingly. Since the wall profile is fully described, the pressure gradient can be evaluated using equations (2.10)-(2.12), and the velocity components can be then calculated by using equations (2.7)-(2.8) respectively. The flow structures at compression time $t = t/4$ and at expansion $t = 3T/4$ snapshots are given. Moreover, the results at these times are compared for two phase lags $\theta_{12} = 0°\&30°$ respectively.

In Fig. 2.3 (a), we show the contour lines for the velocity components, and the streamlines during the compression phase at instant of time $t = T/4$ and at zero phase lag i.e., $\theta_{12} = 0°$. Results have shown that, as the wall contractions undergo compression phase and start to move toward the bottom wall, the axial velocity component increases near the contraction regions and the flow is displaced, bifurcated, and exit the tube from both directions as shown in Fig. 2.3 (a-(i)). The contour lines for the vertical velocity component are also shown and are characterized by two circulation zones regions with opposite direction underneath each contractions as shown in Fig. 2.3 (a-(ii)). The stream lines show that, there will be a stagnation line/region between the two

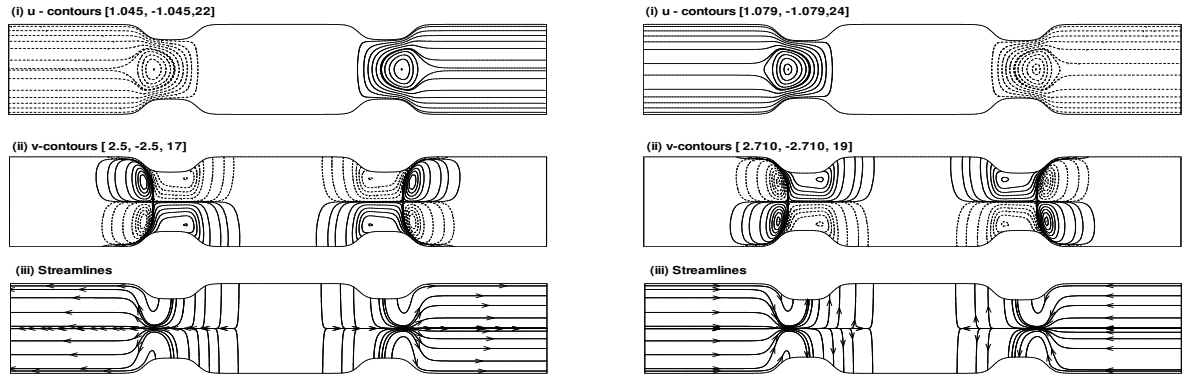

(a) Compression at t = T/4 & $\theta_{12} = 0°$ (b) Expansion at t = 3T/4 & $\theta_{12} = 0°$

Figure 2.3: Induced flow-field during compression and expansion snapshots at instant of time and at $\theta_{12} = 0°$: (i) u - contours (ii) v - contours (iii) streamlines

contractions due to flow cancellation, since each collapse send flow to both directions away from the contraction zone, Fig. 2.3 (a-(iii)). This stagnation line act as a ghost-valve that controls the amount of flow transport from one side to another along the tube length.

Similarly, snapshots that show the flow field during the expansion phase at time $t = 3T/4$ are shown in Fig. 2.3 (b). When the contraction regions expand back away from the bottom wall (i.e., in the expansion phase), an exactly a similar flow field structure is developed but with an opposite direction for the axial and the vertical velocity components as shown in Fig. 2.3 (b-(i-ii)). The velocity stream lines show that, the flow enters the channel from both ends to fill up the tube when the contractions moves back toward their original positions, Fig. 2.3 (b-(iii)).

In Fig. 2.4, the contour lines for the static pressure, pressure gradient, and the shear stress at similar compression and expansion times as mentioned previously are given. For example, results at compression time $t = T/4$ show that as the wall contractions start to move toward the bottom wall, high pressure with adverse and favorable gradients are formed near and in these compression regions. This induces a flow away from the compression sited that exits the channel from both sides as pointed out from the velocity contours. Moreover, the pressure is maximum or total in the stagnation zone "ghost-valve" between the two contractions as shown in Fig. 2.4 (a-(i)). The pressure gradient have its absolute maximum value near the contraction regions and become constant away from these contractions and they are independent from the vertical direction as

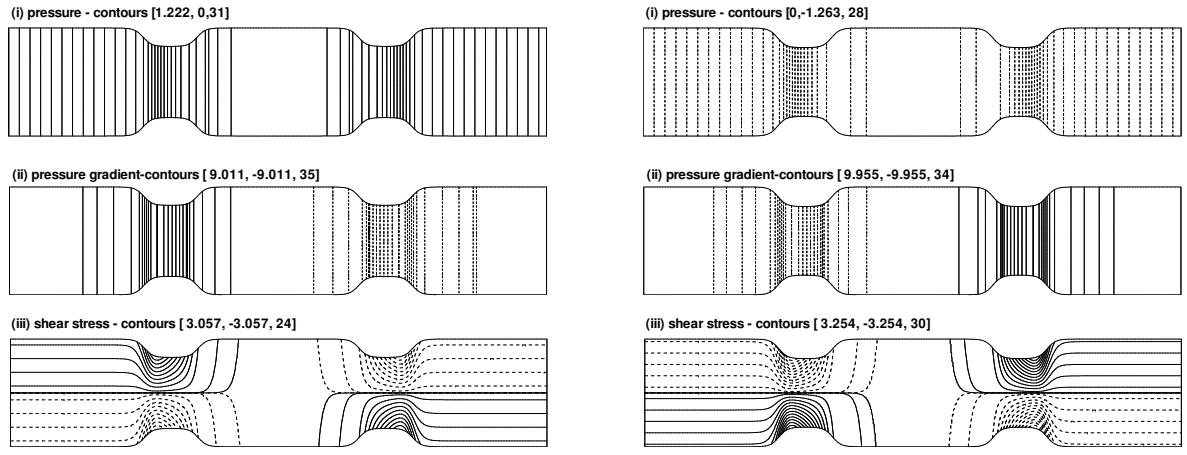

(a) Compression at t = T/4 & $\theta_{12} = 0°$ (b) Expansion at t = 3T/4 & $\theta_{12} = 0°$

Figure 2.4: Induced pressure and shear stress contours during compression and expansion snapshots at instant of time and at $\theta_{12} = 0°$:(i) Pressure, P (ii) pressure gradient, $\frac{dp}{dx}$ (iii) shear stress, τ.

shown in Fig. 2.4 (a-(i-ii)). The shear stress varies linearly with the vertical direction and become maximum at the wall boundaries and have zero values at the locations where, the pressure gradient is zeros. The contour lines for the shear stress have maximum values at the contraction regions as well, Fig. 2.4 (a-(iii)). Similarly, the contour lines for the pressure, pressure gradient, and the shear stress during the expansion phase at time $t = 3T/4$ are shown in Fig. 2.4 (b). Obviously and once again, when the contraction regions expand back away from the bottom wall an exactly similar contour lines are developed but with an opposite signs. In other words, contours lines at $t = 3T/4$ are like mirror plots for the flow field at $t = T/4$ as shown in Fig. 2.4 (b-(i-iii)).

In addition to results presented form the previous scenario, where the two contractions move with no phase lag i.e., $\theta_{12} = 0°$, we show similar contour plots and velocity stream lines in the case of $\theta_{12} = 30°$ at similar snapshot times for both compression $t = T/4$ and expansion $t = 4T/4$. For instance, the velocity contours and the stream lines are shown in Figs. 2.5(a & b) at both times respectively. Similarly, the pressure, pressure gradient and the shear stress contour lines are shown in Fig. 2.6 (a & b) at both compression and expansion times as well. Results have shown that, unlike the situation where $\theta_{12} = 0°$ which is always characterized by having a stagnation "ghost-valve" zone of zero velocities between the two contractions and no flow is transported, when

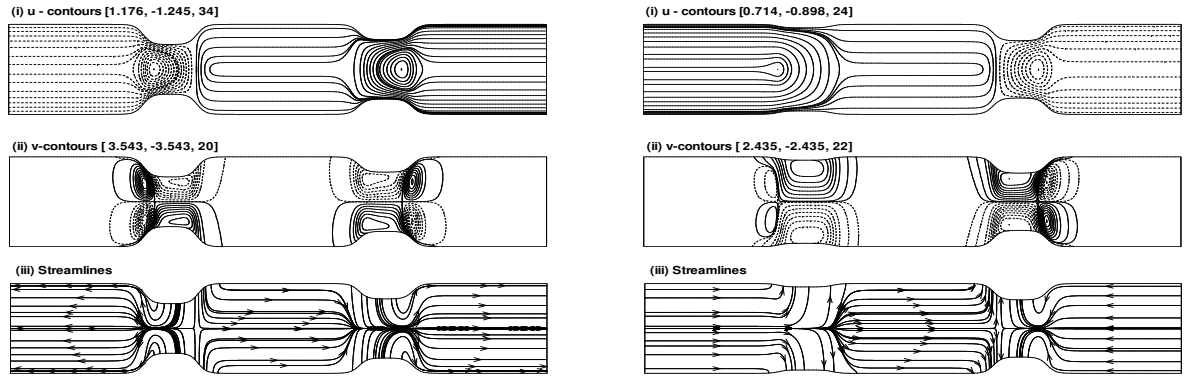

(a) Compression at t = T/4 & $\theta_{12} = 30°$ (b) Expansion at t = 3T/4 & $\theta_{12} = 30°$

Figure 2.5: Induced flow-field during compression and expansion snapshots at instant of time and at $\theta_{12} = 30°$: (i) u - contours (ii) v - contours (iii) streamlines

$\theta_{12} = 30°$ the stagnation zone is relaxed and there will flow transport in the region between the two contractions as shown in Figs. 2.5 & 2.6 respectively. This is will be investigated in details in section 2.1.3 to relate the net flow produced out of this system and the phase lag parameter.

To better understand the flow field induced by the motion of these wall contractions and to be able to compare the results from both cases that use phase lags equal to $\theta_{12} = 0°\&30°$ adequately, we show line plots for different parameters along the tube length In Figs. 2.7 & 2.8. For examples, the pressure p and pressure gradient dp/dx distributions along the axial direction $x - axis$ during the both compression and expansion phases of the actuation cycle at time $t = T/4$ and $t = 3T/4$ respectively and at $\theta_{12} = 0°$ are shown in Figs. 2.7(a & b). Results show that, during compression instant of time $t = T/4$, the pressure is total with maximum absolute constant value in the region between the two collapses and decreases linearly to satisfy the zero boundary conditions at the tube ends.

The pressure gradient is zero in the region between the two contractions and constant away with opposite signs to force the flow to bifurcate and exits from both sides as shown in Fig.2.7 (a). In other words, an adverse pressure gradient, $dp/dx > 0$, forms in the neighbourhood of, and to the left of the first contraction region, while a favourable pressure gradient, $dp/dx < 0$, forms around the second contraction region in a mirror fashion (exactly opposite values) and the region between the two contractions is characterized by zero pressure gradient. Exactly a similar scenario takes

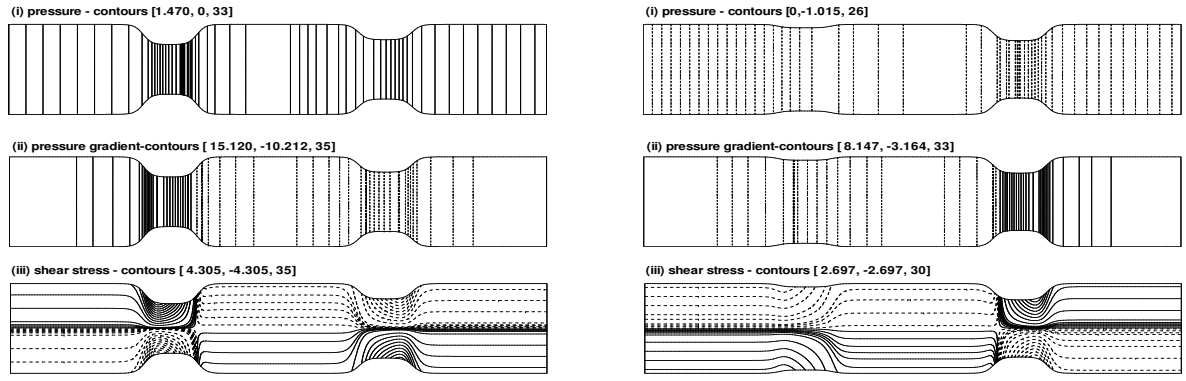

(a) Compression at t = T/4 & $\theta_{12} = 30°$ (b) Expansion at t = 3T/4 & $\theta_{12} = 30°$

Figure 2.6: Induced pressure and shear stress contours during compression and expansion snapshots at instant of time and at $\theta_{12} = 30°$:(i) Pressure, P (ii) pressure gradient, $\frac{dp}{dx}$ (iii) shear stress, τ.

place during the expansion phase at time $t = 3T/4$ but with opposite values as shown in Fig.2.7 (b).

In Fig. 2.7(c & d), the shear stress at the tube wall τ_w and the distributions of axial $u_{C.L}$ velocity are monitored at the tube center line $r = 0$ as a function of the axial direction are shown at similar compression and expansion times as before. The response of the wall shear stress due to the flow motions induced by the pressure gradient variations exhibited by the wall contractions can be explained as follows.

During the compression phase $t = T/4$, the wall shear stress has equal and opposite constant values away from contraction regions which reflects and consistence with the flow bifurcation to both ends of the tube. The wall shear stress has maximum values at the contraction regions and exactly zeros in between these contractions due to the existence of the stagnation zone with zero net velocities. In other words, results have shown that the axial velocity has its maximum value at the channel center line and is zero in the region between the two contractions due to flow cancellation. There will also be flow away from the contraction regions, and that flow exits the tube from both directions, see Fig. 2.7 (c). Once again, an exact similar scenario takes place during the expansion phase at time $t = 3T/4$ but with opposite values as shown in Fig. 2.7 (d). It worthwhile to mention here that, when the wall contractions move with zero phase lag $\theta_{12} = 0°$, the flow behaviour during

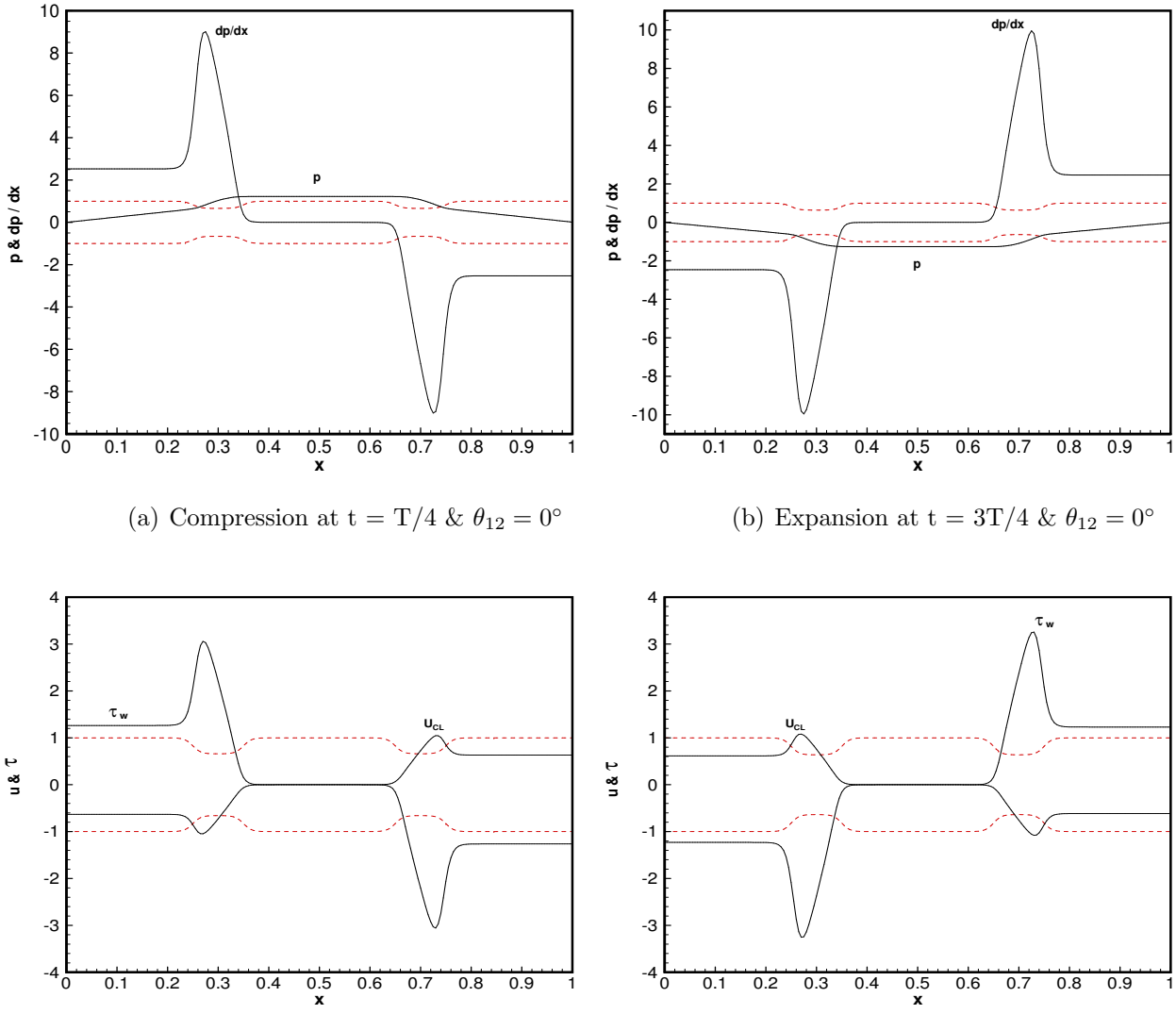

(a) Compression at t = T/4 & $\theta_{12} = 0°$

(b) Expansion at t = 3T/4 & $\theta_{12} = 0°$

(c) Compression at t = T/4 & $\theta_{12} = 0°$

(d) Expansion at t = 3T/4 & $\theta_{12} = 0°$

Figure 2.7: Distributions of the pressure, pressure gradient, wall shear stress, axial and vertical velocity components along the axial direction at $y = 0$ during compression and expansion snapshots at instant of time and at $\theta_{12} = 0°$. Dotted red lines represent the instantaneous channel wall position.

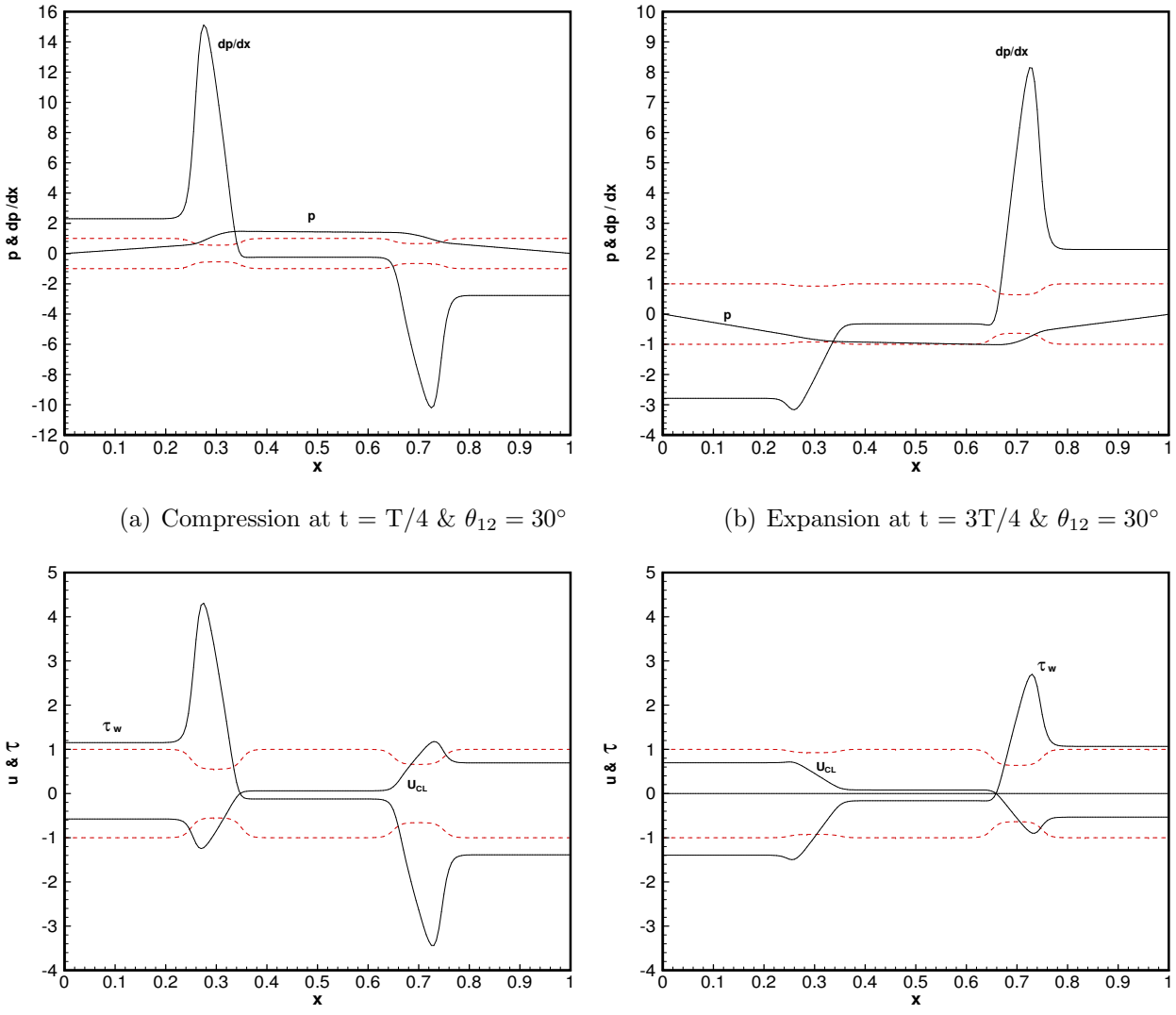

(a) Compression at t = T/4 & $\theta_{12} = 30°$

(b) Expansion at t = 3T/4 & $\theta_{12} = 30°$

(c) Compression at t = T/4 & $\theta_{12} = 30°$

(d) Expansion at t = 3T/4 & $\theta_{12} = 30°$

Figure 2.8: Distributions of the pressure, pressure gradient, wall shear stress, axial velocity component along the axial direction at $t = 0$ during compression and expansion snapshots at instant of time and at $\theta_{12} = 30°$. Dotted red lines represent the instantaneous channel wall position.

compressions and expansions phases is identically the same but with opposite signs that differs between compressions and expansions.

Similarly, plots for the pressure, pressure gradient, wall shear stress, and the center line axial velocity component along the axial direction at $\theta_{12} = 30^{\circ}$ are given in Fig. 2.8. Results are presented for both compression $t = T/4$ and expansion $t = 4T/4$ snapshot times. As the wall contractions move with phase lag value different than zero, flow is developed between the two contractions regions which it will not be stagnation zone any more. The pressure and its gradient along the tube length for both compression and expansion times are shown in Fig. 2.8 (a $ b) respectively.

During the compression instant of time $t = T/4$, the pressure is maximum at the first contraction region and minimum at the second contraction zone. Moreover, the pressure is not a constant over the region between the two contractions but rather varies with the distance between both contractions which lead to non-zero pressure gradient and there will be flow transported from the first contraction to the second counterpart, see Fig. 2.8 (a). During the expansion instant of time $t = 3T/4$, the scenario is reversed but not in a symmetric mirror manner to the values at $t = T/4$ as in the case of $\theta_{12} = 0^{\circ}$ but rather with asymmetric behaviour as shown in Fig. 2.8 (b). The response of the wall shear to these pressure gradient variations and the corresponding flow motions is shown in Fig. 2.8 (c & d). These plots are characterized by non-zero wall shear stress in the region between the two contractions, obviously because there is flow motions in this case, unlike the case when $\theta_{12} = 0^{\circ}$. Moreover, the axial velocity component at center line are given to show the flow movements induced by the pressure gradient variations and against the shear stress behaviour in Figs. 2.8(c & d).

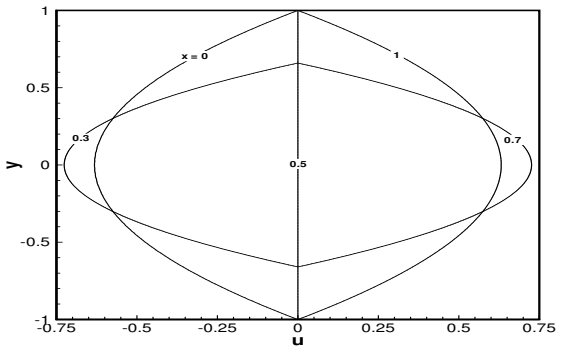

(a) Compression at t = T/4 & $\theta_{12} = 0°$

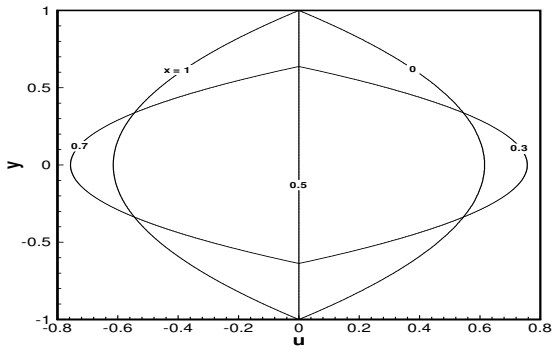

(b) Expansion at t = 3T/4 & $\theta_{12} = 0°$

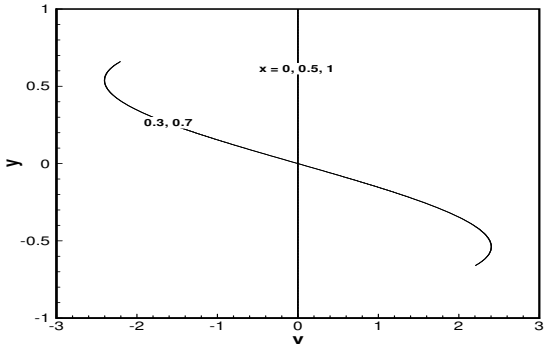

(c) Compression at t = T/4 & $\theta_{12} = 0°$

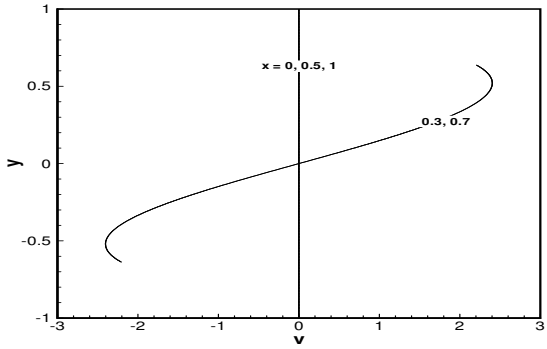

(d) Expansion at t = 3T/4 & $\theta_{12} = 0°$

Figure 2.9: Axial and vertical velocity profiles along the vertical direction at five locations: $x = 0, 0.3, 0.5, 0.7\&1$ during compression and expansion snapshots at instant of time and at $\theta_{12} = 0°$.

More detailed comparisons between the flow fields for both cases of $\theta_{12} = 0°\&30°$ can be drawn from the velocity profiles along the vertical direction. For examples, in Fig.2.9(a & b), the profiles for the velocity component u along the radial at five locations, namely $x = 0, 0.3, 0.5, 0.7$, 1 are given for $\theta_{12} = 0°$ at both compression and expansion times respectively . Unsurprisingly, the velocity profiles are parabolic with maximum value at the tube center line according to equation 2.7.

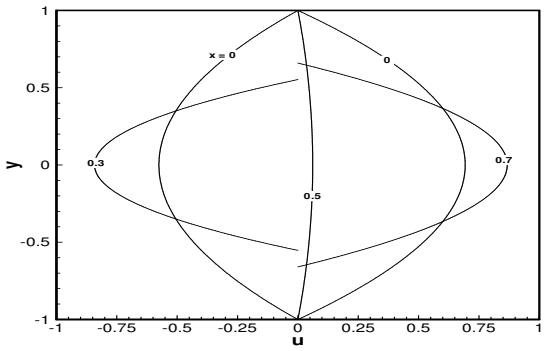

(a) Compression at t = T/4, $\theta_{12} = 30°$

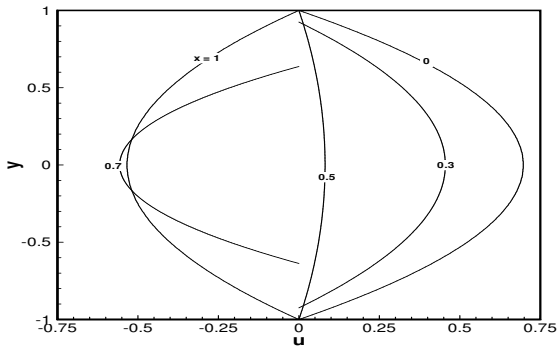

(b) Expansion at t = 3T/4, $\theta_{12} = 30°$

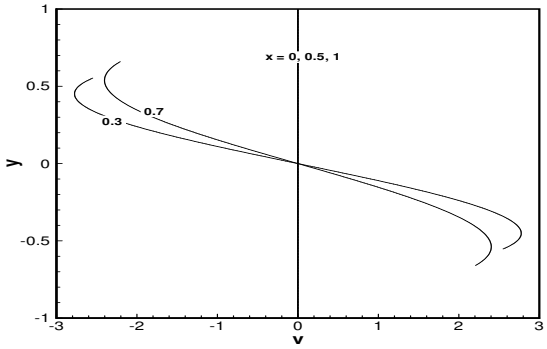

(c) Compression at t = T/4, $\theta_{12} = 30°$

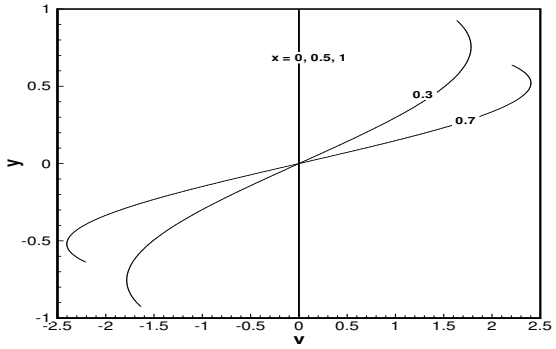

(d) Expansion at t = 3T/4, $\theta_{12} = 30°$

Figure 2.10: Axial and vertical velocity profiles along the vertical direction at five locations: $x = 0, 0.3, 0.5, 0.7\&1$ during compression and expansion snapshots at instant of time and at $\theta_{12} = 30°$.

Zero velocity takes place at the middle of the tube i.e, at $x = 0.5$ which located between the two contraction regions. The zero velocities are due to the fact that, each contraction sending flow to the right and to the left, therefore flow cancellations occur between both contractions. Similarly, in Fig.2.9(c & d) we show the vertical velocity $v - y$ profiles at the same five axial locations. Results shows that, far away from the contraction regions and at the middle of the tube more specifically at (i.e., $x = 0, 0.5$, and 1), the radial velocity is zero. However, at the middle of the contractions more specifically at $x = 0.3, 0.7$, the velocity profile starts by zero values at the tube center line and reaches asymptotically its maximum value and then slightly decrease back to meet the wall boundary condition. It should be noted that, when $\theta_{12} = 0°$ is employed, the velocity profiles shown in Figs.2.9(d & d) at an expansion instant of time $t = 3T/4$ are an exact mirror to profiles

shown in Figs.2.9(a & c) for the compression instant of time $t = T/4$. In other words there is a symmetry behaviour for the induced flow by both compression and expansions when there is no phase lag in the contractions motions. In Fig. 2.10, the profiles for the velocity components u and v along the vertical $y - axis$ direction at similar locations as before i.e., $x = 0, 0.3, 0.5, 0.7,$ 1 are given for $\theta_{12} = 30^{\circ}$ at both compression and expansion times respectively. These profiles are characterized by the existence of flow transport between the two contractions as shown in the non-zero profile given by $x = 0.5$. Moreover, there is a symmetry breaking in the velocity profiles and other variables in the expansion time when they are compared with compression counter part. In other words, results have shown that the compression and expansion process is not completely symmetric over a complete collapsing cycle when the wall contractions move with a non-zero phase lag and a net flow is produced as a result of the contractions motions. These results indicate that, a flow transport and a net flow out of this system can be produced by using slight phase lags between contractions motion protocols. This phase lag has shown to be the key parameter of this study as it will be discussed in the following subsection.

C. Net Flow Produced by Wall Contractions

The effect of the phase lag on the flow transport within this tube system is studied in details inhere. Results in this section are dedicated to investigate the possibility of using a simple tube as described before with local moving non-propagative contractions as a pumping mechanism at microscale flow regime. We claim that, the minimum requirements needed for this setup to produce unidirectional flow without imposing any pressure drop along the tube length are found and explained in details. The maximum travel collapse distance is chosen to be $TC = 70\%$ of the original tube radius W. In other words, contractions are allowed to move until it reach 70% of the tube radius. Ideally, each wall collapse cycle is composed of two main processes, the first one is compression step (C), where the contraction moves until it reaches the maximum allowable travel distance. The second process is an expansion step (E), where the wall contraction expands back to the initial wall position. The kinematics of the collapse function $g_1(t)$ which is given by equation (2.21),and being used to force the first contraction to move is recalled at different values of the phase lag parameter. The second collapse region is being forced to move with $g_2(t)$ function given by equation (2.22) which indicates

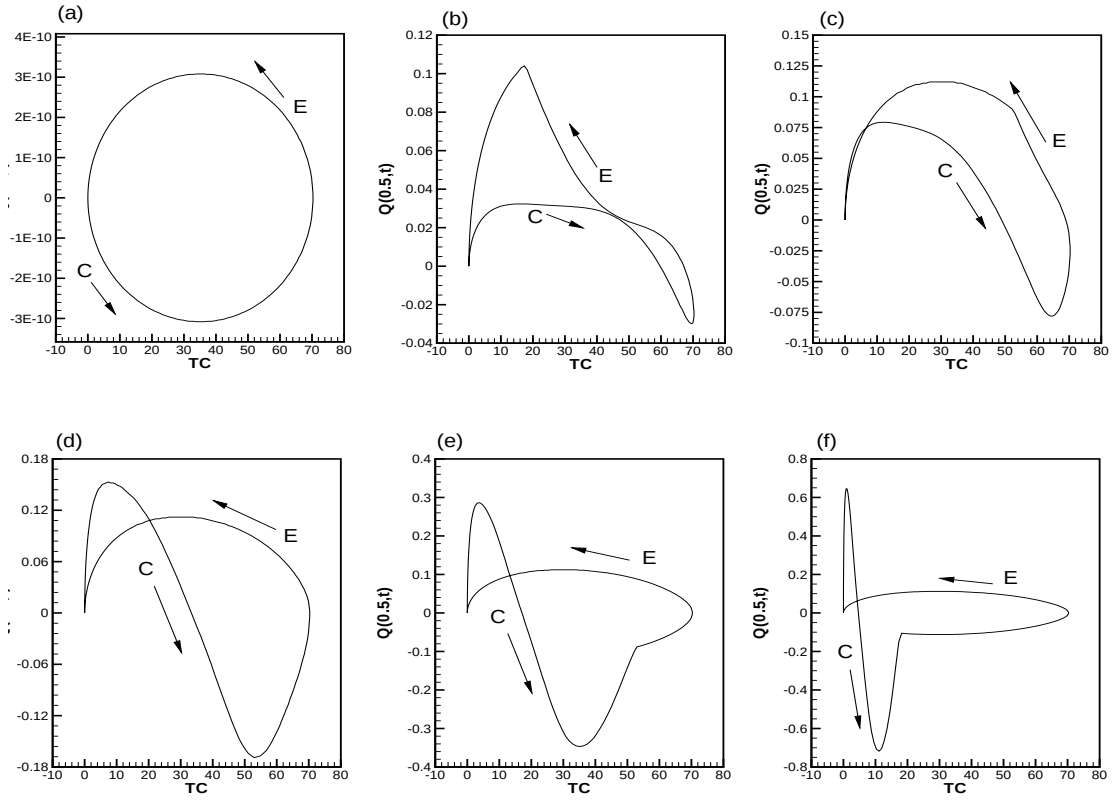

Figure 2.11: Time averaged net flow rate over a single contraction cycle as a function of the phase lag i.e. $Q - \theta_{12}$ at different collapse rations TC. Calculations are done using,$\Delta p(t) = 0$,$TC = 70\%$,$x_1 = 0.25, d_1 = 0.1$,$x_2 = 0.65, d_2 = 0.1$.

that, there is a phase lag θ_{12} between the functions $g_1(t)$ and $g_2(t)$.

The effect of this phase lag θ_{12} parameter on the instantaneous volumetric flow rate $Q(x,t)$ is given. For Instance, in Fig. 2.11, we show the volumetric flow rate $Q(x,t)$ monitored at $x = 0.5$ during a complete contraction-expansion cycle versus the percentage travel contraction $TC\%$ distance at different values of the phase lag parameter θ_{12}. Results have shown that, in case of using a phase lag value equal to $\theta_{12} = 0^\circ$ or 180°, the contraction cycle takes the shape of a pure circle, the volumetric flow rate is completely symmetric, and there will be no net flow produced as shown in Fig. 2.11 (a). If the phase lag between the two contractions set to be not zeros, the contraction-expansion

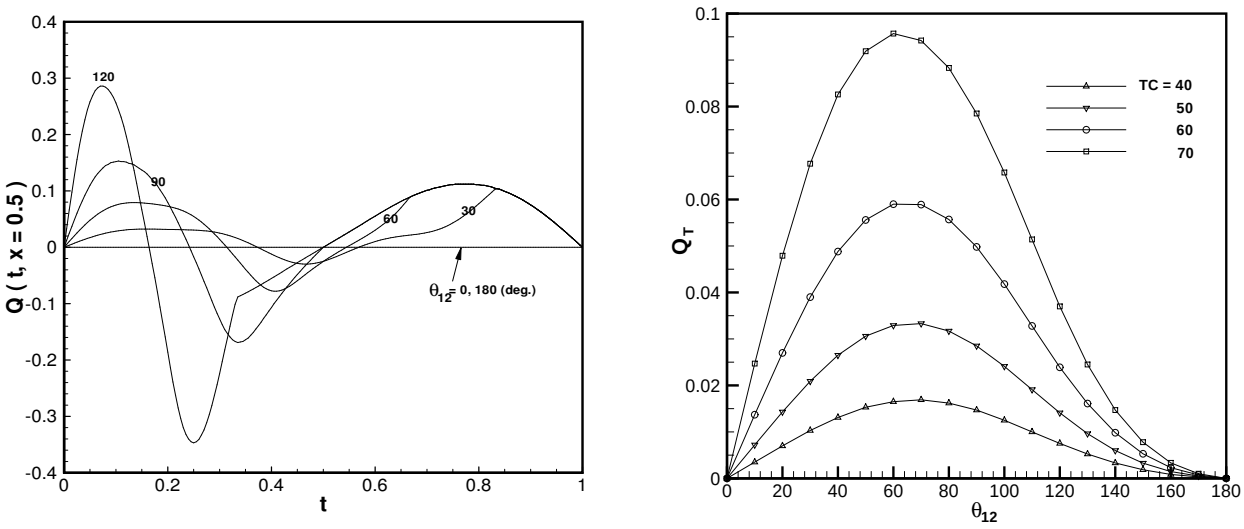

(a) (Q-t) plane

(b) (Q-θ_{12}) plane

Figure 2.12: Net flow rate over a single contraction cycle as a function of the phase lag, θ_{12}, and maximum travel collapse distances, TC.

cycle will take various asymmetric dynamical shapes, which depend on the value of the phase lag assigned as shown in Figs.2.11(b-f). In these situations, a unidirectional net flow is produced and the time-average volumetric flow rate Q_T is not zero, which can be calculated by simply integrating the instance flow rate over a complete cycle as

$$Q_T(x) = \frac{1}{T}\int_0^T Q(x,t)dt \tag{2.23}$$

where, $T = 1/S_t$ is the time period.

Another way to look at the above results, is to draw the instantaneous values of the volumetric flow rate as a function of time for various values of phase lags as shown in Fig. 2.12 (a). It is clear that, if $\theta_{12} \neq \{0°, 180°\}$, the volumetric flow rate distribution is not symmetric in time which indicate that, there will be a net flow produced. In Fig. 2.12 (b), we show the effect of the phase lag and the travel contraction distance on the behavior of the time averaged volumetric flow rate. The time

averaged flow rate as a function of the phase lag at different values of the maximum allowable travel collapse distance $TC\%$. As the phase lag between the motion of the two contraction increases, the time averaged net flow increases until it reach maximum at an optimum value of about $\theta_{opt} = 65°$, afterwards the net flow starts to decay and there will be no net flow produced when $\theta_{12} = 180°$. These result is confirmed qualitatively by performing passive particle simulations as given in section 2.3.

2.2 Bioinspired Channel Pumping Model

A novel bioinspired micropumping mechanism is given in this section, see *Aboelkassem and Staples (2012a). The present analysis is motivated by collapse mechanisms observed in insect physiological systems that use multiple contractions to transport fluid, and the emerging novel microfluidic devices that mimic these systems. The derived theoretical pumping model can be used to describe the flow transport at the microscale. More specifically, the induced flow motions in a microchannel by moving wall contractions at the low Reynolds number flow regime is presented.

In summary, the proposed pumping model is composed of a channel of a length that is much greater than its width ($\delta = W/L << 1$) and the upper wall is subjected to prescribed, non-peristaltic, localized moving contractions. The lubrication theory and quasi-steady approximations for incompressible viscous flow at low Reynolds number ($Re \sim \delta$) regime are used to model the problem mathematically and to derive expressions for velocity components, pressure gradient, wall shear stress, and net flow produced by the dynamics of wall contractions. The effect of contraction parameters such as, amplitude and phase lag on the time averaged net flow over a single cycle of wall motions is studied. The results presented here are supported by passive particle tracking simulations to investigate the possibility of using this system as a pumping mechanism. The present insect-inspired pumping model will be validated using the method of fundamental solutions, Stokeslets-based meshfree computational method in chapter 4.

2.2.1 Problem Formulation

Consider a $2D$ incompressible viscous flow in a channel with a finite length L and width W. We define the channel aspect ratio as $1/\delta$ which is assumed to be very large i.e., $\delta = W/L << 1$.The channel undergoes a single, or multiple, moving localized contractions from the upper wall $H_2(x,t)$, while the lower wall H_1 is kept stationary and straight at all times, as shown in Fig. 2.13 (a). The kinematics and geometry of the contractions are governed by a generic profile assigned to the channel upper side $H_2(x,t)$, which will be prescribed in detail in the result section. The wall profile allows

*Aboelkassem, Y., Staples, A. E., "Flow transport in a microchannel induced by moving wall contractions: a novel micropumping mechanism," *Acta Mechanica*, vol. 223(3), pp. 463–480, 2012. Used with kind permission of Springer Science and Business media. Copyright 2012, Springer

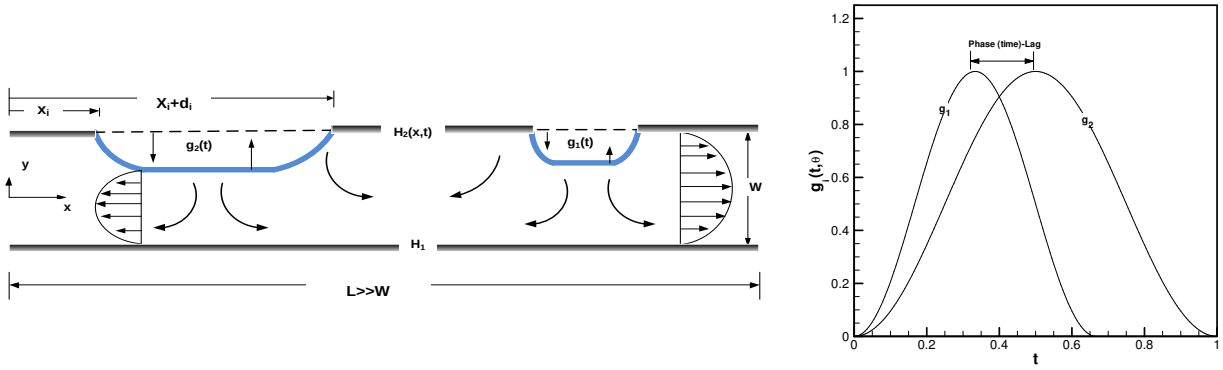

(a) (b)

Figure 2.13: Problem Schematic: (a) $2D$ channel with moving upper wall contraction profile $H_2(x,t)$ and stationary lower wall profile $H_1(x)$ (b) $g_1(t)$ and $g_2(t)$, the motion protocols assigned to the first and second contractions, respectively.

each contraction to move independently along the lateral direction with or without a phase lag with respect to each other. A zero pressure drop, $\Delta p = 0$, is assumed along the channel length, and only two moving contractions with phase lag θ_{12} are actuated. The velocity field, pressure gradient, wall shear stress, and net flow rate induced by the movements of the wall contraction-expansion protocols are derived. The effects of the contraction parameters, such as collapse amplitudes and phase lags, on the net flow produced by these wall contractions are given. The main objective of this work is to investigate the possibility of using this type of channel as a pumping mechanism at the microscale without the help of a pressure drop are presented in Section 2.2.1.

2.2.2 Mathematical Model

In this section we follow lubrication theory Mahmood and Merkin (1990); Li and Brasseur (1993); Batchelor (1967) for a viscous flow inside a 2D channel with a very high aspect ratio ($\delta = W/L << 1$). The peristaltic model Li and Brasseur (1993) is adopted to reformulate the problem in the frame work of a channel with localized non-peristaltic contractions from the upper wall only. The flow is assumed to be Newtonian, incompressible, and isothermal with constant viscosity μ and has a velocity field $\mathbf{V} = (u, v, 0)$. We introduce the following non-dimensional parameters: $x = x^*/L$,

$y = y^*/W$, $H_1 = {H_1}^*/W$, $H_2(x,t) = H_2(x,t)^*/W$, $t = t^*/(L/u_o)$, $u = u^*/u_o$, $v = v^*/\delta u_o$, $p = p^*W^2/(\mu u_o L)$, $\tau_{xy} = {\tau_{xy}}^*/(\mu u_o/W)$, $Q = Q^*/(u_o W)$, $S_t = fL/u_o$, $R_e = \rho u_o W/\mu$. Here, u and v are the velocity components along the axial, x, and vertical, y, directions, respectively. p is the static pressure, τ_{xy} is the shear stress, and Q is the volumetric flow rate. S_t and R_e are the Strouhal and Reynolds numbers, respectively. f is the frequency at which the contractions move and t is the time scale over which the motions take place. u_o is an arbitrary reference velocity. We next substitute the above non-dimensional parameters into the Navier-Stokes equations in Cartesian coordinates, and these equations, in two dimensions, reduce to

$$\frac{\partial u}{\partial x} + \frac{\partial v}{\partial y} = 0 \tag{2.24}$$

$$R_e\delta\left[\frac{\partial u}{\partial t} + u\frac{\partial u}{\partial x} + v\frac{\partial u}{\partial y}\right] = -\frac{\partial p}{\partial x} + \delta^2\frac{\partial^2 u}{\partial x^2} + \frac{\partial^2 u}{\partial y^2} \tag{2.25}$$

$$R_e\delta^3\left[\frac{\partial v}{\partial t} + u\frac{\partial v}{\partial x} + v\frac{\partial v}{\partial y}\right] = -\frac{\partial p}{\partial y} + \delta^4\frac{\partial^2 v}{\partial x^2} + \delta^2\frac{\partial^2 v}{\partial y^2} \tag{2.26}$$

We are interested in solving the above equations analytically by making use of the following facts. The flow is at the microscale, where the viscous effects is dominant i.e., we deal with the low Reynolds number flow regime $R_e \in [0, \delta]$. In addition, the channel geometry is restricted to a very high aspect ratio i.e., ($\delta << 1$) which means that classical lubrication theory is applicable. Therefore, the above system of equations can be further simplified by neglecting all terms that of order δ^2 and higher, leading to

$$\frac{\partial u}{\partial x} + \frac{\partial v}{\partial y} = 0 \tag{2.27}$$

$$-\frac{\partial p}{\partial x} + \frac{\partial^2 u}{\partial y^2} = 0 \tag{2.28}$$

$$\frac{\partial p}{\partial y} = 0. \tag{2.29}$$

We subject these equations to the following boundary conditions

(i) at $y = H_1$, $u = 0, v = 0$
(ii) at $y = H_2(x,t)$, $u = 0, v = \frac{\partial H_2}{\partial t}$
(iii) at $x = 0$, $p = p_o(t)$
(iv) at $x = 1$, $p = p_L(t)$.

From equation (2.29) we conclude that the static pressure is uniform along the vertical direction and varies only with the axial direction, i.e., $p = p(x,t)$. Therefore, equation (2.28) can be directly integrated twice with respect to y, and the associated boundary conditions can be applied. An explicit formula results for the axial velocity component u

$$u(x,y,t) = \frac{1}{2}\frac{\partial p}{\partial x}\left(y^2 - (H_1 + H_2)y + H_1 H_2\right) \tag{2.30}$$

By using the principle of conservation of mass given in equation 2.27 and the related boundary conditions, the vertical velocity component v is given as

$$v(x,y,t) = \frac{1}{4}\left(\frac{\partial p}{\partial x}\frac{\partial H_2}{\partial x} + H_2\frac{\partial^2 p}{\partial x^2}\right)V_1(y,H_1) - \frac{1}{12}\frac{\partial^2 p}{\partial x^2}V_2(y,H_1) \tag{2.31}$$

where, $V_1(y,H_1) = \left(y^2 - 2H_1 y + H_1^2\right)$, $V_2(y,H_1) = \left(2y^3 - 3H_1 y^2 + H_1^3\right)$. Using equation (2.31) with the boundary condition at $y = H_2$, where $v = \frac{\partial H_2}{\partial t}$, a relationship between the pressure derivatives $\frac{\partial p}{\partial x}$, $\frac{\partial^2 p}{\partial x^2}$, and the rate at which the upper wall $\frac{\partial H_2}{\partial t}$ moves, which can be given as

$$\frac{\partial H_2}{\partial t} = \frac{1}{4}\frac{\partial p}{\partial x}\frac{\partial H_2}{\partial x}\left(H_2 - H_1\right)^2 + \frac{1}{12}\frac{\partial^2 p}{\partial x^2}\left(H_2 - H_1\right)^3 \tag{2.32}$$

By rearranging terms in the above equation and integrating once with respect to x, an expression

for the pressure gradient is derived

$$\frac{\partial p}{\partial x} = \frac{1}{\left(H_2(x,t) - H_1\right)^3}\left(G(t) + 12\int_0^x \frac{\partial H_2(s,t)}{\partial t} ds\right) \tag{2.33}$$

where $G(t)$ is the function of integration which depend only on time, t. This function can to be determined after integrating equation (2.33) with respect to x, and the following expression for the pressure can be found

$$p(x,t) = p_o(t) + \int_0^x \frac{\partial p(s,t)}{\partial x} ds. \tag{2.34}$$

Evaluating equation (2.34) at $x^* = Li.e., x = 1$, where $P = P_L(t)$, an expression for $G(t)$ is found

$$G(t) = \frac{\Delta p(t) - 12\int_0^1 \left(H_2(x,t) - H_1\right)^{-3}\left(\int_0^x \frac{\partial H_2(s,t)}{\partial t} ds\right) dx}{\int_0^1 \left(H_2(x,t) - H_1\right)^{-3} dx} \tag{2.35}$$

where $\Delta p(t) = p_L(t) - p_o(t)$. Also, it should be noted that from equation (2.31), the second derivatives of the pressure $\frac{\partial^2 p}{\partial x^2}$ are needed in order to be able to calculate the vertical velocity v component explicitly. This term, $\frac{\partial^2 p}{\partial x^2}$, can be found from equation (2.32), and is given as

$$\frac{\partial^2 p}{\partial x^2} = 12\frac{\partial H_2}{\partial t}\left(H_2 - H_1\right)^{-3} - 3\frac{\partial p}{\partial x}\frac{\partial H_2}{\partial x}\left(H_2 - H_1\right)^{-1} \tag{2.36}$$

The wall shear stress is another important quantity. Using the expression for the shear stress for a two dimensional flow, and the same non-dimensional parameters as before, the non-dimensional shear stress τ_{xy} in $(x - y)$ can be written as

$$\tau(x,t) = \delta^2\frac{\partial v}{\partial x} + \frac{\partial u}{\partial y} \tag{2.37}$$

As before, we neglect all terms that are of order δ^2, and derive a simple expression for the shear stress by taking the first derivative of the axial velocity u component with respect to the vertical variable, y

$$\tau(x,t) = \frac{\partial u}{\partial y} = \frac{1}{2}\frac{\partial p}{\partial x}\left(2y - H_1 - H_2(x,t)\right) \tag{2.38}$$

The value of the shear stress at the channel upper and lower walls is evaluated by setting $y = H_1$

and $y = H_2$, respectively, in the above equation, and is found to be

$$\tau_w(x,t) \downarrow_{y=H_2} = -\tau_W(x,t) \downarrow_{y=H_1} = \frac{1}{2}\frac{\partial p}{\partial x}\left(H_2(x,t) - H_1\right) \tag{2.39}$$

Finally, an expression for the volumetric flow rate induced by the contractions assigned to the upper channel wall is derived

$$Q(x,t) = \int_{H_1}^{H_2(x,t)} u(x,y,t)dy \tag{2.40}$$

using equation 2.33 and perform the integration yield,

$$Q(x,t) = \frac{-1}{12}\frac{\partial p}{\partial x}\left(H_2(x,t) - H_1\right)^3 \tag{2.41}$$

This equation is integrated over a complete contraction-expansion cycle to ascertain if the system does indeed produce unidirectional flow. If so, the minimum requirements of using this particular system as a pumping mechanism are discussed in Section 2.2.3. The analysis presented here is general and can be extended to add contractions from the lower wall as well. However, here we restrict our solution to collapses on the upper wall of the channel only, and the flow is described by equations (2.24)-(2.41). Once the upper wall profile $H_2(x,t)$ is prescribed, the static pressure can be then evaluated using equation (2.33) and all the other flow variables can be determined.

2.2.3 Results and Discussions

The kinematics and the geometry of the channel wall contractions are governed by a generic expression $H_2(x,t)$, which is assigned to the upper wall only. This wall profile allows for a single or multiple contractions that can move with similar or with different amplitudes, and with or without phase lags relative to each other. The specific $H_2(x,t)$ investigated in this study is presented in section 2.2.3. More specifically, The structure and the development of the flow field induced by two wall contractions undergoes cyclic compression and expansion motions are given. For instance, the contours of the velocity components, axial static pressure, pressure gradient, and the wall shear stress are given and compared at specific temporal snapshots $t = T/4$ and $t = 3T/4$ which represents

the motions at both compression and expansion phases respectively as shown in the second section 2.2.3. In additions, the effect of the contraction amplitudes and the phase lags protocol assigned to the wall collapse motions on the net instantaneous volumetric flow is investigated in section 2.2.3. Moreover, the time averaged volumetric flow rate over a complete contraction-expansion cycle for various phase lags values is studied to explore which contraction setting can produce unidirectional net flows. Finally, the trajectories for passive particles which are distributed uniformly underneath these wall contractions and swim with velocities similar to induced background flow are calculated numerically using the particle tracking simulations approach and have shown in section2.3.

A. Channel Wall Profile, $H_2(x,t)$

Let the mathematical model that describes the kinematics and the shape of the contractions from the channel upper wall be given as

$$H_2(x,t) = \frac{1}{2} + \sum_{i=1}^{N} A_i f_i(x) g_i(t) \tag{2.42}$$

where $f_i(x) \in C^r[0,1]$ and $g_i(t) \in C^r[0, T = 1/S_t]$ represent the spatial and the temporal distribution of the upper wall shape, respectively. N defines the number of contractions, and A_i is the amplitude assigned to each contraction. The spatial form of the above equation imitates the geometry of the upper wall contractions as

$$f_i(x) = \tanh(\alpha(x - x_i)) - \tanh(\alpha(x - (x_i + d_i))) \tag{2.43}$$

where $\alpha = 2\pi/\delta$,x_i defines the beginning of each collapse region and $d_i \in (0, 1 - x_i]$ marks its end, as shown in Fig. 2.13 (b). In this part, we only consider two contractions, i.e., $N = 2$ where, the first contraction moves in time according to the following profile

$$g_1(t) = \begin{cases} \frac{1}{2}\left(1 - \cos(2\pi\beta S_t t)\right), & 0 \le t \le 1/\beta S_t \\ 0 & 1/\beta S_t < t \le 1/S_t \end{cases} \tag{2.44}$$

while the second contraction moves according to

$$g_2(t) = \frac{1}{2}\left(1 - \cos(2\pi S_t t)\right), 0 \leq t \leq 1/S_t \tag{2.45}$$

where the non-dimensional parameter β is related to the phase lag between the first and the second contractions according to the assigned motion protocol. Initially, during the compression phase we let both contractions begin to move together. Then, however, we let the first contraction reach the maximum specified channel travel collapse (TC) distance faster than the second contraction. In other words, there will be a time lag, $T_g = (1 - 1/\beta)/(2S_t)$, between these two collapse motions which is equal to the phase lag $\theta_{12} = \pi(1 - 1/\beta)$. Moreover, during the expansion phase, the first contraction returns back to the nominal original position and continues its period with zero amplitude until the second contraction completes its own cycle, then both contractions start the second cycle together with the protocol shown in Fig. 2.13 (b). It should be noted that both contractions have same time period $T = 1/S_t$, and that if $\beta = 1$, there will be no phase lag and both contractions will move in the same manner with time. This protocol is guarantees that after one cycle the channel geometry will be returning to the initial position and there will be no net flow due to volume deformation. The channel wall profile $H_2(x, t)$ and its kinematics prescribed by the local wall contractions motion protocol plays the important role in this study. Once the profile is prescribed, all the flow parameters can be calculated analytically or by using simple numerical integration methods. In this article, the profile $H_2(x, t)$ which is given by equation2.42 is simple enough to calculate all the parameters analytically and to show the instantaneous flow development during a complete cycle of compressions-expansions, see section2.2.3.

B. Flow Field Induced by Wall Contractions

The flow filed induced by motions of wall contractions in a channel with zero pressure drop is given in detail in this section. The channel wall profile as described previously by equations (2.42)-(2.45) with only two contractions, i.e., $N = 2$, located at $x_1 = 0.25, d_1 = 0.1$ and $x_2 = 0.65, d_2 = 0.1$ are considered. The kinematical motion protocol shown in Fig.2.14 (b) will be used to actuate both contractions accordingly. Since the upper wall profile is fully described, the pressure gradient can be evaluated using equations (2.33)-(2.29), and the velocity components can be then calculated

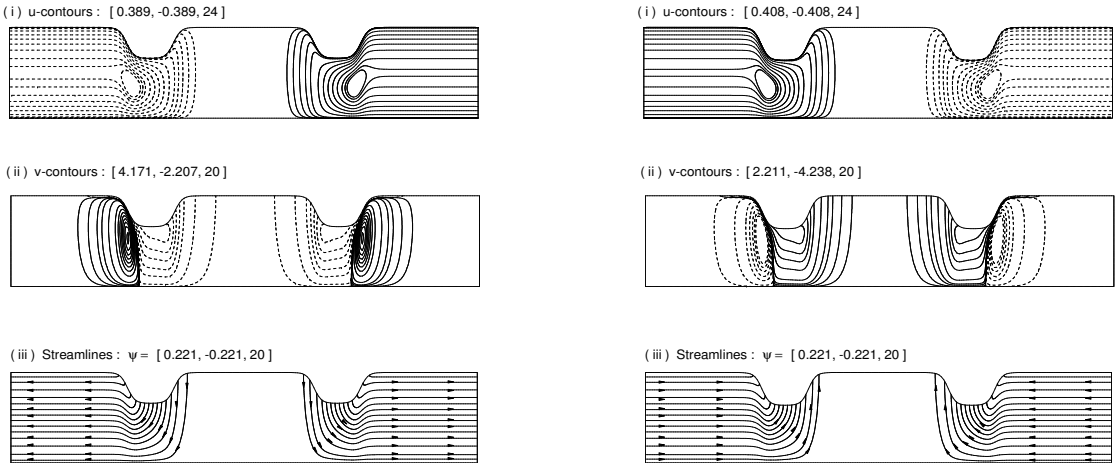

(a) Compression at t = T/4 & $\theta_{12} = 0°$ (b) Expansion at t = 3T/4 & $\theta_{12} = 0°$

Figure 2.14: Induced flow-field during compression and expansion snapshots at instant of time and at $\theta_{12} = 0°$: (i) u - contours (ii) v - contours (iii) streamlines

by using equations (2.30)-(2.31) respectively. The flow structures at times $t = t/4$ and $t = 3T/4$ snapshots are given. Moreover, the results at these times are compared for two phase lags $\theta_{12} = 0°\&30°$ respectively.

In Fig. 2.14 (a), we show the contour lines for the velocity components, and the streamlines during the compression phase at instant of time $t = T/4$ and at zero phase lag i.e., $\theta_{12} = 0°$. Results have shown that, as the wall contractions undergo compression phase and start to move toward the bottom wall, the axial velocity component increases near the contraction regions and the flow is displaced, bifurcated, and exit the channel from both directions as shown in Fig. 2.14 (a-(i)). The contour lines for the vertical velocity component are also shown and are characterized by two circulation zones regions with opposite direction underneath each contractions as shown in Fig. 2.14 (a-(ii)). The stream lines show that, there will be a stagnation region between the two contractions due to flow cancellation, since each collapse send flow to both directions away from the contraction zone, Fig. 2.14 (a-(iii)).

Similarly, snapshots that show the flow field during the expansion phase at time $t = 3T/4$ are shown in Fig. 2.14 (b). When the contraction regions expand back away from the bottom wall (i.e., in the expansion phase), an exactly a similar flow field structure is developed but with an opposite

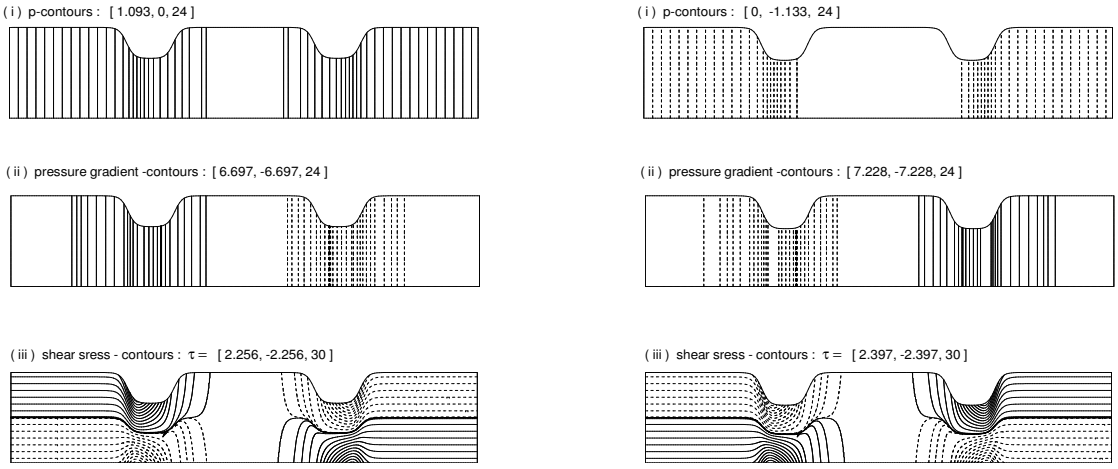

(a) Compression at t = T/4 & $\theta_{12} = 0°$ (b) Expansion at t = 3T/4 & $\theta_{12} = 0°$

Figure 2.15: Induced pressure and shear stress contours during compression and expansion snapshots at instant of time and at $\theta_{12} = 0°$:(i) Pressure, P (ii) pressure gradient, $\frac{dp}{dx}$ (iii) shear stress, τ.

direction for the axial and the vertical velocity components as shown in Fig. 2.14 (b-(i-ii)). The velocity stream lines show that, the flow enters the channel from both ends to fill up the channel when the contractions moves back toward their original positions, Fig.2.14 (b-(iii)).

In Fig. 2.15, the contour lines for the static pressure, pressure gradient, and the shear stress at similar compression and expansion times that mentioned before are given. For example, results at compression time $t = T/4$ show that as the wall contractions start to move toward the bottom wall, high pressure with adverse and favorable gradients are formed near and in these compression regions. This induces a flow away from the compression sited that exits the channel from both sides as pointed out from the velocity contours. Moreover, the pressure is maximum or total in the stagnation zone between the two contractions as shown in Fig. 2.15 (a-(i)). The pressure gradient have its absolute maximum value near the contraction regions and become constant away from these contractions and they are independent from the vertical direction as shown in Fig. 2.15 (a-(i-ii)). The shear stress varies linearly with the vertical direction and become maximum at the wall boundaries and have zero values at the locations where, the pressure gradient is zeros. The contour lines for the shear stress have maximum values at the contraction regions as well, Fig. 2.15 (a-(iii)).

Similarly, the contour lines for the pressure, pressure gradient, and the shear stress during the expansion phase at time $t = 3T/4$ are shown in Fig. 2.15 (b). Obviously and once again, when the contraction regions expand back away from the bottom wall an exactly similar contour lines are developed but with an opposite signs. In other words, contours lines at $t = 3T/4$ are like mirror plots for the flow field at $t = T/4$ as shown in Fig. 2.15 (b-(i-iii)). The contour lines for the vertical velocity component are also shown and are characterized by two circulation zones regions with opposite direction underneath each contractions as shown in Fig. 2.14 (a-(ii)). The stream lines show that, there will be a stagnation region between the two contractions due to flow cancellation, since each collapse send flow to both directions away from the contraction zone, Fig. 2.14 (a-(iii)).

Moreover, snapshots that show the flow field during the expansion phase at time $t = 3T/4$ are shown in Fig. 2.14 (b). When the contraction regions expand back away from the bottom wall, an exactly a similar flow field structure is developed but with an opposite direction for the axial and the vertical velocity components as shown in Fig. 2.14 (b-(i-ii)). The velocity stream lines show that, the flow enters the channel from both ends to fill up the channel when the contractions moves back toward their original positions, Fig. 2.14(b-(iii)).

In Fig. 2.15, the contour lines for the pressure, pressure gradient, and the shear stress at similar compression and expansion times are given. For example, results at time $t = T/4$ show that as the wall contractions start to move toward the bottom wall, high pressure with adverse and favourable gradients are formed near and in these compression regions. This induces a flow away from the compression sites that exits the channel from both ends. Moreover, the pressure is maximum or total in the stagnation zone between the two contractions, Fig. 2.15 (a-(i)). The pressure gradient have its maximum value near the contraction regions and become constant away from these contractions and they are independent from the vertical direction as shown in Fig. 2.15 (a-(i-ii)). The shear stress varies linearly with the vertical direction and become maximum at the wall boundaries and have zero values at the locations where, the pressure gradient is zeros. Similarly, the contour lines for the pressure, pressure gradient, and the shear stress at time $t = 3T/4$ are shown in Fig. 2.15 (b). Obviously, when the contraction regions expand back away from the bottom wall, an exact similar contour lines are developed but with an opposite signs. In other words, contours lines at $t = 3T/4$ are like mirror plots for the flow field at $t = T/4$ as shown in Fig. 2.15 (b-(i-iii)).

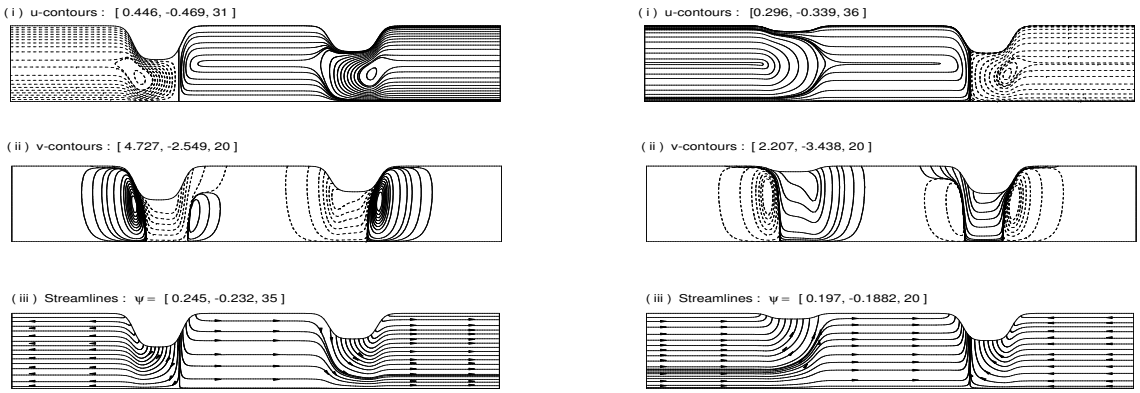

(a) Compression at t = T/4 & $\theta_{12} = 30°$ (b) Expansion at t = 3T/4 & $\theta_{12} = 30°$

Figure 2.16: Induced flow-field during compression and expansion snapshots at instant of time and at $\theta_{12} = 30°$: (i) u - contours (ii) v - contours (iii) streamlines

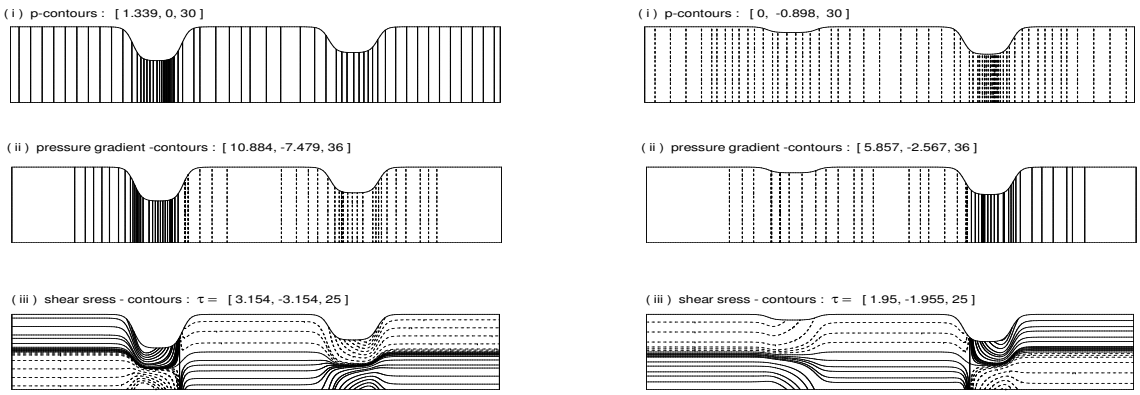

(a) Compression at t = T/4 & $\theta_{12} = 30°$ (b) Expansion at t = 3T/4 & $\theta_{12} = 30°$

Figure 2.17: Induced pressure and shear stress contours during compression and expansion snapshots at instant of time and at $\theta_{12} = 30°$:(i) Pressure, P (ii) pressure gradient, $\frac{dp}{dx}$ (iii) shear stress, τ.

In addition to results presented form the previous scenario, where the two contractions move with no phase lag i.e., $\theta_{12} = 0°$, we show similar contour plots and velocity stream lines in the case of $\theta_{12} = 30°$ at similar snapshot times for both compression $t = T/4$ and expansion $t = 4T/4$. For instance, the velocity contours and the stream lines are shown in Figs. 2.16(a & b) at both times respectively. Similarly, the pressure, pressure gradient and the shear stress contour lines are shown in Fig. 2.17 (a & b) at both compression and expansion times as well. Results have shown that, unlike the situation where $\theta_{12} = 0°$ which is always characterized by having a stagnation zone of zero velocities between the two contractions and no flow is transported, when $\theta_{12} = 30°$ the stagnation zone is relaxed and there will flow transport in the region between the two contractions as shown in Figs. 2.16 & 2.17 respectively. This is will be investigated in details in section 2.2.3 to relate the net flow produced out of this system and the phase lag parameter.

To better understand the flow field induced by the motion of these wall contractions and to be able to compare the results from both cases that use phase lags equal to $\theta_{12} = 0°\&30°$ adequately, we show line plots for different parameters along the channel length In Figs. 2.18 & 2.19. For examples, the pressure p and pressure gradient dp/dx distributions along the axial direction $x-axis$ during the both compression and expansion phases of the actuation cycle at time $t = T/4$ and $t = 3T/4$ respectively and at $\theta_{12} = 0°$ are shown in Figs. 2.18(a & b) . Results show that, during compression instant of time $t = T/4$, the pressure is total with maximum absolute constant value in the region between the two collapses and decreases linearly to satisfy the zero boundary conditions at the channel ends. and constant. The pressure gradient is zero in the region between the two contractions and constant away with opposite signs to force the flow to bifurcate and exits from both sides as shown in Fig. 2.18 (a). In other words, an adverse pressure gradient, $dp/dx > 0$, forms in the neighbourhood of, and to the left of the first contraction region, while a favourable pressure gradient, $dp/dx < 0$, forms around the second contraction region in a mirror fashion (exactly opposite values) and the region between the two contractions is characterized by zero pressure gradient. Exactly a similar scenario takes place during the expansion phase at time $t = 3T/4$ but with opposite values as shown in Fig. 2.18 (b).

In Fig. 2.18 (c & d), the shear stress at the channel upper wall τ_w and the distributions of both axial $u_{C.L}$ and $v_{C.L}$ monitored at the channel center line $y = 0$ as a function of the axial

direction are shown at similar compression and expansion times as before. The response of the wall shear stress due to the flow motions induced by the pressure gradient variations exhibited by the wall contractions can be explained as follows. During the compression phase $t = T/4$, the wall shear stress has equal and opposite constant values away from contraction regions which reflects and consistence with the flow bifurcation to both ends of the channel. the wall shear stress has maximum values at the contraction regions and exactly zeros in between these contractions due to the existence of the stagnation zone with zero net velocities. In other words, results have shown that the axial velocity has its maximum value at the channel center line and is zero in the region between the two contractions due to flow cancellation. There will also be flow away from the contraction regions, and that flow exits the channel from both directions, see Fig. 2.18 (c). Finally, as the wall contractions begin, a confined region with positive vertical velocity surrounded by a negative vertical velocity counterpart region is observed near each contraction region. Away from these the contraction regions, the vertical velocity vanishes. Once again, an exact similar scenario takes place during the expansion phase at time $t = 3T/4$ but with opposite values as shown in Fig. 2.18 (d). It worthwhile to mention here that, when the wall contractions move with zero phase lag $\theta_{12} = 0^{\circ}$, the flow behaviour during compressions and expansions phases is identically the same but with opposite signs that differs between compressions and expansions.

Similarly, plots for the pressure, pressure gradient, wall shear stress, and the center line velocity components along the axial direction at $\theta_{12} = 30^{\circ}$ are given in Fig. 2.19. Results are presented for both compression $t = T/4$ and expansion $t = 4T/4$ snapshot times. As the wall contractions moves with phase lag different that zero, flow is developed between the two contraction regions which it will not be stagnation zone any more. The pressure and its gradient along the channel length for both compression and expansion times are shown in Fig. 2.19 (a & b) respectively.

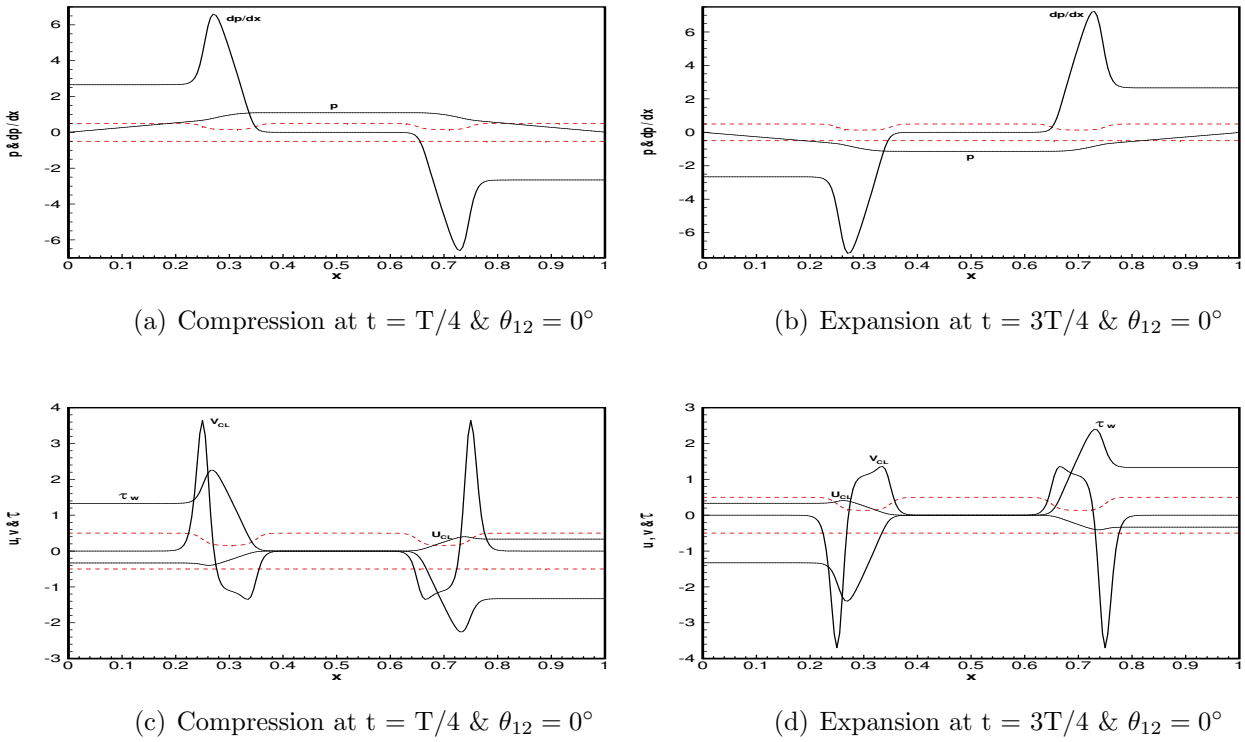

(a) Compression at t = T/4 & $\theta_{12} = 0°$

(b) Expansion at t = 3T/4 & $\theta_{12} = 0°$

(c) Compression at t = T/4 & $\theta_{12} = 0°$

(d) Expansion at t = 3T/4 & $\theta_{12} = 0°$

Figure 2.18: Distributions of the pressure, pressure gradient, wall shear stress, axial and vertical velocity components along the axial direction at $y = 0$ during compression and expansion snapshots at instant of time and at $\theta_{12} = 0°$. Dotted red lines represent the instantaneous channel wall position.

During the compression instant of time $t = T/4$, the pressure is maximum at the first contraction region and minimum and the second contraction zone. Moreover, the pressure is not a constant over the region between the two contractions but rather varies with the distance between both contractions which lead to non-zero pressure gradient and there will be flow transported from the first contraction to the second counterpart, see Fig. 2.19 (a).

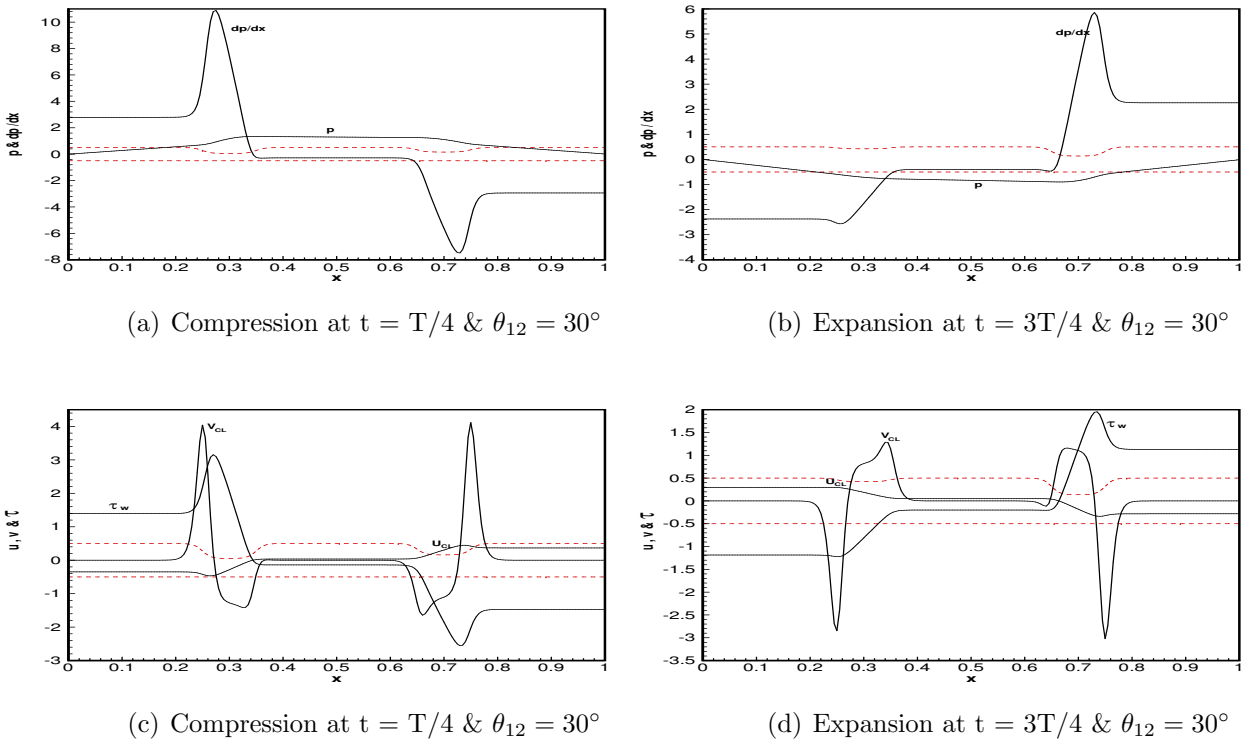

(a) Compression at t = T/4 & $\theta_{12} = 30°$

(b) Expansion at t = 3T/4 & $\theta_{12} = 30°$

(c) Compression at t = T/4 & $\theta_{12} = 30°$

(d) Expansion at t = 3T/4 & $\theta_{12} = 30°$

Figure 2.19: Distributions of the pressure, pressure gradient, wall shear stress, axial and vertical velocity components along the axial direction at $y = 0$ during compression and expansion snapshots at instant of time and at $\theta_{12} = 30°$. Dotted red lines represent the instantaneous channel wall position.

During the expansion instant of time $t = 3T/4$, the scenario is reversed but not in a symmetric mirror manner to the values at $t = T/4$ as in the case of $\theta_{12} = 0°$ but rather with asymmetric behaviour as shown in Fig. 2.19 (b). The response of the wall shear to these pressure gradient variations and the corresponding flow motions is shown in Fig. 2.19 (c & d). These plots are characterized by non-zero wall shear stress in the region between the two contractions, obviously because there is flow motions in this case, unlike the case when $\theta_{12} = 0°$. Moreover, the velocity components at center line are given to show the flow movements induced by the pressure gradient variations and against the shear stress behaviour in Figs. 2.19(c & d).

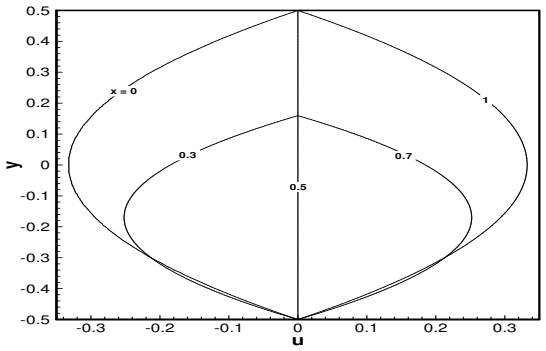

(a) Compression at t = T/4, $\theta_{12} = 0°$

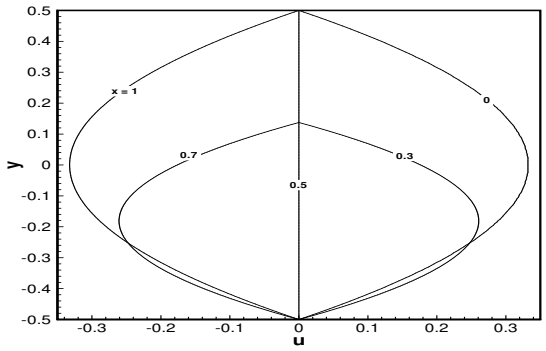

(b) Expansion at t = 3T/4, $\theta_{12} = 0°$

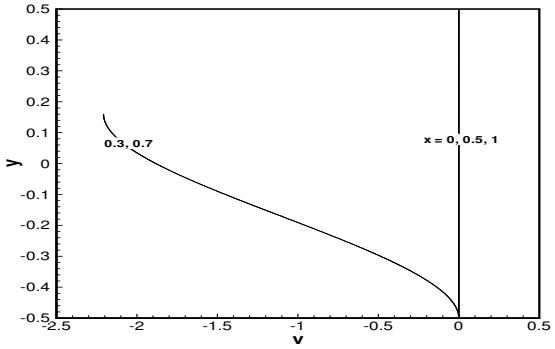

(c) Compression at t = T/4, $\theta_{12} = 0°$

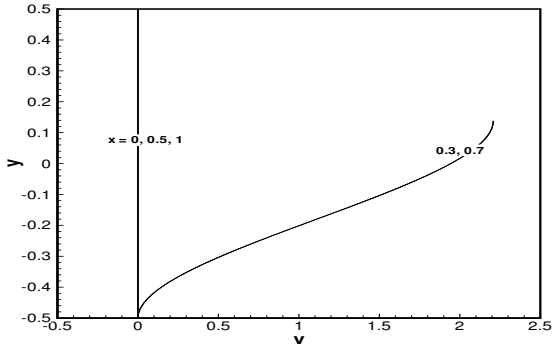

(d) Expansion at t = 3T/4, $\theta_{12} = 0°$

Figure 2.20: Axial and vertical velocity profiles along the vertical direction at five locations: $x = 0, 0.3, 0.5, 0.7\&1$ during compression and expansion snapshots at instant of time and at $\theta_{12} = 0°$.

More detailed comparisons between the flow fields for both cases of $\theta_{12} = 0°\&30°$ can be drawn from the velocity profiles along the vertical direction. For examples, in Fig.2.20 (a & b), the profiles for the velocity component u along the vertical $y - axis$ at five locations, namely $x = 0, 0.3, 0.5, 0.7$ & 1 are given for $\theta_{12} = 0°$ at both compression and expansion times respectively . Unsurprisingly, the velocity profiles are parabolic with maximum value at the midway between the upper and the lower walls according to equation (2.30).

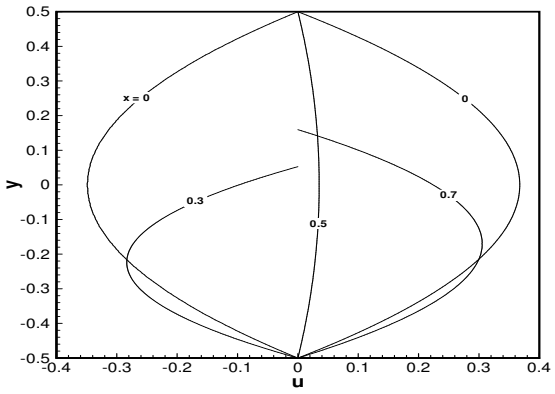

(a) Compression at t = T/4, $\theta_{12} = 30°$

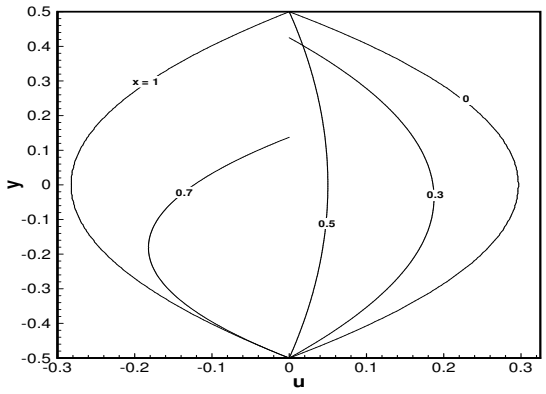

(b) Expansion at t = 3T/4, $\theta_{12} = 30°$

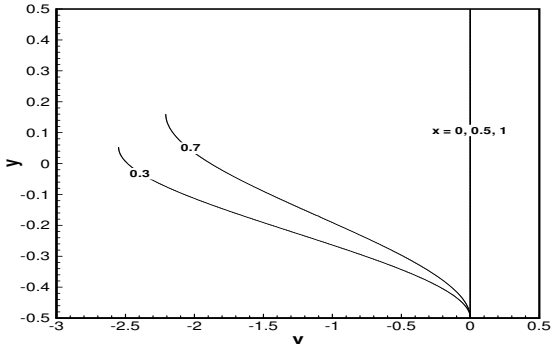

(c) Compression at t = T/4, $\theta_{12} = 30°$

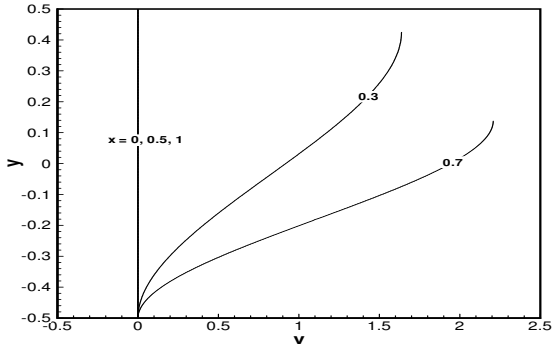

(d) Expansion at t = 3T/4, $\theta_{12} = 30°$

Figure 2.21: Axial and vertical velocity profiles along the vertical direction at five locations: $x = 0, 0.3, 0.5, 0.7\&1$ during compression and expansion snapshots at instant of time and at $\theta_{12} = 30°$.

Zero velocity takes place at the middle of the channel $x = 0.5$ which located between the two contraction regions. The zero velocities are due to the fact that, each contraction sending flow to the right and to the left, therefore flow cancellations occur between both contractions. Similarly, in Fig.2.20 (c & d) we show the vertical velocity $v - y$ profiles at the same five axial locations. Results shows that, far away from the contraction regions and at the middle of the channel more specifically at (i.e., $x = 0, 0.5$, and 1), the vertical velocity is zero. However, at the middle of the contractions more specifically at $x = 0.3, 0.7$, the velocity profile starts by zero values at the bottom wall and reaches asymptotically its maximum value at the upper wall to meet the boundary conditions. It should be noted that, when $\theta_{12} = 0°$ is employed, the velocity profiles shown in Figs.2.20(d & d) at an expansion instant of time $t = 3T/4$ are an exact mirror to the profiles shown in Figs.2.20(a & c)

for the compression instant of time $t = T/4$. In other words there is a symmetry behaviour for the induced flow by both compression and expansions when there is no phase lag in the contractions motions.

In Fig. 2.21, the profiles for the velocity components u and v along the vertical $y - axis$ direction at similar locations as before i.e., $x = 0, 0.3, 0.5, 0.7$ & 1 are given for $\theta_{12} = 30^{\circ}$ at both compression and expansion times respectively. These profiles are characterized by the existence of flow transport between the two contractions as shown in the non-zero profile given by $x = 0.5$. Moreover, there is a symmetry breaking in the velocity profiles and other variables in the expansion time when they are compared with compression counter part. In other words, results have shown that the compression and expansion process is not completely symmetric over a complete collapsing cycle when the wall contractions move with a non-zero phase lag and a net flow is produced as a result of the contractions motions. These results indicate that, a flow transport and a net flow out of this system can be produced by using slight phase lags between contractions motion protocols. This phase lag has shown to be the key parameter of this study as it will be discussed in the following subsection.

C. Net Flow Produced by Wall Contractions

The effect of the phase lag on the flow transport within this tube system is studied in details inhere. Results in this section are dedicated to investigate the possibility of using a simple tube as described before with local moving non-propagative contractions as a pumping mechanism at microscale flow regime. We claim that, the minimum requirements needed for this setup to produce unidirectional flow without imposing any pressure drop along the tube length are found and explained in details. The maximum travel collapse distance is chosen to be $TC = 70\%$ of the original tube radius W. In other words, contractions are allowed to move until it reach 70% of the tube radius. Ideally, each wall collapse cycle is composed of two main processes, the first one is compression step (C), where the contraction moves until it reaches the maximum allowable travel distance. The second process is an expansion step (E), where the wall contraction expands back to the initial wall position. The kinematics of the collapse function $g_1(t)$ which is given by equation (2.44),and being used to force the first contraction to move is recalled at different values of the phase lag parameter. The second

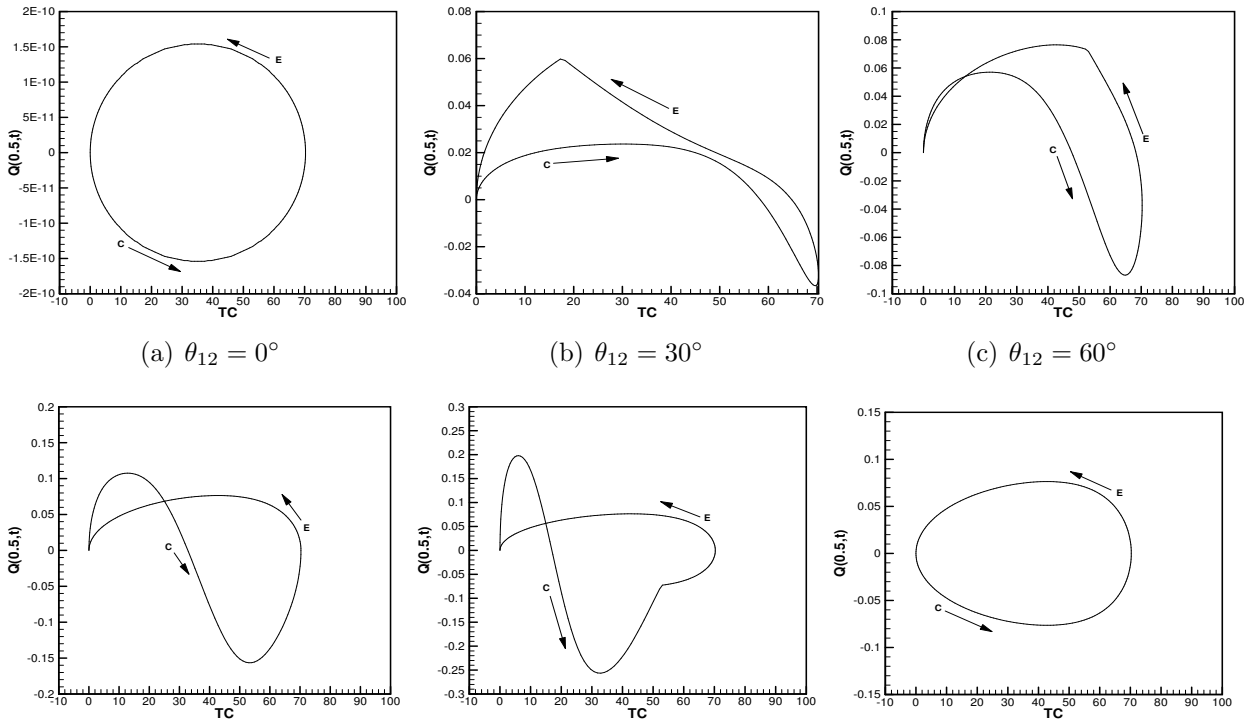

(a) $\theta_{12} = 0°$ (b) $\theta_{12} = 30°$ (c) $\theta_{12} = 60°$

(d) $\theta_{12} = 90°$ (e) $\theta_{12} = 120°$ (f) $\theta_{12} = 180°$

Figure 2.22: Volumetric flow rate at the middle of the channel, $Q(x = 0.5, t)$, as a function of the instantaneous allowable travel contraction distance, TC.

collapse region is being forced to move with $g_2(t)$ function given by equation (2.45) which indicates that, there is a phase lag θ_{12} between the functions $g_1(t)$ and $g_2(t)$.

The effect of this phase lag θ_{12} parameter on the instantaneous volumetric flow rate $Q(x, t)$ is given. For Instance, in Fig. 2.22, we show the volumetric flow rate $Q(x, t)$ monitored at $x = 0.5$ during a complete contraction-expansion cycle versus the percentage travel contraction $TC\%$ distance at different values of the phase lag parameter θ_{12}. Results have shown that, in case of using a phase lag value equal to $\theta_{12} = 0°$ or $180°$, the contraction cycle takes the shape of a pure circle, the volumetric flow rate is completely symmetric, and there will be no net flow produced as shown in Fig. 2.22 (a). If the phase lag between the two contractions set to be not zeros, the contraction-expansion cycle will take various asymmetric dynamical shapes, which depend on the value of the phase lag assigned as shown in Figs.2.22(b-f). In these situations, a unidirectional net flow is produced and the time-average volumetric flow rate Q_T is not zero, which can be calculated by simply integrating

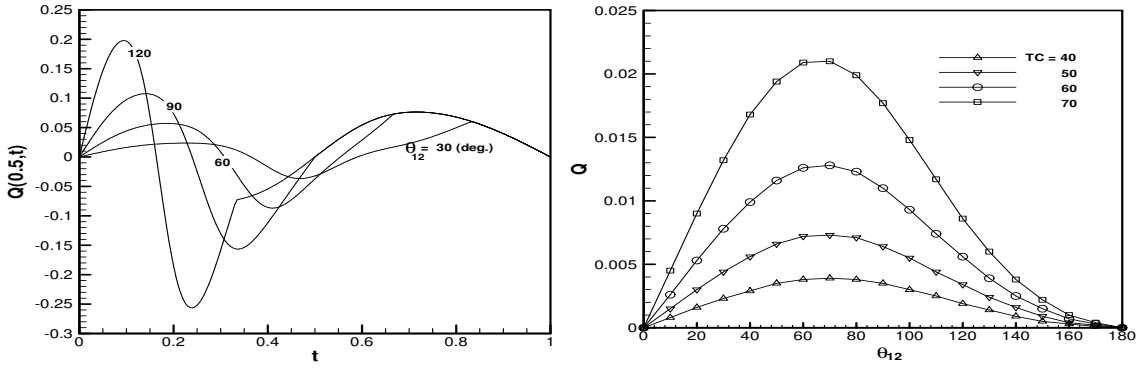

(a) (Q-θ_{12}) plane (b) (Q-TC) plane

Figure 2.23: The time averaged net flow rate over a single contraction cycle as a function of the phase lag, θ_{12}, and maximum travel collapse distances, TC.

the instance flow rate over a complete cycle as

$$Q_T(x) = \frac{1}{T}\int_0^T Q(x,t)dt \tag{2.46}$$

where, $T = 1/S_t$ is the time period.

Another way to look at the above results, is to draw the instantaneous values of the volumetric flow rate as a function of time for various values of phase lags as shown in Fig. 2.23 (a). It is clear that, if $\theta_{12} \neq \{0°, 180°\}$, the volumetric flow rate distribution is not symmetric in time which indicate that, there will be a net flow produced. In Fig. 2.23 (b), we show the effect of the phase lag and the travel contraction distance on the behavior of the time averaged volumetric flow rate. The time averaged flow rate as a function of the phase lag at different values of the maximum allowable travel collapse distance $TC\%$. As the phase lag between the motion of the two contraction increases, the time averaged net flow increases until it reach maximum at an optimum value of about $\theta_{opt} = 70°$, afterwards the net flow starts to decay and there will be no net flow produced when $\theta_{12} = 180°$. These result is confirmed qualitatively by performing passive particle simulations as given in section 2.3.

2.3 Net Flow Visualization by Particle Tracking Simulations

In order to qualitatively validate and strengthen our hypothesis of mimicking the respiratory system in insects for transporting fluids and use the above mentioned setup as a pumping mechanism at the microscale flow regime. The particle tracking simulations are used to visualize the induced unidirectional net flow produced by wall contractions over a complete collapsing cycle for both tube and channel flow cases investigated previously. Consider a collection of particles located underneath the contraction locations of the tube or channel wall. Particles are assumed to be mass less, passive and do not affect the background flow motions. In other words, particles will move with velocities equal to the background flow velocity which is given by equations (2.7)-(2.8) for the tube flow and by equations (2.30)-(2.31) for channel flow. Therefore, based on the Lagrangian frame of work, the particles motion can be governed by

$$\frac{d}{dt}\mathbf{X}_p = \mathbf{V}, \mathbf{X}_p(0) = \mathbf{X}_o \tag{2.47}$$

where, $\mathbf{X}_p$ is the particle position vector and $\mathbf{X}_o$ describes the initial position of any particle. $\mathbf{V}$ is the fluid velocity vector given by the components u and v which are derived previously for both tube and channel cases. Since the particles are passive and do not influence the background fluid, therefore as the wall contractions moves, the particles diffuses and follow exactly the flow path lines. The instantaneous particle positions are evaluated by integrating the initial value problem governed by the ordinary differential system of equations (2.47) using the Runge-Kutta integrator scheme. The adaptive time steeping algorithm ($ode45$) is chosen to calculate the particles positions after a complete cycle i.e., $t = T = 1/S_t = 1$ with an error tolerance of 10^{-6}.

The particle tracking simulation approach is applied for both tube and channel with moving wall contractions. For example, In Fig. 2.24 (a-f), the instantaneous displacements for collection of particles at different times $t = 0, T/4, 3T/4, T$ that represent the initial particles positions, motions during compression, expansion and after completing a single collapsing cycle respectively are given for various values of the phase lags $\theta_{12} \in [0, 180^\circ)$ and at maximum travelling collapse distance $TC = 70\%$. Several cases are chosen to investigate the dependence of the induced time averaged

net flow on the phase lag motions between wall contractions. For examples, the first case deals with the scenario where the tube wall contractions move with a zero phase lag $\theta_{12} = 0^\circ$ and the passive particles were uniformly distributed around the region of contractions as described before by equations (2.19)-(2.22). Simulation have shown that, after the wall contractions complete a whole cycle i.e., $t = T$, particles return back to their initial positions and there will be no net motions as shown in Fig. 2.24 (a). Similarly, particle tracking simulations have been done for phase lags $\theta_{12} = 30^\circ, 70^\circ, 90^\circ, 120^\circ$ and are shown through out Figs. 2.24(b-e). In these cases, results have shown that at $t = T$ there is a net particles displacement motions to the right. That is indicates that, there will be a net flow produced as the wall contractions moves with some phase lags other than the zero. Moreover, there is an optimal phase lag value that maximize the time averaged net flow which has found to be approximately $\theta_{12} = \theta_{opt} = 65^\circ$. Finally, simulations have done for the case where $\theta_{12} = 180^\circ$. In this case, the first contraction will not move at all and only the second contraction moves according to equation 2.22. In other words, the first contraction will be disabled and only the second contraction is actuated. Results have shown that at $t = T$ there is no net particles displacement motions and consequently no net flow is produced, see Fig. 2.24 (f). This implies that, channel with a single contraction will never capable of producing net flows.

Similar results are given in Fig. 2.25 (a-f) at times $t = 0, T/4, 3T/4, T$ for the channel case of study as well. As expected, particles behave in a similar manner as the tube counter part except that, the maximum net flow is produced at different phase lag value. This optimal phase lag value that maximize the time averaged net flow which has found to be approximately $\theta_{12} = \theta_{opt} = 70^\circ$. Results from the particles tracking simulations are consistent with the analytical results given in Fig. 2.12 and Fig. 2.23 respectively. Moreover, it validate our hypothesis which is: in order of this setup to work as a pumping mechanism, at least two local wall contractions that moves with a slight phase lag with respect to each other are indeed required.

As a summary, both tube and channel results presented here lead us to propose the following hypothesis: by using a non-elastic tube or channel with at least two local wall contractions that moves with a slight phase lag with respect to each other, a net flow is produced and the system can be used as a simple pumping mechanism in the microscale flow regime. In order to validate our pumping hypothesis, the Stokeslets-meshfree numerical method will be given in chapter 4.

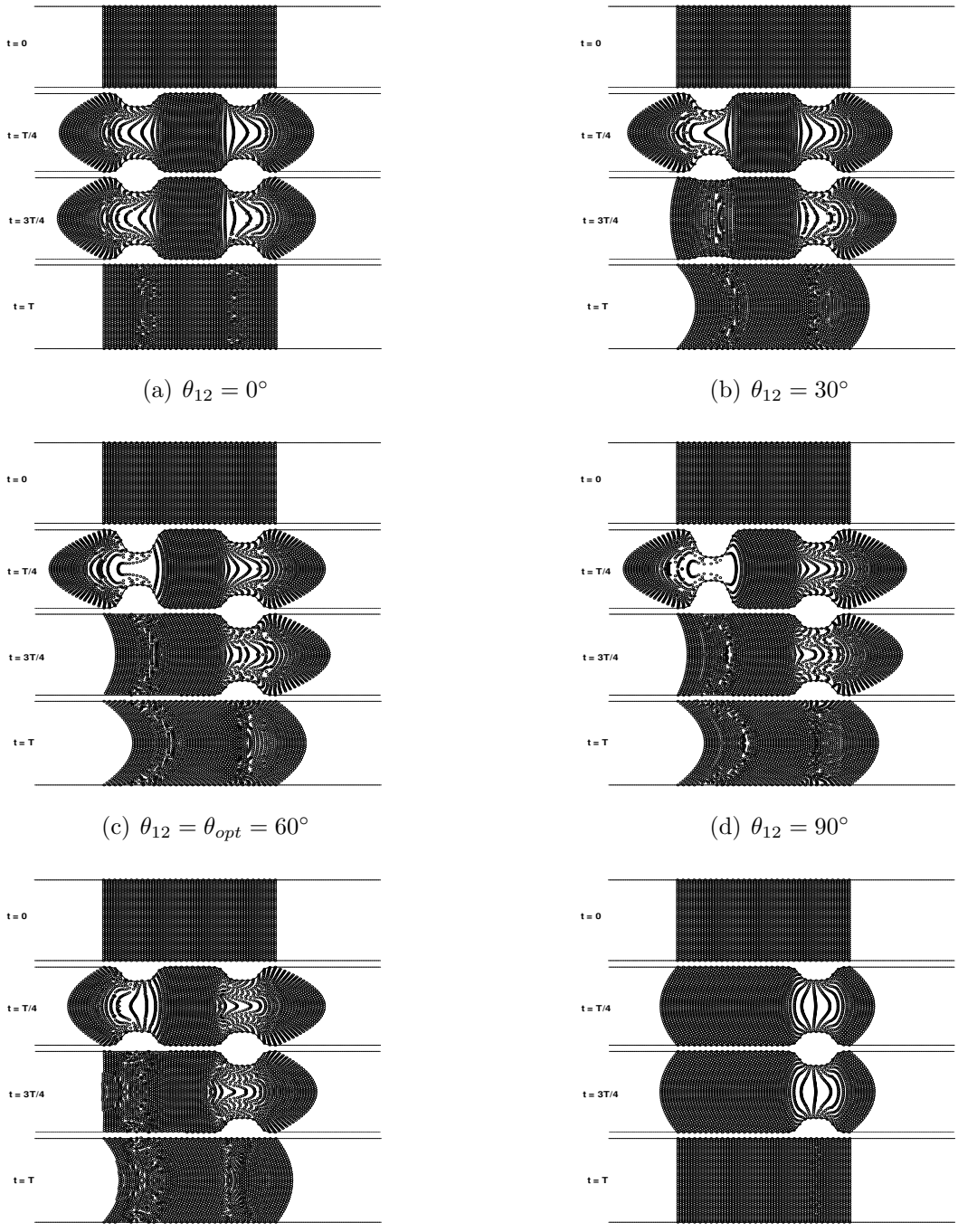

(a) $\theta_{12} = 0°$ (b) $\theta_{12} = 30°$

(c) $\theta_{12} = \theta_{opt} = 60°$ (d) $\theta_{12} = 90°$

(e) $\theta_{12} = 120°$ (f) $\theta_{12} = 180°$

Figure 2.24: Instantaneous passive particles tracking simulations during a complete contraction cycle of a tube wall.

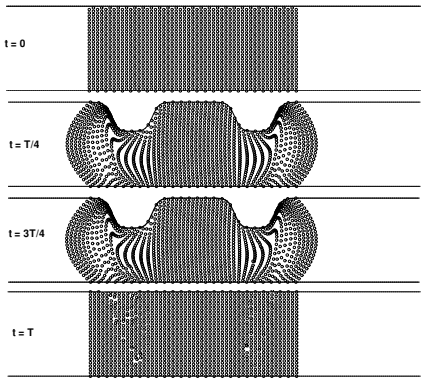

(a) $\theta_{12} = 0°$

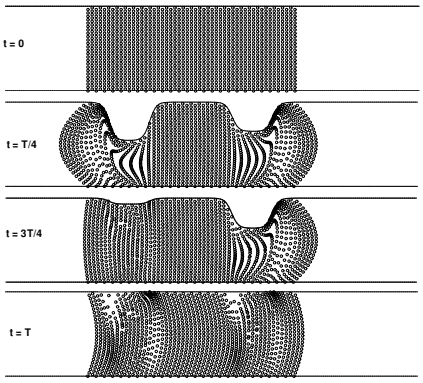

(b) $\theta_{12} = 30°$

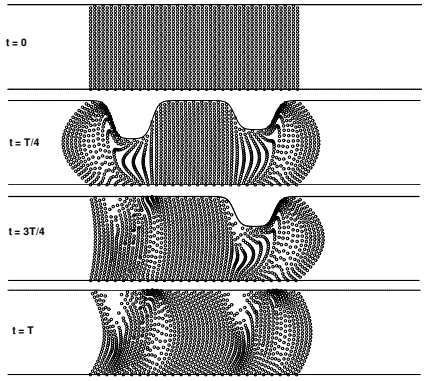

(c) $\theta_{12} = \theta_{opt} = 70°$

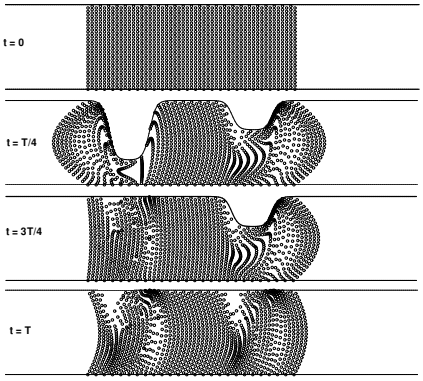

(d) $\theta_{12} = 90°$

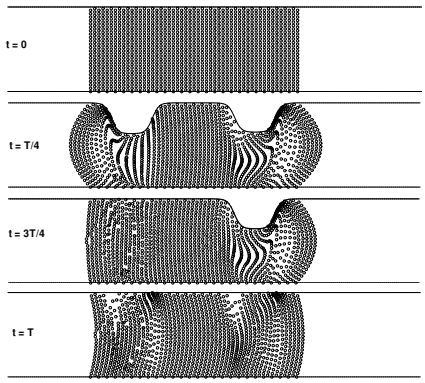

(e) $\theta_{12} = 120°$

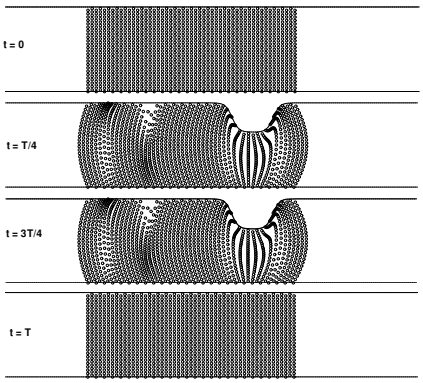

(f) $\theta_{12} = 180°$

Figure 2.25: Instantaneous passive particles tracking simulations during a complete contraction cycle of a channel wall.

Chapter 3

Optimum Parameters for Efficient Flow Pumping Induced by Moving Wall Contractions

This chapter gives the optimum spatial and temporal parameters used to optimize our derived bioinspired pumping models for efficient induced net flow motions and wall shear stress. The optimization results are given for both tube and channel models with moving wall contractions as explained previously in chapter 2. The constrained optimization technique based on the global minima approach is used to find the optimal configuration or design parameters.

3.1 Constrained Optimization Procedure and Objective Functions

A constrained optimization problem based on bounded parameters can be defined as a regular constraint minimization (maximization) of local cost functions in which constraints are typically weighted and or assigned in a bounded form, Kelley (1999). Simply, the goal of constraint optimization problem formulation is to find optimal solution to the problem under consideration whose

evaluated cost functions is maximized or minimized according to constrained platform. In general, the typical constrained optimization problem formulation is seeking to minimize (maximize) a real-valued function $f(\mathbf{x})$ of single or several N design variables. We will refer to $f(\mathbf{x})$ as the objective function and to $f(\mathbf{x}^*)$ as the minimum or maximum value. By this we mean to find a local minimizer, that is, a vector $\mathbf{x}^*$ such that, If a local minimizer $\mathbf{x}^*$ exists, we say a minimum value $f(\mathbf{x}^*)$ is attained at $\mathbf{x}^*$. The constrained optimization problem is to minimize a function $f(\mathbf{x})$ over a set $U \subset R^N$. A local minimizer, therefore, is an $\mathbf{x}^* \subset U$ such that

$$f(\mathbf{x}^*) \leq f(\mathbf{x}) \qquad \forall \qquad \mathbf{x} \in U \qquad near \qquad \mathbf{x}^* \tag{3.1}$$

which can be expressed as,

$$min_{\mathbf{x} \in U} f(\mathbf{x}) \tag{3.2}$$

or say that we seek to solve the problem $min_U f(\mathbf{x})$. A global minimizer is a vector $\mathbf{x}^* \subset U$ such that

$$f(\mathbf{x}^*) \leq f(\mathbf{x}) \qquad \forall \qquad \mathbf{x} \in U \tag{3.3}$$

In this part, we consider only the simplest constrained problems where the design variables are bounded and the objective (cost) functions are smooth with existing gradients and Hessians expressions. For example, the induced time averaged net flow rate and wall shear stress in both tube and channel with moving two wall contractions are chosen to be our objective functions, which we like to be globally optimized according to set of geometrical-temporal constrained parameters.

It should be noted that, the geometrical constrains draw the shape (profile) of the the wall contractions while the temporal constrains describes how the wall contractions are moving with respect to each other. Detailed optimized problem formulations for our derived insect-inspired tube and channel pumping models are given in the following sections.

3.2 Optimization of the Tube Pumping Model

In this section, we recall our insect-inspired tube pumping model derived in section 2.1 which shows that, a tube with moving wall contractions can work as pumping device and produce a unidirectional flow. A natural question can be raised and asks for, under what geometric and temporal considerations this model is optimal. To answer this question, a simplified bounded constrained optimization formulation given above in section 3.1 is employed as follows.

Consider a tube with moving contraction site marked by the distances x_1, x_2 respectively. The length of each collapse site is given d_1, d_2 distances respectively. The distance S marks the spacing between the two contractions. The parameter θ_{12} describes the relative time (phase)-lag between contractions motions. More illustrative details are shown in Fig. 3.1.

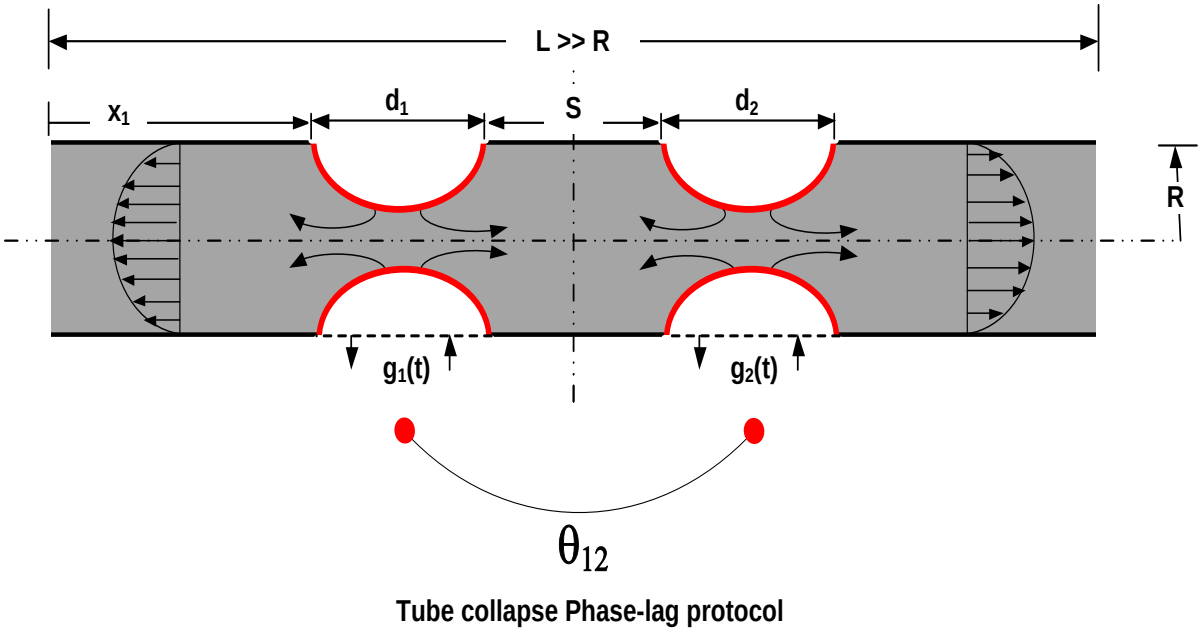

Figure 3.1: Schematic that shows the tube optimization problem formulation to find the optimal geometric x_1, d_1, x_2, d_2, S and temporal design variables θ_{12}

Now, recall the tube wall profile $H(x,t)$ for only two contractions

$$H(x,t) = 1 + A_1 f_1(x, x_1, d_1) g_1(\beta, t) + A_2 f_2(x, x_2, d_2) g_2(t) \tag{3.4}$$

where f_1, f_2, g_1 and g_2 are given as

$$f_1(x) = \tanh(\alpha(x - x_1)) - \tanh(\alpha(x - (x_1 + d_1))) \tag{3.5}$$

$$f_2(x) = \tanh(\alpha(x - x_2)) - \tanh(\alpha(x - (x_2 + d_2))) \tag{3.6}$$

$$g_1(t) = \begin{cases} \frac{1}{2}\left(1 - \cos(2\pi\beta S_t t)\right), & 0 \le t \le 1/\beta S_t \\ 0 & 1/\beta S_t < t \le 1/S_t \end{cases} \tag{3.7}$$

$$g_2(t) = \frac{1}{2}\left(1 - \cos(2\pi S_t t)\right), 0 \le t \le 1/S_t \tag{3.8}$$

where, the non-dimensional parameter β is related to the phase lag between the first and the second contractions by this formula $\theta_{12} = \pi(1 - 1/\beta)$. As previously given in 2.1, the above wall profile was used to derive our objective functions for the induced net flow and wall shear stress as

$$\tau_{rx}(x,t) \downarrow_{r=H} = \frac{H}{2}\frac{\partial p}{\partial x} \tag{3.9}$$

$$Q(x,t) = \frac{-1}{8}\frac{\partial p}{\partial x} H(x,t)^4 \tag{3.10}$$

where,

$$\frac{\partial p}{\partial x} = \frac{1}{H^4(x,t)}\left(G(t) + 16\int_0^x H(s,t)\frac{\partial H(s,t)}{\partial t} ds\right) \tag{3.11}$$

and

$$G(t) = \frac{\Delta p - 16\int_0^1 H^{-4}(s,t)\left(\int_0^s H(s_1,t)\frac{\partial H(s_1,t)}{\partial t} ds_1\right) ds}{\int_0^1 H^{-4}(s,t) ds} \tag{3.12}$$

The goal is to find the optimal design parameters such as x_1, x_2, d_1, d_2 and θ_{12} that maximize (minimize) both the induced net flow $Q(x,t)$ and wall shear stress $\tau_{rx}(x,t)$ objective functions as it will be given in the following separate subsections.

3.2.1 The Effect of Spatial-Temporal of the Tube Wall Contraction Variables

Initially, a parametric study is conducted to understand net flow behaviour as a function of each design variables. In other words, this parametric study is given to show the effect of each design variable on the net flow distribution produced by our derived insect-inspired tube pumping model. For instance, the effect of the percentage tube collapse amplitudes $TC\%$, the phase lag between moving collapses θ_{12}, the start position of first collapse x_1, S and end position of second collapse $x_4 = x_2 + d_2$ are given in details in the following figures.

For instance, The effect of the tube collapse variable $TC\%$ on the time averaged net flow and wall shear stress is given in Fig. 3.2. The time averaged net flow as a function of the phase lag θ_{12} parameter at different $TC\%$ values is given in Fig. 3.2 (a). It is clearly appears that, as the phase lag between contractions increases at a given $TC\%$ value, the induced net flow increase till reach maximum at about $\theta_{12} \simeq 70(deg.)$ the decreases back again and there will be no net flow motions when $\theta_{12} = 180(deg.)$. Furthermore and as expected, as we increase the amount of the tube collapse, the net flow increases as shown 3.2 (b). Since, the time averaged shear stress is induced as a natural consequences to the net flow flow motions. Similar distributions for the time averaged wall shear stress is given as a function of θ_{12} and $TC\%$ in Fig. 3.2 (c & d) respectively. It should be noted that, the shear stress reaches its own maximum at a different phase lag $\theta_{12} \simeq 64(deg.)$ value when it compared with maximum net flow counterpart. This indicates that both net flow and wall shear stress have different rate of increase as a function of the tube collapse.

This observation led us to question at which rate they are increase and which one increase faster as we change the tube collapse for a given of a phase lag value. In Fig. 3.3, the time averaged net flow and wall shear stress is given as a function of the tube collapse ratio. In additions, Polynomial fits are employed in order to determine which one increases faster. For instance, the polynomial fit

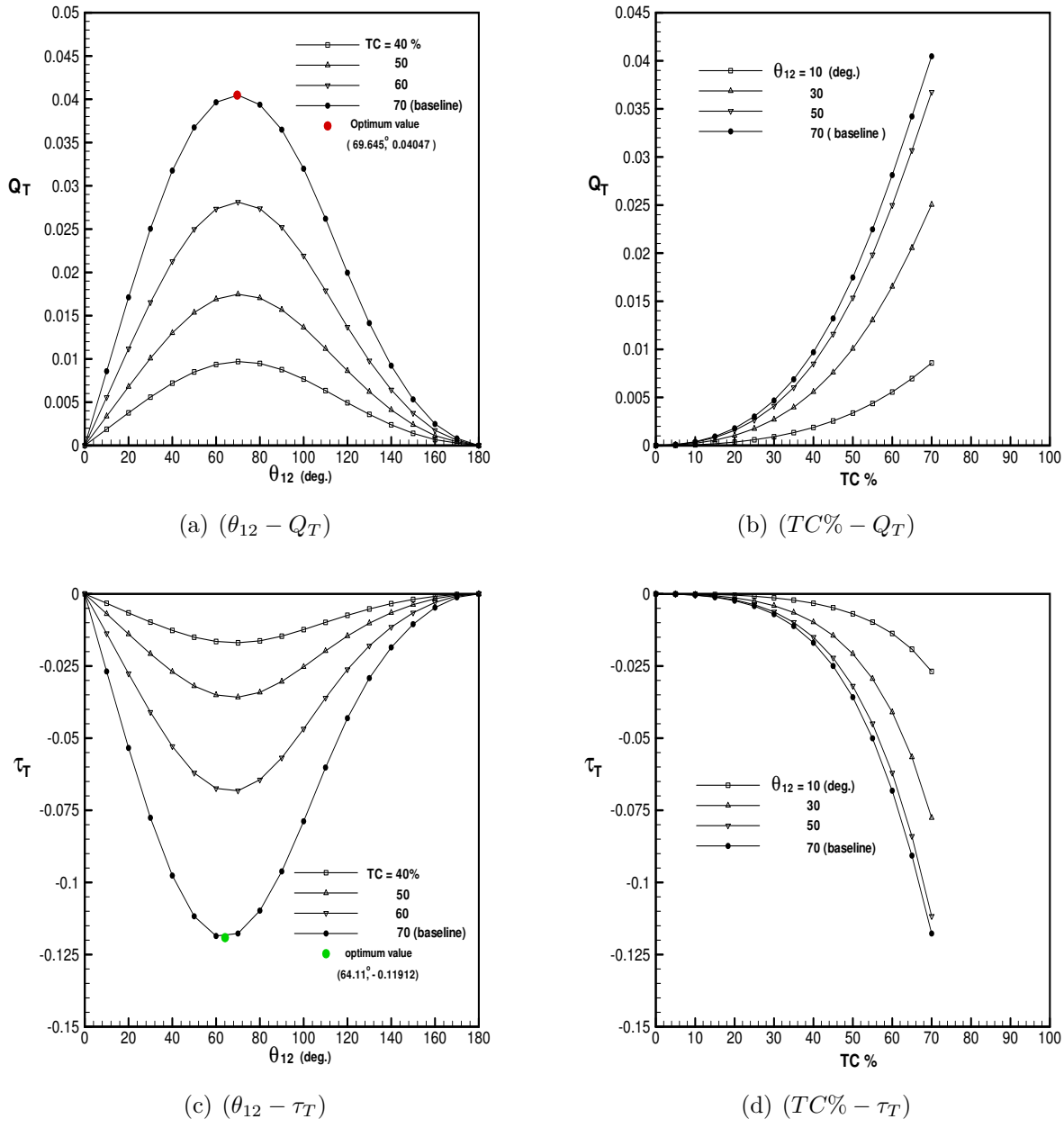

(a) $(\theta_{12} - Q_T)$ (b) $(TC\% - Q_T)$

(c) $(\theta_{12} - \tau_T)$ (d) $(TC\% - \tau_T)$

Figure 3.2: Tube collapse presentage $TC\%$ and phase lag θ_{12} effect on the time averaged net flow and shear stress induced by tube wall contractions.

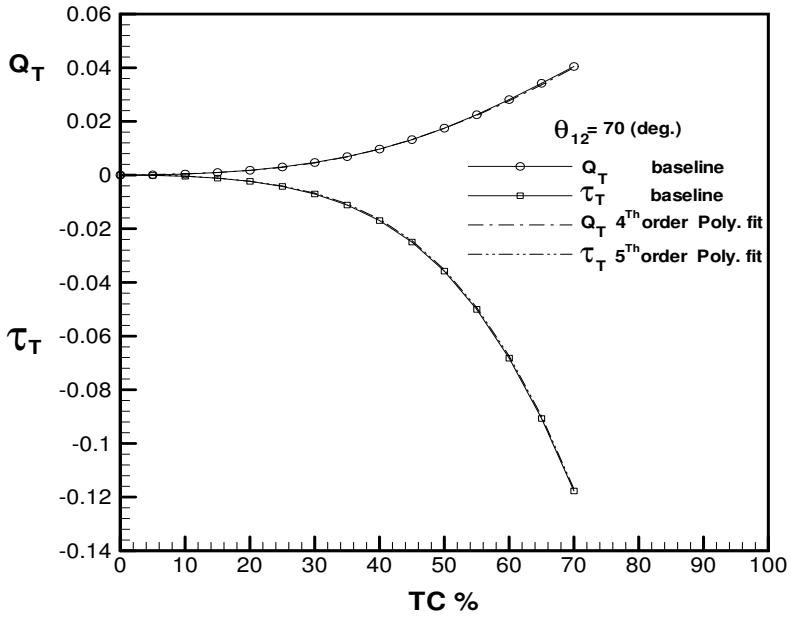

Figure 3.3: Time averaged net flow and wall shear stress as a function of tube collapse presentage $TC\%$ at phase lag $\theta_{12} = 70(deg.)$ along with their polynomial curve fittings

for time averaged flow rate suggests that, net flow scales with the forth order tube collapse ratio and might be given as follows,

$$Q_T \simeq \sum_{i=0}^{4} a_i TC^i \tag{3.13}$$

Similarly, the time averaged wall shear stress is fitted using a polynomial approximations. Results are shown in Fig. 3.3 which shows that, time averaged wall shear stress scales with the fifth order tube collapse ratio and might be expressed as,

$$\tau_T \simeq \sum_{i=0}^{5} b_i TC^i \tag{3.14}$$

where, $a_i \& b_i$ are the polynomial coefficients and can be found in Table 3.1. Since, the rate of increase of the time averaged wall shear stress is one order of magnitude higher than the time averaged net flow induced by the tube collapse ratio. It is not advised to enforce the wall contractions to completely close the tube whereas the wall shear stress will become extremely large and larger

Table 3.1: Polynomial coefficients for tube induced net flow and wall shear stress curve fitting

a_i	value	b_i	value
a_0	$-1.1e^{-4}$	b_0	$-5.0e^{-5}$
a_1	$7.3e^{-5}$	b_1	$7.1e^{-5}$
a_2	$-3.7e^{-6}$	b_2	$-1.4e^{-5}$
a_3	$2.6e^{-7}$	b_3	$4.8e^{-7}$
a_4	$-1.5e^{-9}$	b_4	$-1.3e^{-8}$
a_5	$---$	b_5	$5.6e^{-11}$

supports will be required to hold the tube model in place. Therefore, in the following results a tube collapse ratio of $TC = 70\%$ is chosen and is kept during the entire calculations.

Also, a parametric analysis is used to study effect of the first collapse width distance on the time averaged net flow and wall shear stresses. In Fig. 3.4 (a), we show the distribution of the time averaged net flow as a function of the phase lag timing θ_{12} at a various collapse distance distance x_1. Once again, the time averaged net flow increase as the phase lag increase till it reaches maximum at about phase lag value of $\theta_{12} \simeq= 66(deg.)$ when the $x_1 = 0.1$. This indicates that, as the width of the first collapsing site increase, the net flow induced by the wall motions increases in a non-linear fashion as shown in Fig. 3.4 (b). Similar conclusion can be made with regard to the averaged wall shear stress which also increase whenever a wider collapse distance is used, as shown in Fig. 3.4(c & d).

The effect of another important parameter S which is used to mark the distance between the two contraction sites on the flow parameters is presented in Fig. 3.5. Herein, the two contractions configurations are kept identical and the separation distance S between them has varied accordingly. Results have shown that, when the two contractions are set close to each other, the net flow increases linearly and the maximum net flow takes place at phase lag of about $\theta_{12} \simeq 70.6(deg.)$, as shown in Fig. 3.5 (a & b). Similar behaviour are observed when the averaged wall shear stress τ_T distribution as a function of the collapses separation distance S, is calculated as shown in Fig. 3.5 (c & d). In summary, using two contractions that are located closely to each other results in increase of the net flow rate.

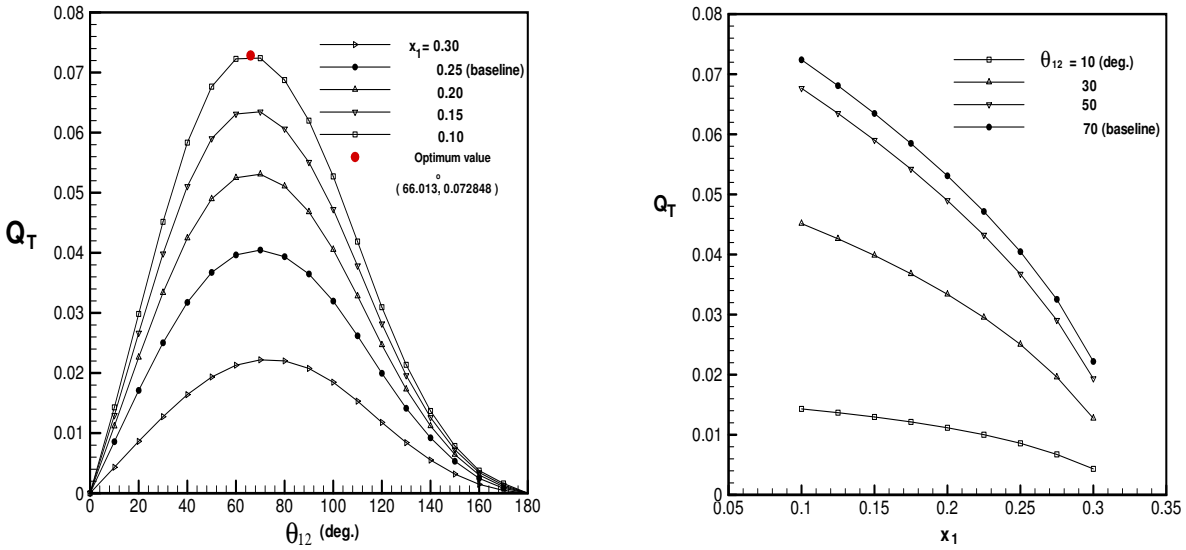

(a) $(\theta_{12} - Q_T)$ (b) $(x_1 - Q_T)$

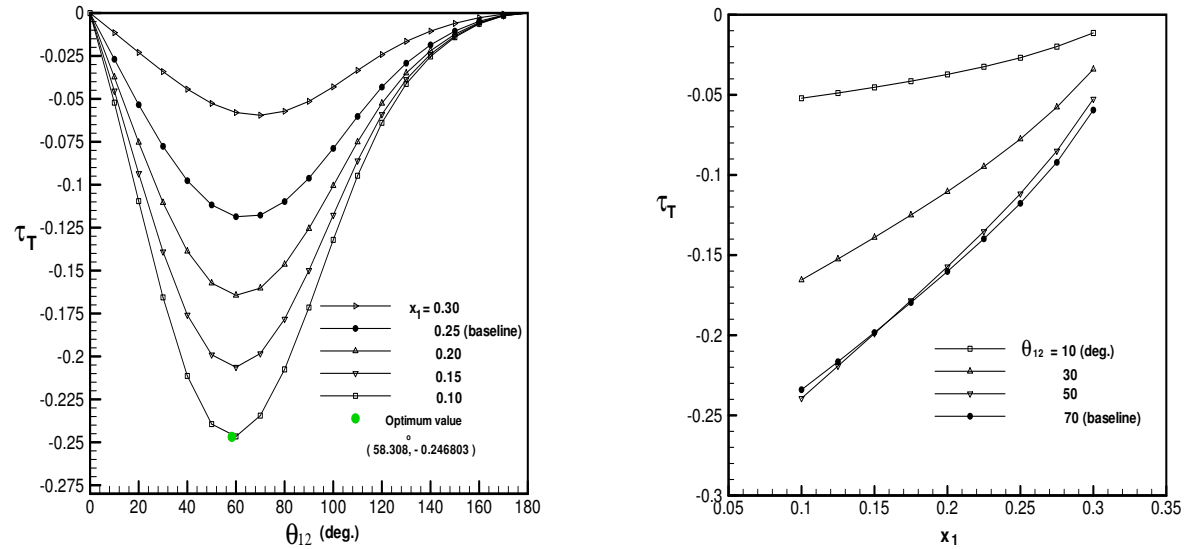

(c) $(\theta_{12} - \tau_T)$ (d) $(x_1 - \tau_T)$

Figure 3.4: The contraction beginning distance x_1 and phase lag θ_{12} effect on the time averaged net flow and shear stress induced by tube wall contractions.

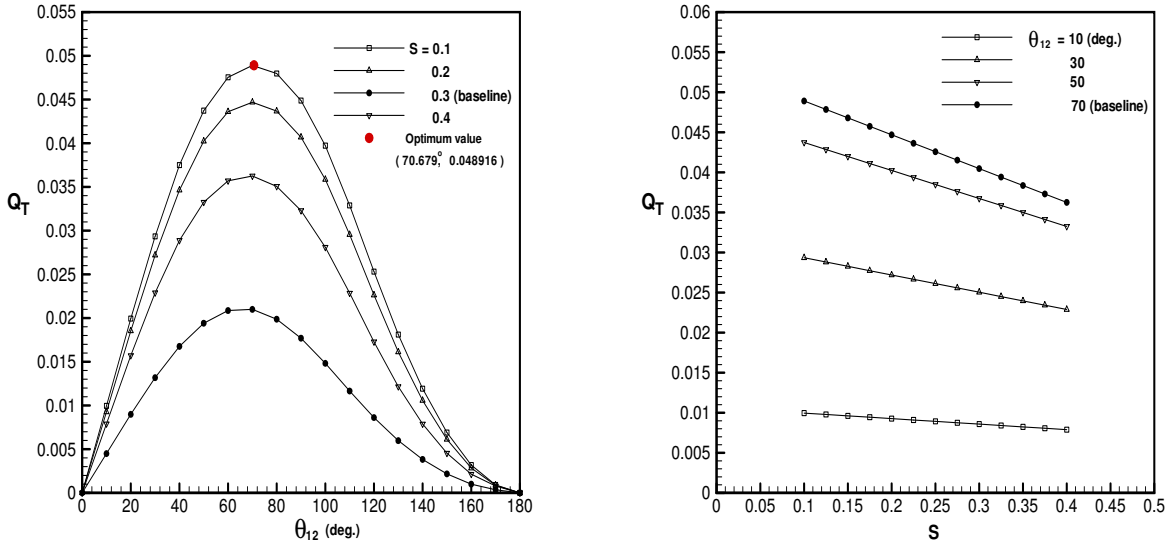

(a) $(\theta_{12} - Q_T)$

(b) $(S - Q_T)$

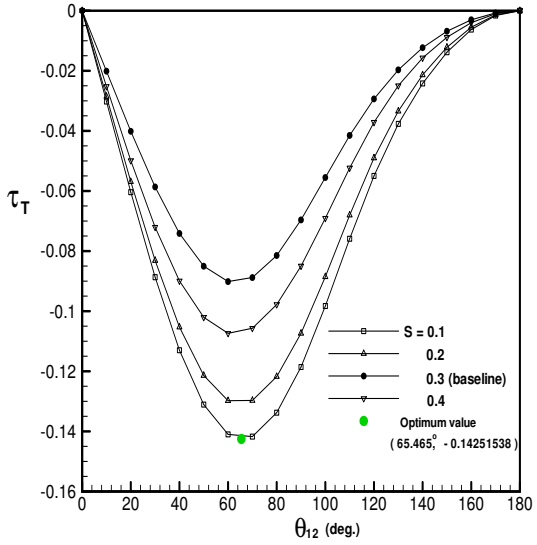

(c) $(\theta_{12} - \tau_T)$

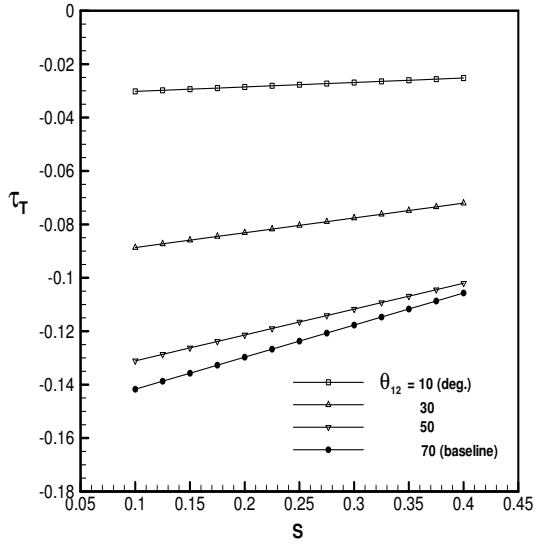

(d) $(S - \tau_T)$

Figure 3.5: The separation distance S between two identical contractions and phase lag θ_{12} effect on the time averaged net flow and shear stress induced by tube wall contractions.

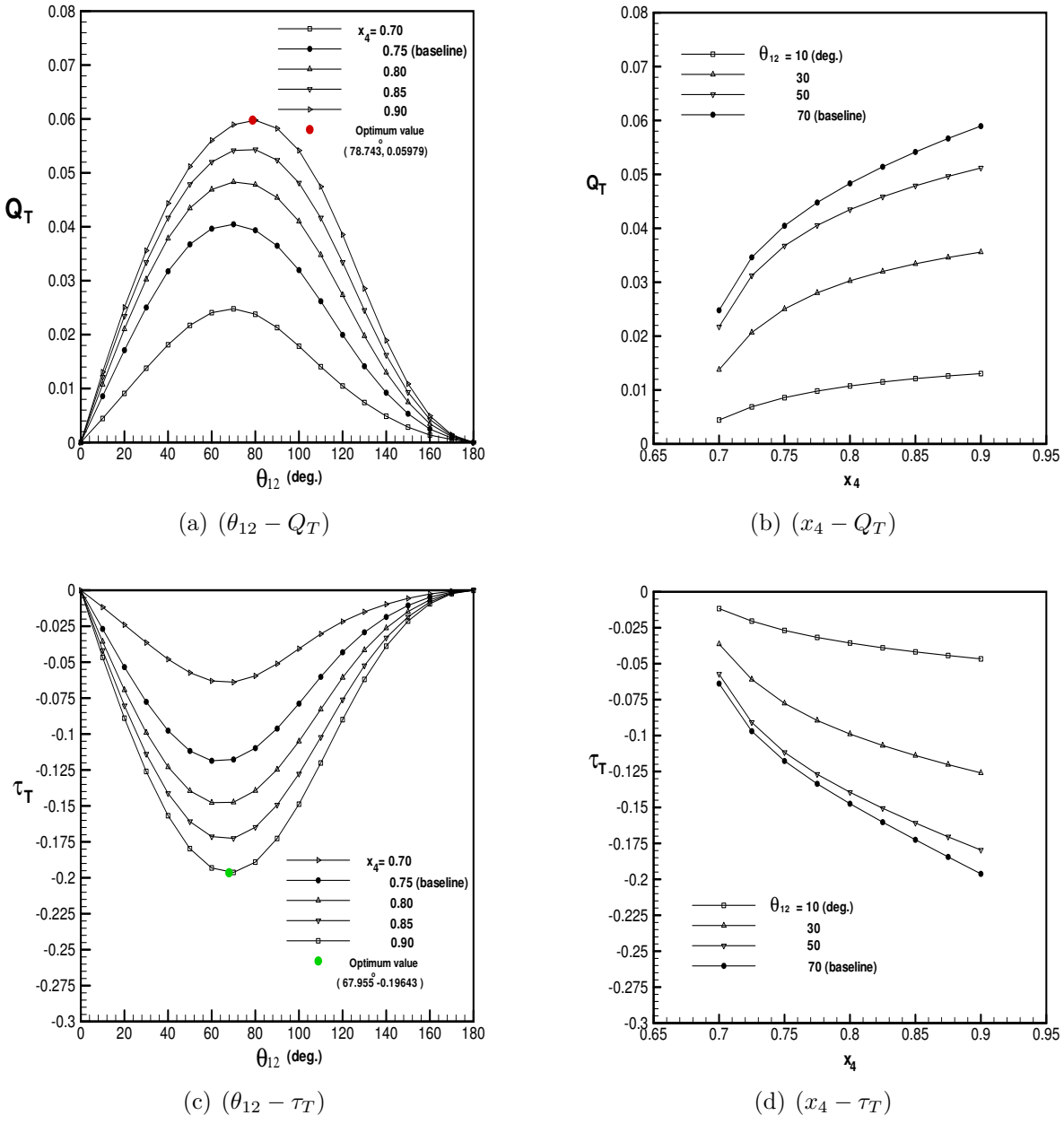

(a) $(\theta_{12} - Q_T)$

(b) $(x_4 - Q_T)$

(c) $(\theta_{12} - \tau_T)$

(d) $(x_4 - \tau_T)$

Figure 3.6: The contraction beginning distance $x_4 = x_2 + d_2$ and phase lag θ_{12} effect on the time averaged net flow and shear stress induced by tube wall contractions.

Finally, we show the effect of extending the width of the second contraction site by using larger collapsing distances $x_4 = x_2 + d_2$ in the mean time we keep the first contraction configurations fixed. Results have shown that, using larger collapsing site will result in increasing the time averaged net flow as shown in Fig. 3.6 (a & b). The maximum net flow occurs at a phase angle of about $\theta_{12} \simeq 78.7(deg.)$ when the furthest second collapse distances is used $x_4 = 0.9$. Once again, a similar behaviour are observed when the averaged wall shear stress τ_T distribution as a function of the second collapse distance x_4 is calculated, as shown in Fig. 3.6 (c & d).

In summary, based on the parametric study given above throughout Figs. (3.2-3.6), one can reach to the following conclusion. The time averaged net flow as well as the averaged wall shear stress induced by these moving tube wall contractions are strong functions of the geometrical and temporal parameters that shape and govern the kinematics of these contractions sites and their movements. Using contractions with larger tube collapse ratio and wider collapse sites that are close enough to each other and moves with different phase lag will result in increasing the net flow produced out of this system. Although, each parameter variations will lead to higher net flow values, it will be great to find the optimum collapsing configurations that induces the ultimate net flow rate out of the system under consideration, as it will be given in the next subsection 3.2.2.

3.2.2 Tube Model Optimization Functions

In this section, we use the constrained optimization method as a complementary analysis to the above parametric study to better find the optimal pumping conditions. From the above section 3.1, the final formulation of the optimization problem for the time average net flow and the averaged wall shear stress can be mathematically represented by

$$Minimize : f_1(\mathbf{x}) = -Q_T = -\frac{1}{T}\int_0^T Q(x,t)dt \tag{3.15}$$

$$Minimize : f_2(\mathbf{x}) = \tau_T = \frac{1}{T}\int_0^1 \int_0^T \tau(x,t)dtdx \tag{3.16}$$

$$Subjected - to : \mathbf{x} = \begin{cases} 0 \leq \theta_{12} \leq 180(deg.) \\ 0.15 < d_1 \leq 0.35 \\ 0.15 < d_2 \leq 0.35 \\ 0.10 < S \leq 0.40 \\ x_1 = L/2 - S/2 - d_1 \\ x_2 = L/2 + S/2 \end{cases} \tag{3.17}$$

where, $\theta_(12)$ is the phase lag between contractions motions, $d_1 \& d_2$ are the first and second contractions widths respectively, S is the separation distance between the two collapses and $x_1 \& x_2$ mark the start positions of the first and second collapse respectively.

The goal herein is to find the value of the minimizer $\mathbf{x}^* = [\theta_(12), d_1, d_2, S]$ that optimize the induced averaged net flow and wall shear stress. The constrained optimization techniques based on the global minima approach is used to find out those optimal parameters. The Matlab optimization tool box is used to do the calculations. Two cases are investigated namely symmetric and non-symmetric configurations and are compared with a baseline configuration for seek of comparisons. We mean by symmetric configuration, is both contractions sites are required to have same geometries and the tube will be symmetric about mid-plane line $x = 0.5$. In the non-symmetric configuration, contractions does not need to be identical. The baseline configuration, is the configuration that has been used frequently throughout this dissertation specially in chapter 2, where $x_1 = 0.25, d_2 = 0.1, d_2 = 0.1, S = 0.3$.

In Fig. 3.7, we show results when the time averaged net flow was used as our optimization function. The minimizer vector has found for both symmetric and non-symmetric configurations and has compared with the baseline case of study as given in Table 3.2. The time averaged net flow distribution and the associated averaged wall shear stress as a function of phase lag parameters are given for each configurations, whereas the optimized values are marked on red symbol as shown in Fig. 3.7. Results have shown that, the optimum net flow produced by non-symmetric configuration is slightly larger than net flow produced by both symmetric and baseline configurations. Furthermore, the optimal value occurs at slightly lower phase lag as documented in Table 3.2.

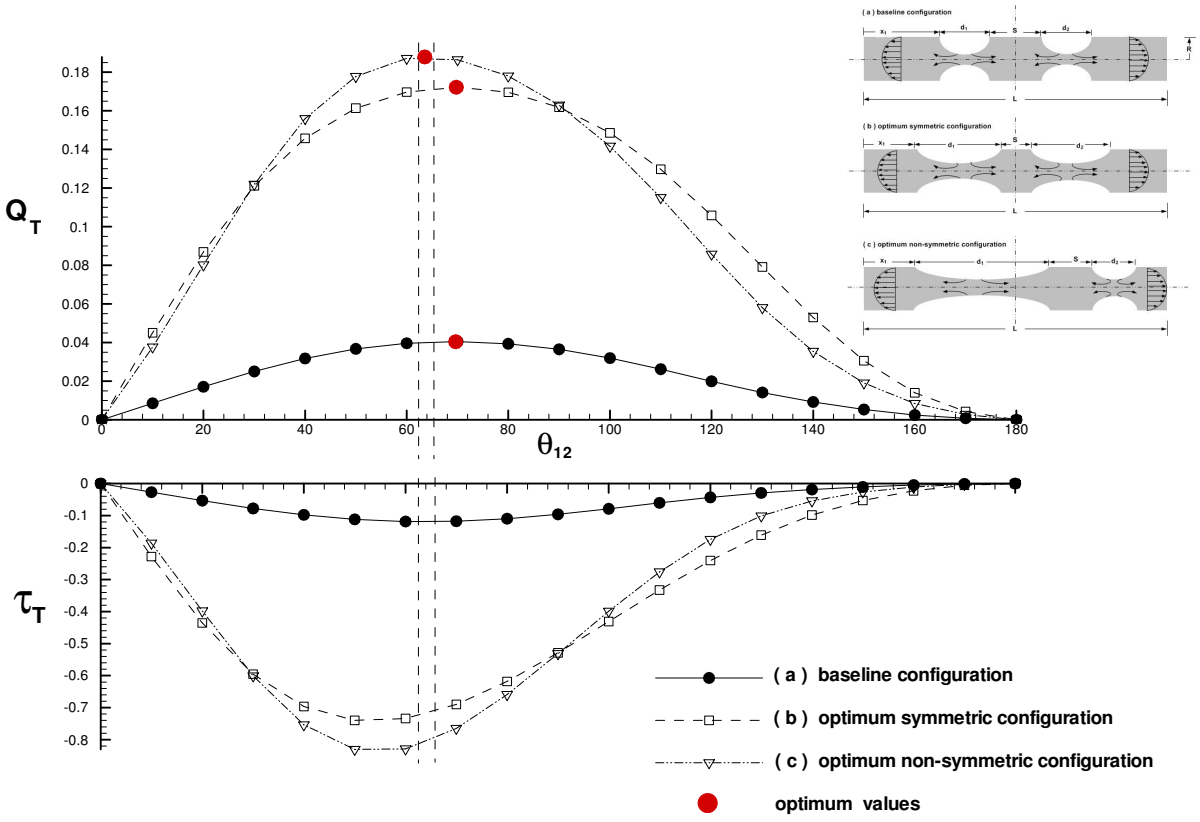

Figure 3.7: Tube net flow optimization function: The time averaged net flow and wall shear stress distribution as a function of phase lag parameter $\theta_(12)$ and the corresponding optimal values at the baseline, symmetric and non-symmetric configurations.

Table 3.2: Tube model time averaged net flow optimization configurations

Tube collapse configurations	$\theta_{12}(deg.)$	d_1	d_2	S	Q_T
Baseline configurations	69.645	0.100	0.100	0.3	0.040444
Optimum symmetric configurations	69.763	0.350	0.350	0.1	0.172226
Optimum non-symmetric configurations	63.561	0.508	0.192	0.1	0.187903

In summary, the non-symmetric configuration is the optimum scenario and work more efficiently when it compared with both symmetric and baselines counterparts.

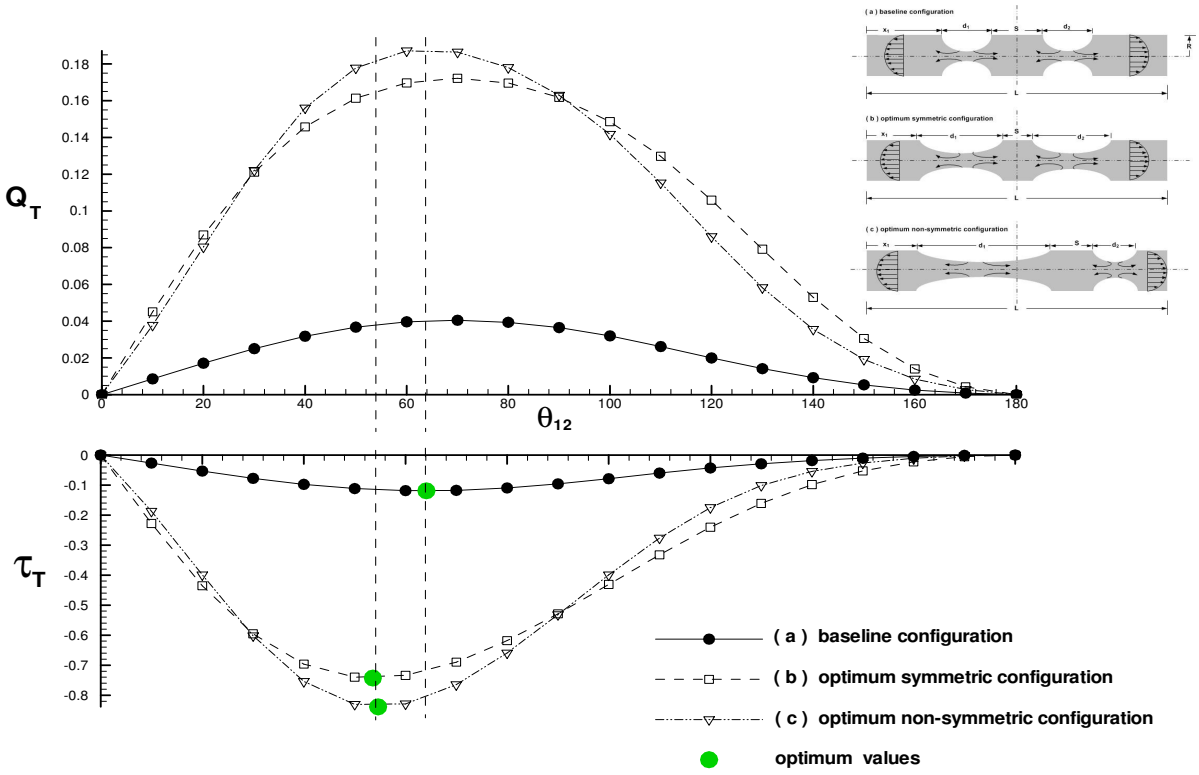

Figure 3.8: Tube wall shear stress optimization function: The time averaged net flow and wall shear stress distribution as a function of phase lag parameter $\theta_(12)$ and the corresponding optimal values at the baseline, symmetric and non-symmetric configurations.

Table 3.3: Tube model time averaged shear stress optimization configurations

Tube collapse configurations	$\theta_{12}(deg.)$	d_1	d_2	S	τ_T
Baseline configurations	64.110	0.100	0.100	0.3	-0.1191256
Optimum symmetric configurations	53.577	0.350	0.350	0.1	-0.7427991
Optimum non-symmetric configurations	54.608	0.507	0.193	0.1	-0.8387404

Similarly, in Fig. 3.8, we show results when the time averaged wall shear stress was used as our optimization function. The optimal values for this case are given in Table 3.3. The time averaged wall shear stress distribution and the associated time averaged net flow a function of phase lag parameters are given for the three configurations, whereas the optimized values are marked on green symbol as shown in Fig. 3.8. Results have shown that, the optimum wall shear stress produced by symmetric and non-symmetric configurations are the same or are slightly different and optimal values occur at almost the same phase lag value as given in Table 3.3.

3.3 Optimization of the Channel Pumping Model

In a similar fashion, optimization and parametric studies for the flow induced by channel with moving wall contractions is given in this part. Recall our insect-inspired channel pumping model derived in section 2.2 which shows that, a channel with moving wall contractions can work as pumping device and produce a unidirectional flow. The simplified bounded constrained optimization formulation given in section 3.1 is employed to find the channel geometrical and temporal optimal values.

Now, if we consider a channel with moving contraction site marked by the distances x_1, x_2 respectively. The length of each collapse site is given d_1, d_2 distances respectively. The distance S marks the spacing between the two contractions. The parameter θ_{12} describes the relative time (phase)-lag between contractions motions. More illustrative details are shown in Fig. 3.9.

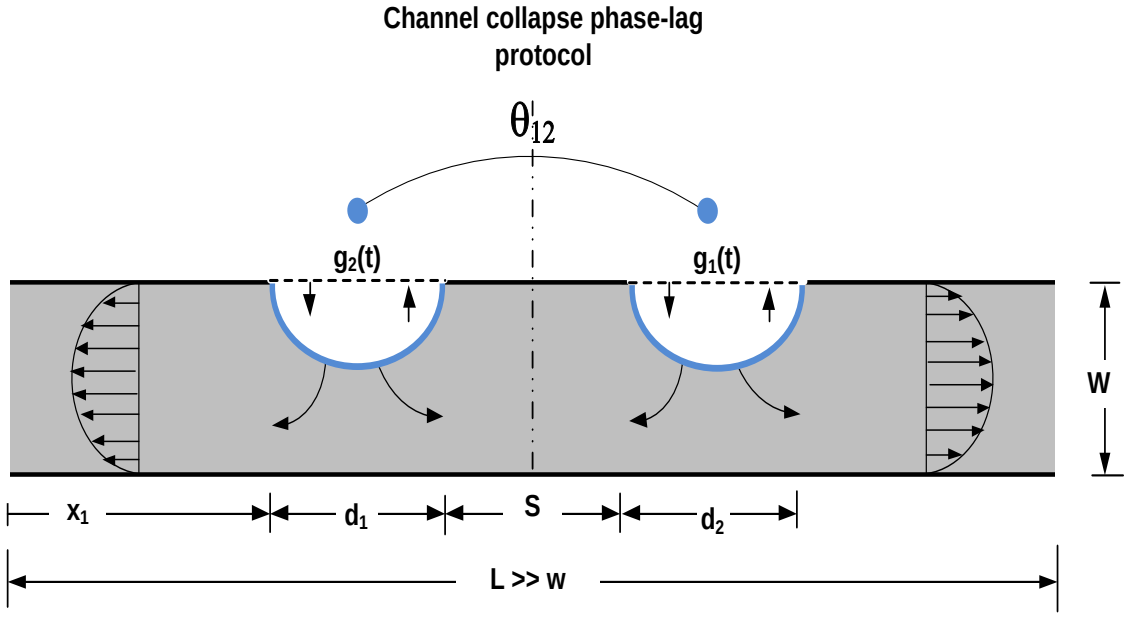

Figure 3.9: Schematic that shows the tube optimization problem formulation to find the optimal geometric x_1, d_1, x_2, d_2, S and temporal design variables θ_{12}.

Recall the channel wall profile $H_2(x,t)$ for only two contractions

$$H(x,t) = \frac{1}{2} + A_1 f_1(x, x_1, d_1) g_1(\beta, t) + A_2 f_2(x, x_2, d_2) g_2(t) \tag{3.18}$$

where f_1, f_2, g_1 and g_2 are given as

$$f_1(x) = \tanh(\alpha(x - x_1)) - \tanh(\alpha(x - (x_1 + d_1))) \tag{3.19}$$

$$f_2(x) = \tanh(\alpha(x - x_2)) - \tanh(\alpha(x - (x_2 + d_2))) \tag{3.20}$$

$$g_1(t) = \begin{cases} \frac{1}{2}\left(1 - \cos(2\pi\beta S_t t)\right), & 0 \le t \le 1/\beta S_t \\ 0 & 1/\beta S_t < t \le 1/S_t \end{cases} \tag{3.21}$$

$$g_2(t) = \frac{1}{2}\left(1 - \cos(2\pi S_t t)\right), 0 \le t \le 1/S_t \tag{3.22}$$

where, the non-dimensional parameter β is related to the phase lag between the first and the second contractions by this formula $\theta_{12} = \pi(1 - 1/\beta)$. As previously given in 2.2, the above wall profile was used to derive our objective functions for the induced net flow and wall shear stress as

$$\tau(x,t) \downarrow_{r=H} = \frac{H_2 - H_1}{2} \frac{\partial p}{\partial x} \tag{3.23}$$

$$Q(x,t) = \frac{-1}{12} \frac{\partial p}{\partial x} \left(H_2 - H_1\right)^3 \tag{3.24}$$

where,

$$\frac{\partial p}{\partial x} = \frac{1}{\left(H_2 - H_1\right)^3} \left(G(t) + 12 \int_0^x \frac{\partial H_2(s,t)}{\partial t} ds \right) \tag{3.25}$$

and

$$G(t) = \frac{\Delta p - 12 \int_0^1 \left(H_2(x,t) - H1\right)^{-3} \left(\int_0^s \frac{\partial H_2(s,t)}{\partial t} ds \right) dx}{\int_0^1 \left(H_2(s,t) - H_1\right)^{-3} ds} \tag{3.26}$$

The goal is to find the optimal design parameters such as x_1, x_2, d_1, d_2 and θ_{12} that maximize (minimize) both the induced net flow $Q(x,t)$ and wall shear stress $\tau(x,t)$ objective functions as it will be given in the following separate subsections.

3.3.1 The Effect of Spatial-Temporal of the Channel Wall Contraction Variables

A parametric study is conducted to understand net flow behaviour as a function of each design variable. This parametric study is given to show the effect of each variable on the net flow distribution produced by our derived insect-inspired channel pumping model. For instance, the effect of the percentage travel collapse amplitudes $TC\%$, the phase lag between moving collapses θ_{12}, the start position of first collapse x_1, S and end position of second collapse $x_4 = x_2 + d_2$ are given in details as follows.

For instance, The effect of the channel travel collapse variable $TC\%$ on the time averaged net flow and wall shear stress is given in Fig. 3.10. The time averaged net flow as a function of the phase lag θ_{12} parameter at different $TC\%$ values is given in Fig. 3.10 (a). It is clearly appears that, as the phase lag between contractions increases at a given $TC\%$ value, the induced net flow increase till reach maximum at about $\theta_{12} \simeq 68.4(deg.)$ the decreases back again and there will be no net flow motions when $\theta_{12} = 180(deg.)$. Furthermore and as expected, as we increase the amount of the channel travel collapse, the net flow increases as shown in Fig. 3.10 (b). Similar distributions for the time averaged wall shear stress is given as a function of θ_{12} and $TC\%$ in Fig. 3.10 (c & d) respectively. it should be noted that, the shear stress reaches its own maximum at a different phase lag $\theta_{12} \simeq 62.7(deg.)$ value when it compared with maximum net flow counterpart. This indicates that both net flow and wall shear stress have different rate of increase as a function of the channel travel collapses.

In order to investigate at which rate both net flow and wall shear stress are increasing and which one increase faster as we change the channel travel collapse distance for a given of a phase lag value. In Fig. 3.11, the time averaged net flow and wall shear stress is given as a function of the tube collapse ratio. In additions, Polynomial fits are employed in order to determine which one increases

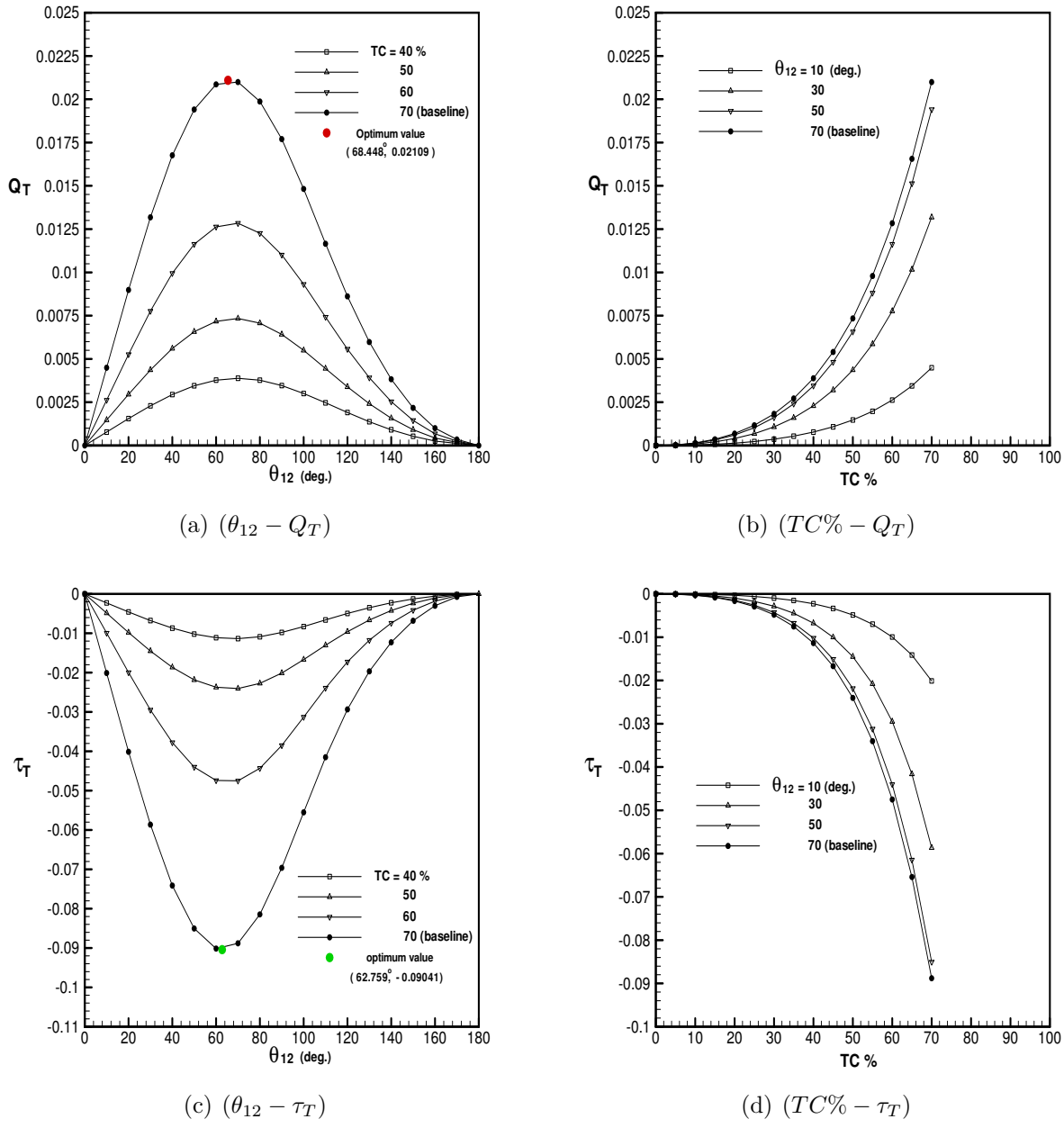

(a) $(\theta_{12} - Q_T)$

(b) $(TC\% - Q_T)$

(c) $(\theta_{12} - \tau_T)$

(d) $(TC\% - \tau_T)$

Figure 3.10: Channel collapse presentage $TC\%$ and phase lag θ_{12} effect on the time averaged net flow and shear stress induced by channel wall contractions.

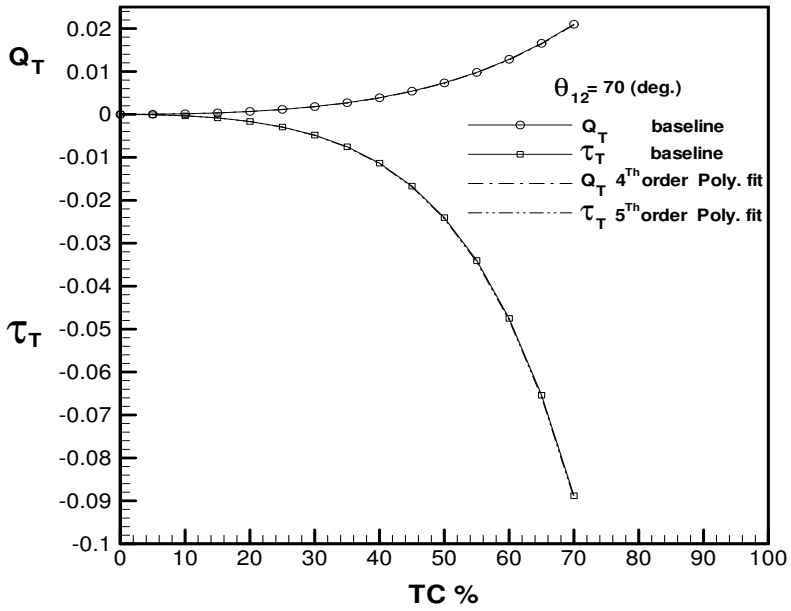

Figure 3.11: Time averaged net flow and wall shear stress as a function of tube collapse presentage $TC\%$ at phase lag $\theta_{12} = 70(deg.)$ along with their polynomial curve fittings

faster. For instance, the polynomial fit for time averaged flow rate suggests that, net flow scales with the forth order channel travel collapse ratio and might be given as follows,

$$Q_T \simeq \sum_{i=0}^{4} a_i TC^i \tag{3.27}$$

Similarly, the time averaged wall shear stress is fitted using a polynomial approximations. Results are shown in Fig. 3.11 which shows that, time averaged wall shear stress scales with the fifth order channel travel collapse ratio and might be expressed as,

$$\tau_T \simeq \sum_{i=0}^{5} b_i TC^i \tag{3.28}$$

where, $a_i \& b_i$ are the polynomial coefficients and can be found in Table 3.4. Since, the rate of increase of the time averaged wall shear stress is one order of magnitude higher than the time averaged net flow induced by the channel travel collapse ratio. It is not advised to enforce the wall contractions to completely close the channel whereas the wall shear stress will become extremely

Table 3.4: Polynomial coefficients for channel induced net flow and wall shear stress curve fitting

a_i	value	b_i	value
a_0	$-5.2e^{-6}$	b_0	$-1.2e^{-6}$
a_1	$1.5e^{-6}$	b_1	$-2.3e^{-6}$
a_2	$1.3e^{-6}$	b_2	$-1.8e^{-6}$
a_3	$5.6e^{-9}$	b_3	$-1.3e^{-7}$
a_4	5.2^{-10}	b_4	$1.8e^{-9}$
a_5	$---$	b_5	$-4.7e^{-11}$

large and larger supports will be required to hold the channel model in place. Therefore, in the following results a channel travel collapse ratio of $TC = 70\%$ is chosen and is kept during the entire following calculations.

Also, a parametric analysis is used to study effect of the first collapse width distance on the time averaged net flow and wall shear stresses. In Fig. 3.12 (a), we show the distribution of the time averaged net flow as a function of the phase lag timing θ_{12} at a various collapse distance distance x_1. Once again, the time averaged net flow increase as the phase lag increase till it reaches maximum at about phase lag value of $\theta_{12} \simeq= 63.5(deg.)$ when the $x_1 = 0.1$. This indicates that, as the width of the first collapsing site increase, the net flow induced by the wall motions increases in a non-linear fashion as shown in Fig. 3.12 (b). Similar conclusion can be made with regard to the averaged wall shear stress which also increase whenever a wider collapse distance is used, as shown in Fig. 3.12 (c & d).

The effect of another important parameter S which is used to mark the distance between the two contraction sites on the flow parameters is presented in Fig. 3.13. Herein, the two contractions configurations are kept identical and the separation distance S between them has varied accordingly. Results have shown that, when the two contractions are set close to each other, the net flow increases linearly and the maximum net flow takes place at phase lag of about $\theta_{12} \simeq 67.1(deg.)$, as shown in Fig. 3.13 (a & b). Similar behaviour are observed when the averaged wall shear stress τ_T distribution as a function of the collapses separation distance S, is calculated as shown in Fig.

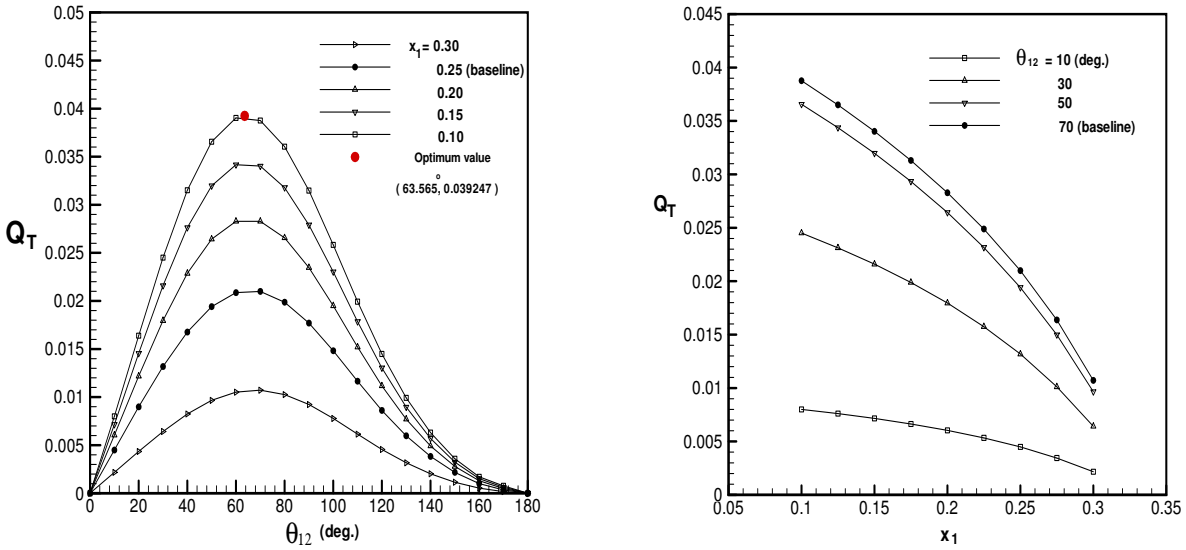

(a) $(\theta_{12} - Q_T)$ (b) $(x_1 - Q_T)$

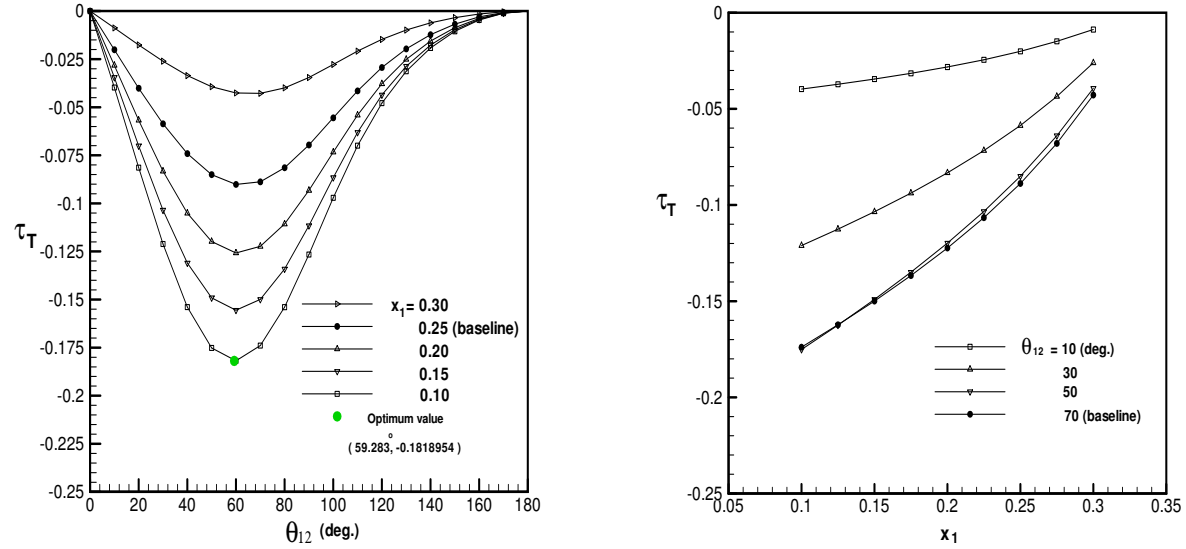

(c) $(\theta_{12} - \tau_T)$ (d) $(x_1 - \tau_T)$

Figure 3.12: The contraction beginning distance x_1 and phase lag θ_{12} effect on the time averaged net flow and shear stress induced by tube wall contractions.

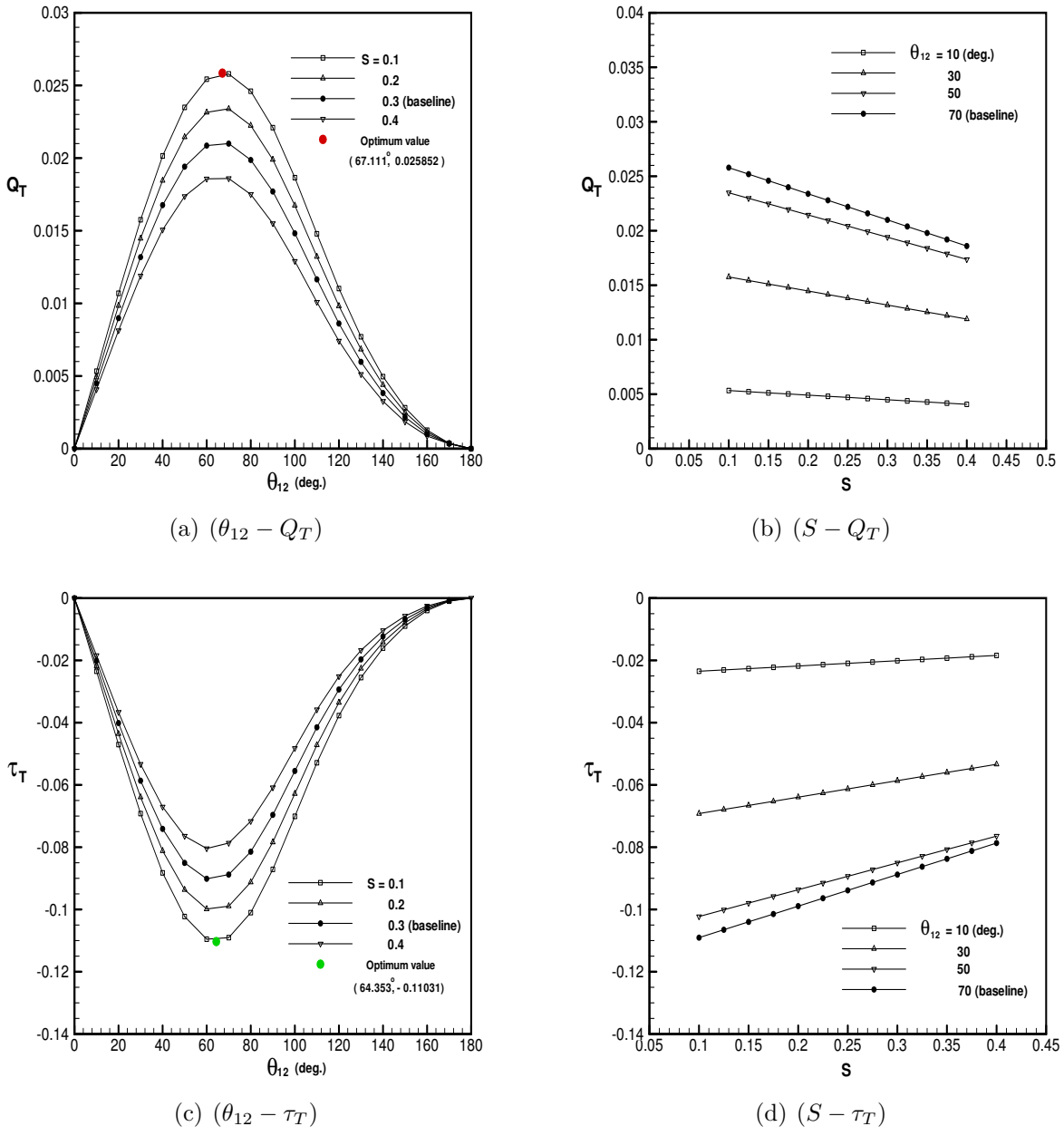

(a) $(\theta_{12} - Q_T)$

(b) $(S - Q_T)$

(c) $(\theta_{12} - \tau_T)$

(d) $(S - \tau_T)$

Figure 3.13: The separation distance S between two identical contractions and phase lag θ_{12} effect on the time averaged net flow and shear stress induced by tube wall contractions.

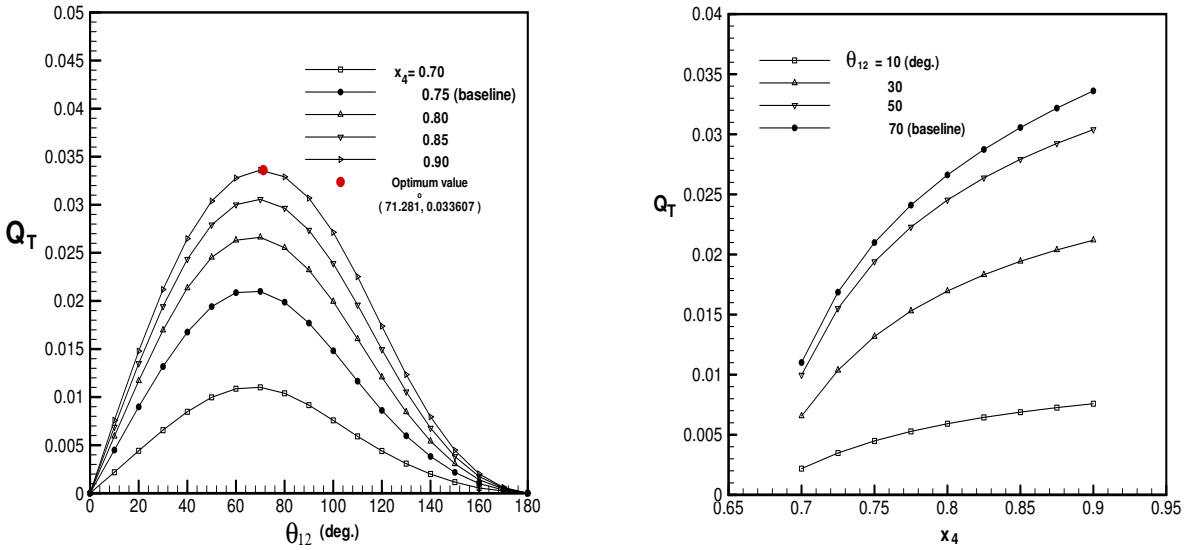

(a) $(\theta_{12} - Q_T)$ (b) $(x_4 - Q_T)$

(c) $(\theta_{12} - \tau_T)$ (d) $(x_4 - \tau_T)$

Figure 3.14: The contraction beginning distance $x_4 = x_2 + d_2$ and phase lag θ_{12} effect on the time averaged net flow and shear stress induced by tube wall contractions.

3.13 (c & d). In summary, using two contractions that are located closely to each other results in increase of the net flow rate.

Finally, we show the effect of extending the width of the second contraction site by using larger collapsing distances $x_4 = x_2 + d_2$ in the mean time we keep the first contraction configurations fixed. Results have shown that, using larger collapsing site will result in increasing the time averaged net flow as shown in Fig. 3.14 (a & b). The maximum net flow occurs at a phase angle of about $\theta_{12} \simeq 71.2(deg.)$ when the furthest second collapse distances is used $x_4 = 0.9$. Once again, a similar behaviour are observed when the averaged wall shear stress τ_T distribution as a function of the second collapse distance x_4 is calculated, as shown in Fig. 3.14 (c & d). Based on the parametric study given above, one can reach to the following conclusion. The time averaged net flow as well as the averaged wall shear stress induced by these moving channel wall contractions are strong functions of the geometrical and temporal parameters that shape and govern the kinematics of these contractions sites and their movements. Using contractions with larger travel collapse ratio and wider collapse sites that are close enough to each other and moves with different phase lag will result in increasing the net flow produced out of this system. Although, each parameter variations will lead to higher net flow values, it will be great to find the optimum collapsing configurations that induces the ultimate net flow rate which will be given in the next subsection 3.3.2.

3.3.2 Channel Model Optimization Functions

Similar to the tube optimization analysis given in section 3.2.2, we use the approach of the constrained optimization method as a complementary analysis to the above channel parametric study to better find the optimal pumping conditions for our derived insect-inspired channel pumping model. Based on the above section 3.1, the final formulation of the optimization problem for the time average net flow and the averaged wall shear stress can be mathematically represented by

$$Minimize : f_1(\mathbf{x}) = -Q_T = -\frac{1}{T}\int_0^T Q(x,t)dt \tag{3.29}$$

$$Minimize : f_2(\mathbf{x}) = \tau_T = \frac{1}{T}\int_0^1 \int_0^T \tau(x,t)dtdx \tag{3.30}$$

$$Subjected - to : \mathbf{x} = \begin{cases} 0 \leq \theta_{12} \leq 180(deg.) \\ 0.15 < d_1 \leq 0.35 \\ 0.15 < d_2 \leq 0.35 \\ 0.10 < S \leq 0.40 \\ x_1 = L/2 - S/2 - d_1 \\ x_2 = L/2 + S/2 \end{cases} \tag{3.31}$$

where, $\theta_(12)$ is the phase lag between contractions motions, $d_1 \& d_2$ are the first and second contractions widths respectively, S is the separation distance between the two collapses and $x_1 \& x_2$ mark the start positions of the first and second collapse respectively. The goal herein is to find the value of the minimizer $\mathbf{x}^* = [\theta_(12), d_1, d_2, S]$ that optimize the induced averaged net flow and wall shear stress. The constrained optimization techniques based on the global minima approach is used to find out those optimal parameters. The Matlab optimization tool box is used to do the calculations. Two cases are investigated namely symmetric and non-symmetric configurations and are compared with a baseline configuration for seek of comparisons. We mean by symmetric configuration, is both contractions sites are required to have same geometries and the tube will be symmetric about mid-plane line $x = 0.5$. In the non-symmetric configuration, contractions does not need to be identical. The baseline configuration has $x_1 = 0.25, d_2 = 0.1, d_2 = 0.1, S = 0.3$.

In Fig. 3.15, we show results when the time averaged net flow was used as our optimization function. The minimizer vector has found for both symmetric and non-symmetric configurations and has compared with the baseline case of study as given in Table 3.5. The time averaged net flow distribution and the associated averaged wall shear stress as a function of phase lag parameters are given for each configurations, whereas the optimized values are marked on red symbol as shown in Fig. 3.15. The optimum net flow produced by non-symmetric configuration is slightly larger than net flow produced by both symmetric and baseline configurations. Furthermore, the optimal

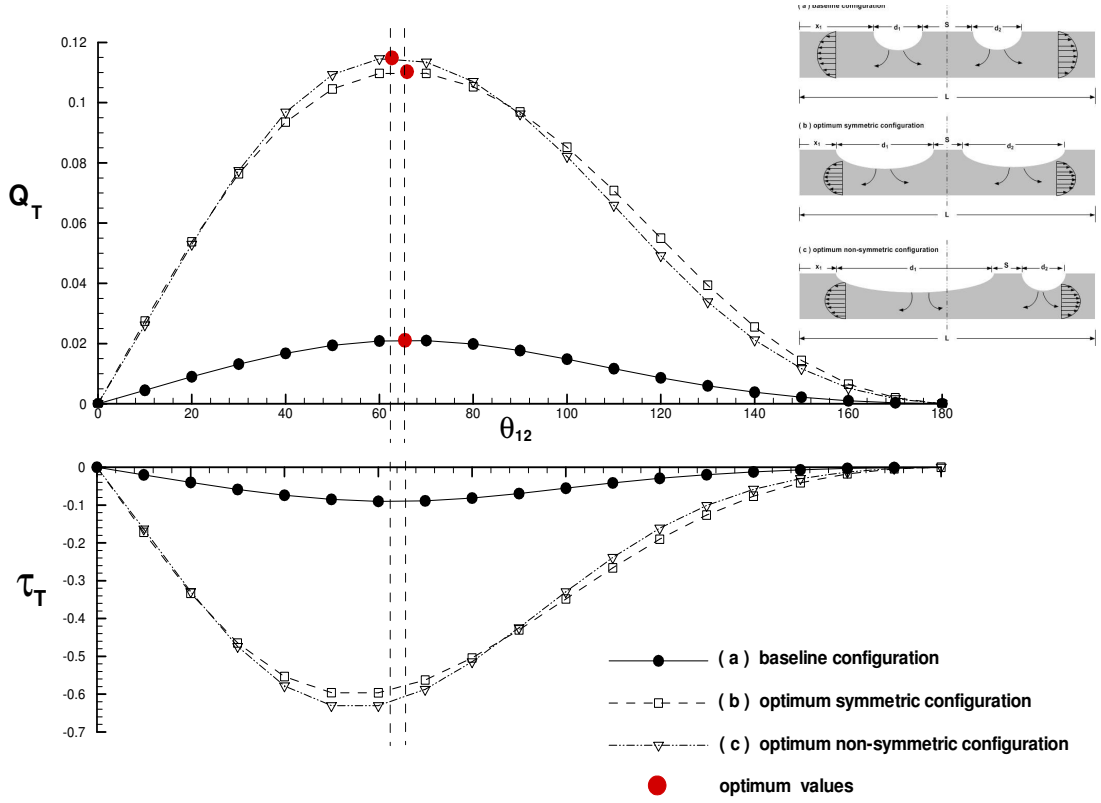

Figure 3.15: Channel net flow optimization function: The time averaged net flow and wall shear stress distribution as a function of phase lag parameter $\theta_(12)$ and the corresponding optimal values at the baseline, symmetric and non-symmetric configurations.

value occurs at slightly lower phase lag value, see Table 3.5. In summary, the non-symmetric configuration is the optimum scenario and work more efficiently when it compared with both symmetric and baselines counterparts.

Table 3.5: Channel model time averaged net flow optimization configurations

Channel collapse configurations	$\theta_{12}(deg.)$	d_1	d_2	S	Q_T
Baseline configurations	65.448	0.100	0.100	0.3	0.021112
Optimum symmetric configurations	65.890	0.350	0.350	0.1	0.110324
Optimum non-symmetric configurations	62.665	0.441	0.259	0.1	0.114880

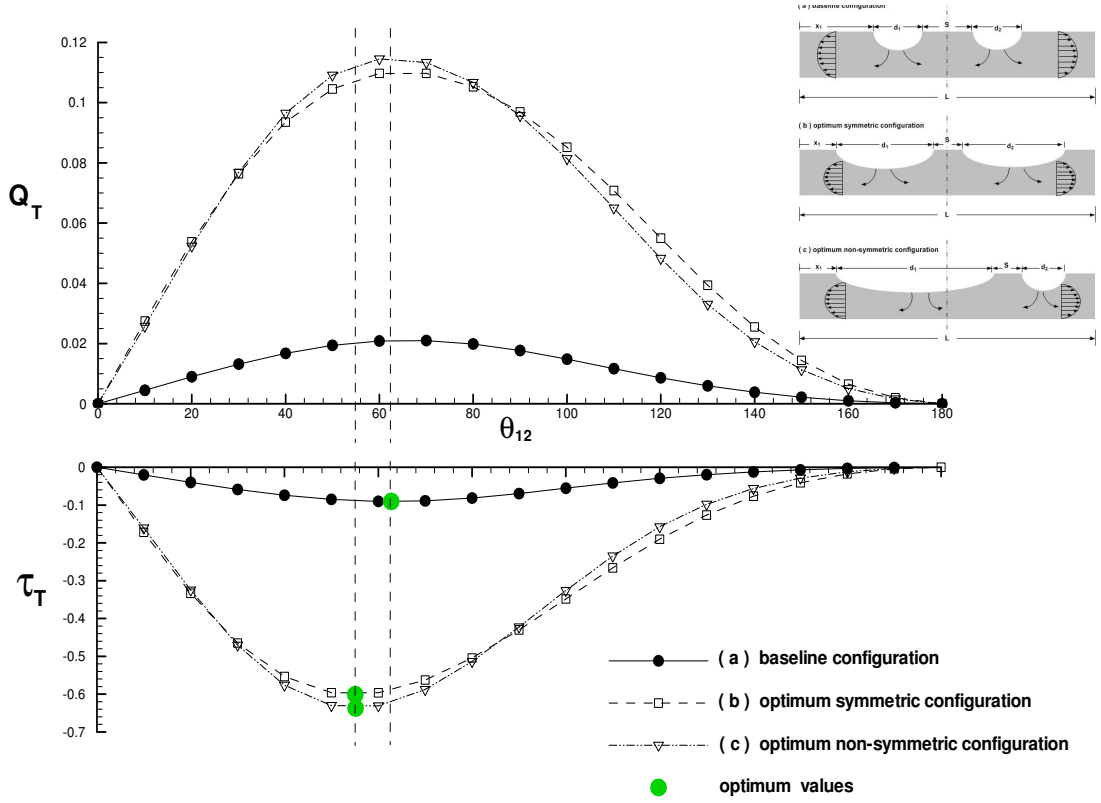

Figure 3.16: Channel wall shear stress optimization function: The time averaged net flow and wall shear stress distribution as a function of phase lag parameter $\theta_(12)$ and the corresponding optimal values at the baseline, symmetric and non-symmetric configurations.

In Fig. 3.16, results for the averaged wall shear stress when used as optimization function are given. The optimal values are provided in Table 3.6. The averaged wall shear stress and the associated averaged net flow as a function of phase lag are given for same three configurations, whereas the optimized values are marked as green symbol. Results have shown that, the optimum

Table 3.6: Channel model time averaged shear stress optimization configurations

Channel collapse configurations	$\theta_{12}(deg.)$	d_1	d_2	S	τ_T
Baseline configurations	62.759	0.100	0.100	0.3	-0.0904108
Optimum symmetric configurations	55.091	0.350	0.350	0.1	-0.6011461
Optimum non-symmetric configurations	55.165	0.451	0.249	0.1	-0.6368854

wall shear stress produced by symmetric and non-symmetric configurations are the same or are slightly different and optimal values occur at almost the same phase lag value as given in Table 3.6. As a summary of this chapter, we conducted a parametric study that aimed to investigate the effect of both geometrical and temporal variables on pumping efficiency. Furthermore, a full constrained optimization calculations is also given to find the optimal net flow. The optimization analysis is given for symmetric and non-symmetric geometrical configurations.

Chapter 4

Numerical Validations using Stokeslets-Meshfree Computations

In this chapter, the Stokeslets-meshfree computational method which is also known as the method of fundamental solutions (MFS) are used to validate our derived bioinspired pumping theory given previously in chapter 2. The numerical validation process covers both tube and channel pumping models.

4.1 Stokeslets-Meshfree Numerical Method Background

In the numerical methods, there are two major families of techniques usually used for integrating flow problems when solving Navier-Stokes equations namely, the conventional computational fluid dynamics (CFD) grid-based schemes and the meshfree (grid-free) methods. In the first technique, the domain of interest is discretized and typical grids are generated such as the finite volume, the finite difference and the finite elements methods. In the second approach, only the boundary is discretized and no mesh (meshless) is required. For examples, the vortex method, the smooth particle hydrodynamics, the boundary element method, and the method of fundamental solutions (MFS) are considered to be relatively new techniques that provides easy algorithms for solving CFD

problems without using the usual grid-based computations. Moreover, these meshless methods are more convenient for flows within complex geometries and problems with moving boundaries. In additions, these meshless methods requires lower storage capacity and less computational time when it compared with the conventional grid-based CFD methods.

This dissertation focuses on the meshfree computations and more specifically on the method of fundamental solutions (MFS) which is considered to be an efficient numerical technique for solving elliptic class of boundary value problems (BVP) such as the Stokes equations. The development of this method over the past decades a combined with supported examples for solving Stokes flow in confined and unconfined domains can be found inFairweather and Karageorghis (1998). Moreover, the method have shown to be useful, practical and not limited to simple flows only, but rather have shown to be applicable even for solving Stokes flow problems with a free surface. For example, the Stokes flow within a capillary tube with a free surface is investigated at different values of the surface tension or capillary numbers using the MFS and is given inPoullikkas et al. (1998). In a recent article, the applicability of the method of fundamental solutions (MFS) for solving boundary value problems of elliptic class is extensively investigatedSmyrlis (2009). The study focused rigorously on the validity concept of approximating the boundary value problem solutions by using linear combinations of fundamental solutions.

In general, the MFS is used to construct or to approximate the flow field by using a set of fundamental solutions based on point force singularities called Stokeslets. The definition and the derivation of the Stokeslets expressions and a formal explaintion to the induced flow motions due to the presence of these concentrated body forces (Stokeslet) in a creeping flow can be found in Hasimoto and Sano (1980) and Pozrikids (1992). Basically, there are two available techniques for implementing the MFS, both techniques require of introducing the Stokeslets with unknown force coefficients which indeed satisfies the governing equations. The unknown coefficients are then evaluated by satisfying the proper boundary conditions and solving the emerging linear system of equations. In the first approach, the Stokeslets act as source points and are usually collocated at locations outside the domain of interest with a specific distanceYoung et al. (2006). This distance can be then optimized iteratively for better performance and solutions convergence of the emerging linear system to obtain accurate Stokeslets coefficients. Furthermore, a practical numerical scheme based on the

MFS to solve 2D and 3D Stokes equations is given Young et al. (2006). The algorithm adopted the Stokeslets expressions as source points to induce the flow field in the lid-driven cavity problem and have been validated versus other CFD schemes used previously for the same problem. Moreover, the MFS is used to solve flow in a cavity with cylindersYoung et al. (2005) and extended to 3-D Stokes problem in an exterior domainTsai et al. (2006b) and the unsteady Stokes flow with time-dependent fundamental solutions Tsai et al. (2006a). The method was also successfully validated by solving Stokes's first and second problems Hu et al. (2005) and the inverse 2D Stokes problem Chen et al. (2005).

In the second approach, the classical Stokeslet velocity expression given in Pozrikids (1992) is modified to derive a regularized version of the method of fundamental solutionsCortez (2001). The method is named as the method of regularized stokeslets and have been used extensively to solve the Stokes flow in the presence of immersed boundaries and obstacles. The approach is then extended and have been used to solve three dimensional Stokes problem. A detailed analysis that shows the method accuracy and the performance of solving the flow on the model problems such as, flow past a sphere and the steady state rotation of rigid helical tubes is given in Cortez et al. (2005). Moreover, the method of regularized Stokeslets Cortez (2001) is developed by using the method images in order to impose zero-flow boundary conditions for for plane wall problems Ainley et al. (2008). The image method is then validated and implemented to different bench mark cases by using smooth functions to approximate the delta distribution in the concentrated force expressions Pozrikids (1992).

Recently, the Stokeslets-meshfree or in general the MFS method has been applied successfully to variety of Stokes flow problems for various microfluidics applications. For examples, the unsteady viscous flows in a capillary tube with a thin porous surface is given using the method of fundamental solutions Wen et al. (2009). The velocity induced by the porous layer is modelled using a slip boundary conditions. The time-dependent of the problem is handled by performing Laplace transformations and expressions for the force singularities in the transformed domain are derived. A Stokeslet-based method of fundamental solutions for 2-D low Reynolds number partial-slip flows has been developedZhao and Povitsky (2009). The method was firstly validated and results have shown that the numerical accuracy increases when the Stokeslets collocated away from the bound-

aries. The 3-D MFS to Stokes flows is extended to include the effect of partial-slip via Knudsen numbers for interior and exterior flows within spherical boundariesZhao and Povitsky (2011).

It should be mentioned here that, although the MFS is relatively easy to implement and does not require any grids, it still suffers from some issues related to non-invertible or ill-conditioning matrix problem associated with finding the force-coefficients when implementing the Stokeslets as fundamental solutions Alves and Silvestre (2004) and Young et al. (2005). This linear algebra matrix problem can lead to inaccurate force coefficients and consequently wrong velocity flow field. A solution to non-invertible matrix problem is found by either collocating the Stokeslets sources a distance away from the domain boundaries as given in Young et al. (2006) or by using regularized Stokeslets expressions as derived by Cortez (2001). A smoothing to the ill-conditioning matrix problem is also introduced by iteratively choosing the Stokeslets positions as shown in Young et al. (2006) or by optimizing the regularization parameter as in Cortez (2001). However, still the ill-conditioning matrix issue represents a challenging problem for the MFS to be correctly implemented. In this chapter, the method of fundamental solutions (MFS) is adopted to solve the flow field in a microchannel with moving wall contractions from the upper side. The numerical results will be used to validate our derived analytical solution to the problem. In addition, we also present a numerical algorithm which has been originally derived by Neumaier (1998) to solve ill-conditioned linear system of equations coupled with the MFS to be able to predict accurate Stokeslets-force coefficients.

In the following sections, the details of using Stokeslets-meshfree computational method to validate our derived insect-inspired tube and channel pumping models and will be given. Moreover, the applicability of using this numerical approach supported by several results are given to validate the theoretical analysis. Quantitative comparisons during compression and expansion time snapshots between theory and meshfree methods will be presented. The goal from this chapter is to generate numerical results that can support the idea of generating net flow out of inelastic tube and channel by using wall contractions that move with a phase (time) lag with respect to each other.

4.2 Numerical Validation of the Tube Pumping Model

This section is dedicated to numerically (using Stokeslets-meshfree method) validate our bioinspired tube pumping theoretical model given previously in chapter 2, section 2.1. Initially, we will recall and list briefly the tube pumping model problem formulation and analysis, then we will proceed with the numerical validation details. At last, detailed comparisons between both theoretical and meshfree methods will be given.

4.2.1 Formulation and Theoretical Analysis

Now, recall the tube formulation given chapter 2, section 2.1.1 which considers the fluid motions inside a single segment of an insect tracheal network, as shown schematically in Fig. 4.1 (a). The tube is assumed to be an axisymmetric with an initial circular cross-section of radius R and a finite length $L >> R$. The tube wall is assumed to have two rhythmic contractions as shown in Fig. 4.1 (b). A zero pressure drop $\Delta p = 0$ is assigned to the tube and only two moving contractions are considered. These contractions are set to move with various phase lags θ_{12} with respect to each other and follow exactly the actuation protocol shown in Fig. 4.3.2 (a). The main objective of this formulation was to investigate the ability of using a tube as described above with local contractions to pump fluids at the microscale without imposing any pressure drop or any mechanical valves.

The mathematical modelling and equations that govern this particular flow problem formulation are derived based on the quasi-steady approximations and the lubrication theory (Batchelor 1967; Meijing & Brasseur 1993; Takagi & Balmforth 2011) as given previously in chapter two, section 2.1.2 as,

$$\frac{1}{r}\frac{\partial}{\partial r}(rV_r) + \frac{\partial V_x}{\partial x} = 0 \tag{4.1}$$

$$\frac{\partial p}{\partial r} = 0 \tag{4.2}$$

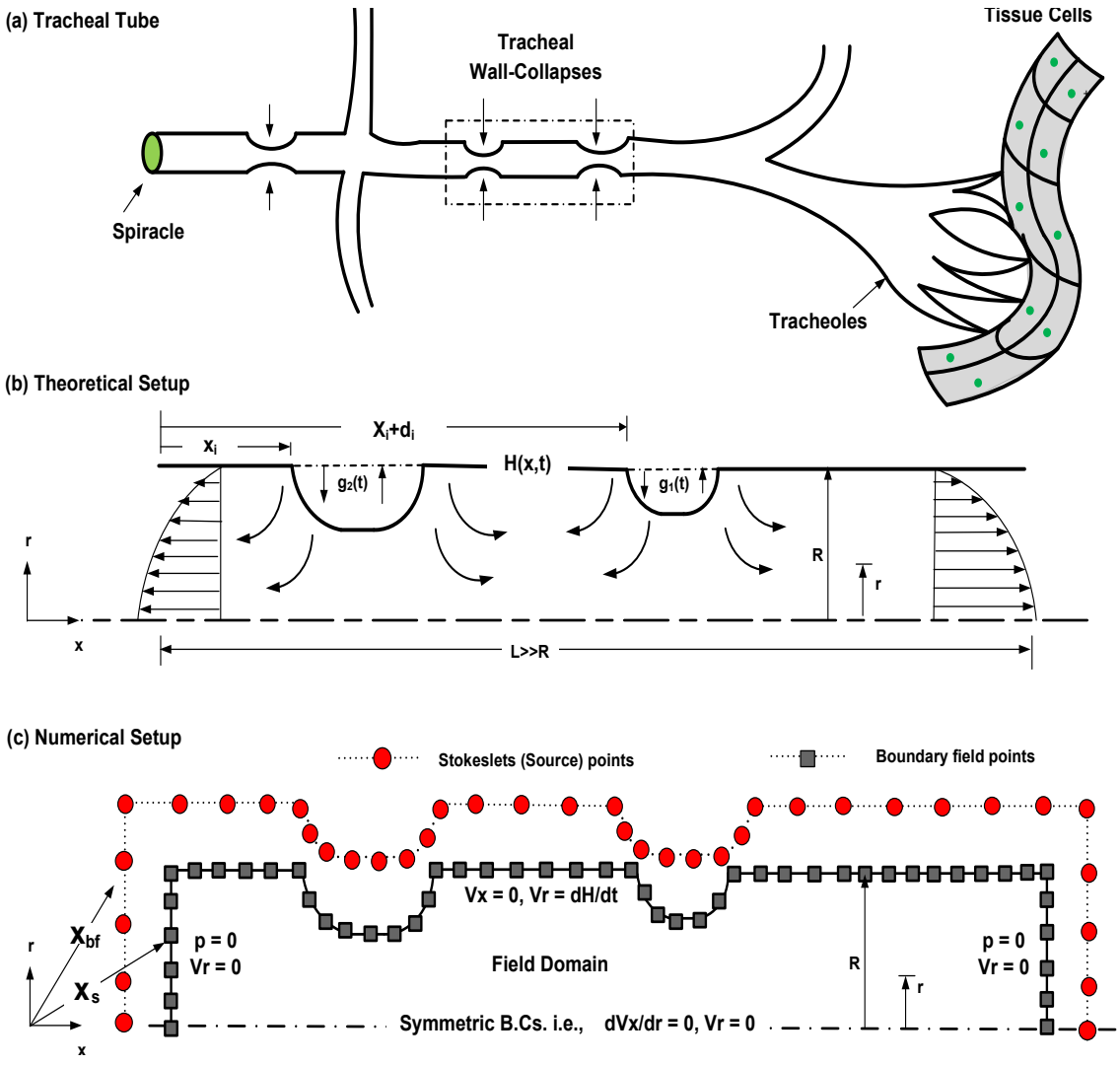

Figure 4.1: Problem Schematic: (a) Theoretical setup of a $2D$ axisymmetric fluid-filled tube with moving wall contractions governed by the profile $H(x,t)$. (b) The numerical (MFS) approach consists of defining distributed source points (Stokeslets) located at $\mathbf{X_s}$ and boundary field points located at $\mathbf{X_{bf}}$, as well as appropriate boundary conditions.

$$\frac{1}{r}\frac{\partial}{\partial r}(r\frac{\partial V_x}{\partial r}) = \frac{\partial p}{\partial x} \tag{4.3}$$

subjected to the following boundary conditions,

(i) at $r = 0$, $V_r = 0, \frac{\partial V_x}{\partial r} = 0$

(ii) at $r = H(x,t)$,$V_r = \frac{\partial H}{\partial t}$,$V_x = 0$

(iii) at $x = 0$, $p = p_o(t)$

(iv) at $x = 1$, $p = p_L(t)$

This system of equations (4.1 - 4.3) along with the above boundary conditions are solved analytically in section 2.1.2, where the velocity components, pressure gradient and pressure expressions were given as follows,

$$V_x(r,x,t) = \frac{1}{4}\frac{\partial p}{\partial x}\left(r^2 - H^2\right) \tag{4.4}$$

$$V_r(r,x,t) = \frac{r}{4}\left[H\frac{\partial H}{\partial x}\frac{\partial p}{\partial x} - \frac{1}{4}\frac{\partial^2 p}{\partial x^2}\left(r^2 - 2H^2\right)\right] \tag{4.5}$$

$$\frac{\partial p}{\partial x} = \frac{1}{H^4(x,t)}\left(G(t) + 16\int_0^x H(s,t)\frac{\partial H(s,t)}{\partial t}ds\right) \tag{4.6}$$

where, $G(t)$ is a function of integration that depends only on time t and to be determined after integrating (4.6) with respect to x where an expression for the pressure can be found as,

$$p(x,t) = p_o(t) + \int_0^x \frac{\partial p(s,t)}{\partial x}ds \tag{4.7}$$

Now, by evaluating (4.7) at $x = L$ where $P = P_L(t)$,an expression to $G(t)$ can be found be as,

$$G(t) = \frac{\Delta p - 16\int_0^1 H^{-4}(s,t)\left(\int_0^s H(s_1,t)\frac{\partial H(s_1,t)}{\partial t}ds_1\right)ds}{\int_0^1 H^{-4}(s,t)ds} \tag{4.8}$$

where,$\Delta p(t) = p_L(t) - p_o(t)$. Moreover, an expression for the volumetric flow rate $Q(x,t)$ induced

by the tube wall contractions were given as,

$$Q(x,t) = \int_0^{H(x,t)} V_x(x,r,t) r dr \tag{4.9}$$

using (4.4) and perform the integration yield,

$$Q(x,t) = \frac{-1}{8}\frac{\partial p}{\partial x} H(x,t)^4 \tag{4.10}$$

It should be noted that, once the tube wall profile $H(x,t)$ is prescribed, the pressure gradient can be evaluated using (4.6) and all other flow variables can be determined. The above solution has shown that, an inelastic tube with moving wall contractions can be used as a micropump as it will be confirmed numerically in the following section 4.2.2.

4.2.2 Axisymmetric Stokeslets-Meshfree Approach

The meshfree computational approach based on the method of fundamental solutions (MFS) will be used to validate our derived analytical solution that was given in section 2.1.2 and also given briefly in section 4.2.1. The axisymmetric Stokeslets based on singularized force elements are used as basis and fundamental solutions in our numerical validation process. Now, consider the same problem formulation stated in section 2.1.1 and let us assume that, the governing equations that describe this particular flow motions are the Stokes equations,

$$\nabla^* \cdot \mathbf{V}^* = 0 \tag{4.11}$$

$$\mu \triangle^* \mathbf{V}^* = \nabla^* p^* - \mathbf{F}^* \tag{4.12}$$

where, μ is the fluid viscosity , p^* is the pressure, $\mathbf{V}^*$ is the velocity, and $\mathbf{F}^*$ is the force per unit volume. A fundamental solution to the above equations is called a Stokeslet, and is characterized by the velocity field induced by a concentrated external point force with a specific intensity acting on the fluid at a certain location. Because of the linearity in the Stokes equations, the superposition principle can be imposed and a total flow field can be obtained by taking the effect from all the

collocated source points as shown in Fig. 4.1 (c). An axisymmetric Stokeslet expression based on the Dircac delta distribution for the force intensity acting on Stokes flow regime can be found in (Pozrikids 1992),

$$V_i^*\left(\mathbf{x}^*\right) = \frac{1}{8\pi\mu} M_{ij}\left(\mathbf{x}^* - \mathbf{x}_s^*\right) f_j^* \tag{4.13}$$

$$p^*\left(\mathbf{x}^*\right) = \frac{1}{8\pi} N_j^*\left(\mathbf{x}^* - \mathbf{x}_s^*\right) f_j^* \tag{4.14}$$

where, M_{ij} is the axisymmetric Stokeslet Green's function and N_j^* is a vector accounts for the pressure calculations which is a direct function of the Dirac delta function. $\mathbf{V}^* = (V_x^*, 0, V_r^*)$ is the induced velocity field by a ring of point forces. $\mathbf{F}^* = f_x^*\mathbf{e}_x + f_r^*\mathbf{e}_r$ is a concentrated point force per unit length. $\sigma^* = \mid \mathbf{x}^* - \mathbf{x}_s^* \mid$ is the distance between any field point located at $\mathbf{x}^* = xe_x + re_r$ and a source (Stokeslet) point at $\mathbf{x}_s^* = x_s e_x + r_s e_r$ as shown schematically in Fig. 4.1 (c). Now, if we use the same non-dimensional parameters defined in chapter 2, section 2.1.2, i.e., let $x = x^*/L$, $r = r^*/R$, $\sigma = \sigma^*/L$,$\delta = R/L$, $V_x = V_x^*/u_o$, $V_r = V_r^*/\delta u_o$, $p = p^* R^2/(\mu u_o L)$,$f_x = f_x^*/(\mu u_o)$, $f_r = f_r^*/(\mu u_o)$, $N_j = N_j^* R^2/L$. Therefore, the above equations in components wise can be re-written in a non-dimensional form,

$$V_x\left(x, r\right) = \frac{1}{8\pi}\left[M_{xx} f_x + M_{xr} f_r\right] \tag{4.15}$$

$$V_r\left(x, r\right) = \frac{1}{8\pi\delta}\left[M_{rx} f_x + M_{rr} f_r\right] \tag{4.16}$$

$$p\left(x, r\right) = \frac{\delta^2}{8\pi}\left[N_x f_x + N_r f_r\right] \tag{4.17}$$

where,

$M_{xx} = 2k\sqrt{\frac{r_s}{r}}\left[F(k) + \frac{\widehat{x}^2}{\sigma^2}E(k)\right]$

$M_{xr} = \frac{k\widehat{x}}{\delta r_s}\sqrt{\frac{r_s}{r}}\left[F(k) - \frac{\delta^2(r^2 - {r_s}^2)\widehat{x}^2}{\sigma^2}E(k)\right]$

$M_{rx} = \frac{-k\widehat{x}}{\delta r}\sqrt{\frac{r_s}{r}}\left[F(k) + \frac{\delta^2(r^2 - {r_s}^2)\widehat{x}^2}{\sigma^2}E(k)\right]$

$M_{rr} = \frac{k}{\delta^2 r r_s}\sqrt{\frac{r_s}{r}}\left[(\delta^2(r^2 + {r_s}^2) + 2\widehat{x}^2)F(k) + \frac{2\widehat{x}^4 + 3\delta^2\widehat{x}^2(r^2 + {r_s}^2) + \delta^4(r^2 - {r_s}^2)^2}{\sigma^2}E(k)\right]$

$N_x = \frac{2\widehat{x}}{\sigma^3}$, $N_r = \frac{2\delta(r - r_s)}{\sigma^3}$

$\widehat{x} = x - x_s$, $k = \sqrt{\frac{4rr_s}{\widehat{x}^2+(r+r_s)^2}}$
$\sigma = \sqrt{(x-x_s)^2 + \delta^2 (r-r_s)^2}$
$F(k) = \int_0^{\pi/2} \frac{d\theta}{\sqrt{1-k^2\sin^2\theta}}$
$E(k) = \int_0^{\pi/2} \sqrt{1-k^2\sin^2\theta} d\theta$

It should be mentioned that, $F(k)$ and $E(k)$ are called the complete elliptic integrals of the first and second kind respectively, and the calculations of these integrals is an important step in this study. Among several methods that have been proposed in the past to find these integrals, we chose, an efficient method proposed by (Abramowitz & Stegun 1972)for computing $F(k)$ and $E(k)$ in terms of convergent infinite series, which is given as

$$F = \frac{\pi}{2}\left[1 + \left(\frac{1}{2}\right)^2 k^2 + \left(\frac{1.3}{2.4}\right) k^4 + \left(\frac{1.3.5}{2.4.6}\right) k^6 + ...\right] = \frac{\pi}{2}\sum_{n=1}^{\infty}\left[\frac{2n!}{2^{2n}n!^2}\right]^2 k^{2n} \tag{4.18}$$

$$E = \frac{\pi}{2}\left[1 - \left(\frac{1}{2}\right)^2 k^2 + \left(\frac{1.3}{2.4}\right) \frac{k^4}{3} + \left(\frac{1.3.5}{2.4.6}\right) \frac{k^6}{5} + ...\right] = \frac{\pi}{2}\sum_{n=1}^{\infty}\left[\frac{2n!}{2^{2n}n!^2}\right]^2 \frac{k^{2n}}{1-2n} \tag{4.19}$$

In the MFS technique, the total solution is formed by the superposition of all bases solutions represented by the Stokeslets expressions with unknown intensities or force coefficients. The strength of these singularities coefficients is then obtained by enforcing the fundamental solutions to satisfy the prescribed boundary conditions by direct collocations (Young *et at.* 2006). Now, consider the problem under consideration with the prescribed boundary conditions as shown in Fig. 4.1 (c). Let us distribute N-Stokeslets (source) points with unknown strength $\mathbf{F}$ vectors collocated a distance ε away from the tube boundary. The flow field can be then approximated by superposition the effect from all the Stokeslets and the velocity field can be evaluated as,

$$V_{x,i}(x_i, r_i) = \frac{1}{8\pi}\sum_{j=1}^{N}\left[M_{xx,j} f_{x,j} + M_{xr,j} f_{r,j}\right] \tag{4.20}$$

$$V_{r,i}(x_i, r_i) = \frac{1}{8\pi\delta}\sum_{j=1}^{N}\left[M_{rx,j} f_{x,j} + M_{rr,j} f_{r,j}\right] \tag{4.21}$$

$$p_{,i}\,(x_i, r_i) = \frac{\delta^2}{8\pi}\sum_{j=1}^{N}\left[N_{x,j} f_{x,j} + N_{r,j} f_{r,j}\right] \tag{4.22}$$

where,

$$M_{xx,j} = 2k_{ij}\sqrt{\frac{r_{sj}}{r_i}}\left[F(k_{ij}) + \frac{\widehat{x_i}^2}{\sigma_{ij}^2}E(k_{ij})\right]$$

$$M_{xr,j} = \frac{k_{ij}\widehat{x_i}}{\delta r_{sj}}\sqrt{\frac{r_{sj}}{r_i}}\left[F(k_{ij}) - \frac{\delta^2({r_i}^2-{r_{sj}}^2)\widehat{x_i}^2}{\sigma_{ij}^2}E(k_{ij})\right]$$

$$M_{rx,j} = \frac{-k_{ij}\widehat{x_i}}{\delta r_i}\sqrt{\frac{r_{sj}}{r_i}}\left[F(k_{ij}) + \frac{\delta^2({r_i}^2-{r_{sj}}^2)\widehat{x_i}^2}{\sigma_{ij}^2}E(k_{ij})\right]$$

$$M_{rr,i} = \frac{k_{ij}}{\delta^2 r_i r_{sj}}\sqrt{\frac{r_{sj}}{r_i}}\left[(\delta^2({r_i}^2+{r_{sj}}^2)+2\widehat{x_i}^2)F(k_{ij}) + \frac{2\widehat{x_i}^4+3\delta^2\widehat{x_i}^2({r_i}^2+{r_{sj}}^2)+\delta^4({r_i}^2-{r_{sj}}^2)^2}{\sigma_{ij}^2}E(k_{ij})\right]$$

$$N_{x,j} = \frac{2\widehat{x_i}}{\sigma_{ij}^3},\ N_{r,j} = \frac{2\delta(r_i-r_{sj})}{\sigma_{ij}^3}$$

$$\widehat{x_i} = xi - x_{sj},\ k_{ij} = \sqrt{\frac{4r_i r_{sj}}{\widehat{x_i}^2+(r_i+r_{sj})^2}}$$

and f_{xj} and f_{rj} are the unknown force coefficients that represent the strengths of the Stokeslets in x and r-directions respectively. $\mathbf{x}_i = (x_i, r_i)$ is the position of any field point including the boundary points. $\mathbf{x}_{sj} = (x_{sj}, r_{sj})$ is the location of the Stokeslets source points. $\sigma_{ij} = |\mathbf{x}_i - \mathbf{x}_{sj}| = \sqrt{(x_i - x_{sj}) + \delta^2\,(r_i - r_{sj})}$ is the distance between any field point and another source point. The Stokeslets are chosen to be distributed around the physical domain boundaries with a separation distance ε where, the equation that govern the locations of the distributed Stokeslets points can be given by

$$\mathbf{x}_{sj} = \mathbf{x}_{bj} + \varepsilon\,(\mathbf{x}_{bj} - \mathbf{x}_c) \tag{4.23}$$

where $\mathbf{x}_{sj}$ refer to the location of Stokeslets source points, $\mathbf{x}_{bj}$ is the boundary points, ε is the separation distance away from the domain boundary, and $\mathbf{x}_c$ is the geometric center of the domain of interest.

In order to determine the unknown force coefficients $\mathbf{F} = (f_{xj}, f_{rj})$, the boundary conditions for the velocity components and pressure are imposed and collocated at certain field points on the tube boundary as shown in Fig. 4.1(c). By superposition of each fundamental solution as given by Eqs. (4.20 - 4.22), a system of equations is formed

$$\mathbb{A}\mathbf{F} = \mathbf{b} \tag{4.24}$$

where $\mathbb{A}$ is a matrix of size $2NX2N$ with real entries formed by evaluating the right hand side of the above expressions in Eqs. (4.20 - 4.22). $\mathbf{b}$ is a vector of size $1X2N$ of real entries formed by evaluating the left hand side of the same equations. In other words, all the entries in both $\mathbb{A}$ and

b are filled by enforcing the fundamental solutions to satisfy the boundary conditions by direct collocation. **F** represent the Stokeslets unknown force coefficients. Eventually, once the emerging above system of equations is solved, the final solution can be obtained, details of this process is given in section 4.3.2.

It should be mentioned here that although the MFS is relatively easy to implement and does not require any grids, it still suffers from some issues related to the non-invertible or ill-conditioned matrix problem associated with finding the force coefficients. This linear algebra problem can lead to inaccurate force coefficients and consequently wrong flow field. A solution to the above mentioned non-invertiblity matrix problem is found by either collocating the Stokeslets (sources) a distance away from the domain boundaries as given in (Young *et at.* 2005; Young *et at.* 2006) or by using the method of regularized Stokeslets expressions as derived by (Cortez 2001). A smoothing to this ill-conditioning matrix problem is also introduced by iteratively choosing the Stokeslets positions as shown by (Young *et at.* 2006) or by optimizing the regularization parameter as in (Cortez 2001). However, still the ill-conditioning matrix issue represents a challenging problem for the MFS to be correctly implemented. In this study, we show an efficient algorithm by (Neumaier 1998) to overcome this ill-conditioning matrix problem. This algorithm is implemented along with standard MFS (Young *et at.* 2006) to find an efficient Stokeslets force coefficients, details is given in section 4.3.2.

Table 4.1: Parameters and values used in the tube meshfree computations

parameter	value	parameter	value	parameter	value	parameter	value
x_1	0.25	d_1	0.1	N_c	2	N	550
x_2	0.35	d_2	0.1	S_t	1	ε	0.15
x_3	0.65	A_1, A_2	-0.3528	T	1	h	0.01
x_4	0.75	TC	70%	$\Delta p(t)$	0	tol	10^{-6}

4.3 Tube Numerical Results and Discussions

In this section, we present results from both theoretical model and meshfree computational method for comparisons and cross-validation purposes. In other words, the meshfree-MFS results will be used to justify the assumptions made during the derivation of the analytical solution. Conversely, the analytical solution will be used to justify that, the MFS numerical approach can be used successfully for solving Stokes flow problem in a domain with moving boundaries, similar to this induced flow motions by the rhythmic contractions found in the insect tracheal system, which is under consideration in this paper. Two cases are chosen for this comparisons and validation process between results computed analytically and numerically. In the first case of study, the tube wall contractions are set to move with no phase lag i.e., $\theta_{12} = 0^{\circ}$, where in second case of study, contractions are set to move with phase lags 30°. Comparisons between these two cases are made at the same geometric and flow conditions with values listed in table 4.1.

This section is organized as follows: we first show the kinematics and geometry of the tube wall contractions by a generic expression $H(x,t)$. This specific wall profile is designed to allow for a single or multiple contractions that can move with similar or with different amplitudes, and with or without time or phase lags relative to each other as it will be given in section 2.1.3. Once the wall profile is given, all the flow variables can be computed exactly using our analytical model throughout Eqs. (4.1 - 4.10). Secondly, the strengths of the Stokeslets points are obtained by solving the linear system of equations given by Eq.(4.24) iteratively and then, the MFS are applied to reconstruct the induced flow motions inside this fluid-filled axisymmetric tube with moving contractions. The detailed algorithm used to obtain the Stokeslets strengths will be given in § 4.3.2. Thirdly, analytical and numerical results that show the structures and developments of the flow field induced by only two wall rhythmic contractions are compared in the § 4.3.3. Fourthly, the effect of the contraction amplitudes and the phase lags motion protocol assigned to each contraction sites on the instantaneous and on the time averaged volumetric flow rate is investigated in § 4.3.4. More specifically, the time averaged volumetric flow rate over a complete contraction-expansion cycle for various phase lags values is studied to explore which contraction setting can produce unidirectional net flows and can work as a pumping system.

4.3.1 Tube Wall Profile, $H(x,t)$

Let the mathematical model that describes the kinematics and the shape of the tube wall contractions be given as

$$H(x,t) = 1 + \sum_{i=1}^{N_c} A_i f_i(x) g_i(t) \tag{4.25}$$

where $f_i(x) \in C^r[0,1]$ and $g_i(t) \in C^r[0, T = 1/S_t]$ represent the spatial and the temporal distribution of the tube wall shape respectively. N_c defines the number of contractions and A_i is the amplitude assigned to each contraction. The spatial form of the above equation imitates the geometry of these wall contractions as

$$f_i(x) = \tanh(\alpha(x - x_i)) - \tanh(\alpha(x - (x_i + d_i))) \tag{4.26}$$

where $\alpha = 2\pi/\delta$, x_i defines the beginning of each collapse region and $d_i \in (0, 1 - x_i]$ marks its end, as shown in Fig. 4.3.2 (a). In this paper, we only consider two contractions, i.e., $N_c = 2$ located at $x_1 = 0.25, d_1 = 0.1$ and $x_2 = 0.65, d_2 = 0.1$ respectively. The first contraction moves in time according to the following profile

$$g_1(t) = \begin{cases} \frac{1}{2}\left(1 - \cos(2\pi\beta S_t t)\right), & 0 \le t \le 1/\beta S_t \\ 0 & 1/\beta S_t < t \le 1/S_t \end{cases} \tag{4.27}$$

while the second contraction moves according to

$$g_2(t) = \frac{1}{2}\left(1 - \cos(2\pi S_t t)\right), 0 \le t \le 1/S_t \tag{4.28}$$

where, the non-dimensional parameter β is related to the phase lag between the first and the second contraction according to the following assigned motion protocol as shown in Fig. 4.3.2 (a). During the compression phase, we initially let both contractions start to move together. However, the first contraction reaches the maximum specified tube travel collapse (TC) distance faster than the second contraction. In other words, there will be a time lag $T_g = (1 - 1/\beta)/(2S_t)$ between these two collapses which is equivalent to phase lag $\theta_{12} = \pi(1 - 1/\beta)$. During the expansion phase, the first

contraction returns back to the original position (un-collapsed diameter) and continues its period with zero amplitude until the second contraction completes its own cycle and returns back too, then both contractions start together the second cycle. It should be noted that both contractions have same time period $T = 1/S_t$, and if $\beta = 1$, there will be no phase lag and both contractions move in the same manner with time. The above motion protocol is intentionally proposed to grantee that, after one cycle of collapsing, the tube geometry has returned to the initial position, and does not suffer from any contractions, i.e., there will be no net flow due to volume deformation. Moreover, it should be noted that, the tube wall profile $H(x, t)$ and its prescribed kinematics plays the most important role in this study. For examples, the analytical derivation given by (4.11)-(4.28) show that, once the profile is prescribed, all the flow parameters can be calculated analytically. On the numerical side, the strengths of the Stokeslets points which will be used to reconstruct the induced flow field numerically are also strong function of the tube wall profile as will be given next § 4.3.2.

4.3.2 Tube Stokeslets Strengths and Solving Ill-Conditioned System of Equations

Finding an accurate solution to the emerging ill-conditioned system of equations given by Eq. 4.24 is considered to be the most critical step when implementing the Stokeslets-MFS method. Here, we present a numerical algorithm which has been originally derived by (Neumaier 1998) to solve ill-conditioned linear system of equations. The algorithm is mainly based on introducing a regularization parameter h to the original matrix $\mathbb{A}$ which will be then transformed to a modified and symmetric matrix A_R. The modified matrix will act as a pre-conditioner matrix and leads to a modified system of equations with an enhanced condition number. In principle, the preconditioner matrix changes the eigenvalues of the original matrix $\mathbb{A}$ to modified eigenvalue spectrum, which will be clustered away from the zero and consequently lead to a better conditioned number.

The algorithm is simple and only requires the matrix of coefficients $\mathbf{A}$, the vector $\mathbf{b}$, the regularization parameter h, and convergence criteria based on an assigned specific tolerance value, tol. The steps of the algorithm are listed in 4.2 which is easy to follow. This algorithm is and efficient and general and the most important part of this algorithm is the third step where regularization to the

Table 4.2: Tube pumping model: Algorithm for solving ill-conditioned systems of equations

Algorithm for finding the strengths of each Stokeslets-source point
Input: $\mathbb{A}, \mathbb{I} \in M_{2NX2N}(R)$, $\mathbf{b} \in R^{2N}$, h, $tol \in R$
1. $\mathbf{f^{(0)}} = \mathbf{0}$, $\mathbf{r^{(0)}}$ =**b** - $\mathbf{f^{(0)}}$ =**b**
2. Do while $\| \mathbf{r} \|_\infty \geq$ **tol**
3. $\mathbb{A}_R = \mathbb{A}^*\mathbb{A} + h^2\mathbb{I}$
4. $\mathbf{f^{(k)}} = \mathbf{f^{(k-1)}} + {\mathbb{A}_R}^{-1}\mathbb{A}^*\mathbf{r^{(k-1)}}$
5. $\mathbf{r^{(k)}} = \mathbf{b} - \mathbb{A}\mathbf{f^{(k)}}$
end Do
Output: Stokeslets strengths: $\mathbf{f} = [f_{xj} f_{yj}]^T$, $j = 1 : N$

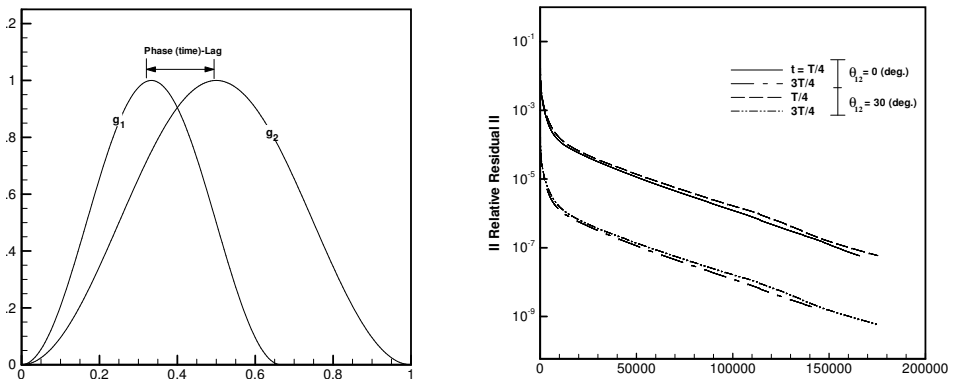

Figure 4.2: (a) Wall collapse protocol with functions $g_1(t)$ and $g_2(t)$ assigned to the first and second collapses, respectively. (b) Convergence of the iterative procedure outlined in Table 2. The ∞-norm of the relative residual versus iteration number.

eigenvalues is applied. This regularization parameter h can really affect the maximum number of iterations k_{max} required for the relative residuals to convergence within the prescribed tolerance. One way to verify the accuracy of the above algorithm shown in Table 4.2, is to use the output force strengths $\mathbf{F}$ vector to re-calculate back the velocities and pressure at all boundary points to ensure that, all the boundary conditions are met and satisfied within the prescribed degree of accuracy.

As a direct implementation of the above algorithm, we show the residual convergence history and the output Stokeslets strength distributions for the above mentioned two cases of study. These simulation cases are for situations where the wall contractions move with phase lags $\theta_{12} = 0°\&30°$ and for only two snapshots of times namely, compression time $t = t/4$ and expansion $t = 3T/4$ respectively. For examples, the residual convergence history for these two cases at both compression and expansion time snapshot are shown in Fig. 4.3.2 (b). The convergence history exhibit q-super linearity behaviour. Results have shown that, when the two contractions move with zero phase lag $\theta_{12} = 0°$, the required number of iterations to convergence to the given tolerance is greater than when the contractions move with $\theta_{12} = 30°$. There is always more iterations are required for convergence when calculations are done during compression snapshot $t = t/4$ compared with calculations during expansion time $t = 3T/4$. The strengths f_x and f_r distributions along x and r directions for each Stokeslet point are plotted for the same both cases of study and at compression time $t = t/4$ and at expansion $t = 3T/4$ snapshots in Fig. 4.3 (a-b) respectively.

Results have shown that, Stokeslets in and near to the contractions regions have large gradients and stronger strengths then compared with other force points. There are almost self-similar behaviour in the Stokeslets strength distributions for the cases studied. It should be noted that at each time step, which is corresponding to specific wall positions, new force strengths must be calculated by solving the linear system given by 4.24 iteratively. Then, after prescribing the wall motion profile and calculating the strengths for each source points, the flow field using both analytical and numerical methods can be calculated and compared at any instant of time during the collapsing cycle, as will be presented in the following subsections.

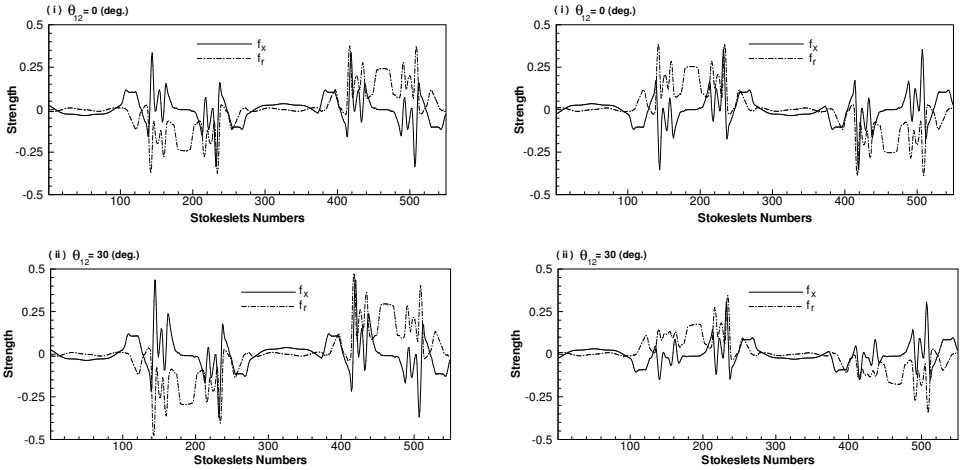

(a) Compression at t = $T/4$ (b) Expansion at t = $3T/4$

Figure 4.3: Stokeslet strength coefficients f_x and f_r in the x- and y-directions, respectively, at two different phase lags, $\theta_{12} = 0$ and 30°, during compression and expansion.

4.3.3 Flow Field Induced by Tube Wall Contractions

The flow field induced by the motions of wall contractions in an axisymmetric tube subjected to a zero pressure drop $\Delta p(t) = 0$ is given in detail in this section using both analytical and Stokeslets-MFS computational method. The structures and developments for the flow induced by tube wall contractions for both cases under considerations are given in this section. A detailed comparison between results obtained analytically and numerically is held to validate and justify assumptions made in each method. The first comparison case deals with a scenario where the two contractions are set to move with zero phase lag $\theta_{12} = 0°$, where in the second set of results, the wall contractions are forced to move with $\theta_{12} = 30°$.

More specifically, the contour lines of both axial and radial velocity components and pressure in addition to the velocity streamlines are compared at both compression time $t = t/4$ and at expansion $t = 3T/4$ snapshot. Now, If we recall the analytical solution derived in Eqs. (4.1 - 4.10) and use the tube wall profile $H(x, t)$ which was fully described by Eqs. (4.25 - 4.28), it is clear that all the flow variables can be calculated exactly. For instance, the pressure gradient is evaluated by using Eqs. (4.6 - 4.8), and the velocity components are then calculated by using Eqs. (4.4 - 4.5).

On the numerical side, the geometry and boundary conditions are fully prescribed and source points are collocated around the computional domain see Fig. 4.1 (c). The force strength coefficients are calculated using algorithm shown in Table 4.2 and values are given in Fig. 4.3. Therefore, all the induced flow variables at any field point can be easily calculated using Eqs. (4.20 - 4.22). Results that show the comparisons between both analytical and meshfree computations are shown in Figs. 4.4-4.11.

In Fig. 4.4 (a-b), we show the contour lines of the axial, radial velocity components, pressure, and the velocity streamlines obtained analytical and numerically, when the tube wall contractions are set to move with a zero phase lag ($\theta_{12} = 0^{\circ}$) and during the compression phase at instant of time $t = T/4$. As the wall contractions undergo the compression phase and start to move toward the tube center line, the axial velocity component increases near the contraction regions and the flow is displaced, bifurcated, and exit the tube from both directions. There will be a stagnation region between the two contractions due to flow cancellation, since each collapse sends flow to both directions away from the contraction zone as given analytically in Fig. 4.4 (a-(i)) and numerically in Fig. 4.4 (b-(i)). The contour lines for the radial velocity component are characterized by two regions with opposite direction located underneath each contraction as shown analytically in Fig. 4.4(a-(ii)) and numerically in Fig. 4.4 (b-(ii)).

Furthermore, a comparison between the pressure contours and flow streamlines obtained analytical and numerically is also given. For example, high pressure with adverse and favorable gradients are formed in and near the contraction regions. These pressure gradients induces a flow away from the compression sited and force the fluid to exits the tube from both sides as pointed out from the velocity contours. Moreover, the pressure is maximum or total in the stagnation zone between the two contractions. The pressure gradient have its absolute maximum value near the contraction regions and become constant away from contractions and independent from the vertical direction as shown as shown analytically in Fig. 4.4 (a-(iii)) and numerically in Fig. 4.4 (b-(iii)). The streamlines as a result of contractions motion at this specific time $t = T/4$ are shown analytically in Fig. 4.4 (a-(iv)) and numerically in Fig. 4.4 (b-(iv)). The streamlines show that, there will be a stagnation region between the two contractions due to flow cancellation results from the fact that each collapse sends flow to both directions away from the contraction zone.

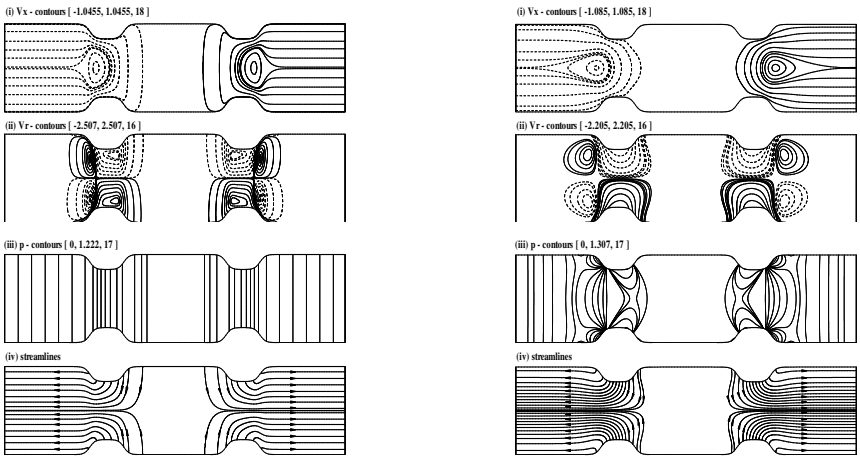

(a) Theory at t = $T/4$, $\theta_{12} = 0^\circ$ (b) Numerical at t = $T/4$, $\theta_{12} = 0^\circ$

Figure 4.4: Comparison of flow fields between the (a) analytical solution and (b) meshfree computations during compression for wall contractions with phase lag $\theta_{12} = 0^\circ$ and time $t = T/4$: (i) V_x-contours, (ii) V_r-contours, (iii) P-contours, and (iv) streamline patterns. Contour values are given on the top of each plot in the standard format of [Min., Max., No of lines]

Similar results that show the flow field during the expansion phase at time $t = 3T/4$ and $\theta_{12} = 0^\circ$ are shown in Fig. 4.5. As the contraction regions expand back away from the tube center line, exactly a similar flow field structure is developed but with an opposite directions when compared with results obtained at $t = T/4$ as shown analytically in Fig. 4.5 (a-(i-iv)) and numerically in Fig. 4.5 (b-(i-iv)). In other words, there is symmetry behavior in the flow field when the tube wall contractions move with $\theta_{12} = 0^\circ$. Results have shown that, there is a fair agreement between the flow filed obtained analytically and numerically using meshfree approach.

In Figs. 4.6 & 4.7, we show similar plots for velocity and pressure contours in addition to flow streamlines for a situation where the wall contractions are set to move with a phase lag of $\theta_{12} = 30^\circ$. Both analytical and MFS computational results are given at similar times that represent compression $t = T/4$ and expansion $t = T/4$ snapshots. Results have shown that, unlike the situation where $\theta_{12} = 0^\circ$ which is always characterized by having a stagnation zone of zero velocities between the two contractions and the flow is not allowed to transport. When $\theta_{12} = 30^\circ$, this stagnation zone is relaxed and there will be flow transport within the region between these two

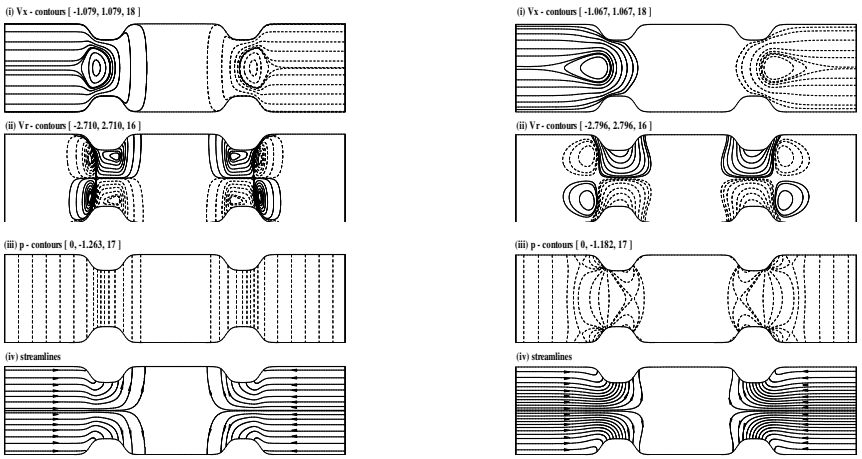

(a) Theory at t = $3T/4$, $\theta_{12} = 0°$ (b) Numerical at t = $3T/4$, $\theta_{12} = 0°$

Figure 4.5: Comparison of flow fields between the (a) analytical solution and (b) meshfree computations during compression for wall contractions with phase lag $\theta_{12} = 0°$ and time $t = 3T/4$: (i) V_x-contours, (ii) V_r-contours, (iii) P-contours, and (iv) streamline patterns. Contour values are given on the top of each plot in the standard format of [Min., Max., No of lines]

contractions as shown by the axial velocity contour lines calculated analytically and numerically and given in Figs. 4.6(a-i) & 4.6 (b-i) respectively. Moreover, there is a pressure gradients in the region between the two contractions which indicate that, there is a flow transport through this region. This is also confirmed by plotting the flow streamlines analytically in Fig. 4.6 (a-(iii-iv)) and numerically in Fig. 4.6 (b-(iii-iv)). Similarly, the flow field obtained from both analytical and numerical simulations during the expansion phase at time $t = 3T/4$ and $\theta_{12} = 30°$ are shown in Fig. 4.7.

To summarize the results presented in Figs. (4.4- 4.7), when the wall contractions move with a zero phase lag $\theta_{12} = 0°$, the flow field structures have a complete symmetry behaviour during compression and expansion phases of the collapsing cycle and there will be no flow transport between the contraction regions. This symmetry behaviour breaks down when the wall contractions move with a phase lag other than zero as shown for the case of $\theta_{12} = 30°$ and flow is transported after a complete collapsing cyclic motion. In general, it seems there is a strong dependence between motion protocol and the flow transport between these wall contractions. Therefore, the relationship

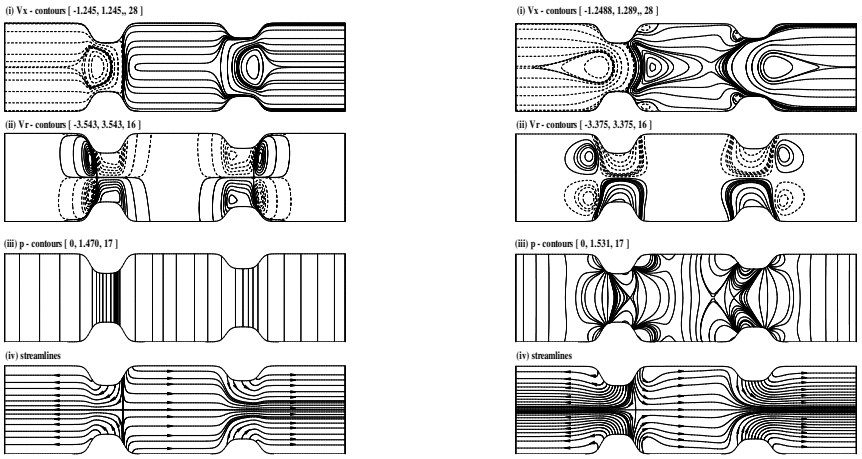

(a) Theory at t = $T/4$, $\theta_{12} = 30°$ (b) Numerical at t = $T/4$, $\theta_{12} = 30°$

Figure 4.6: Comparison of flow fields between the (a) analytical solution and (b) meshfree computations during compression for wall contractions with phase lag $\theta_{12} = 30°$ and time $t = T/4$: (i) V_x-contours, (ii) V_r-contours, (iii) P-contours, and (iv) streamline patterns. Contour values are given on the top of each plot in the standard format of [Min., Max., No of lines]

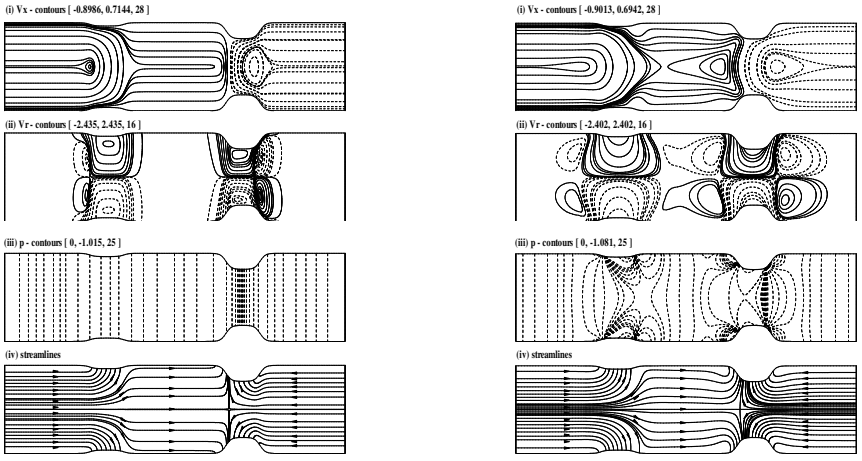

(a) Theory at t = $3T/4$, $\theta_{12} = 30°$ (b) Numerical at t = $3T/4$, $\theta_{12} = 30°$

Figure 4.7: Flow field comparison between (a) analytical and (b) meshfree computations during compression for wall contractions with phase lag $\theta_{12} = 30°$ and time $t = 3T/4$: (i) V_x-contours, (ii) V_r-contours, (iii) P-contours, and (iv) streamline patterns. Contour values are given on the top of each plot in the standard format of [Min., Max., No of lines]

between the flow transport, time averaged net flow produced out of this system and the phase lag parameter will be investigated in details in § 4.3.4.

Although there is a very good agreement between the analytical and Stokeslets-MFS results, there are still some important differences to be addressed. For instance, when the wall contractions move with $\theta_{12} = 0^\circ$, the contour lines computed analytically and numerically for the axial velocity components are exactly the same. However, when The $\theta_{12} = 30^\circ$, the V_x-contours computed numerically have shown an extra small structure which made the MFS results be a slightly different from the ones calculated analytically. Also, for both phase lags cases studied inhere, the contour lines for radial velocity component computed numerically are somehow stretched when it compared with analytical counterpart. These small discrepancies in the velocity contours can be clearly seen from the pressure contour lines as well. Where, the pressure calculated using MFS exhibits some variations along the radial direction specially near to the contraction regions when it compared with analytical counterpart which is assumed to be totally invariant in the radial direction, Eq. 4.2.

To better understand the flow field induced by the prescribed wall contractions protocols, and to be able to adequately compare between the analytical and MFS numerical results, we show line plots for V_x&V_r velocity components along the tube radial direction at different axial locations as shown in Figs. 4.8 & 4.9. Results are given for the same two cases of study i.e, when contractions move with phase lags equal to $\theta_{12} = 0^\circ$&30° at both compression $t = T/4$ and expansion $t = 3T/4$ snapshots respectively.

For examples, in Fig. 4.8 we show the radial velocity $V_r - r$ profiles at the contraction regions, specifically at $x = 0.3$&0.7 locations along the tube length. These two locations are chosen based on the conclusion made from the contour plots which suggest that, far away from and in between the contraction regions, the vertical velocity is always zero. However, right at the middle of each contraction i.e., at $x = 0.3, 0.7$, the V_r - profiles starts by zero values at the center line and increase until it reaches asymptotically the tube wall velocity to meet the wall speed boundary condition.

Both analytical and numerical results at $x = 0.3$ and $\theta_{12} = 0^\circ$ shows that, the V_r profiles shown in Fig. 4.8 (b) at an expansion instant of time $t = 3T/4$ are an exact mirror to the profiles shown in Fig. 4.8 (a) at compression instant of time $t = T/4$. However, this symmetry is no longer exist

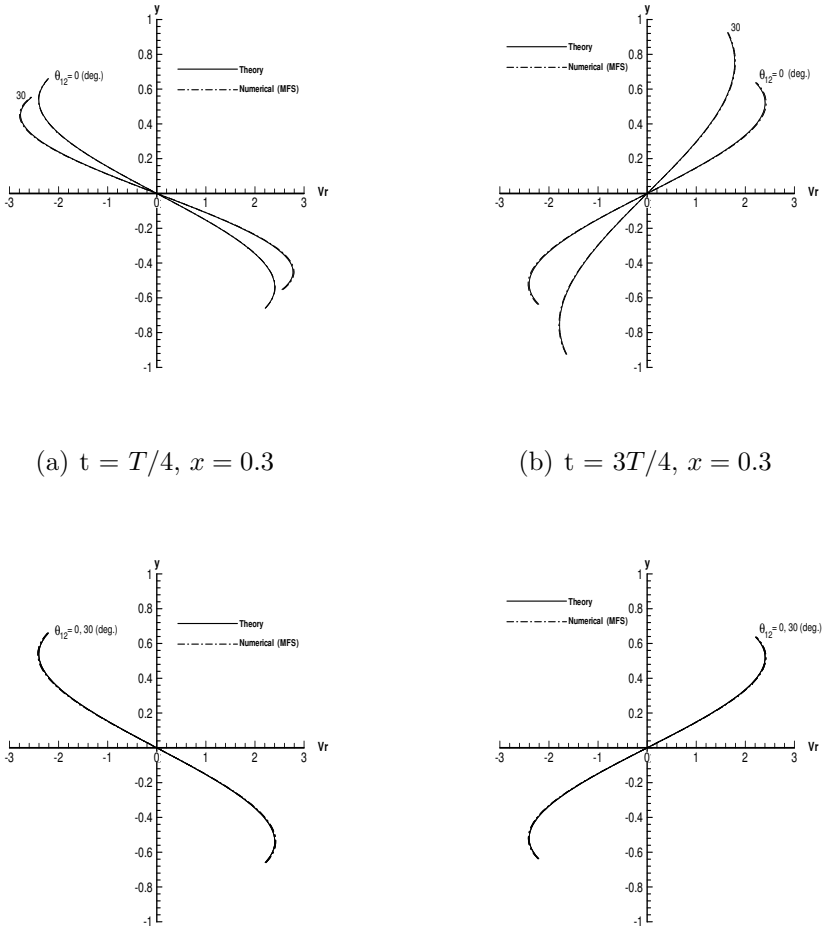

(a) t = $T/4$, $x = 0.3$

(b) t = $3T/4$, $x = 0.3$

(c) t = $T/4$, $x = 0.7$

(d) t = $3T/4$, $x = 0.7$

Figure 4.8: Comparison of the analytical solution and the meshfree calculations for the (V_r-r) velocity profiles at $\theta_{12} = 0°$ and 30° during compression and expansion: (i) $x = 0.3$ and (ii) $x = 0.7$.

when $\theta_{12} = 30°$. Similarly, at $x = 0.7$ there is a symmetry behaviour in the V_r-profiles as shown from Fig. 4.8 (d) at time $t = 3T/4$ which are an exact mirror to the profiles shown in Fig. 4.8 (c) at compression instant of time $t = T/4$ for both $\theta_{12} = 0°\&30°$. This suggests that the V_r-profiles at $x = 0.7$ is independent of the value of the phase lags.

In Fig. 4.9, the axial velocity V_x-profiles along the radial direction at the beginning and end of the

tube length ($x = 0\&1$) are given. Not surprisingly, the velocity profiles are parabolic with maximum value at the tube center line according to Eq. (4.4). When $\theta_{12} = 0^\circ$ and at $x = 0\&1$, V_x-profiles at expansion times $t = 3T/4$ are exactly similar to ones obtained at compression time $t = T/4$ but with opposite signs i.e., there is a complete symmetry in the behaviour during compressions and re-inflations times of the collapsing protocol. However, when $\theta_{12} = 30^\circ$ still the V_x-profiles are the same but the maximum values are different when comparing results between compression with expansion snapshot instant of times. In other words, the symmetry behaviour shown when $\theta_{12} = 0^\circ$ breaks down when $\theta_{12} = 30^\circ$ is used.

To summarize the results shown in Figs. (4.8-4.9), there is very good agreement between the analytical and meshfree solutions. The MFS-Stokeslets approximates well the velocity profiles at various locations along the tube lengths specially when $\theta_{12} = 0^\circ$. There is small differences between numerical and analytical results when $\theta_{12} = 30^\circ$. Furthermore, results have shown that, the compression and expansion process is not completely symmetric over a complete collapsing cycle when the wall contractions move with a non-zero phase lag and a net flow is produced as a result of the wall contraction motions. Results indicated that, a flow transport can be induced by using slight phase lags in the motion protocol that govern these rhythmic wall contractions. Therefore, this phase lag has shown to be the key parameter of this study as it will be discussed in the following section 4.3.4.

4.3.4 Net Flow Induced by Tube Wall Contractions

The effect of the phase lag and collapsing amplitude parameters on the flow transport within a fluid-filled axisymmetric tube with two local rhythmic contractions are given in this section. Results presented here demonstrate the possibility of using this simple tube as a pumping mechanism at the microscale flow regime. The minimum requirements needed for producing a unidirectional flow without imposing any pressure drop are found and explained in details. Results are validated and confirmed by using meshfree computations.

First, we show the effect of the phase lags θ_{12}, which are governed by the kinematic functions $g_1(t)$ and $g_2(t)$, on the instantaneous volumetric flow rate $Q(x,t)$. The volumetric flow rate is recorded

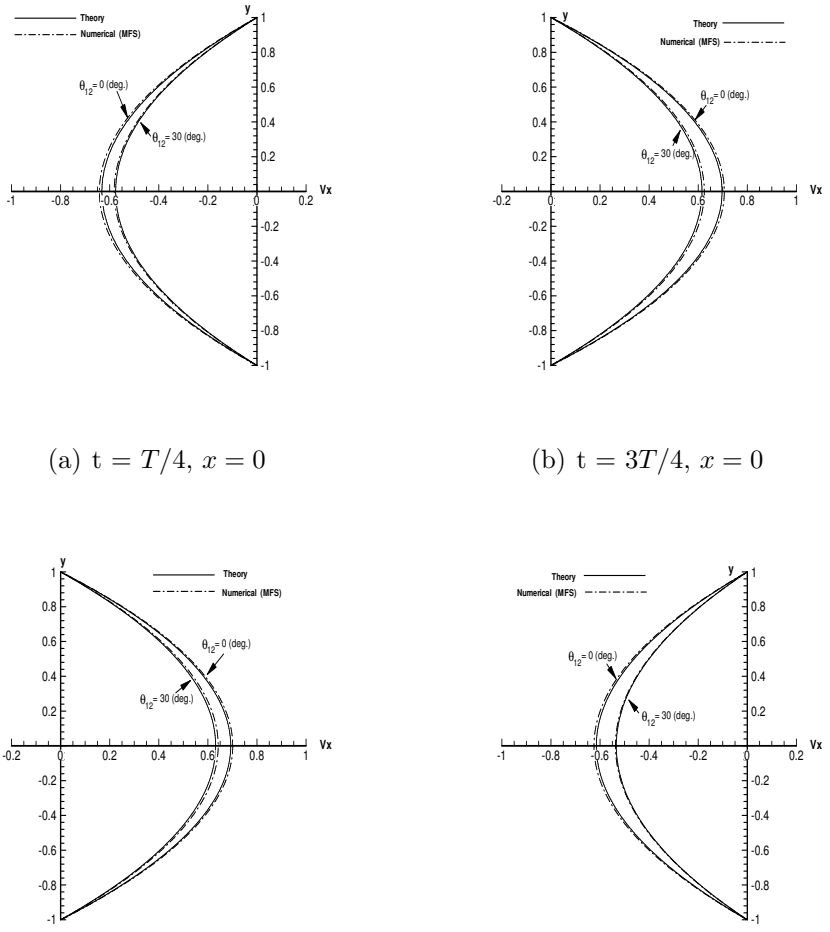

(a) t = $T/4$, $x = 0$

(b) t = $3T/4$, $x = 0$

(c) t = $T/4$, $x = 1$

(d) t = $3T/4$, $x = 1$

Figure 4.9: Comparison of the analytical solution and the meshfree calculations for the (V_x-y) velocity profiles at $\theta_{12} = 0°$ and $30°$ during compression and expansion: (i) $x = 0$ and (ii) $x = 1$.

over a complete collapsing cycle and for various values of phase lags. Ideally, each wall collapse cycle is composed of two main phases, the first one is compression phase (C), where the contraction moves until it reaches the maximum allowable travel distance. The second phase is an expansion phase (E), where the wall contraction expands back to the initial tube radius as marked on the Figs. 4.10 (a-f). In these results, the maximum travel collapse distance $TC(t) = (1 - Min(H(x,t)))\%$

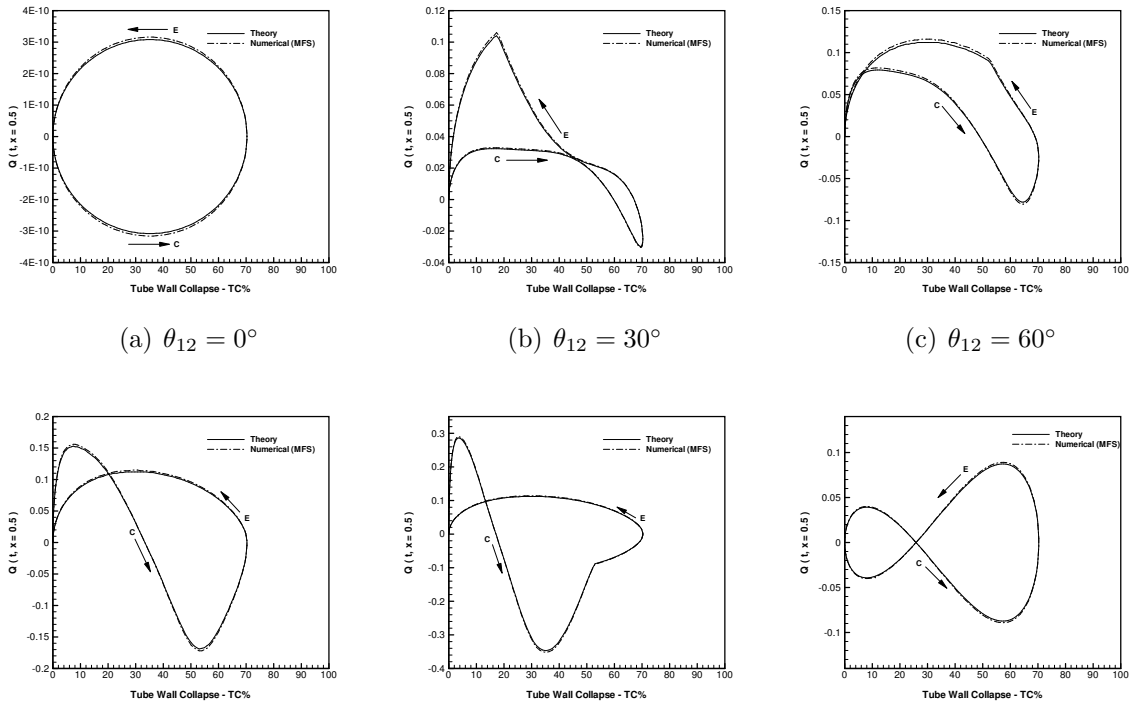

(a) $\theta_{12} = 0°$ (b) $\theta_{12} = 30°$ (c) $\theta_{12} = 60°$

(d) $\theta_{12} = 90°$ (e) $\theta_{12} = 120°$ (f) $\theta_{12} = 180°$

Figure 4.10: Comparison of the analytical solution and the meshfree computations for the instantaneous volumetric flow rate $Q(x = 0.5, t)$ monitored at the tube center line, versus the instantaneous travel collapse (TC) parameter for various phase lags.

is chosen to be $TC = 70\%$ of the original tube radius R. In other words, the contractions are allowed to move until they reach 70% of the nominal radius. In Fig. 4.10 (a-f), the volumetric flow rate $Q(x, t)$ monitored at $x = 0.5$ during a complete contraction-expansion cycle versus the percentage travel contraction $TC\%$ distance at different values of the phase lag parameter θ_{12} is given. Results from both analytical and MFS computations have shown that, in the case of using a phase lag value equal to $\theta_{12} = 0°$ or $180°$, the contraction cycle takes the shape of a pure circle or the standard $8 - shape$, the volumetric flow rate is completely symmetric, and there will be no net flow produced as shown in Fig. 4.10 (a & f). Unlike the other investigated cases, when the phase lag between the two contractions is not zero, the contraction-expansion cycle will take various asymmetric dynamical shapes, which depend on the value of the phase lag assigned, see examples shown in Fig. 4.10 (b-f). These symmetric and asymmetry dynamical shapes can also be viewed

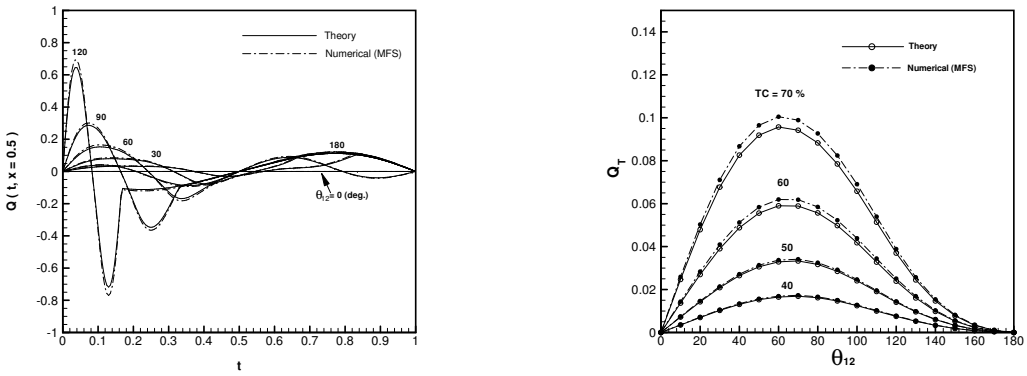

(a) Instantaneous flow rate

(b) Time averaged net flow

Figure 4.11: Comparison of the analytical solution and the meshfree computations for the instantanous and time averaged net flow rates over a single contraction cycle: (a) $Q(x = 0.5, t)$ versus t for various values of θ_{12}, (b) Q_T versus θ_{12} for different collapse ratios, TC (%).

by plotting the volumetric flow rate versus the instantaneous collapsing time rather than using the collapsing ratio TC in the x-axis. Results have shown that, if $\theta_{12} \neq \{0°, 180°\}$, the volumetric flow rate distribution is not symmetric in time as shown in Fig. 4.11 (a). In these situations, the time-average volumetric flow rate is not zero and a unidirectional net flow is produced. The time-average volumetric flow rate Q_T can be calculated by simply integrating the instance flow rate over a complete cycle as

$$Q_T(x) = \frac{1}{T}\int_0^T Q(x,t)dt \tag{4.29}$$

where, $T = 1/S_t$ is the time period. The time averaged flow rate as a function of the phase lag at different values of the maximum allowable travel collapse distance $TC = 50, 60, 70\%$ is given in Fig. 4.11 (b). Results have shown that, as the phase lag between contractions motions increases, the time averaged net flow increases until it reach an optimum value of about $\theta_{opt} = 60°$, afterwards the net flow starts to decrease and there will be no net flow produced when $\theta_{12} = 180°$. Also, as expected whenever the contraction travel distance TC increase, the net flow increases. We also noted that, the optimum value of motion phase lag θ_{opt} that maximize the net flow, is independent from the collapsing amplitude TC.

The results shown that there is a fair agreement between results obtained analytically and by using Stokeslets-meshfree computations when evaluating the instantaneous volumetric flow rate as shown in Fig. 4.10 and Fig. 4.11(a). However, the time averaged net flow calculations have shown significant differences between the analytical and numerical results. For example, the MFS overestimates the time averaged net flow when compared with the analytical counterpart. However, both methods predicts the same optimum value of the motion phase lag $\theta_{opt} = 60^{\circ}$, as shown in Fig. 4.11 (b). This differences in calculating the time averaged net flows may be due to fact that: The meshfree calculations are done exactly for stokes flow where $Re = 0$, unlike the theoretical analysis is given for a finite Reynolds number with $Re = \delta$, with ($\delta = R/L << 1$).

As a summary from this section, the theoretical and meshfree results presented inhere lead us to propose the following hypothesis: by using a non-elastic fluid field axisymmetric tube with at least two local wall contractions that moves with a slight phase lag with respect to each other, a net flow is produced and the system can be used as a simple pumping mechanism at the microscale flow regime.

Inspired by the physiological system in insects, in particular the rhythmic wall contractions found in insect tracheal tubes, a novel biomimetic pumping model is proposed in this study. The model shows that a fluid-filled, inelastic, axisymmetric tube with localized collapse sites can function as a pump. The only requirement for this setup to produce a unidirectional net flow is the presence of at least two collapse sites that can move with a slight time lag with respect to each other. A maximum net flow is produced when the collapse sites are actuated with the optimum phase lag $\theta_{opt} = 60^{\circ}$. It should be mentioned that the present model relies neither on wave dynamics, nor on tube elasticity, and therefore it is not a type of peristaltic pumping. Furthermore, one actuation frequency appears in peristaltic pumping, whereas here at least two actuation frequencies appear. The model is derived using lubrication theory and is validated using the axisymmetric Stokeslets-MFS numerical method. The results presented in this article can ideally provide some guidance for the fabrication of novel valveless microfluidic pumping devices.

4.4 Numerical Validation for the Channel Pumping Model

In this section, we use the planar Stokeslets-meshfree computational technique to validate our bioinspired channel pumping theoretical model, which is given previously in chapter 2, section 2.2 and also is given in (Aboelkassem and Staples, 2012b). The derived channel pumping model formulation and analysis will be re-given briefly at the beginning and before proceeding with the numerical validation details. Finally, detailed comparisons between both theoretical and meshfree methods will be given.

4.4.1 Formulation and Theory

Recall the channel pumping model given chapter 2, section 2.2.1, which considers the motions of a $2-D$ incompressible viscous flow in a channel with a finite length L and width W. The channel have two moving localized contractions from the upper wall $H_2(x,t)$, while the lower wall H_1 is kept stationary, as shown in Fig. 4.12 (a). The upper wall profile allows each contraction to move independently along the lateral direction with or without a phase lag θ_{12} with respect to each other as shown in Fig. 4.12 (b). A zero pressure drop, $\Delta p = 0$, is assumed along the channel length, and hence all the flow motions will be induced as a results of the wall motions only.

The main objective of this formulation was to investigate the ability of using a channel as described above with local contractions to pump fluids at the microscale without imposing any pressure drop or any mechanical valves. The mathematical modelling and equations that govern this particular flow problem formulation are derived based on the quasi-steady approximations and the lubrication theory (Batchelor 1967; Meijing & Brasseur 1993; Takagi & Balmforth 2011) as given previously

*Aboelkassem, Y., Staples, A. E., "Stokeslets-meshfree computations and theory for flow in a collapsible microchannel," *Theor. Comput. Fluid Dyn.*, Published online, DOI 10.1007/s00162-012-0269-7, 2012. Used with kind permission of Springer Science and Business media. Copyright 2012, Springer

in chapter two, section 2.2.1 as,

$$\frac{\partial u}{\partial x} + \frac{\partial v}{\partial y} = 0 \tag{4.30}$$

$$-\frac{\partial p}{\partial x} + \frac{\partial^2 u}{\partial y^2} = 0 \tag{4.31}$$

$$\frac{\partial p}{\partial y} = 0. \tag{4.32}$$

We subject these equations to the following boundary conditions

(i) at $y = H_1$, $u = 0, v = 0$
(ii) at $y = H_2(x,t)$, $u = 0, v = \frac{\partial H_2}{\partial t}$
(iii) at $x = 0$, $p = p_o(t)$
(iv) at $x = 1$, $p = p_L(t)$.

This system of Eqs. (4.30 - 4.32) along with the above boundary conditions are solved analytically in section 2.2.2, where the velocity components, pressure gradient and pressure expressions were given as follows,

$$u(x,y,t) = \frac{1}{2}\frac{\partial p}{\partial x}\left(y^2 - (H_1 + H_2)y + H_1 H_2\right) \tag{4.33}$$

$$v(x,y,t) = \frac{1}{4}\left(\frac{\partial p}{\partial x}\frac{\partial H_2}{\partial x} + H_2\frac{\partial^2 p}{\partial x^2}\right)V_1(y,H_1) - \frac{1}{12}\frac{\partial^2 p}{\partial x^2}V_2(y,H_1) \tag{4.34}$$

where, $V_1(y,H_1) = \left(y^2 - 2H_1 y + H_1^2\right)$, $V_2(y,H_1) = \left(2y^3 - 3H_1 y^2 + H_1^3\right)$.

$$\frac{\partial p}{\partial x} = \frac{1}{\left(H_2(x,t) - H_1\right)^3}\left(G(t) + 12\int_0^x \frac{\partial H_2(s,t)}{\partial t}ds\right) \tag{4.35}$$

where $G(t)$ is the function of integration which depend only on time, t. This function can to be determined after integrating Eq. (4.35) with respect to x, and the following expression for the

pressure can be found

$$p(x,t) = p_o(t) + \int_0^x \frac{\partial p(s,t)}{\partial x} ds. \tag{4.36}$$

Evaluating Eq. (4.36) at $x = L$, where $P = P_L(t)$, an expression for $G(t)$ is found

$$G(t) = \frac{\Delta p(t) - 12 \int_0^1 \left(H_2(x,t) - H_1\right)^{-3} \left(\int_0^x \frac{\partial H_2(s,t)}{\partial t} ds\right) dx}{\int_0^1 \left(H_2(x,t) - H_1\right)^{-3} dx} \tag{4.37}$$

where $\Delta p(t) = p_L(t) - p_o(t)$. Finally, an expression for the volumetric flow rate induced by the contractions assigned to the upper channel wall is derived

$$Q(x,t) = \int_{H_1}^{H_2(x,t)} u(x,y,t) dy \tag{4.38}$$

using Eq. 4.33 and perform the integration yield,

$$Q(x,t) = \frac{-1}{12} \frac{\partial p}{\partial x} \left(H_2(x,t) - H_1\right)^3 \tag{4.39}$$

It should be noted that, once the tube wall profile $H_2(x,t)$ is prescribed, the pressure gradient can be evaluated using Eq. (4.35) and all other flow variables can be determined. The above solution has shown that, an inelastic tube with moving wall contractions can be used as a micropump as it will be confirmed numerically in the following section 4.4.2.

4.4.2 Planar Stokeslets-Mesfree Approach

The meshfree computational approach based on the method of fundamental solutions (MFS) that use the Stokeslets-force elements as basis solutions is developed inhere and will be used to validate our analytical solution derived in chapter 2. More specifically, consider the same problem formulation stated in section 2.2.2 and lets assume that, the governing equations that describe this particular flow motion are the Stokes equations,

$$\nabla^* \cdot \mathbf{V}^* = 0 \tag{4.40}$$

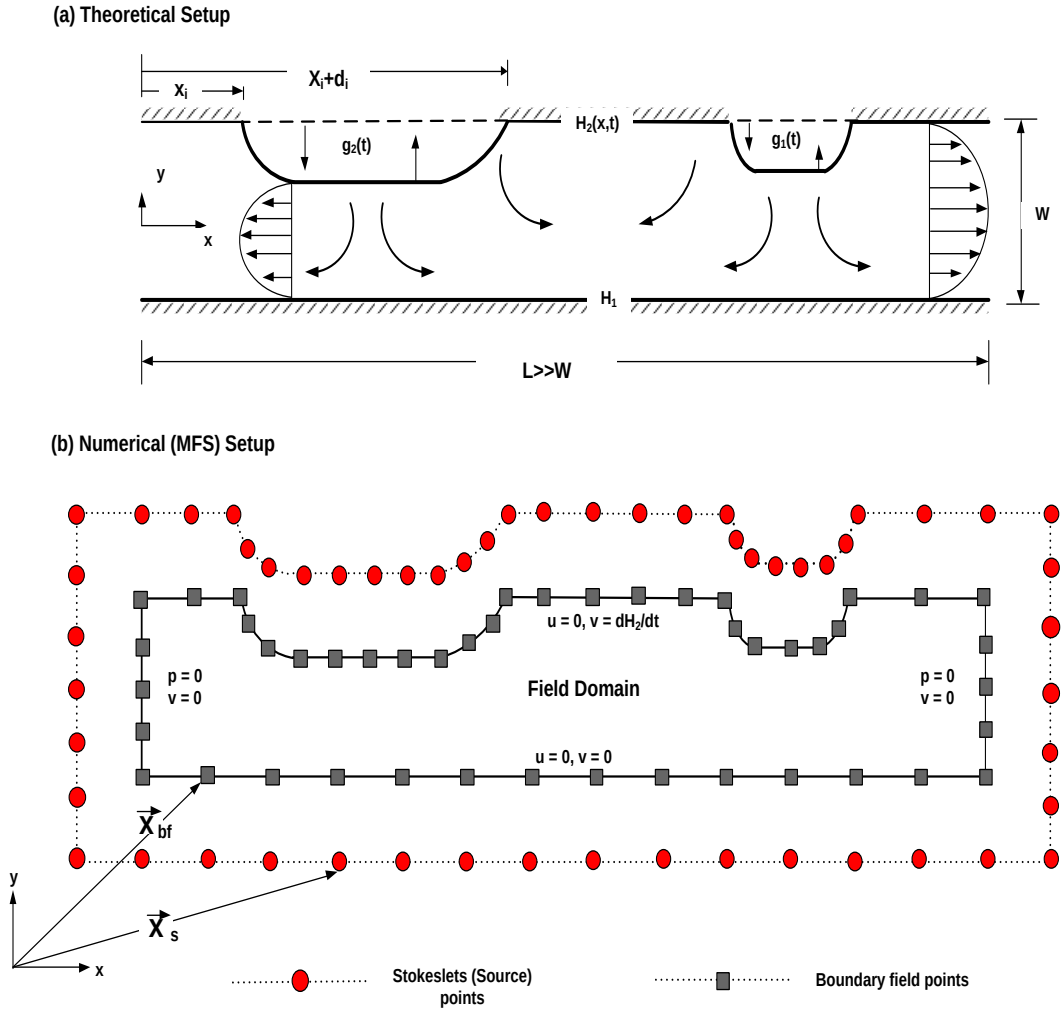

Figure 4.12: Problem Schematic: (a) Theoretical setup of a 2-D channel with moving contractions in the upper wall governed by $H_2(x,t)$ profile and stationary lower wall $H_1(x,t)$, (b) Numerical (MFS) setup consists of distributed source points (Stokeslets) located at $\mathbf{X_s}$ and boundary field points located at $\mathbf{X_{bf}}$, as well as the boundary conditions used in the simulations.

$$\mu \triangle^* \mathbf{V}^* = \nabla^* p^* - \mathbf{F}^* \tag{4.41}$$

where, μ is the fluid viscosity , p^* is the pressure, $\mathbf{V}^*$ is the velocity, and $\mathbf{F}^*$ is the force per unit volume.

A fundamental solution to the above equations is called Stokeslet which is characterized by the velocity field induced by a concentrated external point force with a specific intensity acting on the fluid at a certain location. Because of the linearity in the governing equations, the superposition principle can be imposed and a total flow field can be obtained by taking the effect from all point forces acting on the fluid under considerations. A standard Stokeslet expression based on the Dircac delta distribution for the force intensity in two dimensional Stokes flow regime can be found in Pozrikids (1992),

$$\mathbf{V}^* (\mathbf{x}^*) = \frac{1}{4\pi\mu} \left[-\mathbf{q}^* \ln (r^*) + [\mathbf{q}^* \cdot (\mathbf{x}^* - \mathbf{x}_s^*)] \frac{(\mathbf{x}^* - \mathbf{x}_s^*)}{r^{*2}} \right] \tag{4.42}$$

$$p^* (\mathbf{x}^*) = \frac{1}{2\pi} \left[\mathbf{q}^* \cdot \frac{(\mathbf{x}^* - \mathbf{x}_s^*)}{r^{*2}} \right] \tag{4.43}$$

where, $\mathbf{V}^* = (u^*, v^*, 0)$ is the induced velocity field by a point force. $\mathbf{q}^* = q_x^* \mathbf{i} + q_y^* \mathbf{j}$ is a concentrated point force per unit length. $r^* = \mid \mathbf{x}^* - \mathbf{x}_s^* \mid$ is the distance between any field point located at $\mathbf{x}^*$ and a source (Stokeslet) point at $\mathbf{x}_s^*$. Now, if we use the same non-dimensional parameters defined in section 2.2.2, i.e., let $x = x^*/L$, $y = y^*/W$, $r = r^*/L$,$\delta = W/L$, $u = u^*/u_o$, $v = v^*/\delta u_o$, $p = p^* W^2/(\mu u_o L)$,$q_x = q_x^*/(\mu u_o)$, $q_y = q_y^*/(\mu u_o)$. Therefore, the above equations can be re-written in a non-dimensional form,

$$u (x, y) = \frac{1}{4\pi} \left[q_x \left(-\ln (r) + \frac{(x - x_s)^2}{r^2} \right) + q_y \left(\frac{\delta (x - x_s) (y - y_s)}{r^2} \right) \right] \tag{4.44}$$

$$v (x, y) = \frac{1}{4\pi\delta} \left[q_x \left(\frac{\delta (x - x_s) (y - y_s)}{r^2} \right) + q_y \left(-\ln (r) + \frac{\delta^2 (y - y_s)^2}{r^2} \right) \right] \tag{4.45}$$

$$p (x, y) = \frac{\delta^2}{2\pi} \left[q_x \frac{(x - x_s)}{r^2} + q_y \frac{\delta (y - y_s)}{r^2} \right] \tag{4.46}$$

where, $r = \sqrt{(x - x_s) + \delta^2 (y - y_s)}$.

In the MFS technique, the total solution is formed by superposition of all basis represented by the Stokeslets expressions with unknown intensities as shown above. The strength of the Stokeslets singularities is then obtained by enforcing the fundamental solutions to satisfy the prescribed boundary conditions by direct collocations Young et al. (2006).

Now, consider the problem under consideration with the prescribed boundary conditions as shown in Fig.4.12(b). Let's distribute N-Stokeslets (source) points with unknown strength $\mathbf{q}$ vectors collocated a distance ε away from the channel boundary. The flow field can be then approximated by superposition the effect from all the Stokeslets and the velocity field can be evaluated as,

$$u(x_i, y_i) = \frac{1}{4\pi} \sum_{j=1}^{N} \left[q_{xj} \left(-\ln (r_{ij}) + \frac{(x_i - x_{sj})^2}{r_{ij}^2} \right) + q_{yj} \left(\frac{\delta (x_i - x_{sj}) (y_i - y_{sj})}{r_{ij}^2} \right) \right] \tag{4.47}$$

$$v (x_i, y_i) = \frac{1}{4\pi\delta} \sum_{j=1}^{N} \left[q_{xj} \left(\frac{\delta (x_i - x_{sj}) (y_i - y_{sj})}{r_{ij}^2} \right) + q_{yj} \left(-\ln (r_{ij}) + \frac{\delta^2 (y_i - y_{sj})^2}{r_{ij}^2} \right) \right] \tag{4.48}$$

$$p (x_i, y_i) = \frac{\delta^2}{2\pi} \sum_{j=1}^{N} \left[q_{xj} \frac{(x_i - x_{sj})}{r_{ij}^2} + q_{yj} \frac{\delta (y_i - y_{sj})}{r_{ij}^2} \right] \tag{4.49}$$

where, q_{xj} and q_{yj} are the unknown force coefficients that represent the strengths of the Stokeslets in x and y-directions respectively. $\mathbf{x}_i = (x_i, y_i)$ is the position of any field point including the boundary points. $\mathbf{x}_{sj} = (x_{sj}, y_{sj})$ is the location of the Stokeslets source points. $r_{ij} = |\mathbf{x}_i - \mathbf{x}_{sj}| = \sqrt{(x_i - x_{sj}) + \delta^2 (y_i - y_{sj})}$ is the distance between any field point and another source point. The Stokeslets are chosen to be located very close to the boundaries with a distance ε where, the equation that govern the locations of the distributed Stokeslets points is given by

$$\mathbf{x}_{sj} = \mathbf{x}_{bj} + \varepsilon (\mathbf{x}_{bj} - \mathbf{x}_c) \tag{4.50}$$

where, $\mathbf{x}_{sj}$ refer to the location of Stokeslets source points, $\mathbf{x}_{bj}$ is the boundary points, ε is the separation distance away from the domain boundary, and $\mathbf{x}_c$ is the geometric center of the domain

of interest. In order to determine the unknown force coefficients $\mathbf{q} = (q_{xj}, q_{yj})$, the boundary conditions for the velocity components and pressure are imposed and collocated at certain field points on the channel boundary as shown in Fig. 4.12(b). Adding each fundamental solution to the Stokes Eqs. Eqs. (4.47-4.49), the final induced solution can be obtained by solving an emerging system of equations

$$\mathbb{A}\mathbf{q} = \mathbf{b} \tag{4.51}$$

where $\mathbb{A}$ is a matrix of size $2Nx2N$ with real entries formed by evaluating the right hand side of the above expressions in Eqs. (4.47-4.49). $\mathbf{b}$ is a vector of size $1x2N$ of real entries formed by evaluating the left hand side of the same equations. In other words, all the entries in both $\mathbb{A}$ and $\mathbf{b}$ are filled by enforcing the fundamental solutions to satisfy the boundary conditions by direct collocation. $\mathbf{q}$ represent the Stokeslets force coefficients which to be determined by solving the above system of equations as it will be given in details in the subsection4.5.2.

It should be mentioned here that, although the MFS is relatively easy to implement and does not require any grids, it still suffers from some issues related to non-invertible or ill-conditioning matrix problem associated with finding the force-coefficients when implementing the Stokeslets as fundamental solutions Alves and Silvestre (2004) and Young et al. (2005). This linear algebra matrix problem can lead to inaccurate force coefficients and consequently wrong flow field is induced. A solution to non-invertible matrix problem is found by either collocating the Stokeslets sources a distance away from the domain boundaries as given in Young et al. (2006) or by using regularized Stokeslets expressions as derived by Cortez (2001). A smoothing to the ill-conditioning matrix problem is also introduced by iteratively choosing the Stokeslets positions as shown in Young et al. (2006) or by optimizing the regularization parameter as in Cortez (2001). However, still the ill-conditioning matrix issue represents a challenging problem for the MFS to be correctly implemented.

4.5 Channel Numerical Results and Discussions

In this part, we present results from both theoretical model and meshfree computations based on the MFS method for the seek of comparisons and as two-ways validation approach for both

Table 4.3: Parameters and values used in the channel meshfree computations

parameter	value	parameter	value	parameter	value	parameter	value
x_1	0.25	d_1	0.1	N_c	2	N	742
x_2	0.35	d_2	0.1	S_t	1	ε	0.15
x_3	0.65	A_1, A_2	-0.3528	T	$[0, 1]$	h	0.01
x_4	0.75	TC	70%	$\Delta p(t)$	0	tol	10^{-6}

methods. In other words, the meshfree computations will be used to justify the assumptions made during the derivation of the analytical solution, meanwhile the analytical solution will be used to validate the (MFS)numerical approach as a proper method that can be used for physiological flows with moving boundaries. Two main cases for situations where, the wall contractions move with phase lags $\theta_{12} = 0°\&30°$ respectively will be used for this validation process and to compare between results computed analytically and numerically at the same geometric and flow conditions with values listed in Table 4.3.

The result section is organized as follows: at the beginning, we recall the prescribe kinematics and geometry of channel wall contractions which have been given by a generic expression $H_2(x, t)$ in section 2.2.3. This specific wall profile is designed to allow for a single or multiple contractions that can move with similar or with different amplitudes, and with or without phase lags relative to each other as will be given in subsection. Once the wall profile is given, all the flow variables can be computed exactly using our analytical model throughout Eqs. (4.30 - 4.39). Also, the strengths of the Stokeslets points can be calculated by solving the linear system of equations given by Eq. 4.51 iteratively and then, the MFS can be then applied to reconstruct the induced flow inside the channel. The detailed algorithm used to obtain the Stokeslets strengths will be given in subsection 4.5.2. The structure and development of the flow field induced by only two wall contractions undergoes cyclic compression and expansion motions using both analytical and meshfree computations are computed and compared as it will be shown in the next subsection 4.5.3. Finally, the effect of the contraction amplitudes and the phase lags protocol assigned to the wall collapse motions on the instantaneous and on the time averaged volumetric flow rate is investigated in section 4.5.4. Specifically, the time averaged volumetric flow rate over a complete contraction-expansion cycle for

various phase lags values is studied to explore which contraction setting can produce unidirectional net flows out of this system.

It should be noted here that, the channel wall profile $H_2(x,t)$ and its kinematics prescribed by the local wall contractions motion protocol shown in Fig. 4.5.2(a) plays the important role in this study. For examples, the analytical derivation given by Eqs. (4.30)-(4.39) show that, once the profile is prescribed, all the flow parameters can be calculated analytically. On the numerical side, the strengths of the Stokeslets points which will be used to reconstruct the induced flow field numerically are also strong function of the channel wall profile as will be given next.

4.5.1 Channel Wall Profile, $H_2(x,t)$

Let the mathematical model that describes the kinematics and the shape of the contractions from the channel upper wall be given as

$$H_2(x,t) = \frac{1}{2} + \sum_{i=1}^{N} A_i f_i(x) g_i(t) \tag{4.52}$$

where $f_i(x) \in C^r[0,1]$ and $g_i(t) \in C^r[0, T = 1/S_t]$ represent the spatial and the temporal distribution of the upper wall shape, respectively. N defines the number of contractions, and A_i is the amplitude assigned to each contraction. The spatial form of the above equation imitates the geometry of the upper wall contractions as

$$f_i(x) = \tanh(\alpha(x - x_i)) - \tanh(\alpha(x - (x_i + d_i))) \tag{4.53}$$

where $\alpha = 2\pi/\delta$,x_i defines the beginning of each collapse region and $d_i \in (0, 1 - x_i]$ marks its end, as shown in Fig. 4.12(a). In this part, we only consider two contractions, i.e., $N = 2$ where, the first contraction moves in time according to the following profile

$$g_1(t) = \begin{cases} \frac{1}{2}\left(1 - \cos(2\pi\beta S_t t)\right), & 0 \le t \le 1/\beta S_t \\ 0 & 1/\beta S_t < t \le 1/S_t \end{cases} \tag{4.54}$$

while the second contraction moves according to

$$g_2(t) = \frac{1}{2}\left(1 - \cos(2\pi S_t t)\right), 0 \leq t \leq 1/S_t \tag{4.55}$$

where the non-dimensional parameter β is related to the phase lag between the first and the second contractions according to the assigned motion protocol. Initially, during the compression phase we let both contractions begin to move together. Then, however, we let the first contraction reach the maximum specified channel travel collapse (TC) distance faster than the second contraction. In other words, there will be a time lag, $T_g = (1 - 1/\beta)/(2S_t)$, between these two collapse motions which is equal to the phase lag $\theta_{12} = \pi(1 - 1/\beta)$. Moreover, during the expansion phase, the first contraction returns back to the nominal original position and continues its period with zero amplitude until the second contraction completes its own cycle, then both contractions start the second cycle together with the protocol shown in Fig. 4.5.2(a). It should be noted that both contractions have same time period $T = 1/S_t$, and that if $\beta = 1$, there will be no phase lag and both contractions will move in the same manner with time. This protocol is guarantees that after one cycle the channel geometry will be returning to the initial position and there will be no net flow due to volume deformation. The channel wall profile $H_2(x, t)$ and its kinematics prescribed by the local wall contractions motion protocol plays the important role in this study. Once the profile is prescribed, all the flow parameters can be calculated analytically or by using simple numerical integration methods. In this article, the profile $H_2(x, t)$ which is given by Eq. (4.52) is simple enough to calculate all the parameters analytically and to show the instantaneous flow development during a complete cycle of compressions-expansions, see section 4.5.3.

4.5.2 Channel Stokeslets Strengths and Solving Ill-Conditioned System of Equations

Finding an accurate solution to the ill-conditioned system given by Eq. 4.51 is considered to be the most important step when using meshfree computations that use the Stokeslets elements as the fundamental basis to the Stokes equations. In this part, we present a numerical algorithm which has been originally derived by Neumaier (1998) to solve ill-conditioned linear system of equations.

The algorithm is mainly based on introducing a regularization parameter h to the original matrix $\mathbb{A}$ which will be then transformed to a modified and symmetric matrix $\mathbb{A}_h$. This modified matrix will act as a pre-conditioner matrix and leads to a modified system of equations with an enhanced condition number. In principle, the preconditioner matrix changes the eigenvalues of the original matrix $\mathbb{A}$ to modified ones. These modified eigenvalues will be clustered away from the zero and consequently lead to a better conditioned number.

Table 4.4: Channel pumping model: Algorithm for solving ill-conditioned systems of equations

Algorithm for Finding the strengths of each Stokeslets-source point
Input: $\mathbb{A}, \mathbb{I} \in \mathbf{M_{2NX2N}}$, $\mathbf{b} \in \mathbf{R^{2N}}$, $h, tol \in \mathbf{R}$
1. $\mathbf{q^{(0)}} = \mathbf{0}$, $\mathbf{r^{(0)}} = \mathbf{b}$ - $\mathbf{q^{(0)}} = \mathbf{b}$
2. Do While $\| \mathbf{r} \|_\infty \geq \mathbf{tol}$
3. $\mathbb{A}_h = \mathbb{A}^*\mathbb{A} + h^2\mathbb{I}$
4. $\mathbf{q^{(k)}} = \mathbf{q^{(k-1)}} + {\mathbb{A}_h}^{-1}\mathbb{A}^*\mathbf{r^{(k-1)}}$
5. $\mathbf{r^{(k)}} = \mathbf{b} - \mathbb{A}\mathbf{q^{(k)}}$
end
Output: Stokeslets Strengths, $\mathbf{q} = [q_{xj}\ q_{yj}]^T$, $j = 1 : N$

The algorithm is simple and only requires to have in hand, the matrix of coefficients $\mathbb{A}$, the vector $\mathbf{b}$, the regularization parameter h and the convergence criteria based on an assigned specific tolerance *tol* value. The detailed steps of the algorithm are listed in Table 4.4 which is easy to follow. It should be also noted that, the above mentioned algorithm is general and the preconditioner matrix given in step 3 is the most important part of the algorithm because of, it can affect the maximum number if iteration required for residual to convergence within a prescribed tolerance. One way to verify the accuracy of the above algorithm shown in Table 4.4, is to use the output force strengths $\mathbf{q}$ to re-calculate the velocities and pressure at all boundary points to ensure that, the boundary conditions are met and satisfied within the prescribed degree of accuracy.

As a direct implementation of the above algorithm, we show the residual convergence history and the output Stokeslets strength distributions for two main cases. These two cases are for situations

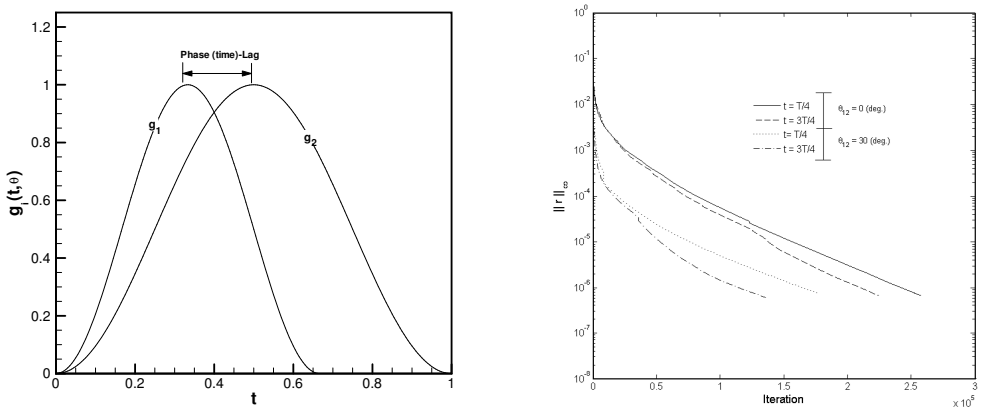

(a) (b)

Figure 4.13: (a) Collapsing motion protocol with $g_1(t)$ and $g_2(t)$ functions assigned to the first and second contractions respectively. (b) Iterative procedure for solving the ill-conditioned linear system: convergence of the relative residuals ∞-norm versus the number iterations.

where the wall contractions move with phase lags $\theta_{12} = 0°\&30°$ and for only two snapshots of times namely, compression time $t = t/4$ and expansion $t = 3T/4$ respectively. For examples, the residual convergence history for both cases and at both snapshot times are shown in Fig. 4.5.2 (b). Results have shown that, when the two contractions move with zero phase lag $\theta_{12} = 0°$, the required number of iterations to convergence to a specific tolerance is greater than when the contractions move with $\theta_{12} = 30°$. There is always more iterations are required for convergence when calculations are done during compression snapshot $t = t/4$ compared with calculations during expansion time $t = 3T/4$. The strengths q_x and q_y distributions along x and y directions for each Stokeslet point are plotted for the same both cases of study and at compression time $t = t/4$ and at expansion $t = 3T/4$ snapshots in Fig. 4.14(a-b) respectively. Results have shown that, we need Stokeslets with low strengths whenever the wall contractions move with phase lags other than zero. Stokeslets in and near to the contractions regions have large gradients and stronger strengths then compared with other force points.

It should be noted that, at each time step corresponding to wall contractions positions, new force strengths must be calculated via-solving the linear system given by Eq. 4.51 iteratively. Now, after prescribing the wall motion profile and calculating the strength for each source point, the flow field using both analytical and numerical methods can be calculated and compared at any instant of

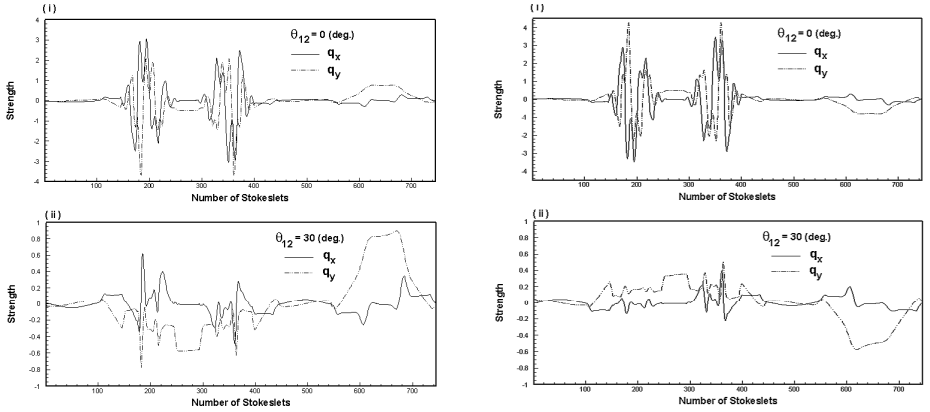

(a) Compression at t = $T/4$ (b) Expansion at t = $3T/4$

Figure 4.14: Stokeslets strength q_x and q_y coefficients along both x and y directions respectively at two different phase lags $\theta_{12} = 0, 30°$ during compression and expansion snapshots:(i)$\theta_{12} = 0°$,(ii)$\theta_{12} = 30°$.

time during the collapse cycle as will be given in the following subsections.

4.5.3 Flow Field Induced by Channel Upper Wall Contractions

The flow field induced by the motions of upper wall contractions in a channel subjected to a zero pressure drop $\Delta p(t) = 0$ is given in detail in this section using both analytical and meshfree computations. The structures and developments of the induced flow for two cases are investigated. In the first case, the two contractions are set to move with zero phase lag i.e., $\theta_{12} = 0°$, where in the second case contractions are forced to move with $\theta_{12} = 30°$. A comparison between results obtained analytically and numerically is held to validate and verify assumptions made in each method. More specifically, the contour lines of the velocity components and pressure in addition to the velocity streamlines are compared at both compression time $t = t/4$ and at expansion $t = 3T/4$ snapshots. Based on the analytical solution derived inhere, since the upper wall profile is fully described by Eqs. (4.52 - 4.55), all the flow variables can be calculated. For instance, the pressure gradient is evaluated by using Eqs. (4.35 - 4.37), and the velocity components are then calculated by using Eqs. (4.33 - 4.34) respectively. On the numerical side, since the geometry is prescribed, Stokeslets are collocated, and force points strengths are calculated using algorithm shown in Table 4.4 and

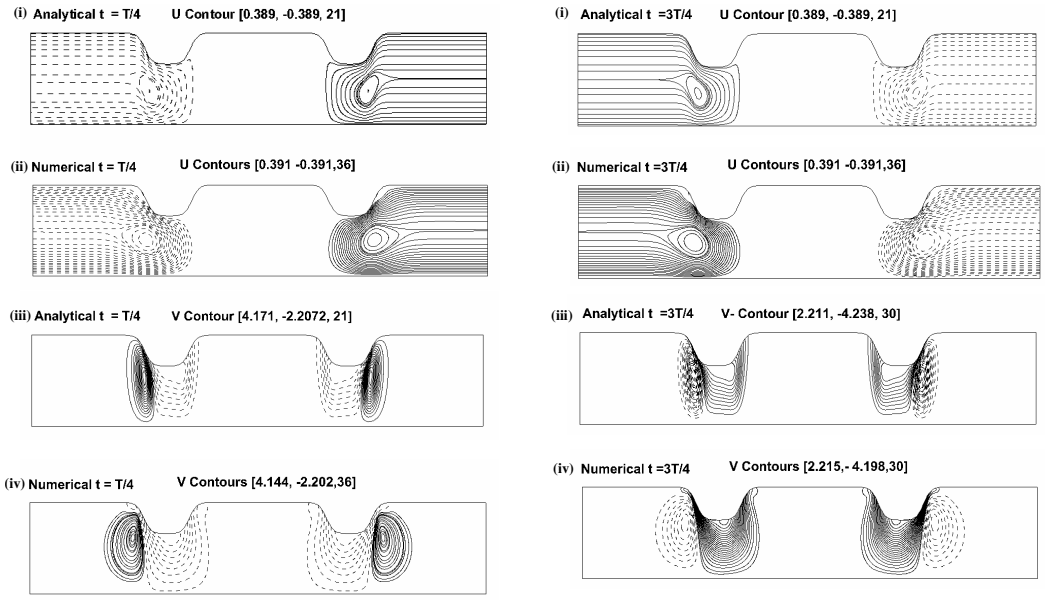

(a) Compression at t = $T/4$ & $\theta_{12} = 0°$ (b) Expansion at t = $3T/4$ & $\theta_{12} = 0°$

Figure 4.15: Velocity flow field comparison: (i) Analytical- u contours,(ii)Numerical-u contours,(iii) Analytical- v contours and (iv)Numerical- v contours.

values are shown in Fig. 4.14. Therefore, all the induced flow variables at each field point can be easily calculated using Eqs. (4.47 - 4.49). Results obtained using both analytical and meshfree computations are compared and shown in Figs. (4.15 - 4.18).

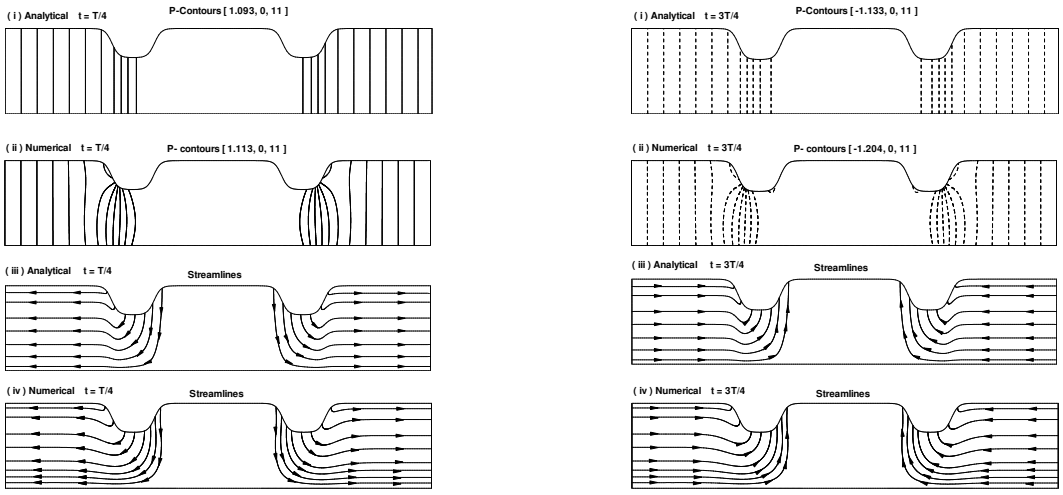

(a) Compression at t = $T/4$ & $\theta_{12} = 0°$ (b) Expansion at t = $3T/4$ & $\theta_{12} = 0°$

Figure 4.16: Pressure and streamlines comparison : (i)Analytical - p contours, (ii) Numerical - p contours, (iii) Analytical- velocity streamlines and (iv) Numerical-velocity streamline.

For examples, in Fig. 4.15 (a), we show a comparison between the velocity components contour lines obtained analytical and numerically when wall contractions are set to move with a zero phase lag i.e., $\theta_{12} = 0°$. Contour lines are given during the compression phase at instant of time $t = T/4$. The labels for contour lines are given on the top of each plot in the standard format of [max. values, min. values , num. of contours]. Results have shown that, as the wall contractions undergo compression phase and start to move toward the bottom wall, the axial velocity component increases near the contraction regions and the flow is displaced, bifurcated, and exit the channel from both directions. There will be a stagnation region between the two contractions due to flow cancellation, since each collapse sends flow to both directions away from the contraction zone as given analytically in Fig. 4.15 (a-(i)) and numerically in Fig. 4.15 (a-(ii)).

The contour lines for the vertical velocity component are also shown to be characterized by two circulation zones regions with opposite direction underneath each contraction as shown analytically in Fig. 4.15 (a-(iii)) and numerically in Fig. 4.15 (a-(iv)). Similarly, snapshots that show the velocity field during the expansion phase at time $t = 3T/4$ are shown in Fig. 4.15 (b). When the contraction regions expand back away from the bottom wall, an exactly a similar flow field structure

is developed but with an opposite direction for the axial and the vertical velocity components as shown analytically in Fig. 4.15 (b-(i-iv)) and numerically in Fig. 4.15 (b-(ii-iii)). There is a fair agreement between the flow contour lines obtained analytically and numerically using meshfree approach. Except that, the contour lines obtained numerically for the vertical velocity component is stretched, however same order of magnitudes are attained.

In Fig. 4.16 (a), a comparison between the pressure contours and velocity streamlines obtained analytical and numerically when wall contractions are set to move with a zero phase lag i.e., $\theta_{12} = 0^\circ$ is given. The contour lines for the static pressure and streamlines are given at similar compression and expansion times that mentioned before. For example, results at compression time $t = T/4$ show that as the wall contractions start to move toward the bottom wall, high pressure with adverse and favorable gradients are formed in and near the contraction regions. This induces a flow away from the compression sited that exits the channel from both sides as pointed out from the velocity contours. Moreover, the pressure is maximum or total in the stagnation zone between the two contractions. The pressure gradient have its absolute maximum value near the contraction regions and become constant away from these contractions and they are independent from the vertical direction as shown as shown analytically in Fig. 4.16 (a-(i)) and numerically in Fig. 4.16 (a-(ii)). The streamlines patterns as a result of contractions motion at this specific time $t = T/4$ are shown analytically in Fig. 4.16 (a-(iii)) and numerically in Fig. 4.16(a-(iv)). The streamlines show that, there will be a stagnation region between the two contractions due to flow cancellation, since each collapse send flow to both directions away from the contraction zone. Similarly, data for pressure contours and velocity streamlines during the expansion phase at time $t = 3T/4$ are shown in Fig. 4.16(b). As expected, when the contraction regions expand back away from the bottom wall, an exactly similar contour lines and streamlines are developed but with opposite signs when compared with data at compression time $t = T/4$.

In addition to results presented from the previous case study, where the two contractions move with no phase lag i.e., $\theta_{12} = 0^\circ$, we show similar plots for velocity and pressure contours in addition to flow streamlines for a situation where the wall contractions are set to move with a phase lag $\theta_{12} = 30^\circ$. Analytical and MFS computational results are given at similar snapshot times that represent both compression $t = T/4$ and expansion $t = 4T/4$. For instance, contour lines for

both velocity components are shown in Figs. 4.17. Similarly, the pressure contours and velocity streamlines shown in Fig. 4.18 at both compression and expansion times as well. Results have shown that, unlike the situation where $\theta_{12} = 0^\circ$ which is always characterized by having a stagnation zone of zero velocities between the two contractions and the flow is not allowed to transport. When $\theta_{12} = 30^\circ$, this stagnation zone is relaxed and there will be flow transport within the region between the two contractions as shown by the axial velocity contour lines calculated analytically and numerically and given in Figs. 4.17 (i) & 4.17 (ii) respectively. Moreover, there is a pressure gradients in the region between the two contractions which indicate that, there is a flow transport in this region. This is also confirmed by plotting the flow streamlines in Fig 4.18 (iii-iv) during both compression and expansion times as before.

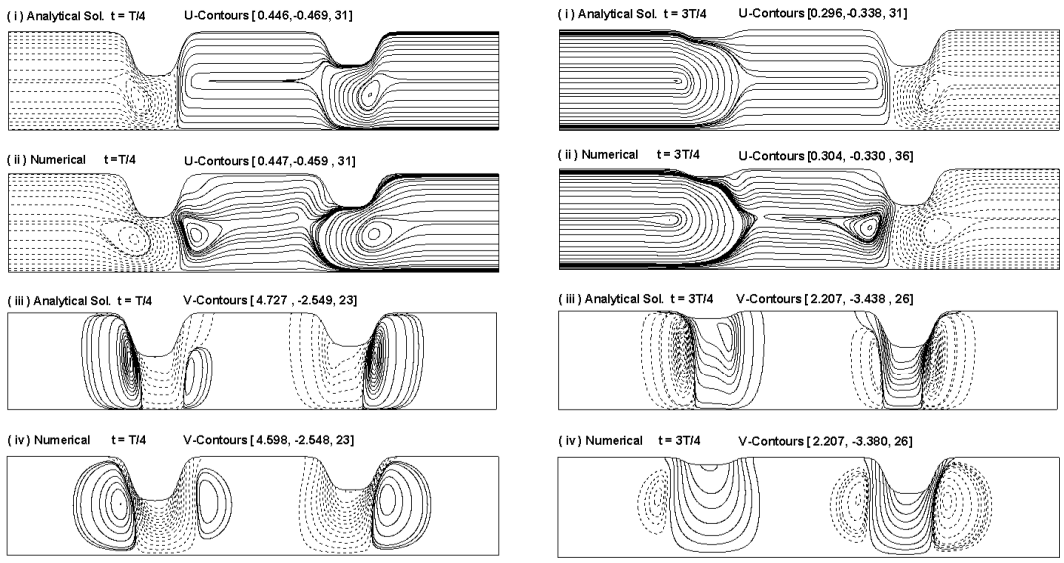

(a) Compression at t = $T/4$ & $\theta_{12} = 30^\circ$ (b) Expansion at t = $3T/4$ & $\theta_{12} = 30^\circ$

Figure 4.17: Velocity flow field comparison: (i) Analytical- u contours,(ii)Numerical-u contours,(iii) Analytical- v contours and (iv) Numerical- v contours.

As a summary from results presented in Figs. (4.15 - 4.18), when the wall contractions move with a zero phase lag i.e., $\theta_{12} = 0^\circ$, the flow field structures have a complete symmetry behaviour during compression and expansion phases of the collapsing cycle and there will be no flow transport between

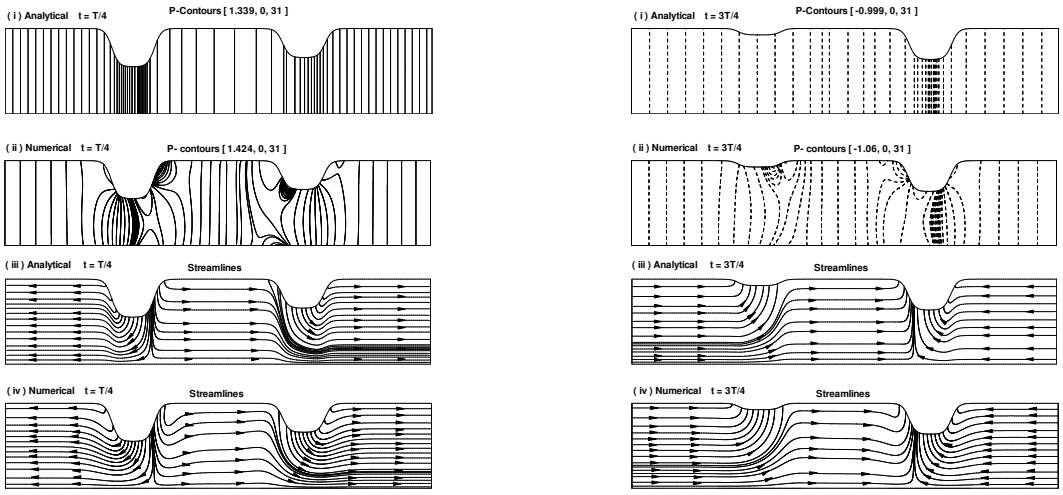

(a) Compression at t = $T/4$ & $\theta_{12} = 30°$

(b) Expansion at t = $T/4$ & $\theta_{12} = 30°$

Figure 4.18: Pressure and streamlines comparison: (i)Analytical - p contours, (ii) Numerical - p contours, (iii) Analytical- velocity streamlines and (iv) Numerical-velocity streamline.

the contraction regions. This symmetry behaviour breaks down when the wall contractions move with a phase lag other than zero as shown for $\theta_{12} = 30°$ and flow is transported after a complete collapsing cyclic motion. In general, it seems there is a strong dependence between motion protocol and the flow transport between these wall contractions. Therefore, the relationship between the flow transport, time averaged net flow produced out of this system and the phase lag parameter will be investigated in details in section 4.5.4.

Although, there is a relatively great agreement between the analytical and MFS-Stokeslets results, there still some differences that can be drawn. For instance, when the wall contractions move with $\theta_{12} = 0°$, the contour lines computed analytically and numerically for the axial velocity components are exactly the same. However, when The $\theta_{12} = 30°$, the u-contours computed numerically have shown an extra small structure which made the MFS results be a slightly different from the ones calculated analytically. Also, for both phase lags cases studied inhere, the contour lines for vertical velocity component computed numerically are somehow stretched when it compared with analytical counterpart. These small discrepancies in the velocity contours can be clearly seen from the pressure contour lines as well. Where, the pressure calculated using MFS exhibits some variations along

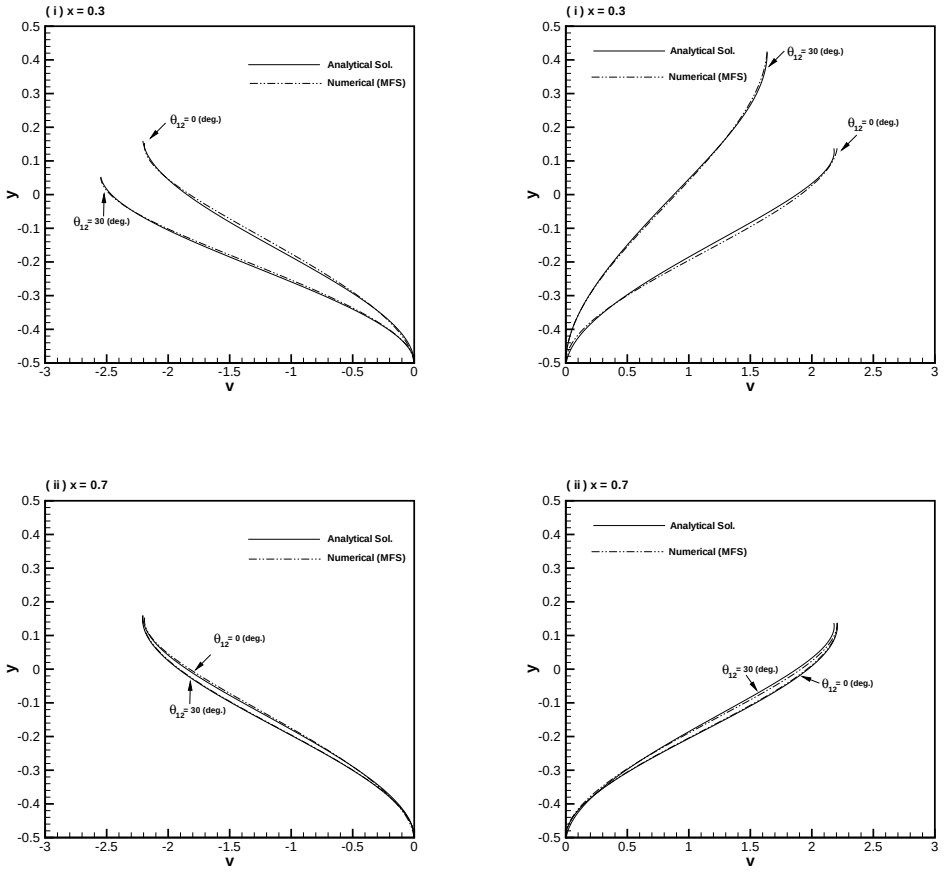

(c) Compression at t = $T/4$ (d) Expansion at t = $3T/4$

Figure 4.19: Comparison of the analytical solution and the meshfree calculations for the (v-y) velocity profiles at $\theta_{12} = 0°$ and $30°$ during compression and expansion: (i) $x = 0.3$ and (ii) $x = 0.7$.

the vertical direction specially near to the contraction regions when it compared with analytical counterpart which is assumed to be totally invariant in the vertical direction.

To better understand the flow field induced by the motion protocols of wall contractions and to be able to adequately compare between the analytical and MFS results, we show line plots for $u\&v$ velocity components along the channel width at different axial locations as shown in Figs. (4.19 & 4.20). Results are given for the same two cases of study i.e, when contractions move with phase lags equal to $\theta_{12} = 0°\&30°$ at compression $t = T/4$ and expansion $t = 3T/4$ snapshots respectively.

For examples, in Fig.4.19 (a & b) we show the vertical velocity $v - y$ profiles at the contraction regions, specifically at $x = 0.3\&0.7$ locations along the channel length. These two locations are chosen based on the conclusion made from the contour plots which suggest that, far away from and in between the contraction regions, the vertical velocity is always zero. However, right at the middle of contractions i.e., at $x = 0.3, 0.7$, the v - profiles starts by zero values at the bottom wall and reaches asymptotically its maximum value at the upper wall to meet the boundary conditions. At $x = 0.3$ and when $\theta_{12} = 0^\circ$ is employed, the v velocity profiles shown in Figs.4.19 (b-i) at an expansion instant of time $t = 3T/4$ are an exact mirror to the profiles shown in Figs.4.19 (a-i) at compression instant of time $t = T/4$. However, this symmetry is no longer exist when $\theta_{12} = 30^\circ$. Also, at $x = 0.7$ there is a symmetry behaviour for v-profiles as shown from plots at an expansion instant of time $t = 3T/4$ 4.19(b-ii) are an exact mirror to the profiles shown in Figs.4.19 (a-ii) at compression instant of time $t = T/4$ for both $\theta_{12} = 0^\circ\&30^\circ$. This suggests that the v-profiles at $x = 0.7$ is independent of the value of the phase lags.

In Fig. 4.20, the axial velocity u-profiles along the $y - axis$ at beginning and at the end of the channel length i.e., at $x = 0\&1$ are given. No surprising, the velocity profiles are parabolic with maximum value at the midway between the upper and the lower walls according to Eq. (4.36). When $\theta_{12} = 0^\circ$ and at $x = 0\&1$, u-profiles at expansion times $t = 3T/4$ are exactly similar to ones obtained at compression time $t = 3T/4$ but with opposite signs i.e., there is a complete symmetry in the behaviour during compressions and re-inflations times of the collapsing protocol. However, when $\theta_{12} = 30^\circ$ still the u-profiles shapes are the same but the maximum values are different when comparing results between compression with expansion snapshot instant of time. In other words, the symmetry behaviour shown when $\theta_{12} = 0^\circ$ breaks down when $\theta_{12} = 30^\circ$ is used.

As a summary from Figs.4.19 - 4.20, there is a great agreement between the analytical and meshfree solutions. The MFS-Stokeslets approximates well the velocity profiles at various locations along the channel lengths specially when $\theta_{12} = 0^\circ$. There is tiny differences between numerical and analytical results when $\theta_{12} = 30^\circ$. Furthermore, results have shown that, the compression and expansion process is not completely symmetric over a complete collapsing cycle when the wall contractions move with a non-zero phase lag and a net flow is produced as a result of the contractions motions. Results indicate that, a flow transport and a net flow out of this system can be produced by using

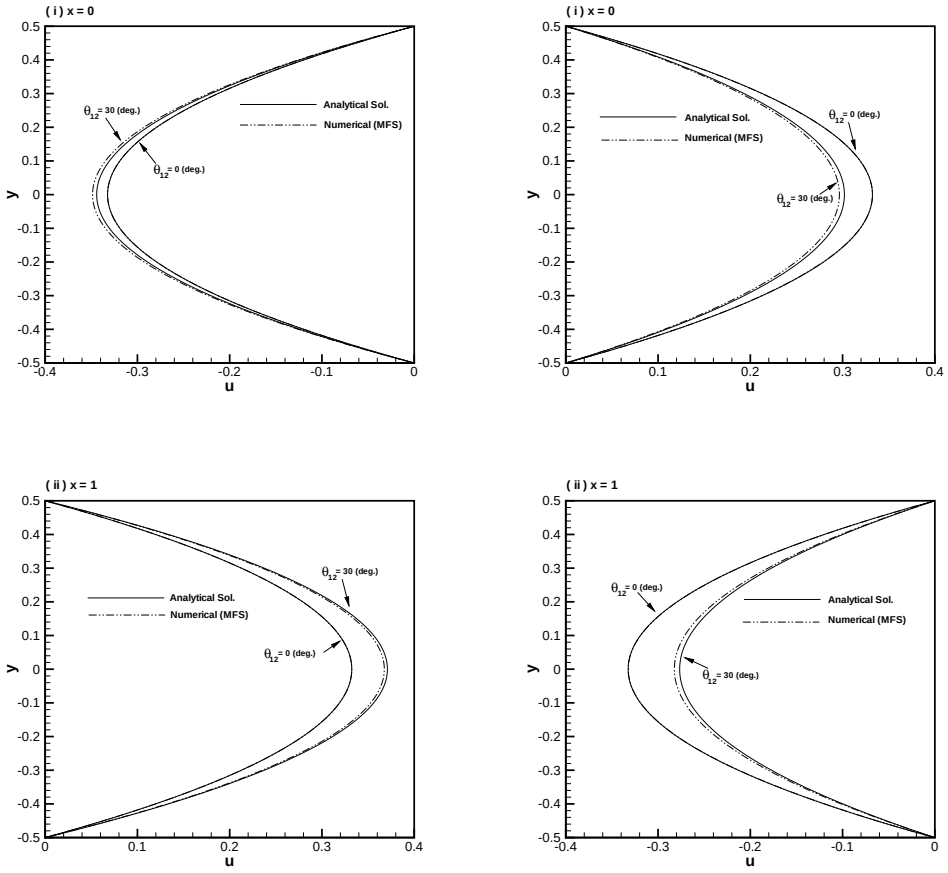

(c) Compression at t = $T/4$

(d) Expansion at t = $3T/4$

Figure 4.20: Comparison of the analytical solution and the meshfree calculations for the (u-y) velocity profiles at $\theta_{12} = 0°$ and $30°$ during compression and expansion: (i) $x = 0$ and (ii) $x = 1$.

slight phase lags between contractions motion protocols. This phase lag has shown to be the key parameter of this study as it will be discussed in the following subsection.

4.5.4 Net Flow Induced by Channel Upper Wall Contractions

The effect of the phase lag and collapsing amplitude parameters on the flow transport within this channel system are given in details in this part. Results presented inhere are dedicated to show the

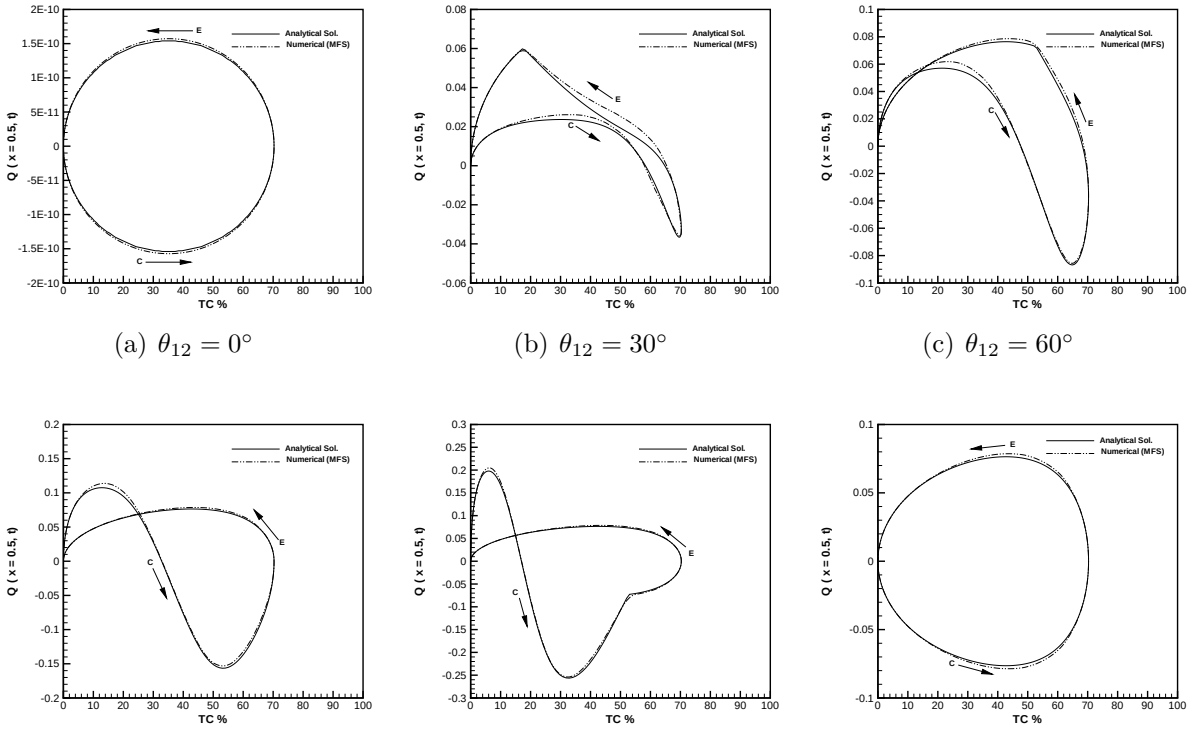

(a) $\theta_{12} = 0°$ (b) $\theta_{12} = 30°$ (c) $\theta_{12} = 60°$

(d) $\theta_{12} = 90°$ (e) $\theta_{12} = 120°$ (f) $\theta_{12} = 180°$

Figure 4.21: Comparison of the analytical solution and the meshfree computations for the instantaneous volumetric flow rate $Q(x = 0.5, t)$ monitored at the middle of the channel, versus the instantaneous travel collapse (TC) parameter for various phase lags.

possibility of using this simple channel setup as described previously as a pumping mechanism at the microscale flow regime. The minimum requirements needed for producing a unidirectional flow without imposing any pressure drop are found and explained in details. Results are validated and confirmed by using meshfree computations.

Firstly, we show the effect of phase lags θ_{12} which is governed by $g_1(t)$ and $g_2(t)$ kinematical functions on the instantaneous volumetric flow rate $Q(x, t)$. The volumetric flow rate is recorded over a complete collapsing cycle and for various values of phase lags. Ideally, each wall collapse cycle is composed of two main phases, the first one is compression phase (C), where the contraction moves until it reaches the maximum allowable travel distance. The second phase is an expansion phase (E), where the wall contraction expands back to the initial wall position as marked on the

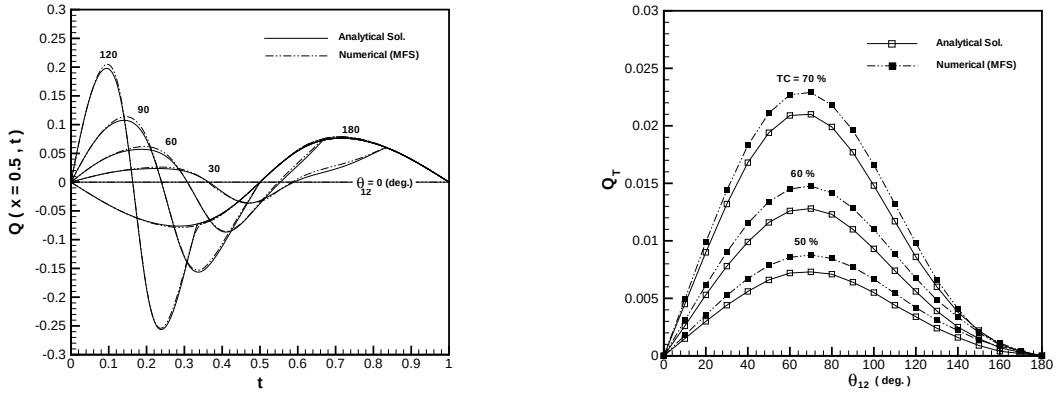

(a) Instantaneous flow rate

(b) Time averaged net flow

Figure 4.22: Comparison of the analytical solution and the meshfree computations for the instantanous and time averaged net flow rates over a single contraction cycle: (a) $Q(x = 0.5, t)$ versus t for various values of θ_{12}, (b) Q_T versus θ_{12} for different collapse ratios, TC (%).

figures. In these results, the maximum travel collapse distance $TC(t) = (1 - Min(H(x,t)))\%$ is chosen to be $TC = 70\%$ of the original channel width W. In other words, the contractions are allowed to move until they reach 70% of the nominal channel width. In Fig.4.21 (a-f), the volumetric flow rate $Q(x,t)$ monitored at $x = 0.5$ during a complete contraction-expansion cycle versus the percentage travel contraction $TC\%$ distance at different values of the phase lag parameter θ_{12} is given. Results from both analytical and MFS computations have shown that, in case of using a phase lag value equal to $\theta_{12} = 0^\circ$ or 180°, the contraction cycle takes the shape of a pure circle, the volumetric flow rate is completely symmetric, and there will be no net flow produced as shown in Fig.4.21(a). Unlike the other investigated cases, when the phase lag between two contractions is not zero, the contraction-expansion cycle will take various asymmetric dynamical shapes, which depend on the value of the phase lag assigned, see examples shown in Figs.4.21 (b-f). These symmetric and asymmetry dynamical shapes can also be viewed by plotting the volumetric flow rate versus the instantaneous collapsing time rather than using the collapsing ratio TC. Results have shown that, if $\theta_{12} \neq \{0^\circ, 180^\circ\}$, the volumetric flow rate distribution is not symmetric in time as shown in Fig.4.22 (a). In these situations, the time-average volumetric flow rate is not zero and

a unidirectional net flow is produced. The time-average volumetric flow rate Q_T can be calculated by simply integrating the instance flow rate over a complete cycle as

$$Q_T(x) = \frac{1}{T}\int_0^T Q(x,t)dt \tag{4.56}$$

where, $T = 1/S_t$ is the time period. The time averaged flow rate as a function of the phase lag at different values of the maximum allowable travel collapse distance $TC = 50, 60, 70\%$ is given in Fig.4.22(b). Results have shown that, as the phase lag between contractions motions increases, the time averaged net flow is increase until it reach an optimum value of about $\theta_{opt} = 70^\circ$, afterwards the net flow starts to decay and there will be no net flow produced when $\theta_{12} = 180^\circ$. Moreover, as the contraction travel distance increase, the net flow increases dramatically. The optimum value of motion phase lag θ_{opt} which maximize the net flow is independent from the collapsing amplitude TC.

Although, there is a good agreement between results obtained analytically and by using Stokeslets-meshfree computations when evaluating the instantaneous volumetric flow rate as shown in Fig.4.21 and Fig. 4.22 (a). However, the time averaged net flow calculations have shown significant differences between the analytical and numerical results. For example, the MFS overestimates the time averaged net flow when compared with the analytical counterpart. However, both methods predicts the same optimum value of the motion phase lag θ_{opt} Fig. 4.22 (b). This differences in calculating the time averaged net flows may be due to fact that: The meshfree calculations are done exactly for stokes flow where $Re = 0$, unlike the theoretical analysis is given for a finite Reynolds number with $Re = \delta$, with ($\delta = W/L << 1$). As a summary, the theoretical and meshfree results presented inhere lead us to propose the following hypothesis: by using a non-elastic channel with at least two local wall contractions that moves with a slight phase lag with respect to each other, a net flow is produced and the system can be used as a simple pumping mechanism in the microscale flow regime.

Chapter 5

Selective Pumping in an Insect Tracheal-Like Network with Multiple Contractions

This chapter presents a new paradigm for selectively pumping and controlling fluids at the microscale in a complex network of channels, which we call "selective-pumping-in-a-network." The approach is inspired by internal flow distributions induced by rhythmic wall contraction phenomena in insect tracheal networks. The selective pumping concept presented enables fluids to be transported, controlled and directed into specific branches in networks while avoiding other possible branching routes, without the use of any mechanical valves. The results presented here might help guide efforts to fabricate novel microfluidic devices with improved efficiency for mixing purposes and targeted drug delivery applications.

5.1 Selective-Pumping-in-a-Network

Selective pumping protocol in a network of channels is given as a natural extension to our bioinspired pumping models that have been derived previously in chapter 2 and validated numerically in chapter

4. The ability of transporting and manipulating fluids as well as controlling its directionality in a network of channels by using wall contractions are termed here as a "selective-pumping-in-a-network." The approach relies on using a set of multiple, localized and non-propagative wall contractions located at different spots along the network segmental walls. These contractions are set to move with or without synchronized phase (time) lags with respect to each other. The selective pumping idea presented here is inspired mainly by respiratory systems in insects, in particular the rhythmic wall contractions found in their tracheal tubes.

Transporting small amount of fluids within network of channels by using an efficient means is a challenging problem and of importance in many of scientific applications. For example, microfluidic devices are normally composed of multiple branches that usually used for mixing purposes, cell manipulations, drug delivery and several other. These applications are normally done via transporting microliters amount of fluid from one site to another in a controlled and directional manner. Generally, there are two main techniques that are currently used to transport fluid at the microscale regime. The first technique uses the conventional pressure-driven flow, which is not recommended whenever the geometry becomes very small. This is because of, an excessive amount of pressure drop is required to overcome the emerging surface forces, which become extremely large as the device geometry become smaller and smaller. The second technique includes several valveless mechanisms such as, impedance mismatch, peristaltic and electro-osmotic pumps. Normally, these valveless pumping techniques are preferred over the pressure-driven methods, since they have the advantage of requiring fewer moving parts and therefore lower maintenance.

Although, these valveless pumping mechanisms are commercially available, they still might suffer from some functional drawbacks. For instance, the electroosmotic pumping requires the use of patching and doping of electrodes along the tube wall. Moreover, it is known that the peristaltic pumping and other valveless pumping techniques rely on wave dynamics induced by elasticity of the tube wall, which is difficult to manufacture an entire elastic microfluidic device with the current microfabrication techniques. Therefore, research efforts that seek a novel techniques for transporting fluids at the microscales are considered to be of importance. For instance, researches in the field of bioinspiration and biomimetics which are increasingly multi-disciplinary field that seeks to imitate systems and processes from life sciences to design improved engineering devices,

are one of potential routes that might lead to find a novel transporting and manipulating fluids at the micro and nano scale flow regime.

In this chapter, inspired by respiratory systems in insects, in particular the non-propagative, rhythmic wall contractions found in insect tracheal tubes, we propose a bioinspired, non-peristaltic new paradigm for selective-pumping-in-a-network of channels. This model is expected to work at different scales and particularly well in the low Reynolds number flow regime. This proposed selective pumping paradigm might leads for proper flow transport, manipulations, and directive control of fluids on a chip of multiple network of channels. Therefore, the present study is expected to yield useful results that can serve as valveless type of selective pumping mechanism for novel biomimetic microfluidic devices. It should be mentioned that, the progress in the microfabrication techniques can make this study feasible to be built. For instance, the multilayer soft lithography (MSL) techniques Pandolfi and Ortiz (2007) can be easily used to fabricate a tracheal tube with flexible membrane at the desired contraction regions within a complex network of channels to test our new insect-inspired selective-pumping-in-a-chip paradigm.

5.1.1 Insect Tracheal Network and Rhythmic Wall Contractions

In order to show the importance of insect respiration process to the present study conducted in this dissertation. A brief introduction about the insects respiratory system was given in Chapter 1 in a separate section 1.2.1. In this part, we will focus only on the tracheal network, which consists of main tubes that eventually branches into smaller tubes known as tracheoles and their rhythmic collapsing patterns. These rhythmic tracheal wall motions are believed to be the main driving mechanism for transporting the airflow within the tracheal network,Westneat et al. (2003). More details about the structure of the insect respiratory system can be found in Harrison (2003b,a); Nation (2008).

To promote the present study we use insects tracheal network as our inspiration pumping model. An image that shows the complexity of a real tracheal network of a Carabid beetle insect is given in Fig. 5.1. The image was experimented by using x-rays techniques by Westneat et al. (2003); Socha et al. (2008) and shows also schematically the locations of multiple contractions along the

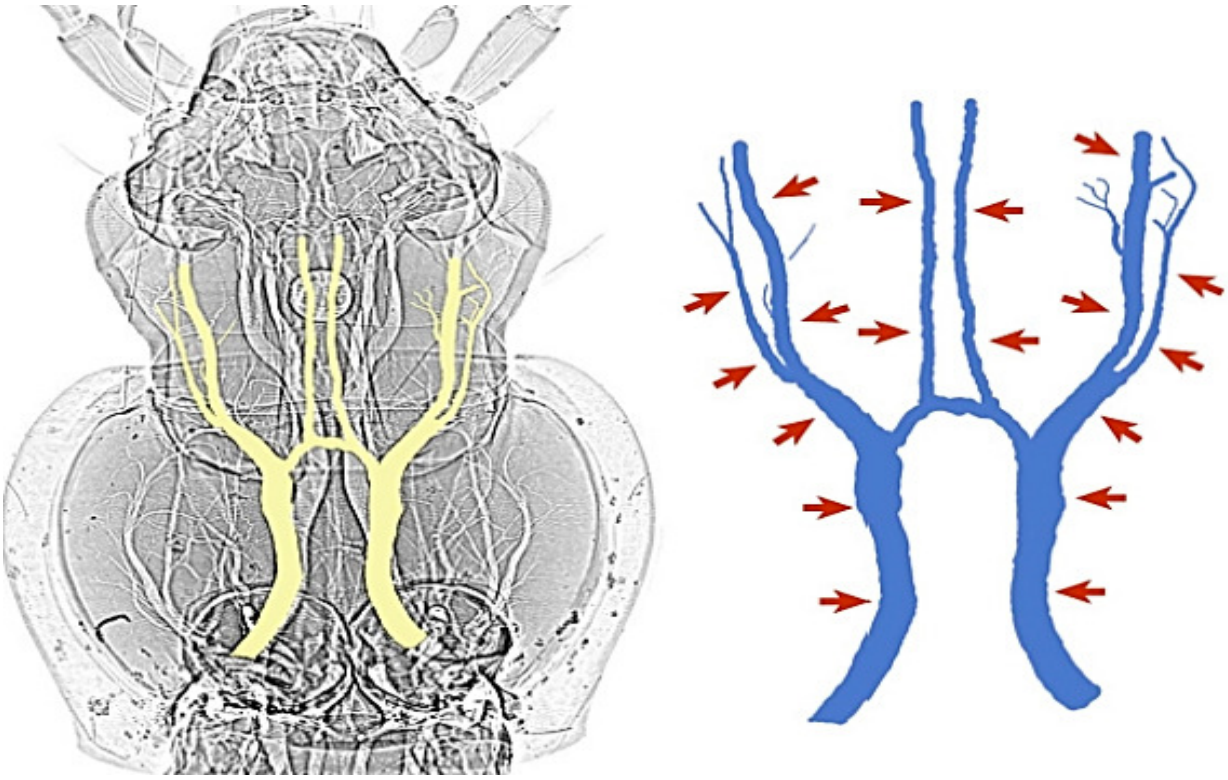

Figure 5.1: Left:X-ray image of the tracheal system of the carabid beetle, Right: Schematic has arrows to indicate the locations of the rhythmic tracheal compressions. This image is a courtesy of EFRI-2010 research group in Virginia Polytechnic Institute and State University and published after permission.

tracheal network branching walls.

In this dissertation, inspired by the above mentioned insects respiratory system and their rhythmic tracheal compression phenomena as a natural pumping mechanism. We study the induced flow motions by moving wall contractions in an insect-like branching network of channels. The contractions are set to move with various phase lags with respect to each other. The goal is to find a proper collapsing protocol that can support the idea of our new selective pumping paradigm 5.1 and use it to control the flow directionality in a network of branching channels. The network problem formulation, channel wall contraction moving protocol and the numerical methods used for solving the internal induced flow motions in this network will be given in the subsequent sections.

5.1.2 Insect-Like Tracheal Network Problem Formulation

Consider the motion of a 2-D incompressible viscous flow inside an insect-like tracheal network of channels similar to the one shown in Fig. 5.1. Each branching segment of the network have a finite length L_i and width W_i, where the subscript i is refereed to each branch number. We define the network segment aspect ratio as $1/\delta_i$ which is assumed to be very large i.e., $\delta_i = W_i/L_i << 1$. Each channel has assigned a single or multiples of moving localized contractions from the side walls $H_s(x,t), s = 1, 2$, where the subscript s is refereed to each branch side wall as shown in Fig. 5.2 (b). In this study, we restrict our attention in studying the induced flow pumping by moving wall actions only. Therefore, a zero pressure drop $\Delta p = 0$ is assumed along each branch inlet/outlet port.

The kinematics and geometry of each wall contraction are governed by a generic wall profile $H_s(x,t), s = 1, 2$ which is assigned to each channel branch side wall. This wall profile allows each contraction to move independently along the lateral direction with or without a phase lag with respect to each other as shown in Fig. 5.2 (a). Furthermore, a maximum of three contractions that move with phase lags θ_{12} and θ_{23} can be activated and move according to the motion protocol prescribed by temporal functions $g_i(t)$ of $H_s(x,t)$, Fig. 5.2 (a). The details of side wall profile is given in the following subsection 5.1.3.

5.1.3 Network Side Wall Contraction Profile

The mathematical model that describes the kinematics and the shape of wall contractions in each branching channel can be given as

$$H_s(x,t) = \frac{1}{2} + \sum_{i=1}^{N_c} A_i f_i(x) g_i(t) \tag{5.1}$$

where, the subscript s is refereed to each branch side wall, $f_i(x) \in C^r\,[0, L_i]$ and $g_i(t) \in C^r\,[0, T = 1/S_t]$ represent the spatial and the temporal distribution of the wall shape respectively. N_c defines the number of contractions, and A_i is the amplitude assigned to each contraction. The spatial form of

the above equation imitates the geometry of the wall contractions and is given as

$$f_i(x) = \tanh(\alpha(x - x_i)) - \tanh(\alpha(x - (x_i + d_i))) \tag{5.2}$$

where $\alpha = 2\pi/\delta_i$, x_i defines the beginning of each collapse region and $d_i \in (0, 1 - x_i]$ marks its end. In other words, we exactly follow our terminology given previously in chapter 2, section 2.2.

In this part, a maximum of three contractions will be considered, i.e., $N_c = 3$ where, the first contraction moves in time according to the following profile

$$g_1(t) = \begin{cases} \frac{1}{2}\left(1 - \cos(2\pi\beta S_t t)\right), & 0 \le t \le 1/\beta S_t \\ 0 & 1/\beta S_t < t \le 1/S_t \end{cases} \tag{5.3}$$

while the second contraction moves according to

$$g_2(t) = \begin{cases} \frac{1}{2}\left(1 - \cos(2\pi\gamma S_t t)\right), & 0 \le t \le 1/\gamma S_t \\ 0 & 1/\gamma S_t < t \le 1/S_t \end{cases} \tag{5.4}$$

and the third contraction act as a reference motion profile and is given by

$$g_3(t) = \frac{1}{2}\left(1 - \cos(2\pi S_t t)\right), 0 \le t \le 1/S_t \tag{5.5}$$

where the non-dimensional parameters $\beta\&\gamma$ are related to the phase lags between the first second and the third contractions according to the assigned motion protocol shown in Fig. 5.2 (a), which can be explained as follows.

Initially, during the compression phase we let the three contractions begin to move together. However, the first and second contractions are forced to reach the maximum specified travel collapse (TC) distance faster than the reference or the third contraction. In other words, there will be a time lags $T_{13} = (1 - 1/\beta)/(2S_t)$ between the first and third collapsing motion which is equal to a phase lag $\theta_{13} = \pi(1 - 1/\beta)$. Similarly, the time lag between the second and the third collapse is defined by $T_{23} = (1 - 1/\gamma)/(2S_t)$ which is equivalent to a phase lag $\theta_{23} = \pi(1 - 1/\gamma)$. Moreover,

during the expansion phase, the first and second contractions return back to their nominal original positions and continue their periods with zero amplitude until the third contraction completes its own cycle. Then, all the three contractions start the second cycle together with the protocol shown in Fig.5.2 (a). It should be noted that all contractions have same time period $T = 1/S_t$, and that if $\beta = 1$ and $\gamma = 1$, there will be no phase lags and all the three contractions will move in the same manner in time.

This proposed wall motion protocol guarantees that, after one contraction cycle, all the channels geometry will be returning back to their initial positions and there will be no net flow due to any volume deformations. It should be noted that, the segmental channel wall profile $H_s(x,t)$ and its kinematics prescribed by the local wall contractions motion protocol $g_i(t)$ plays the most important role in this study. For instance, by tuning the timing or phase lags θ_{13} , θ_{23} between the wall contractions motions, a net flow is produced and the network acts as a micropuming system. Moreover, phase lag parameters can be carefully adjusted to induce selective pumping effect. Once again, we mean by selective pumping, is to be able to control the flow directionality and force the fluid elements to run through a specific branch and ignore other branching routes.

In order to show the selective-pumping-in-a-network working principle at the microscale, the velocity field, pressures, and net flow induced by the prescribed wall contractions are calculated numerically by integrating Stokes equations using the method of fundamental solutions (MFS). More specifically, the Stokeslets-meshfree method are used here to solve the Stokes equations that govern the flow motions within network branches with moving wall contractions as given in the next section 5.2.

5.2 Stokeslets-Meshfree Network Simulations

In this part, we use the regularized Stokeslets computational approach developed by Cortez (2001) to solve the flow field in a network of channels with moving wall contractions as explained in the problem formulation section 5.1.2. This numerical approach is based on the method of fundamental solutions MFS for the Stokes equations, which uses a set of regularized expressions of the Stokeslets force elements Cortez (2001), Cortez et al. (2005) and Ainley et al. (2008).

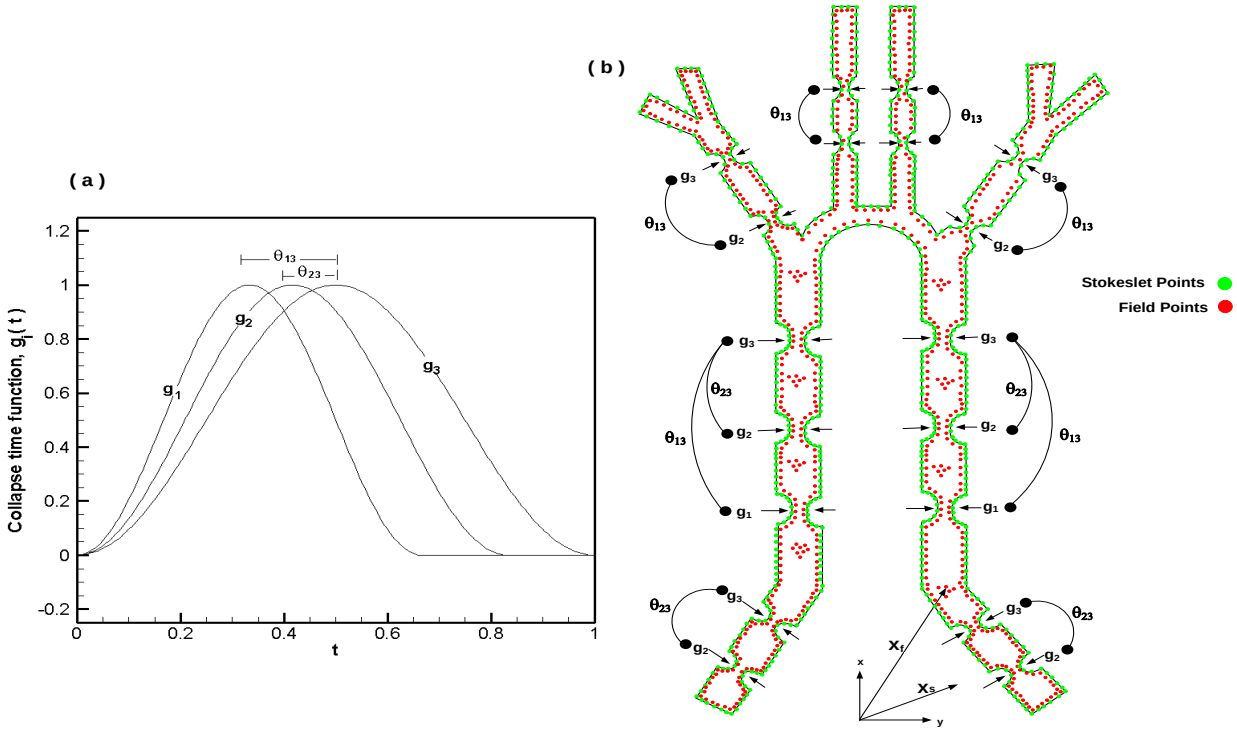

Figure 5.2: The Problem formulation: (a) collapsing function motion protocol,(b)schematic to a simplified insect physiological network with multiple collapse indicated by arrows.

Now, consider the network problem formulation stated in section 5.1.2. Based on the lubrication theory and the quasi-steady approximations, the governing equations that describe this particular flow motion are the Stokes equations,

$$\nabla^* \cdot \mathbf{V}^* = 0 \tag{5.6}$$

$$\mu \triangle^* \mathbf{V}^* = \nabla^* p^* - \mathbf{F}^* \tag{5.7}$$

where, μ is the fluid viscosity , p^* is the pressure, $\mathbf{V}^*$ is the velocity, and $\mathbf{F}^*$ is the force per unit volume.

A fundamental solution to the above equations is called a Stokeslet, which is characterized by the velocity field induced by a concentrated external point force having a specific intensity acting on the fluid at a certain location. Because of the linearity in the governing equations, the superposition principle can be imposed and a total flow field can be obtained by taking the effect from all point

forces acting on the fluid under considerations. A standard Stokeslet expression based on the Dirac delta distribution for the force intensity in two dimensional Stokes flow regime can be found in Cortez (2001),

$$\mathbf{V}^*(\mathbf{x}^*) = \frac{1}{4\pi\mu}\left[-\mathbf{q}^*\left(\ln(A^*) + B^*\right) + \left[\mathbf{q}^* \cdot (\mathbf{x}^* - \mathbf{x}_s^*)\right](\mathbf{x}^* - \mathbf{x}_s^*)\, C^*\right] \tag{5.8}$$

$$p^*(\mathbf{x}^*) = \frac{D^*}{2\pi}\left[\mathbf{q}^* \cdot (\mathbf{x}^* - \mathbf{x}_s^*)\right] \tag{5.9}$$

where, $\mathbf{V}^* = (u^*, v^*, 0)$, p^* are the velocity field and static pressure induced by a point force. $\mathbf{q}^* = q_x^*\mathbf{i} + q_y^*\mathbf{j}$ is a concentrated point force per unit length. A, B, C, and D, are coefficients to be calculated in terms of r^*, where $r^* = \mid \mathbf{x}^* - \mathbf{x}_s^* \mid$ is the distance between any field point located at $\mathbf{x}^*$ and a source (Stokeslet) point at $\mathbf{x}_s^*$. Now, if we use the same non-dimensional parameters defined in section 2.2.2, i.e., let $x = x^*/L$, $y = y^*/L$, $r = r^*/L$, $u = u^*/u_o$, $v = v^*/u_o$, $p = p^*L/(\mu u_o)$, $q_x = q_x^*/(\mu u_o)$, $q_y = q_y^*/(\mu u_o)$, $A = A^*/L$, $B = B^*$, $C = C^*L^2$ $D = D^*L^2$. Therefore, the above equations can be re-written in a non-dimensional form,

$$u(x,y) = \frac{1}{4\pi}\left[q_x\left(-\ln(A) + B + (x - x_s)^2\, C\right) + q_y\left((x - x_s)(y - y_s)\, C\right)\right] \tag{5.10}$$

$$v(x,y) = \frac{1}{4\pi}\left[q_x\left((x - x_s)(y - y_s)\, C\right) + q_y\left(-\ln(A) + B + (y - y_s)^2\, C\right)\right] \tag{5.11}$$

$$p(x,y) = \frac{D}{2\pi}\left[q_x(x - x_s) + q_y(y - y_s)\right] \tag{5.12}$$

where,
$A = \epsilon + \sqrt{r^2 + \epsilon^2}$, $B = \frac{\epsilon\left(2\epsilon + \sqrt{r^2+\epsilon^2}\right)}{\left(\epsilon + \sqrt{r^2+\epsilon^2}\right)\left(\sqrt{r^2+\epsilon^2}\right)} = \frac{\epsilon(A+\epsilon)}{A(A-\epsilon)}$, $C = \frac{2\epsilon + \sqrt{r^2+\epsilon^2}}{\left(\epsilon + \sqrt{r^2+\epsilon^2}\right)^2\left(\sqrt{r^2+\epsilon^2}\right)} = \frac{(A+\epsilon)}{A^2(A-\epsilon)}$, $D = \frac{\left(r^2+2\epsilon^2\right)+\epsilon(A-\epsilon)}{A(A-\epsilon)^3}$, $r = \sqrt{(x - x_s) + \delta^2(y - y_s)}$, ϵ is the regularization parameter, more details are given in Cortez (2001). In the MFS technique, the total solution is formed by the superposition of all bases represented by the Stokeslets expressions with unknown intensities or strengths as given above. The strength of the Stokeslet singularities is then obtained by enforcing the fundamental solutions to satisfy a set of prescribed boundary conditions by direct collocation methods Young

et al. (2006).

Now, consider the problem under consideration with the prescribed boundary conditions as shown in Fig. 1(b). Let's distribute N- source points of regularized Stokeslets forces with unknown strength $\mathbf{q}$ vectors collocated at the network boundary. The flow field can be then approximated by superposition the effect from all the Stokeslets and the velocity field can be evaluated as,

$$u(x_i, y_i) = \frac{1}{4\pi} \sum_{j=1}^{N} \left[q_{xj} \left(-\ln\left(A_{ij}\right) + B_{ij} + \left(x_i - x_{sj}\right)^2 C_{ij} \right) + q_{yj} \left(\left(x_i - x_{sj}\right) \left(y_i - y_{sj}\right) C_{ij} \right) \right] \quad (5.13)$$

$$v\left(x_i, y_i\right) = \frac{1}{4\pi} \sum_{j=1}^{N} \left[q_{xj} \left(\left(x_i - x_{sj}\right) \left(y_i - y_{sj}\right) Cij \right) + q_{yj} \left(-\ln\left(A_{ij}\right) + B_{ij} + \left(y_i - y_{sj}\right)^2 C_{ij} \right) \right] \quad (5.14)$$

$$p\left(x_i, y_i\right) = \frac{1}{2\pi} \sum_{j=1}^{N} \left[q_{xj} D_{ij} \left(x_i - x_{sj}\right) + q_{yj} M_{ij} \left(y_i - y_{sj}\right) \right] \quad (5.15)$$

where,
$A_{ij} = \epsilon + \sqrt{r_{ij}^2 + \epsilon^2}$, $B_{ij} = \frac{\epsilon(A_{ij}+\epsilon)}{A_{ij}(A_{ij}-\epsilon)}$, $C_{ij} = \frac{(A_{ij}+\epsilon)}{{A_{ij}}^2(A_{ij}-\epsilon)}$, $D_{ij} = \frac{\left(r_{ij}^2+2\epsilon^2\right)+\epsilon(A_{ij}-\epsilon)}{A_{ij}(A_{ij}-\epsilon)^3}$, and q_{xj} and q_{yj} are the unknown coefficients that represent the strengths of the Stokeslets in x and y-directions respectively. $\mathbf{x}_i = (x_i, y_i)$ is the position of any field point including the boundary points. $\mathbf{x}_{sj} = (x_{sj}, y_{sj})$ is the location of the Stokeslets source points. $r_{ij} = |\mathbf{x}_i - \mathbf{x}_{sj}| = \sqrt{\left(x_i - x_{sj}\right) + \delta^2 \left(y_i - y_{sj}\right)}$ is the distance between any field point and another source point.

In order to determine the unknown coefficients $\mathbf{q} = (q_{xj}, q_{yj})$, the boundary conditions for the velocity components and pressure are imposed and collocated at certain field points on the network boundary as shown Fig.5.2 (b). Adding each fundamental solution to the Stokes Eqs. (5.13-5.15), the final induced solution can be obtained by solving an emerging system of equations

$$\mathbb{A}\mathbf{q} = \mathbf{b} \quad (5.16)$$

where $\mathbb{A}$ is a matrix of size $2N$ X $2N$ with real entries formed by evaluating the right hand side of the above expressions in Eqs. (5.13 - 5.15). $\mathbf{b}$ is a vector of size 1 X $2N$ of real entries formed

by evaluating the left hand side of the same equations. In other words, all the entries in both $\mathbb{A}$ and $\mathbf{b}$ are filled by enforcing the fundamental solutions to satisfy the boundary conditions by direct collocation. $\mathbf{q}$ represent the Stokeslets strength coefficients which to be determined by solving the above system of equations as given in details in the subsection 4.5.2.

It should be mentioned here that, although the MFS is relatively easy to implement and does not require any grids, it still suffers from some issues related to the non-invertible or ill-conditioned matrix problem associated with finding the unknown force strengths when implementing the Stokeslets as fundamental solutions Alves and Silvestre (2004) and Young et al. (2005). This linear algebra matrix problem can lead to inaccurate strengths and consequently wrong flow field. A solution to non-invertible matrix problem is found by either collocating the Stokeslets sources a distance away from the domain boundaries as given in Young et al. (2006) or by using regularized Stokeslets expressions as derived by Cortez (2001). A smoothing to the ill-conditioning matrix problem is also introduced by iteratively choosing the Stokeslets positions as shown in Young et al. (2006) or by optimizing the regularization parameter as in Cortez (2001). However, still the ill-conditioning matrix issue represents a challenging problem for the MFS to be correctly implemented.

In our simulations, we chose to use the regularized Stokeslets approach developed by Cortez (2001) in addition to the algorithm given in Table 4.4 to overcome the ill-conditioning matrix problem and be able to calculate accurate Stokeslets strengths. This numerical method have been tested over several benchmark cases and are used inhere to simulate the induced flow in a branching tracheal-like network of channels subjected to moving wall contractions, see next section 5.3. Several cases are simulated, however we only present three main cases that confirm our selective-pumping-in-a-network hypotheses explained in section 5.1.

5.3 Results and Discussions

Results that show the selective-pumping-in-a-network working principle are given in this section in details. The presented results are given to support the selective pumping idea and clearly show the ability of manipulating and controlling the flow directionality in an insect-like network of channels. Three simulation cases that we believe of their importance in delivering the selective pumping

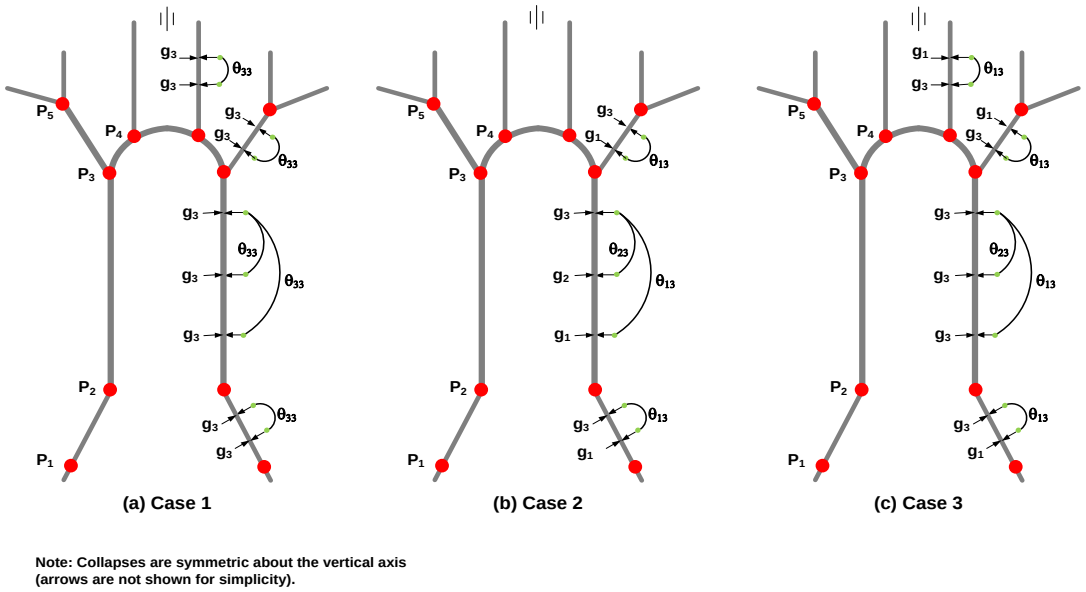

Figure 5.3: Schematic that shows the collapsing functional motion protocol assigned to specific branches to test the idea of selective pumping in an insect-like tracheal network of channels:
(a) Case 1: No net flow benchmark scenario
(b) Case 2: Net flow induced through $P_3 - P_5$ branch only
(c) Case 3: Net flow induced through $P_3 - P_4$ branch only.

approach will be given in the following subsections. In the first case of study, all the contraction sites are set to move with the same collapsing profile namely, the reference function $g_3 t$, which is given by Eq. 5.5. In other words, there will be no phase lag between the motions of the three contractions. In the second case of study, the contractions along the network are activated and set to move with a specific non-zero phase lags with respect to each other. This second case is characterized by inducing a net flow in the $P_3 - P_5$ branch only. Lastly, the motions of the wall contractions are then tuned and adjusted in third case of study to induce a net flow the $P_3 - P_4$ branch only. A schematic that shows the three cases of study along with their motion protocols is given in Fig. 5.3. The details of each case of study will be given in following subsections.

5.3.1 Case 1: No-Pumping Baseline Study

Consider the network of channels explained in section 5.1.2 with moving wall contractions in each branch. Let's consider two contractions along the lower segment in the network termed by $P_1 - P_2$ route. While, the middle segment $P_2 - P_3$ has assigned three contraction sites. The branch channel $P_3 - P_5$ will have two collapsing regions as shown in Fig. 5.3 (a). Finally, the segment that starts at P_4 will also have two contractions. In this case of study, all the contraction sites are set to move with the same collapsing profile namely, the reference function $g_3 t$, which is given by Eq. 5.5 and shown in Fig. 5.2 (a). In other words, there will be no phase lags between the motions of the three contractions.

This case of study is selected to be presented at the beginning for several reasons. Firstly, to validate and confirm our pumping hypothesis given previously in chapter 2, which indicates that, wall contractions must move with non-zero phase lags in order to produce a unidirectional net flow. Secondly, to serve as benchmark or baseline case of study the next selective pumping case of studies. The details of the first case of study is given as next.

A. Induced Flow Field

In this part, the velocity field and pressure induced by the movements of the wall contraction protocol assigned to the first case of study as shown in Fig. 5.3 (a) are given in details. Several plots are given to the show the flow filed developments and structures during compression and expansion time snapshots times. For instance, In Fig. 5.4, we show the contour lines for the pressure and the velocity components during the compression phase at instant of time $t = T/4$ and at zero phase lag i.e., $\theta_{12} = 0°$. Results have shown that, as the wall contractions undergo compression phase and start to move toward the mid-plane line, high pressure with adverse and favourable gradients are formed near and underneath these compression regions as shown in Fig. 5.4 (a). As a results, the axial velocity component increases near the contraction regions and the flow is displaced, bifurcated, and exit the network from all inlet/outlet ports as shown in Fig. 5.4 (b). The contour lines for the vertical velocity component are also shown and are characterized by two regions with opposite direction underneath each contraction as shown in Fig. 5.4 (c).

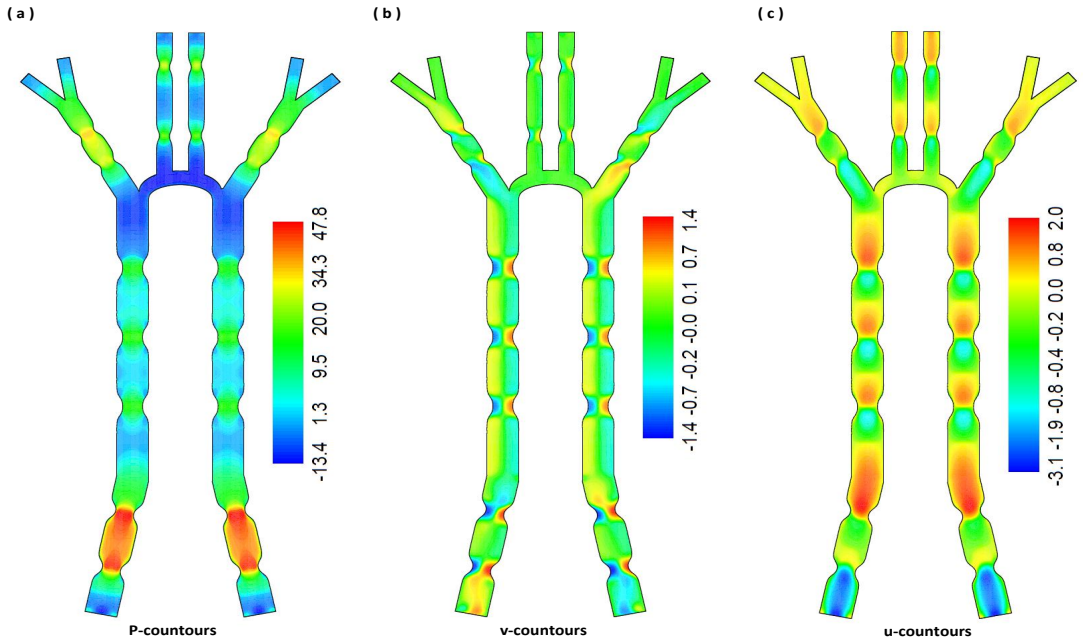

Figure 5.4: Case 1: flow field contour lines at t = T/4, (a) pressure, (b) axial velocity (c) vertical velocity.

Similarly, snapshots that show the flow field during the expansion phase at time $t = 3T/4$ are shown in Fig. 5.5. When the contraction regions expand back away (i.e., in the expansion phase), exactly a similar flow field structure is developed but with an opposite signs for the pressure, axial and the vertical velocity components as shown in Fig. 5.5 (a-c). It is worthwhile to mention here that, when the wall contractions move with zero phase lags $\theta_{13} = 0^\circ$ and $\theta_{23} = 0^\circ$, the flow behaviour during compression and expansion phases is identically the same but with opposite signs. In other words, there is a complete symmetry behaviour during compression and expansion motions whenever $\theta_{13} = 0^\circ$ and $\theta_{23} = 0^\circ$.

To better understand the flow field induced by the motions of the network wall contractions, we show line plots for the velocity components along the vertical direction at different locations along the network axial direction. For example, in Fig. 5.6 (a & b), we show the axial velocity profiles across each segmental width W_i and at different axial locations $x_i = 1, 2, ...7$ as listed in Table 5.1 during both compression $t = T/4$ and expansion $t = 3T/4$ snapshots of times. No surprising, the velocity profiles attain the standard parabolic flow away from any contraction regions and is nearly

Table 5.1: Locations used along the network for velocity profile plots

Position:	x_1	x_2	x_3	x_4	x_5	x_6	x_7
x	0.1	5.0	10.0	15.0	15.8	21.1	18.15
y	-2.5	-1.5	-1.50	-1.50	-0.50	-0.50	-3.350

parabolic as we move closer to contraction spots as shown in 5.7. Furthermore, the vertical velocity component is also given at the same axial locations along the network. The profiles are consistence and very similar to results given by the single channel pumping model derived previously in chapter 2 and shown in Fig. 2.9. It should be noted that, velocity profiles during the expansion snapshot time $t = 3T/4$ is identically the same as profiles at compression time $t = T/4$, which again shows the flow symmetry behaviour during both compression and expansion times.

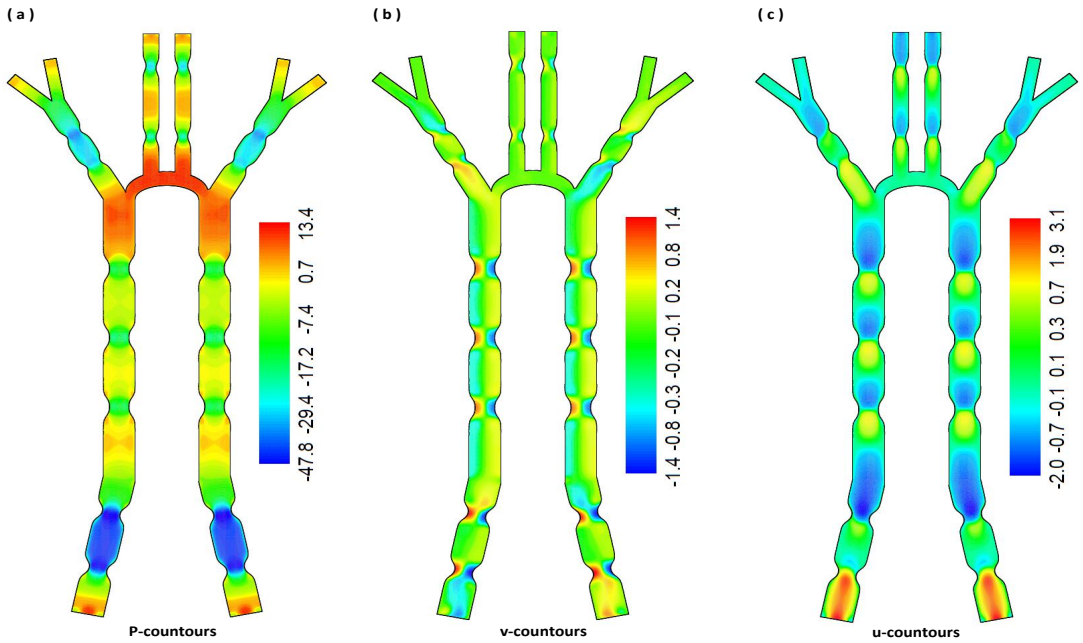

Figure 5.5: Case 1: flow field contour lines at t = 3T/4, (a) pressure, (b) axial velocity (c) vertical velocity.

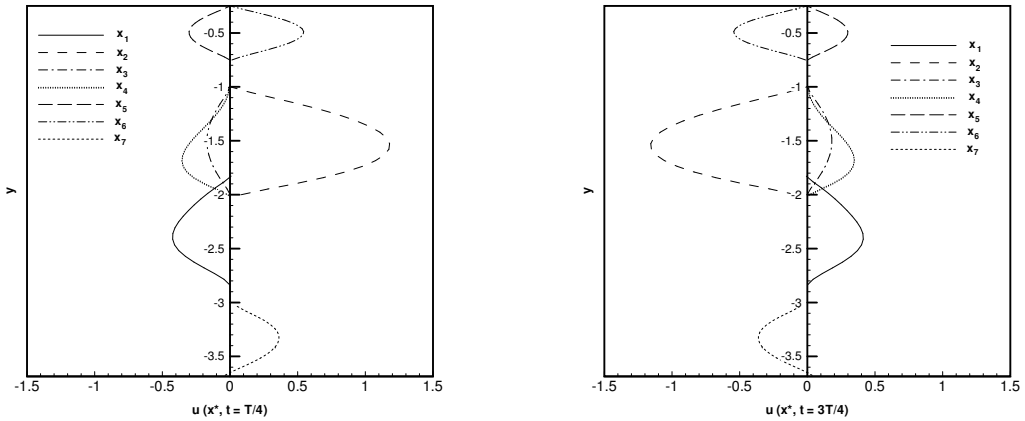

(a) $t = T/4$ (b) $t = 3T/4$

Figure 5.7: Case 1: axial velocity profiles along the vertical directions (u-y) plane at different x-locations across the network during compression and expansion snapshots

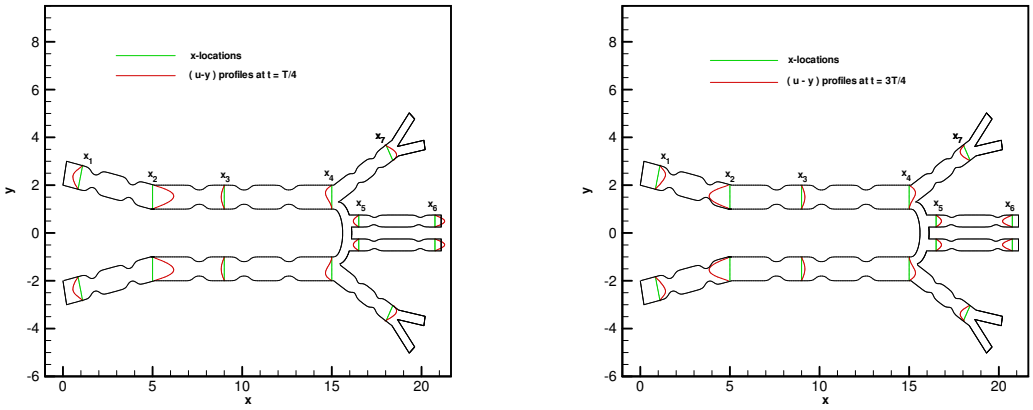

(a) $t = T/4$ (b) $t = 3T/4$

Figure 5.6: Case 1: axial-velocity profiles at different locations across the network at two time snapshots

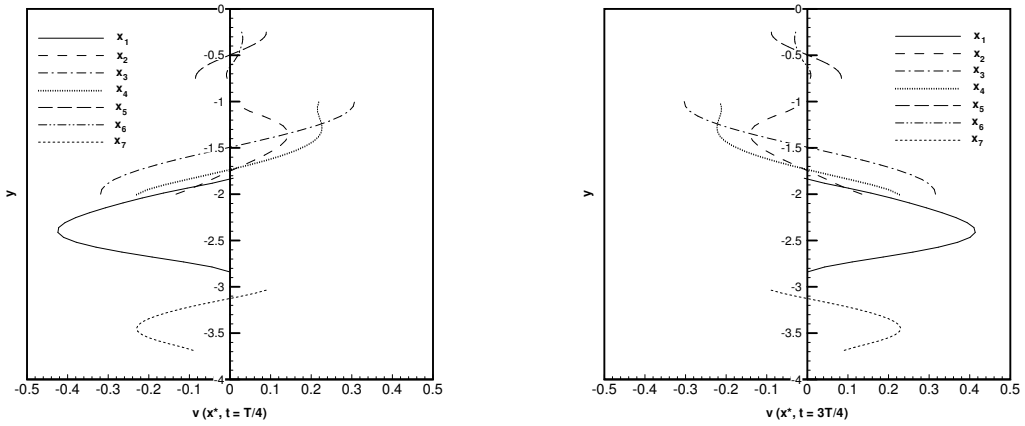

(a) $t = T/4$ (b) $t = 3T/4$

Figure 5.8: Case 1: vertical velocity profiles along the vertical directions (v-y) plane at different x-locations across the network during compression and expansion snapshots

B. time averaged Quantities

The time averaged quantities are important to understand the flow behaviour in the network after a complete collapsing cycle. In this part, we monitor the velocity components and pressure at specific points $P_i = 1, 2, 3, 4\&5$ along the mid-plane line of the network as shown in Fig 5.3. In Fig 5.9 (a), we show the axial velocity component as a function of time for each position point P_i. The behaviour is harmonic as expected due to fact that, the wall contraction motions follow a harmonic collapsing pattern as given by Eqs. (5.3 - 5.5). Moreover, instead of plotting the velocity versus time, we can show the velocity behaviour versus the percentage of its travel collapse distance $TC\%$, as shown in Fig. 5.9 (b). Similar plots are given for the vertical velocity component and the pressure along the same tracking points $P_i = 1, 2, 3, 4\&5$ over a complete collapsing cycle in time, as shown in Fig. 5.9 (c & d) and Fig. 5.9 (e & f) respectively. It should be mentioned here that, the symbols C and E on these figures indicate compression and expansion respectively.

Furthermore, the time-average of the pressure P_T and its gradient P_{xT}, which are monitored along the entire mid-plane over a complete collapsing cycle of is calculated by simply integrating each quantity over a complete cycle of time. The results are shown in Figs. 5.10 and Fig. 5.11 re-

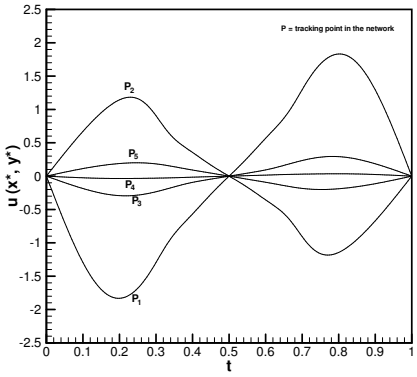

(a) $(t-u)plane$

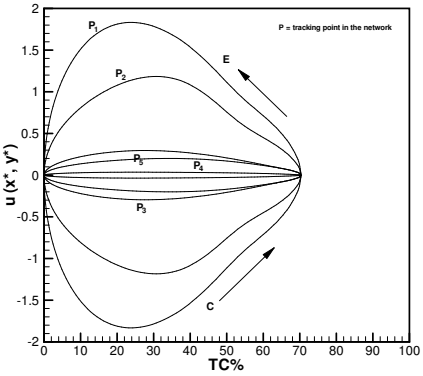

(b) $(TC-u)plane$

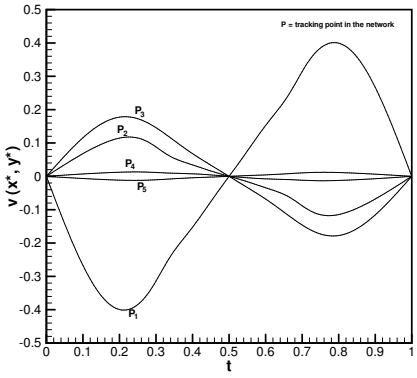

(c) $(t-v)plane$

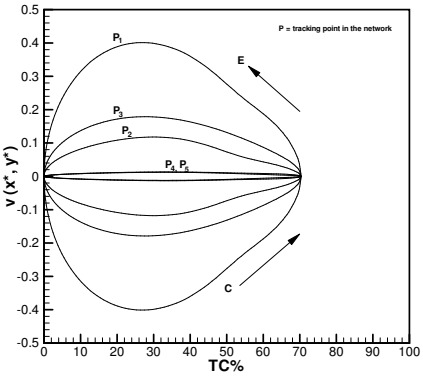

(d) $(TC-v)plane$

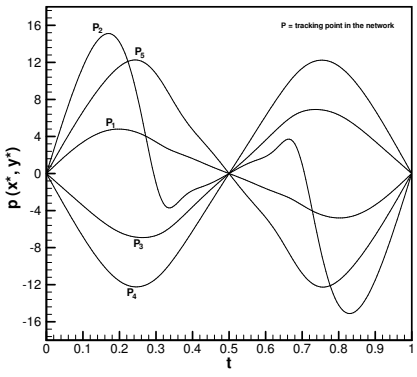

(e) $(t-P)plane$

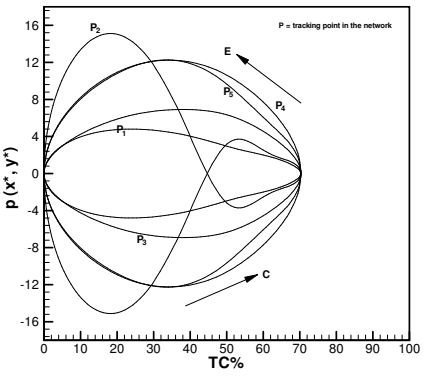

(f) $(TC-P)plane$

Figure 5.9: Case 1: velocity and pressure distributions as a functions of the time t and channels travel distance $Tc\%$ monitored over a complete collapsing

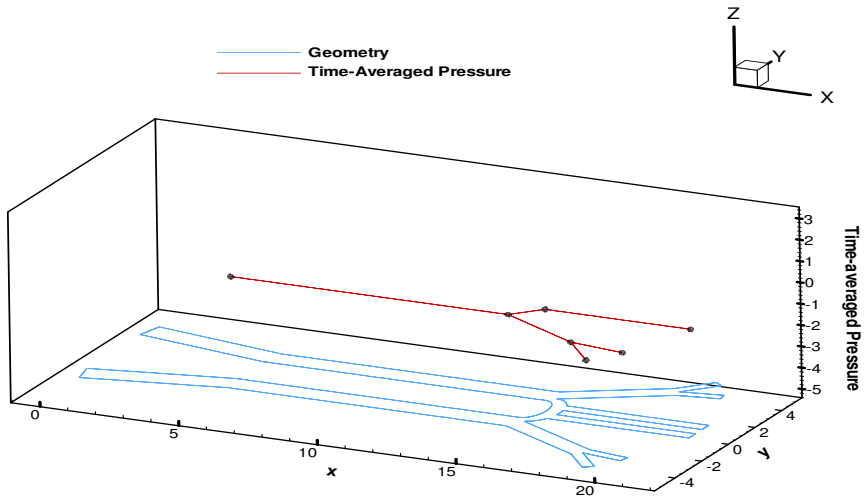

Figure 5.10: Case 1: time averaged pressure distribution along the network mid-plane line.

spectively. As expected, the time averaged for both pressure and pressure gradient are identically zero along the network mid-plane. This indicates that, whenever the wall contractions move with similar collapsing functions and there is no phase lags between their motion protocols, a zero net flow is produced. This is also very consistence with our pumping hypotheses given previously in chapter 2. Moreover, in order to further confirm these results, a particle tracking simulations will be given in the next subsection.

C. Selective Pumping via Particle Tracking Simulations

In order to conceptually validate our proposed selective-pumping-in-a-network idea of controlling the flow directionality in a network with moving wall contractions, we use the standard particle tracking simulation method. The particle tracking approach is mainly used here to visualize the instantaneous flow motions and to predict the flow displacements produced by the network wall contractions over a complete collapsing cycle.

In this part, we follow the same approach given in chapter 2, section 2.3. Let us consider a collection

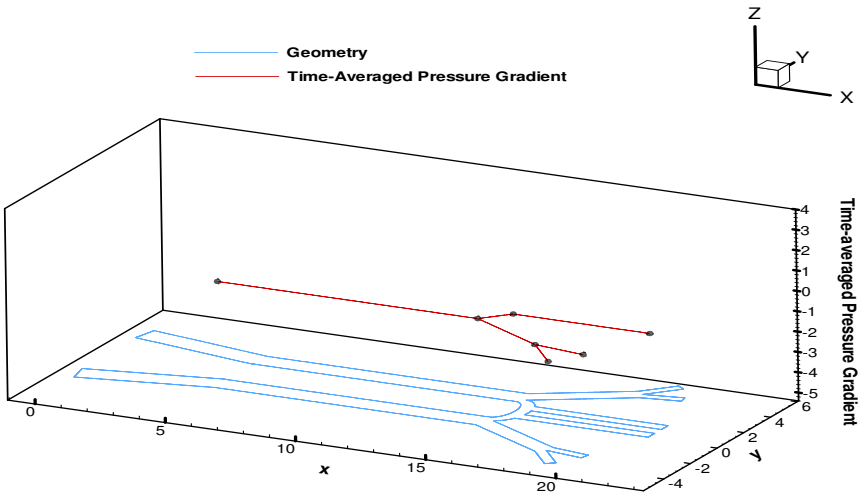

Figure 5.11: Case 1: time averaged pressure gradient distribution along the network mid-plane line.

of particles located underneath the contraction locations of the network side wall. Particles are assumed to be passive and do not affect the background flow motions and swim with velocities equal to the background flow velocities. Based on the Lagrangian frame of reference, the particles motion can be governed by

$$\frac{d}{dt}\mathbf{X}_p = \mathbf{V}, \mathbf{X}_p(0) = \mathbf{X}_o \tag{5.17}$$

where, $\mathbf{X}_p$ is the particle position vector and $\mathbf{X}_o$ describes the initial position of any particle. $\mathbf{V}$ is the fluid velocity vector given by the components u and v which are given previously by equations (5.13-5.14).

Since the particles are passive and do not influence the background fluid, therefore as the wall contractions moves, the particles diffuses and follow exactly the flow path lines. The instantaneous particle positions are evaluated by integrating the initial value problem governed by the ordinary differential system of equations(5.17) using the Adams-Bashforth integrator scheme. This time steeping algorithm is used to calculate the particles positions after a complete cycle i.e., $t = T = 1/S_t = 1$ with an error tolerance of 10^{-6}.

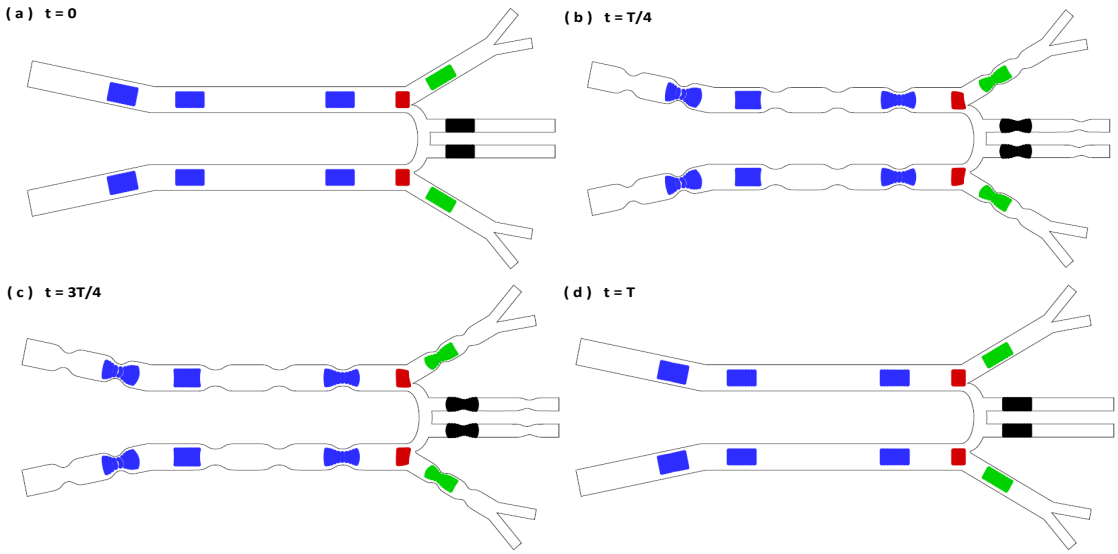

Figure 5.12: Case 1: particles tracking simulations that show the, no net flow is produced whenever contractions move with no phase lags.

In Figs. 5.10, the instantaneous particle tracking simulations for collection of particle batches distributed at different spots in the network and marked by different colors for illustration purposes. Snapshots for the particles motions are given at different times $t = 0, T/4, 3T/4, T$ that represent the initial particles positions, motions during compression, expansion and after completing a single collapsing cycle respectively. This case deals with the scenario where the network wall contractions move with zero phase lags $\theta_{13} = 0^\circ$ and $\theta_{23} = 0^\circ$ with respect to each other. Simulations have shown that, after the wall contractions complete a whole contraction cycle i.e., $t = T$, particles return back to their initial positions and there will be no net motions (i.e., no net flow is produced) as shown in in Fig. 5.10. It should be noted that, the particles tracking simulations are consistent with the results conducted by using a single segment pumping model given in chapter 2. This zero net flow situation will be changed by proper tuning and adjusting the phase lags between all the contractions as it will be given in the second and third cases of studies, which are given shortly in the following subsections.

5.3.2 Case 2: Selective-Pumping into $P_3 - P_5$ Branch

Consider the same network of channels explained in section 5.1.2 with moving wall contractions in each branch. Let us assign two contractions along the lower segment in the network termed by $P_1 - P_2$ route that move with a non zero phase lag $\theta_{13} \neq 0$. The middle segment $P_2 - P_3$ has assigned three contraction sites that move with zero phase lag, i.e., $\theta_{13} = 0$. The branch segment $P_3 - P_5$ will have two collapsing regions that move with $\theta_{13} \neq 0$, as shown in Fig. 5.3 (b). In this case of study, contraction sites are set to move with different collapsing profiles as given by Eqs. (5.3 - 5.5) and shown in Fig. 5.2 (a). In other words, there will be phase lags between the motions of the three contractions. The goal of this case of study, is to control the fluid directionality and selectively pump the fluid into $P_3 - P_5$ branch only.

A. Induced Flow Field

In this part, the velocity field and pressure induced by the movements of the wall contractions protocol assigned to the second case of study as shown in Fig. 5.3 (b) are give. For instance, in Fig. 5.13, we show the contour lines for the pressure and the velocity components during the compression phase at instant of time $t = T/4$ and at zero phase lag $\theta_{12} = 0°$. Once again, results have shown that, as the wall contractions undergo compression phase and start to move toward the mid-plane line, high pressure with adverse and favourable gradients are formed near and underneath these compression regions as shown in Fig. 5.13 (a). As a result of this movement, the axial velocity component increases near the contraction regions and the flow is displaced, bifurcated, and exit the network from all inlet/outlet ports as shown in Fig. 5.13 (b). The contour lines for the vertical velocity component are also shown and are characterized by two regions with opposite direction underneath each contractions as shown in Fig. 5.13 (c).

Similarly, snapshots that show the flow field during the expansion phase at time $t = 3T/4$ are shown in Fig. 5.14. When the contraction regions expand back away from the mid-plane line, the structures and development of the flow field are different from the compression phase counterpart as shown in Fig. 5.14 (a-c). Specifically, when the wall contractions move with non-zero phase lag $\theta_{13} \neq 0°$ and $\theta_{23} \neq 0°$, the flow behaviour during compressions and expansions phases are different

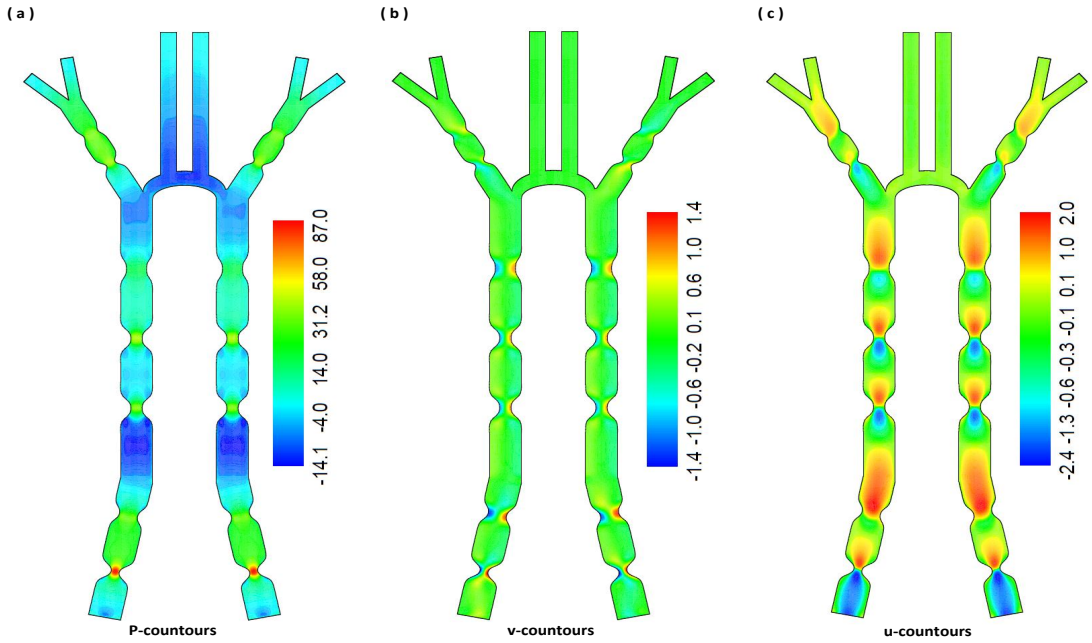

Figure 5.13: Case 2: flow field contour lines at t = T/4, (a) pressure, (b) axial velocity (c) vertical velocity.

from each other. In other words, there is no symmetry in the flow behaviour is observed in the second case of study during compression and expansion motions.

Similar to case 1 of study. Here, we show line plots for the velocity components along the vertical direction for different locations along the network axial direction. For example, in Fig. 5.15 (a & b), we show the axial velocity profiles across each segmental width W_i and at different axial locations $x_i = 1, 2, ..., 7$ as listed in listed Table 5.1 during both compression $t = T/4$ and expansion $t = 3T/4$ snapshots of times. No surprising, the velocity profiles are parabolic away from any contraction regions and is nearly parabolic as we proceed closer to contraction spots as shown in 5.16. Further more, the vertical velocity component is also given at the same axial locations along the network, as shown in 5.17. It should be noted that, velocity profiles at the expansion snapshot time $t = 3T/4$ is different from velocity profiles at compression time $t = T/4$. This implies that, there is no symmetry behaviour during compression and expansion is observed in the second case of study.

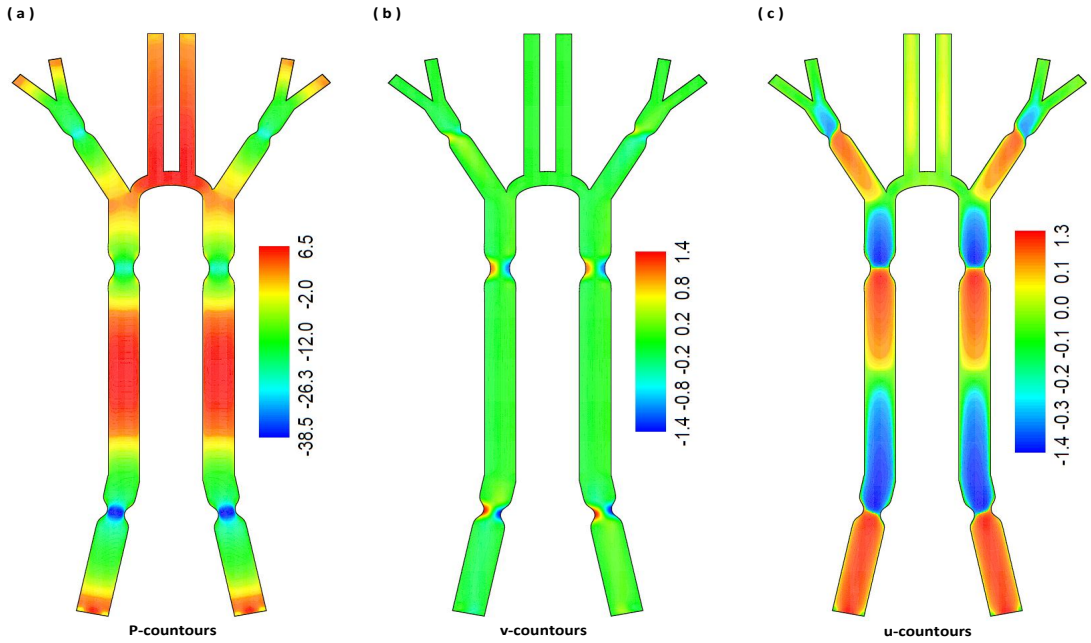

Figure 5.14: Case 2: flow field contour lines at t = 3T/4, (a) pressure, (b) axial velocity (c) vertical velocity.

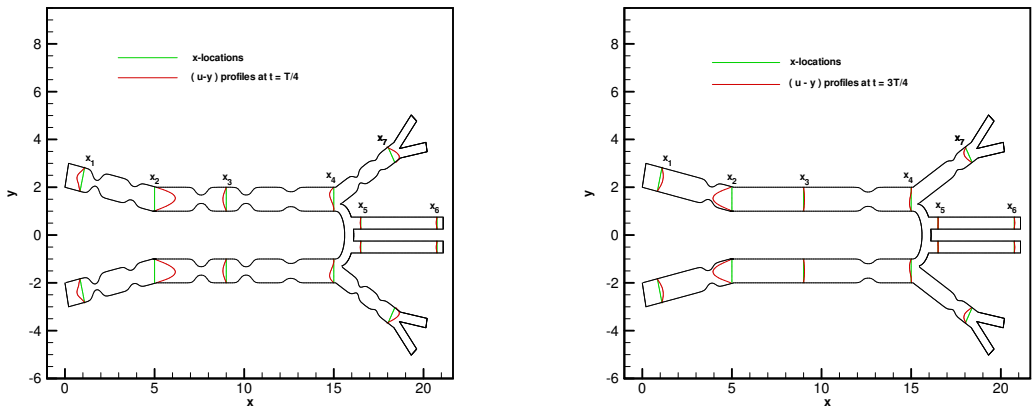

(a) $t = T/4$ (b) $t = 3T/4$

Figure 5.15: Case 2: axial-velocity profiles at different locations across the network at two time snapshots

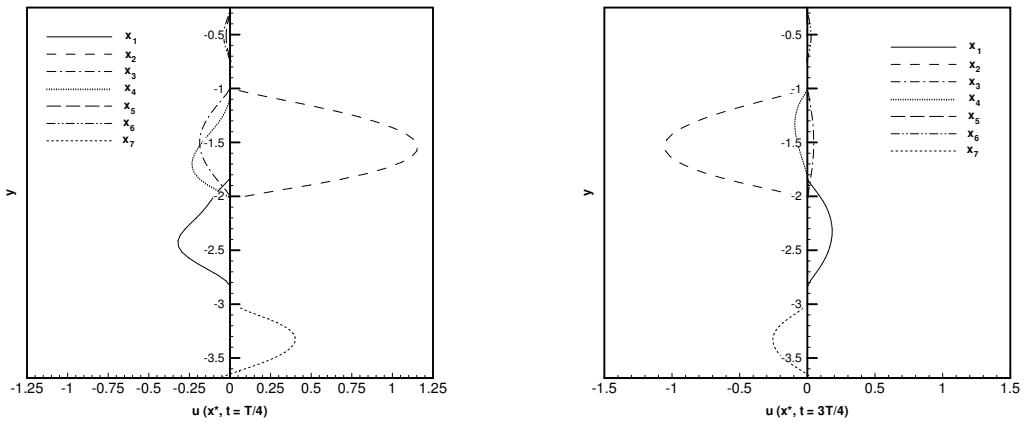

(a) $t = T/4$ (b) $t = 3T/4$

Figure 5.16: Case 2: axial velocity profiles along the vertical directions (u-y) plane at different x-locations across the network during compression and expansion snapshots

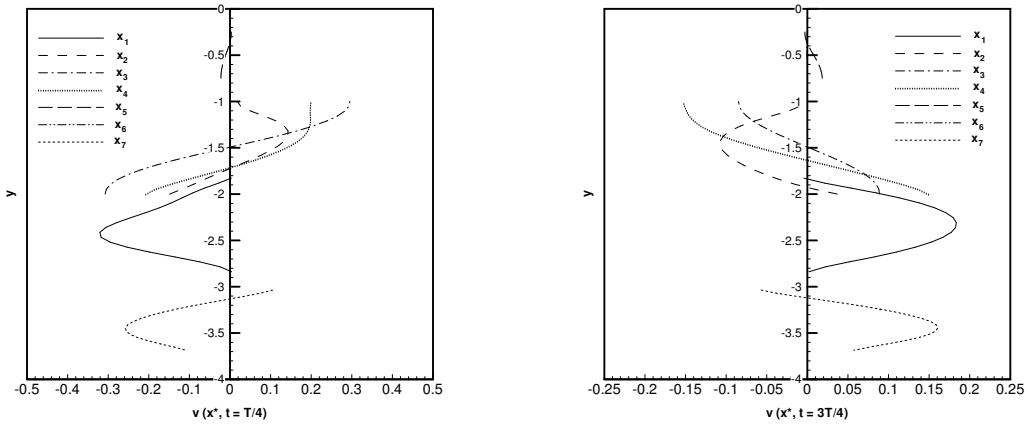

(a) $t = T/4$ (b) $t = 3T/4$

Figure 5.17: Case 2: vertical velocity profiles along the vertical directions (v-y) plane at different x-locations across the network during compression and expansion snapshots

B. time averaged Quantities

Similar to the time averaged results presented in case 1 of study. Here, we monitor the velocity components and pressure at specific points $P_i = 1, 2, 3, 4\&5$ along the mid-plane line of the network as shown in Fig 5.3 (b). In Fig 5.18 (a), we show the axial velocity component as a function of time for each position point P_i. Moreover, instead of plotting the velocity versus time, we show the velocity behaviour versus the the travel collapse distance $TC\%$ percentage, as shown in Fig. 5.18 (b). Similar plots are given for the vertical velocity component and the pressure along the same tracking points $P_i = 1, 2, 3, 4\&5$ over a complete collapsing cycle in time, as shown in Fig. 5.18 (c & d) and Fig. 5.18 (e & f) respectively. In this case, the profiles are not symmetric about the time axis which also confirm that, there is asymmetry behaviour between compression and expansion flow developments in this case of study.

Furthermore, the time-average of the pressure P_T and its gradient P_{xT}, which are monitored along the entire mid-plane over a complete collapsing cycle are calculated by simply integrating each quantity over a complete cycle of time. The results are shown in Figs. 5.20 and Fig. 5.19 respectively. As expected, the time averaged for both pressure and pressure gradient are not zeros any more and have specific variant distributions along the network mid-plane. This distribution induces pressure drops along the network mid-plane and there will be a net flow motion after complete collapsing cycle and the flow will particularly run through $P_3 - P_5$ branch only. In order to further confirm this results, the particle tracking simulation method will be given in the next subsection.

C. Selective Pumping via Particle Tracking Simulations

In a similar fashion to case 1 of study, the particle tracking simulation for the case 2 is given in this part. In Figs. 5.21, the instantaneous particle tracking simulations for collection of particles batches distributed at different spots in the network and marked by different colors for illustration purposes. Snapshots for the particles motions at two times $t = 0, 10T$ that represent the initial particles positions and after completing of $10T$ collapsing cycle respectively. This case deals with the scenario where the network wall contractions move with a zero phase lag $\theta_{13} \neq 0^\circ$ and $\theta_{23} \neq 0^\circ$ with respect to each other. Simulation have shown that, after the wall contractions completed ten

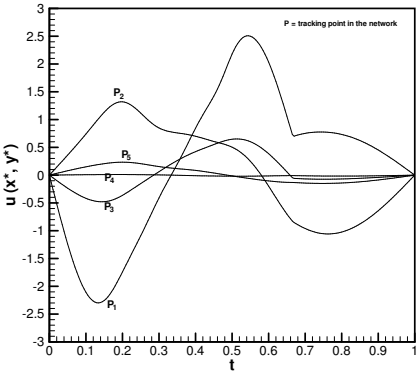

(a) $(t-u)plane$

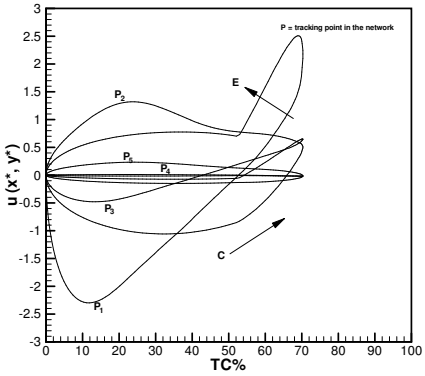

(b) $(TC-u)plane$

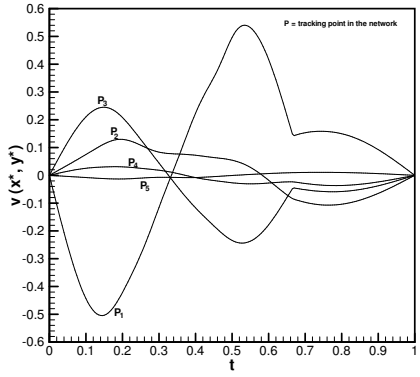

(c) $(t-v)plane$

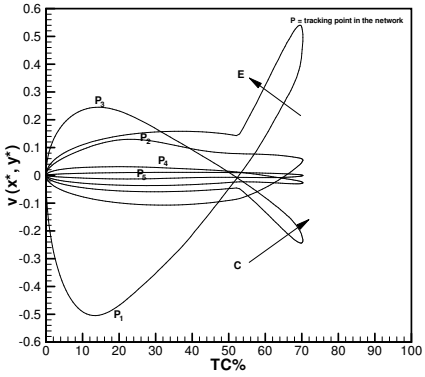

(d) $(TC-v)plane$

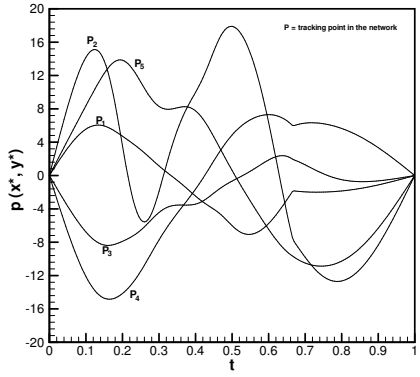

(e) $(t-P)plane$

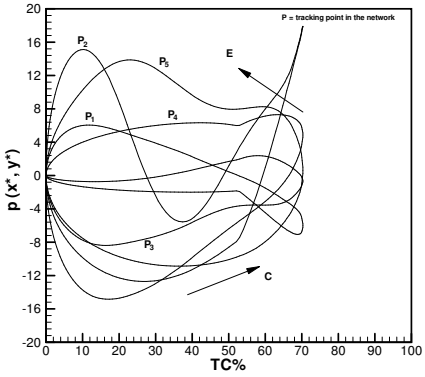

(f) $(TC-P)plane$

Figure 5.18: Case 2: velocity and pressure distributions as a functions of the time t and channels travel distance $Tc\%$ monitored over a complete collapsing

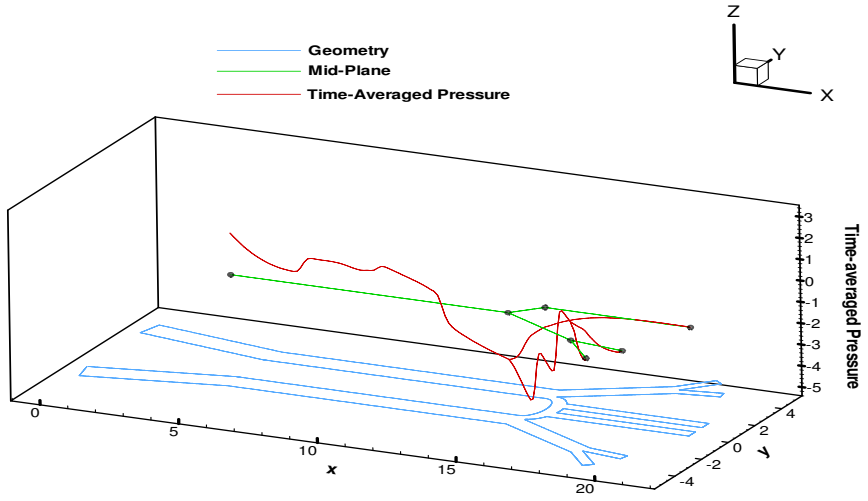

Figure 5.19: Case 2: time averaged pressure distribution along the network mid-plane line.

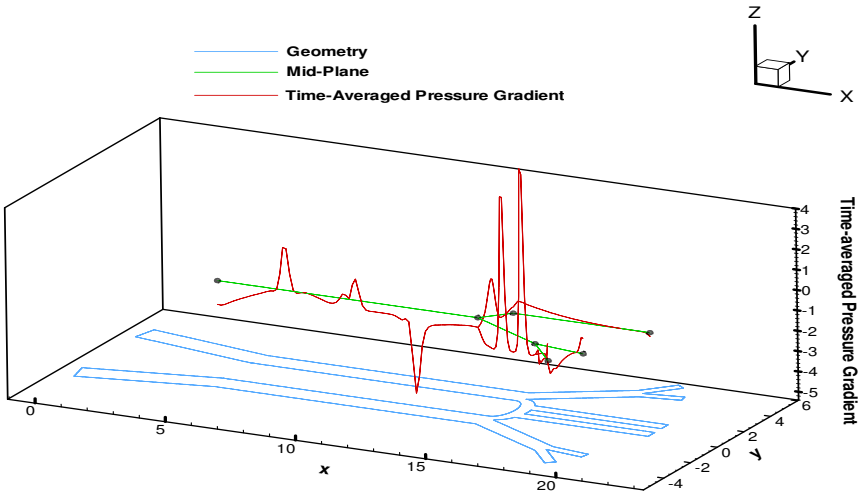

Figure 5.20: Case 2: time averaged pressure gradient distribution along the network mid-plane line

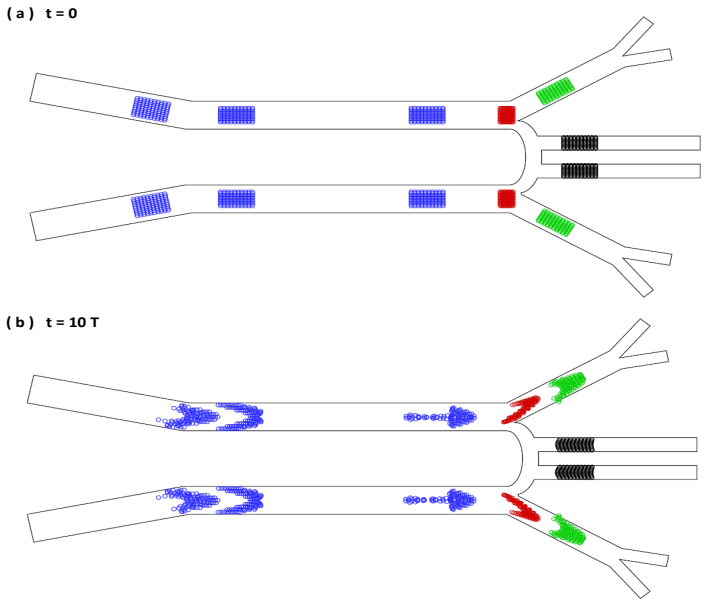

Figure 5.21: Case 2: particles tracking simulations that show the, no net flow is produced whenever contractions move with no phase lags

contraction cycles i.e., $t = 10T$, particles never return back to their initial positions and there will be net motions (i.e., net flow is produced) as shown in in Figs. 5.21. In other words, The flow has selectively moved to $P_3 - P_5$ branch as claimed in case 2 of study.

5.3.3 Case 3: Selective-Pumping into $P_3 - P_4$ Branch

Here, we consider the same network of channels as explained in section 5.1.2 with moving wall contractions in each branch. Let us assign two contractions along the lower segment in the network termed by $P_1 - P_2$ route that move with a non zero phase lag $\theta_{13} \neq 0$. The middle segment $P_2 - P_3$ has assigned three contraction sites that move with non-zero phase lag, i.e., $\theta_{13} \neq 0$ and $\theta_{23} \neq 0$ respectively. The branched channel $P_3 - P_5$ will have two collapsing regions that move with $\theta_{13} \neq 0$. Finally, the segment that starts at P_4 will also have two moving contractions $\theta_{13} \neq 0$, as shown in Fig. 5.3 (c). The goal of this case of study, is to control the fluid directionality and selectively pump the fluid into $P_3 - P_4$ branch.

A. Induced Flow Field

Similar result patterns as given in the previous cases are given in this case of study. For instance, the velocity field and pressure induced by the movements of the wall contractions protocol assigned to the third second case of study as shown in Fig. 5.3 (c) are give here. In Fig. 5.22, we show the contour lines for pressure and velocity components during the compression phase at instant of time $t = T/4$. Results have shown that, high pressure gradients are formed near and underneath these compression regions as shown in Fig. 5.22 (a). As a result, the axial velocity component increases near the contraction regions and the flow is displaced, bifurcated, and exit the network from all directions as shown in Fig. 5.22 (b). The contour lines for the vertical velocity component are also shown and are characterized by two regions with opposite direction underneath each contractions as shown in Fig. 5.22 (c).

Similarly, snapshots that show the flow field during the expansion phase at time $t = 3T/4$ are also shown in Fig. 5.23. The pressure, axial and the vertical velocity components as shown in Fig. 5.23 (a-c). As discussed in case 2 of study, when the wall contractions move with non-zero phase lag $\theta_{13} \neq 0^\circ$ and $\theta_{23} \neq 0^\circ$, the flow behaviour during compression and expansion phases are different from each other. In other words, there is no symmetry is observed in the third case of study during compression and expansion motions.

Similar to the case 1 and 2 of studies. Here, we show line plots for the velocity components along the vertical direction at different locations along the network axial direction. For example, in Fig. 5.24 (a & b), we show the axial velocity profiles across each segmental width W_i and at different axial locations $x_i = 1, 2, ..., 7$ as listed in listed Table 5.1 for both compression $t = T/4$ and expansion $t = 3T/4$ snapshots of times. No surprising, the velocity profiles are parabolic away from the any contraction regions and is nearly parabolic as we go closer to contraction spots as shown in 5.25. Further more, the vertical velocity component is also given at the same axial locations along the network, as shown in 5.26. It should be noted that, velocity profiles at the expansion snapshot time $t = 3T/4$ is different than profiles at compression time $t = T/4$, which show that, no symmetry behaviour during compression and expansion is observed in the third case of study as well.

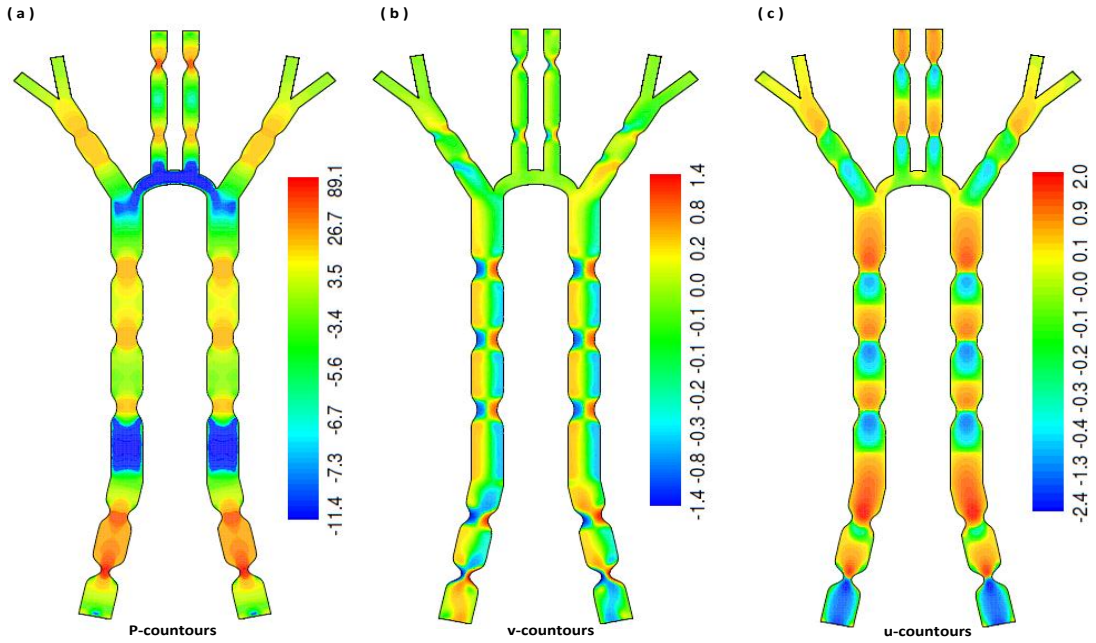

Figure 5.22: Case 3: flow field contour lines at t = T/4, (a) pressure, (b) axial velocity (c) vertical velocity

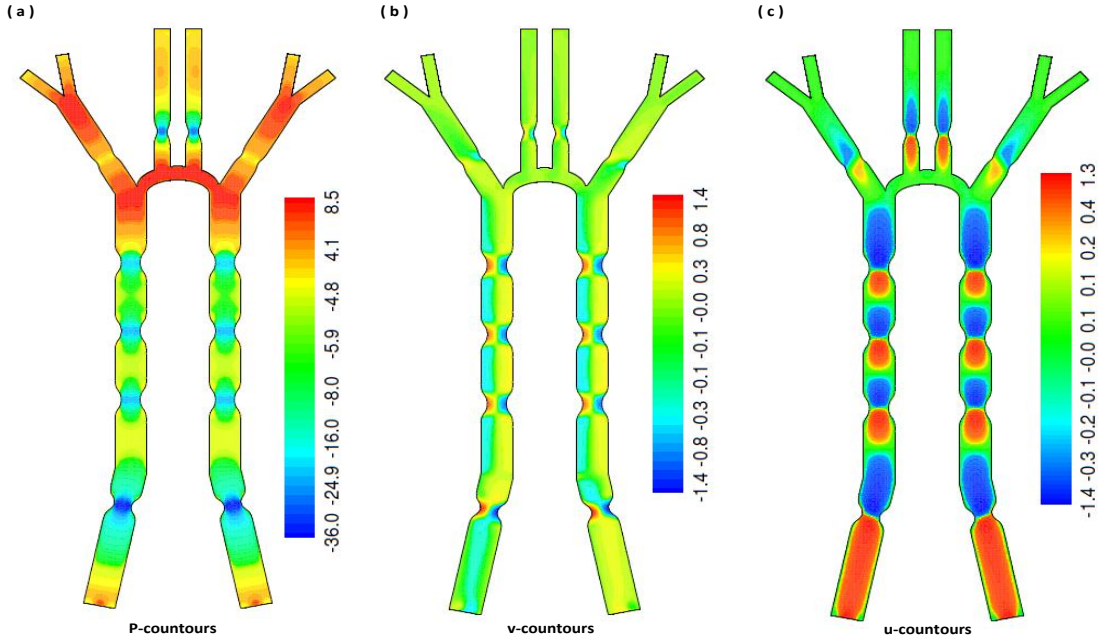

Figure 5.23: Case 3: flow field contour lines at t = 3T/4, (a) pressure, (b) axial velocity (c) vertical velocity

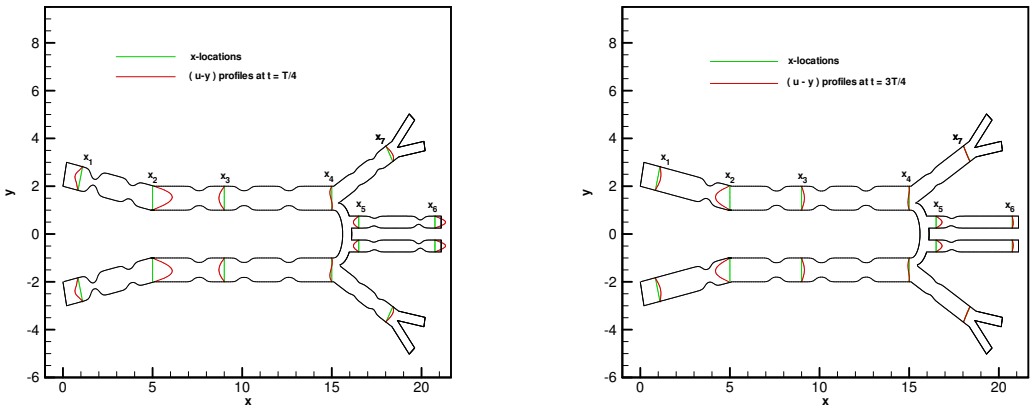

(a) $t = T/4$ (b) $t = 3T/4$

Figure 5.24: Case 3: axial-velocity profiles at different locations across the network at two time snapshots

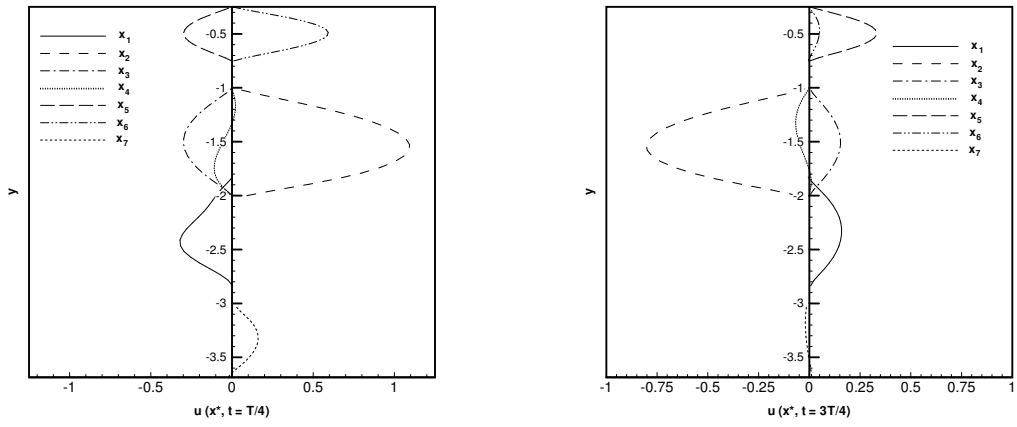

(a) $t = T/4$ (b) $t = 3T/4$

Figure 5.25: Case 3: axial velocity profiles along the vertical directions (u-y) plane at different x-locations across the network during compression and expansion snapshots

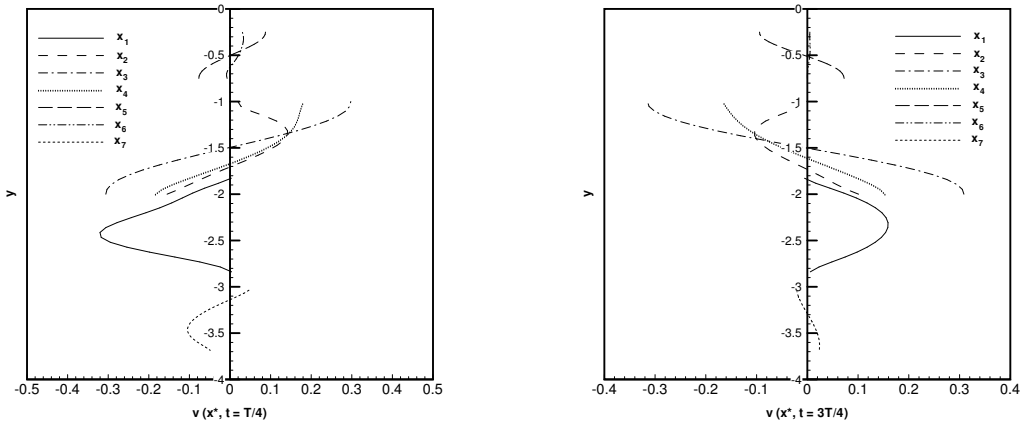

(a) $t = T/4$ (b) $t = 3T/4$

Figure 5.26: Case 3: vertical velocity profiles along the vertical directions (v-y) plane at different x-locations across the network during compression and expansion snapshots

B. time averaged Quantities

Once again and similar to results presented in both previous cases. In this part, we monitor the velocity components and pressure at specific points $P_i = 1, 2, 3, 4\&5$ along the mid-plane line of the network as shown in Fig 5.3 (c). In Fig 5.27 (a), we show the axial velocity component as a function of time for each position point P_i. Moreover, instead of plotting the velocity versus time, we show the velocity distributions versus the travel collapse distance $TC\%$, as shown in Fig. 5.27 (b). Similar plots are given for the vertical velocity component and the pressure along the same tracking points $P_i = 1, 2, 3, 4\&5$ over a complete collapsing cycle in time, as shown in Fig. 5.27 (c & d) and Fig. 5.27 (e & f) respectively. In this case, the profiles are not symmetric about the time axis which also confirm that, non symmetry behaviour between compression and expansion flow developments has observed.

Also, the time-average of the pressure P_T and its gradient P_{xT}, which are monitored along the entire mid-plane over a complete collapsing cycle are calculated by simply integrating each quantity over a complete cycle of time. Results are shown in Figs. 5.28 and Fig. 5.29 respectively. As expected, the time averaged for both pressure and pressure gradient are not zeros along the network mid-plane

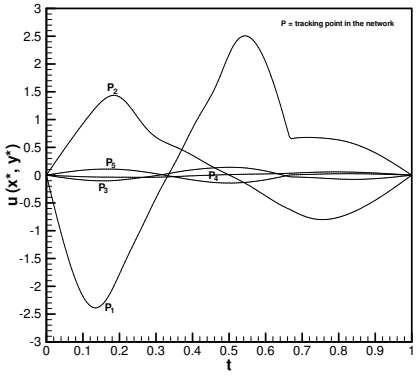

(a) $(t-u)plane$

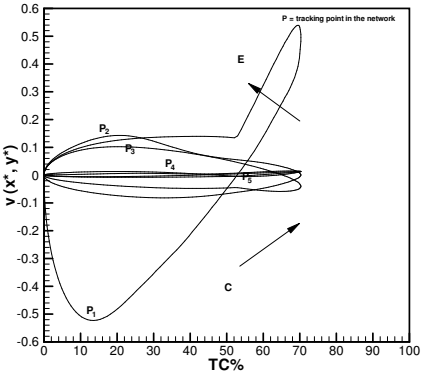

(b) $(TC-u)plane$

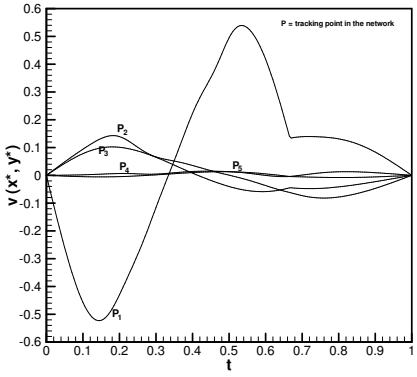

(c) $(t-v)plane$

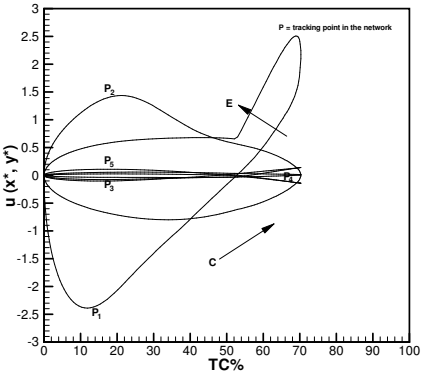

(d) $(TC-v)plane$

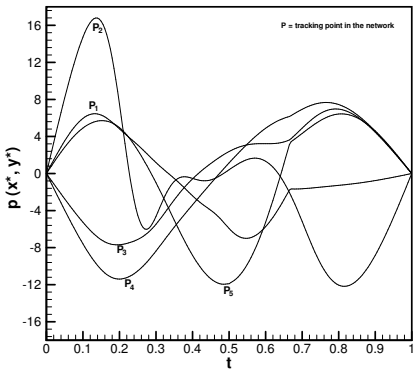

(e) $(t-P)plane$

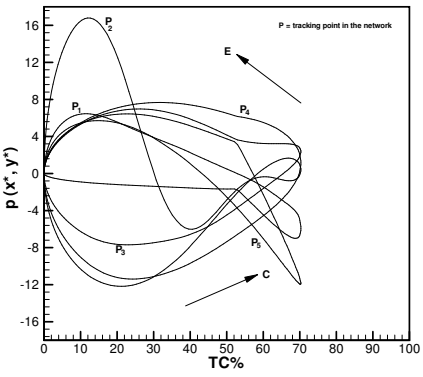

(f) $(TC-P)plane$

Figure 5.27: Case 3: velocity and pressure distributions as a functions of the time t and channels travel distance $Tc\%$ monitored over a complete collapsing

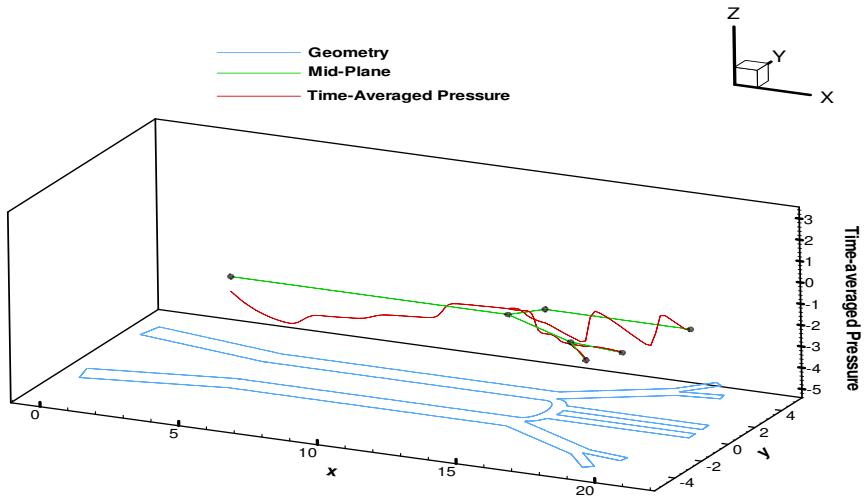

Figure 5.28: Case 3: time averaged pressure distribution along the network mid-plane line.

and have quite variable distributions along the network. This variations in pressure gradient/drops along the network mid-plane indicate that, there will be a net flow motion after complete collapsing cycle, however it is different from the second case of study. Therefore, the flow has been transported and run through $P_3 - P_4$ branch only. In order to confirm these results, the particle tracking simulations will be given in the next subsection.

C. Selective Pumping via Particle Tracking Simulations

In a similar fashion to cases 1 and 2 of studies. Here, we show the particle tracking simulation for the case 3. In Figs. 5.21, the instantaneous particle tracking simulations for collection of particles batches distributed at different spots in the network and marked by different colors for illustration purposes. Snapshots for the particles motions at two times $t = 0, 10T$ that represent the initial particle positions and after completing of $10T$ collapsing cycle respectively. This case deals with the scenario where the network wall contractions move with non-zero phase lags $\theta_{13} \neq 0^\circ$ and $\theta_{23} \neq 0^\circ$ with respect to each other. Simulation have shown that, after the wall contractions completed ten contraction cycle $t = 10T$, particles never return back to their initial positions and there will be

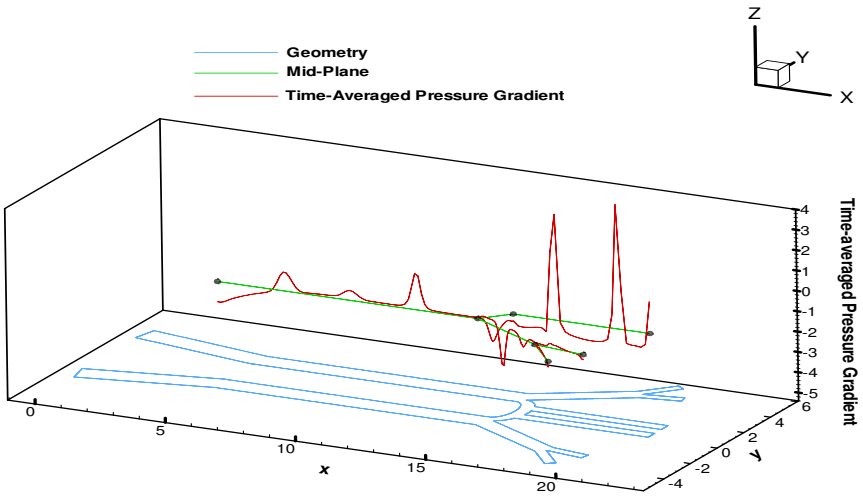

Figure 5.29: Case 3: time averaged pressure gradient distribution along the network mid-plane line.

net motions (i.e., net flow is produced) as shown in in Figs. 5.21. In other words, The flow has selectively moved to $P_3 - P_4$ branch as claimed in case 3 of study.

As a summary from this chapter, we present a new paradigm for selectively pumping and controlling fluids at the microscale in a complex network of channels, which we call "selective pumping in a network." The approach is inspired by internal flow distributions induced by rhythmic wall contraction phenomena in insect tracheal networks. The selective pumping concept presented enables fluids to be transported, controlled and directed into specific branches in networks while avoiding other possible branching routes, without the use of any mechanical valves. The results presented here might help guide efforts to fabricate novel microfluidic devices with improved efficiency for mixing purposes and targeted drug delivery applications.

In this study, both theoretical analysis and Stokeslets-meshfree computational methods are used to solve for the 2D viscous flow transport in an insect-like tracheal network of channels with prescribed moving wall contractions. The meshfree numerical method is based on the method of fundamental solutions (MFS) that uses a set of singularized force elements "Stokeslets" to induce the flow

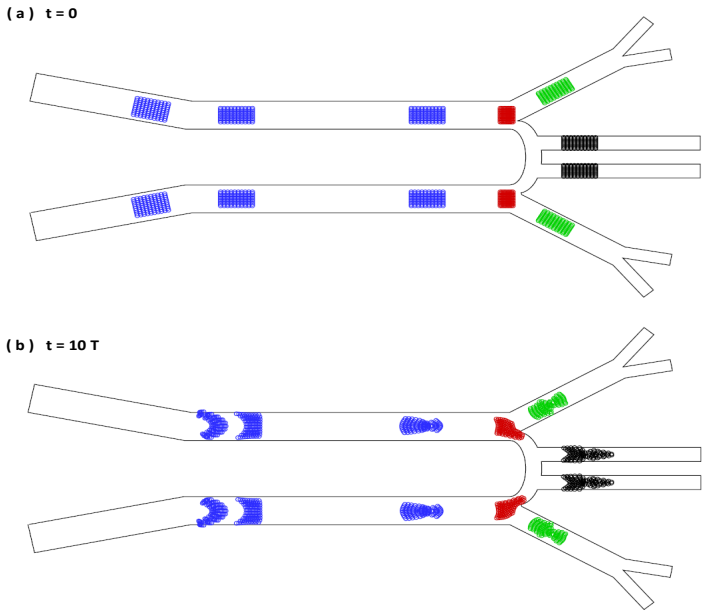

Figure 5.30: Case 3: particles tracking simulations that show the, no net flow is produced whenever contractions move with no phase lags.

motions. Moreover, the passive particle tracking simulation approach in the Lagrangian frame of reference is also used to strengthen and support our selective pumping in a network technique. Three major cases are selected for simulation in order to convey the selective-pumping-in-a-network hypothesis and working principle.

Chapter 6

Three-Dimensional Bioinspired Pumping Models using Stokeslets-Meshfree Computations

In this chapter, the three-dimensional Stokeslets-meshfree method are used to solve for the induced flow motions in both tubular and channel structures with moving wall contractions. These 3D numerical results will be used for comparing and validating our 2D theoretical analysis derived previously in chapter 2. Several cases including tubes with symmetric and asymmetric contractions will be given to study the contraction shapes on the time averaged net flow rate. The main goal in this chapter is to use 3D Stokeslets simulations to confirm our pumping hypothesis claimed throughout this dissertation.

6.1 Fluid Transport in 3D Tubular Structure

The flow motions inside many of physiological systems are normally driven by waves propagation of the muscular wall contractions known as peristaltic pumping. Peristalsis induced flow motions has been a central research sport in classical biological fluid dynamics. There are several an-

alytical analyses and numerical methods have been used to study flow in two-dimensional and three-dimensional channels and/or tubes. For instance, Aranda et al. (2011) have recently studied the three dimensional peristalsis in a non-axisymmetric tube.

Unlike peristalsis, there is another class of wall driven flows which can be induced as a result of the dynamics of non-propagative (non-peristaltic) wall wavy motions. These waves are standing in nature and normally generated by localized wall contractions along many of physiological tubular structures. Although this class of wall induced flow motions can exist in many of biological systems (Westneat et al., 2003). Yet, it have received little attention as documented by Macagno and Christensen (1980); Macagno et al. (1982). Therefore, this dissertation focuses more in this non-peristaltic flow motions. More specifically, we are inspired and motivated by the physiological flow in insect tracheal network and their observed non-propagative rhythmic wall contractions. Since, these networks compose mostly from tubular symmetric and non-symmetric structures, it is worthwhile to simulate the flow inside symmetric and non-symmetric three-dimensional tubes with various wall contractions. Therefore, in this chapter we present a Stokeslets-meshfree computational model based on the method of regularized Stokeslets Cortez (2001) to study the contraction-induced flow pumping of viscous fluid in three dimensional tubular structures.

In particular, we study the flow structures and developments in three-dimensional symmetric and non-symmetric tubes with two wall contractions govern by a generic tube wall profile that allows for contractions to move with phase(time) lags with respect to each other. This tube wall profile is similar to the one that have been used in the analytical analysis in chapter 2, section 2.1.3. Furthermore, similar approach will be used to study the induced flow motions in a three-dimensional channel with moving wall contractions from the upper wall only. In summary, the main goal of this chapter, is to study the effect of using non-symmetrical tubular structures on the induced unidirectional net flow and our novel pumping paradigm hypotheses claimed in this dissertation.

The numerical method given in this chapter will firstly validated by comparing the computational results with our derived analytical channel and tube pumping models, given previously in chapter 2. The details of the three-dimensional computational approach used in this chapter can be found in Cortez (2001); Cortez et al. (2005); Ainley et al. (2008); Aranda et al. (2011). However, a brief version will be summarized and given in the following section 6.2.

6.2 3D Stokeslets-MFS Numerical Solutions

In this section, we present the method of regularized Stokeslet derived by Cortez (2001) based on exact solutions of the Stokes equations for body forces represented by smooth localized elements satisfying the Stokes incompressible flow equations

$$\nabla^* \cdot \mathbf{V}^* = 0 \tag{6.1}$$

$$\mu \triangle^* \mathbf{V}^* = \nabla^* p^* - \mathbf{F}^* \tag{6.2}$$

where, μ is the fluid viscosity , p^* is the pressure, $\mathbf{V}^*$ is the velocity, and $\mathbf{F}^*$ is the force per unit volume which can be written in terms of Green's function and cut-off (regularization) expression as follows,

$$\mathbf{F}^* = -\alpha^* \phi^* \left(\mathbf{x}^* - \mathbf{x}_0^*\right) \tag{6.3}$$

where, $\phi^* \left(\mathbf{x}^* - \mathbf{x}_0^*\right)$ is a cut-off function with a property that $\int \phi^* \left(\mathbf{x}^*\right) d\mathbf{x} = 1$. In our computations, we use a specific cut-off function that is given as Aranda et al. (2011),

$$\phi^* \left(\mathbf{x}^* - \mathbf{x}_0^*\right) = \frac{15\epsilon^{*4}}{8\pi \left(r^{*2} + \epsilon^{*2}\right)^{7/2}} \tag{6.4}$$

where, $r^* = \parallel \mathbf{x}^* - \mathbf{x}_0^* \parallel$. ϵ^* is a small regularization parameter that controls the spreading of the cut-off function. The velocity and pressure solution to the above governing equations 6.1 and 6.2 can be given as

$$V_i^* \left(\mathbf{x}^*\right) = \frac{1}{8\pi\mu} S_{ij} \left(\mathbf{x}^* - \mathbf{x}_0^*\right) \alpha_j^* \tag{6.5}$$

$$p^* \left(\mathbf{x}^*\right) = \frac{1}{8\pi} P_j \left(\mathbf{x}^* - \mathbf{x}_0^*\right) \alpha_j^* \tag{6.6}$$

Here and throughout this chapter, the indices i,j =1,2,3 follow the Einstein summation convention. Also, $V_i^* = (w^*, v^*, u^*)$ is the flow velocity vector and p^* is the static pressure. $\mathbf{x}_i^* = (z^*, y^*, x^*)$ is the position vector. $\alpha^* = (\alpha_z^*, \alpha_y^*, \alpha_x^*)$ is the force vector strength along z^*, y^*, x^* directions. S_{ij} is known as a regularized Stokeslet and P_j is the stress tensor, which can be given as

$$S_{ij} = \delta_{ij} A_1^* + \frac{(\mathbf{x}_i^* - \mathbf{x}_0^* i)\left(\mathbf{x}_j^* - \mathbf{x}_0^* j\right)}{A_2^*} \tag{6.7}$$

$$P_j = \left(\mathbf{x}_j^* - \mathbf{x}_0^* j\right) A_3^* \tag{6.8}$$

where, $A_1^* = \frac{\left(r^{*2}+2\epsilon^2\right)}{\left(r^{*2}+\epsilon^2\right)^{3/2}}$, $A_2^* = \left(r^{*2}+\epsilon^2\right)^{3/2}$ and $A_3^* = \frac{\left(2r^{*2}+5\epsilon^2\right)}{\left(r^{*2}+\epsilon^2\right)^{5/2}}$. For clarity, the velocity expression using above equations can be easily rewritten in component wise as follows,

$$\begin{aligned} u^* = {} & \frac{\alpha_x^*}{8\pi\mu A_2^*}\left(\frac{A_1^*}{A_2^*} + (x^* - x_0^*)^2\right) + \frac{\alpha_y^*}{8\pi\mu A_2^*}(x^* - x_0^*)(y^* - y_0^*) \\ & + \frac{\alpha_z^*}{8\pi\mu A_2^*}(x^* - x_0^*)(z^* - z_0^*) \end{aligned} \tag{6.9}$$

$$\begin{aligned} v^* = {} & \frac{\alpha_x^*}{8\pi\mu A_2^*}(x^* - x_0^*)(y^* - y_0^*) + \frac{\alpha_y^*}{8\pi\mu A_2^*}\left(\frac{A_1^*}{A_2^*} + (y^* - y_0^*)^2\right) \\ & + \frac{\alpha_z^*}{8\pi\mu A_2^*}(y^* - y_0^*)(z^* - z_0^*) \end{aligned} \tag{6.10}$$

$$\begin{aligned} w^* = {} & \frac{\alpha_x^*}{8\pi\mu A_2^*}(x^* - x_0^*)(z^* - z_0^*) + \frac{\alpha_y^*}{8\pi\mu A_2^*}(y^* - y_0^*)(z^* - z_0^*) \\ & + \frac{\alpha_z^*}{8\pi\mu A_2^*}\left(\frac{A_1^*}{A_2^*} + (z^* - z_0^*)^2\right) \end{aligned} \tag{6.11}$$

Similarly, the pressure is given as

$$p^* = \frac{A_3^*}{8\pi}\left[\alpha_x^*\left(x^* - x_0^*\right) + \alpha_y^*\left(y^* - y_0^*\right) + \alpha_z^*\left(z^* - z_0^*\right)\right] \tag{6.12}$$

Now, if we use the same non-dimensional parameters defined in chapter 4 for both tube and channel. For example, in case of solving the flow in a tube, we let $z = z^*/L$,$y = y^*/R$, $x = x^*/R$, $r = r^*/L$, $\delta = R/L$, where R is the tube nominal radius. Also, we let $w = w_x^*/u_o$, $v = v_r^*/\delta u_o$, $u = u_x^*/\delta u_o$, $p = p^*R^2/(\mu u_o L)$, $\alpha_z = \alpha_z^*/(\mu u_o)$, $\alpha_y = \alpha_y^*/(\mu u_o)$, $\alpha_x = \alpha_x^*/(\mu u_o)$, $A_1 = A_1^*/L$, $A_2 = A_2^*/L$, $A_3 = A_3^*/L$, $\epsilon = \epsilon^*/L$.

While solving the flow in three-dimensional channel requires the use of the following non-dimensional parameters, we let $x = x^*/L$,$y = y^*/W$, $z = z^*/W$, $r = r^*/L$, $\delta = W/L$, where W is the channel width and depth. Also, we let $u = u_x^*/u_o$, $v = v_r^*/\delta u_o$, $w = w_x^*/\delta u_o$, $p = p^*W^2/(\mu u_o L)$, $\alpha_z = \alpha_z^*/(\mu u_o)$, $\alpha_y = \alpha_y^*/(\mu u_o)$, $\alpha_x = \alpha_x^*/(\mu u_o)$, $A_1 = A_1^*/L$, $A_2 = A_2^*/L$, $A_3 = A_3^*/L$, $\epsilon = \epsilon^*/L$.

The above velocity expressions in components wise and pressure that are valid for both tube and channel simulations, can be re-written in a non-dimensional form as,

$$u = \frac{\alpha_x}{8\pi\delta A_2}\left(\frac{A_1}{A_2} + \delta^2\left(x - x_0\right)^2\right) + \frac{\alpha_y\delta}{8\pi A_2}\left(x - x_0\right)\left(y - y_0\right) + \frac{\alpha_z}{8\pi A_2}\left(x - x_0\right)\left(z - z_0\right) \tag{6.13}$$

$$v = \frac{\alpha_x\delta}{8\pi A_2}\left(x - x_0\right)\left(y - y_0\right) + \frac{\alpha_y}{8\pi\delta A_2}\left(\frac{A_1}{A_2} + \delta^2\left(y - y_0\right)^2\right) + \frac{\alpha_z}{8\pi A_2}\left(y - y_0\right)\left(z - z_0\right) \tag{6.14}$$

$$w = \frac{\alpha_x\delta}{8\pi A_2}\left(x - x_0\right)\left(z - z_0\right) + \frac{\alpha_y\delta}{8\pi A_2}\left(y - y_0\right)\left(z - z_0\right) + \frac{\alpha_z}{8\pi A_2}\left(\frac{A_1}{A_2} + \left(z - z_0\right)^2\right) \tag{6.15}$$

Similarly, the non-dimensional pressure is given by

$$p = \frac{A_3 \delta^2}{8\pi} \left[\delta \alpha_x \left(x - x_0 \right) + \delta \alpha_y \left(y - y_0 \right) + \alpha_z \left(z - z_0 \right) \right] \tag{6.16}$$

where, $r = \sqrt{\delta^2 \left(x - x_0 \right)^2 + \delta^2 \left(y - y_0 \right)^2 + \left(z - z_0 \right)^2}$, $A_1 = \frac{\left(r^2 + 2\epsilon^2 \right)}{\left(r^2 + \epsilon^2 \right)^{3/2}}$, $A_2 = \left(r^2 + \epsilon^2 \right)^{3/2}$, and $A_3 = \frac{\left(2r^2 + 5\epsilon^2 \right)}{\left(r^2 + \epsilon^2 \right)^{5/2}}$

6.3 3-D Axisymmetric Tubes with Moving Two Contractions

In this section, the method of fundamental solutions MFS along with the regularized Stokeslets approach Cortez (2001) are used to solve for the induced flow field in a three-dimensional tube with two moving wall contractions. Here, these contractions are assigned to the tube in a symmetric manner and are set to move according to similar wall profile that have been given previously in chapter 2, section 2.1.3. A schematic that shows the problem setting along with the distributions of the source points is given in Fig. 6.1 (a). The motion protocol profiles that have been used to actuate the wall contractions are given in Fig. 6.1 (b). A typical 3-D meshing that shows a pair of symmetric collapses for a 3-D tube with circular cross section subjected to wall contractions is shown in Fig. 6.2.

The goals of this section is to perform 3-D simulations and compare the flow field with our previously derived 2-D analytical model which was given in chapter 2. In addition, is to calculate the net flow induced by the 3-D meshfree simulations and compare it with the 2-D counter part. In other words, results from both the 3-D Stokeslets meshfree computations and from the 2-D theoretical model are compared at different snapshots. The comparison process will be given at two snapshots of times $t = T/4 \& 3T/4$ that represent compression and expansion collapsing phases respectively. Moreover, two distinct phase lags $\theta_{12} = 0^\circ \& 30^\circ$ are also used during the comparison process.

To be specific, two main cases for situations, where the wall contractions are set to move with phase lags $\theta_{12} = 0^\circ \& 30^\circ$ respectively will be used for this validation process and to compare between

results computed 2-D analytically and 3-D numerically. Same geometric and flow conditions with values listed in Table 4.3 are used in this comparison. The details of the results from both cases are given as follows,

6.3.1 Moving Two Contractions with $\theta_{12} = 0(deg.)$

Once the strengths of the Stokeslets points are calculated by solving the linear system of equations as discussed before in section 4.2, the MFS can be then applied to reconstruct the induced flow motions inside the tube. Here, we follow up the similar algorithm used to obtain the Stokeslets strengths as given previously in subsection 4.3.2. As such, the structure and development of the flow field induced by only two wall contractions undergoes cyclic compression and expansion motions using both the 3-D meshfree and the 2-D analytical computations are computed and compared as given below.

In Fig. 6.3, we show a comparison between the axial velocity contour lines obtained numerically and analytical when the wall contractions are set to move with a zero phase lag i.e., $\theta_{12} = 0^{\circ}$. The contour lines that are obtained numerically using the 3-D Stokeslets meshfree method are given at different planes during the compression and expansion snapshot times $t = T/4\&3T/4$ in Fig. 6.3 (a & b) respectively. The contour lines computed based on the 2-D analytical model at the same times are shown in Fig. 6.3 (c & d) respectively. Results have shown that, as the wall contractions undergo compression phase and start to move toward the tube centreline, the axial velocity component increases near the contraction regions and the flow is displaced, bifurcated, and exits the channel from both directions. There will be a stagnation region between the two contractions due to flow cancellation, since each collapse sends flow to both directions away from the contraction zone, as clearly shown by drawing the axial velocity iso-surfaces as shown in Fig. 6.4 (a & b). As a summary from those figures, we have observed good agreements between the axial velocity obtained numerically ans theoretically.

Similarly, the numerically obtained contour lines for the other velocity components namely v-velocity and u-velocity at different planes during the compression and expansion snapshot times, $t = T/4\&3T/4$ are shown in Figs. 6.5(a& b) and 6.6) respectively. Similar contour lines that are

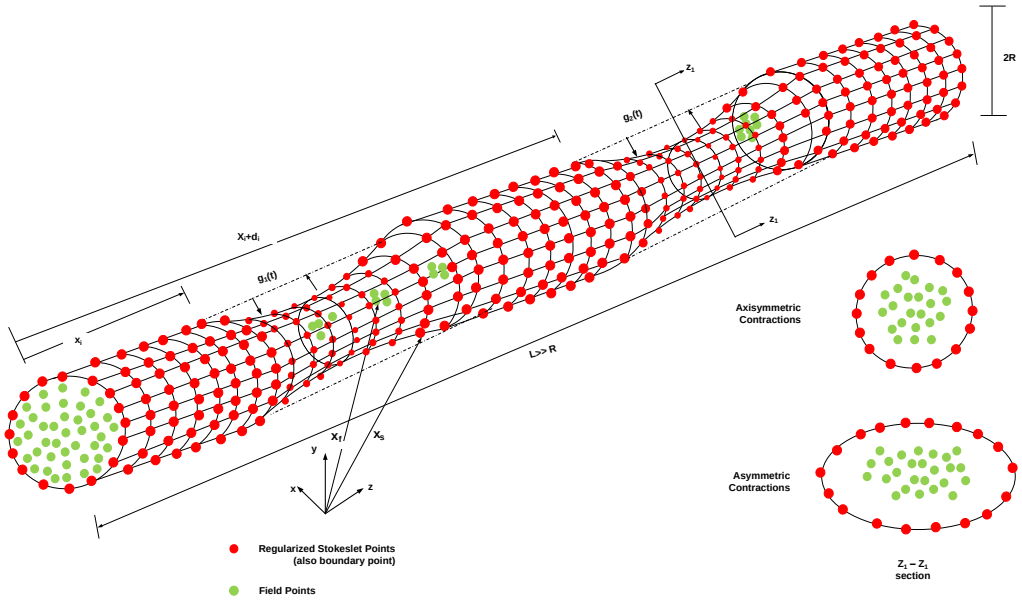

(a)

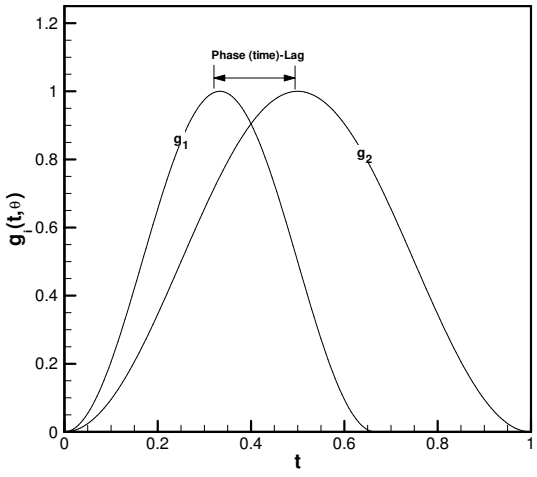

(b)

Figure 6.1: Problem Schematic and Stokeslets-meshfree numerical setup: (a) $3-D$ tube with moving upper wall contraction profile $H(z,t)$ (b) $g_1(t)$ and $g_2(t)$, the motion protocols assigned to the first and second contractions, respectively.

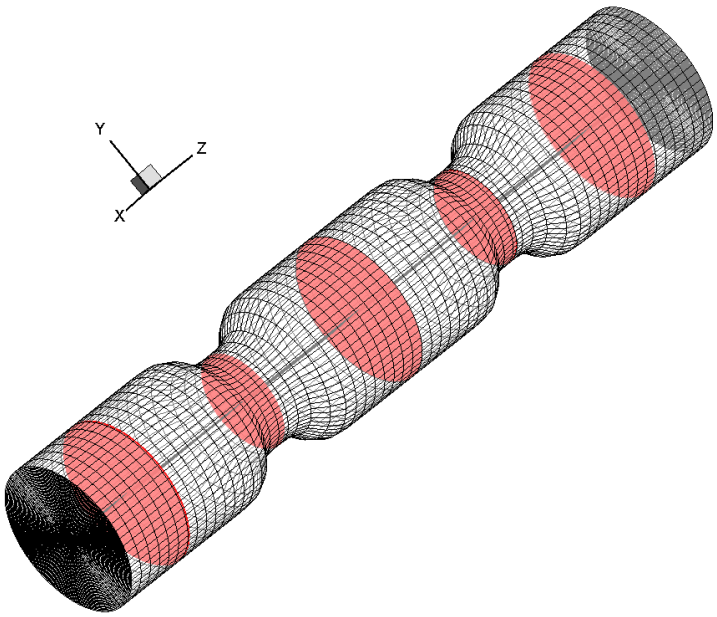

(a) 3-D view of symmetric contractions

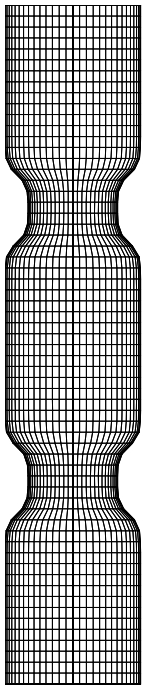

(b) (y-z) plane

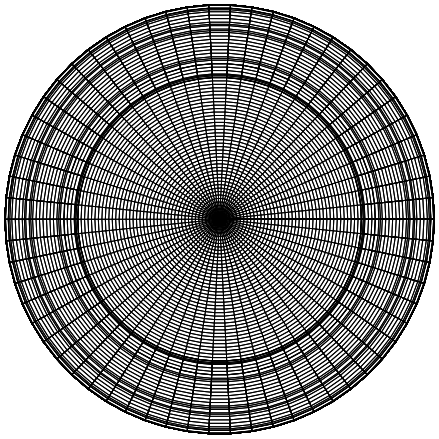

(c) (x-y)plane

Figure 6.2: Typical 3-D meshing: (a) Axis-symmetric collapses of a $3-D$ tube with circular cross section subjected to two wall contractions. (b) $(y-z)$ plane of the tube that show the symmetric collapses. (c) $(x-y)$ plane to show the circular contractions.

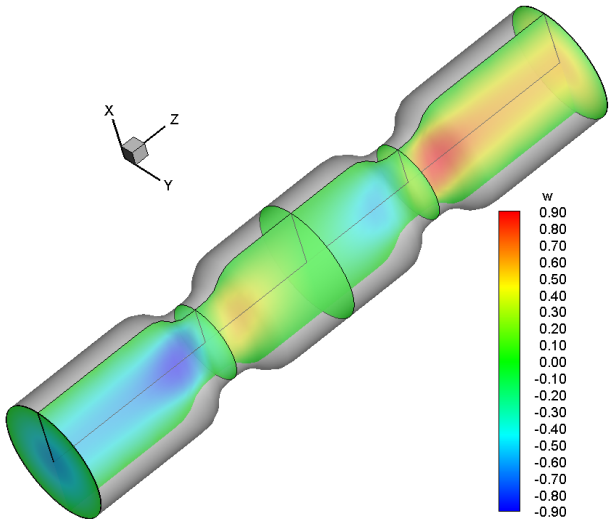

(a) 3-D Computations at $t = T/4$, $\theta_{12} = 0(deg.)$

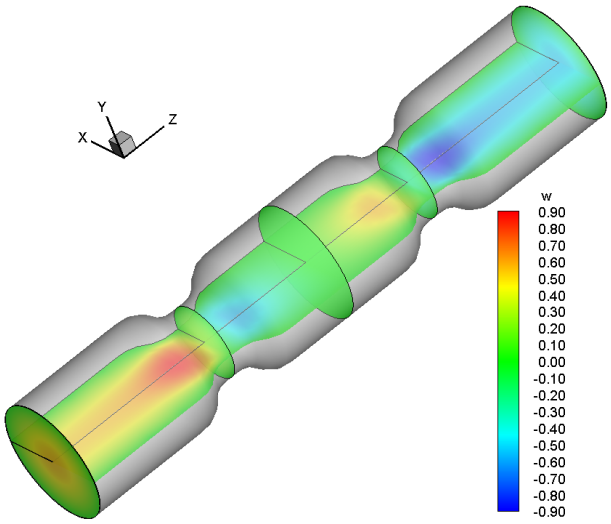

(b) 3-D Computations at $t = 3T/4$, $\theta_{12} = 0(deg.)$

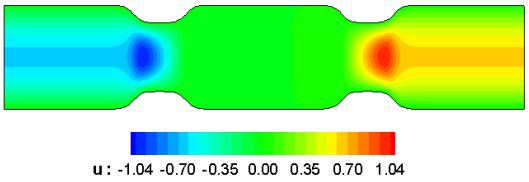

(c) 2-D Theory at $t = T/4$, $\theta_{12} = 0(deg.)$

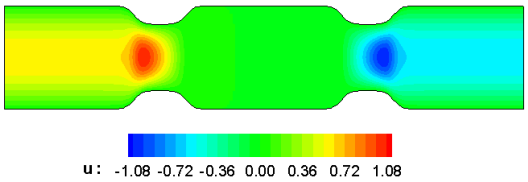

(d) 2-D Theory at $t = 3T/4$, $\theta_{12} = 0(deg.)$

Figure 6.3: Axial velocity contour lines: (a-b) $3-D$ Stokeslets-meshfree computations, (c-d) Derived $2-D$ theoretical solution. Results are given for wall contractions with phase lag $\theta_{12} = 0(deg.)$ during compression time $t = T/4$ and expansion time at $t = 3T/4$.

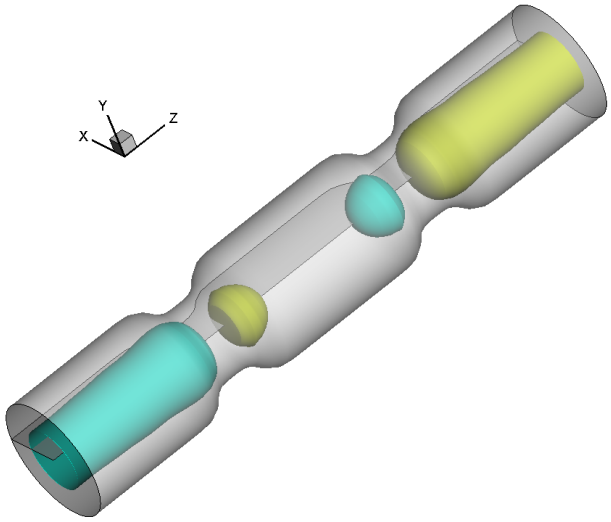

(a) 3-D Computations at $t = T/4$, $\theta_{12} = 0(deg.)$

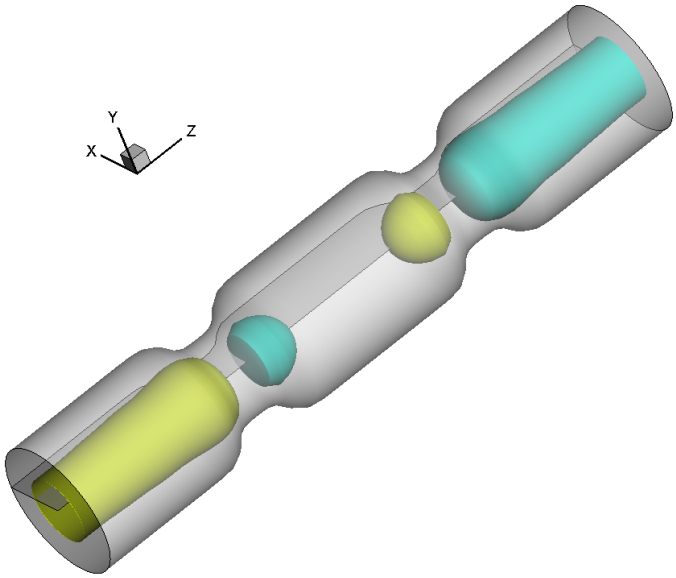

(b) 3-D Computations at $t = 3T/4$, $\theta_{12} = 0(deg.)$

Figure 6.4: Axial velocity iso-surfaces using $3 - D$ Stokeslets-meshfree computations: (a) compression time $t = T/4$, (b) expansion time at $t = 3T/4$. Results are given for wall contractions with phase lag $\theta_{12} = 0(deg.)$.

computed based on the 2-D analytical model are shown in Fig. 6.5 (c & d). These contour lines have found to be characterized by two regions with opposite direction underneath each contraction as shown analytically in Fig. 6.5 (c & d). Results shows a fair agreement between the flow contour lines obtained analytically and numerically using meshfree approach. Except that, these two observed region could not been captured using the 3D Stokeslets computations and the vertical velocity component is stretched, however same order of magnitudes are attained.

A comparison between the pressure contours obtained numerically as shown in Fig. 6.7 (a & b) and analytical in Fig. 6.31 (c & d) when the tube wall contractions are set to move with a zero phase lag i.e., $\theta_{12} = 0^{\circ}$ are given below. The contour lines for the static pressure are given at similar compression and expansion times that mentioned before. For example, results at compression time $t = T/4$ show that, as the wall contractions start to move toward the tube centreline, high pressure distribution levels with adverse and favourable gradients are formed in and near the contraction regions. This is eventually induces a flow away from the contraction sites and the flow is enforce to exit the tube from both ends as pointed out from the velocity contours. Moreover, the pressure is maximum or total in the stagnation zone between the two contractions. Similarly, data for pressure contours during the expansion phase at time $t = 3T/4$ are given. As expected, when the contraction regions expand back away from the tube centreline, an exactly similar contour lines and streamlines are developed but with opposite signs when compared with data at compression time $t = T/4$. Results have shown that, unlike the vertical velocity, the pressure contours obtained numerically have good agreements with the 2-D analytical counterpart.

6.3.2 Moving Two Contractions with $\theta_{12} = 30(deg.)$

In addition to results presented from the previous case study, whereas the two wall contractions are forced to move with no phase lag i.e., $\theta_{12} = 0^{\circ}$, we show similar plots for velocity and pressure contours for a situation where the wall contractions are set to move with a phase lag $\theta_{12} = 30^{\circ}$. Here, a comparison between the 3-D Stokeslets meshfree based on the MFS computational method and the 2-D analytical results are given at similar snapshot times that represent both compression $t = T/4$ and expansion $t = 4T/4$ and for a phase lag value of $\theta_{12} = 30^{\circ}$.

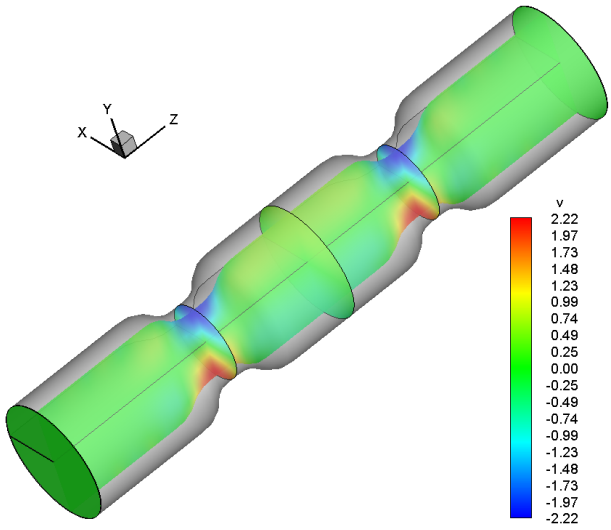

(a) 3-D Computations at $t = T/4$, $\theta_{12} = 0(deg.)$

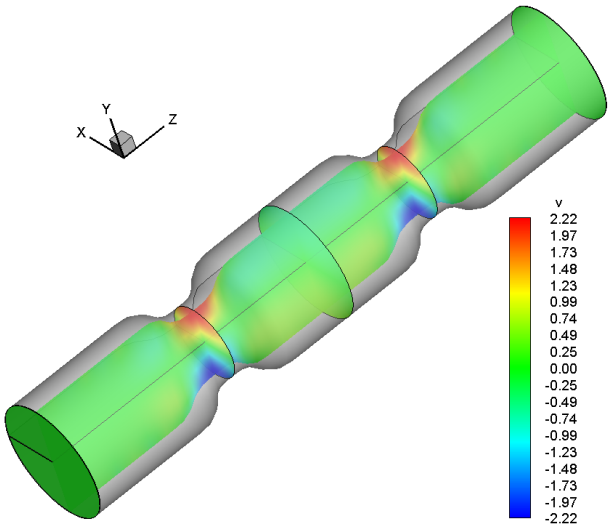

(b) 3-D Computations at $t = 3T/4$, $\theta_{12} = 0(deg.)$

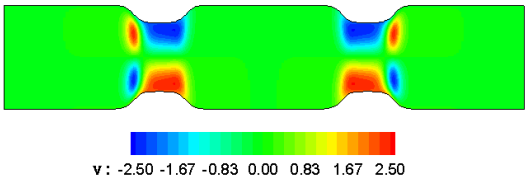

(c) 2-D Theory at $t = T/4$, $\theta_{12} = 0(deg.)$

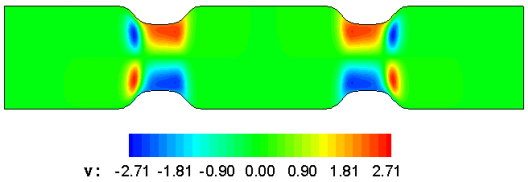

(d) 2-D Theory at $t = 3T/4$, $\theta_{12} = 0(deg.)$

Figure 6.5: Vertical velocity contour lines: (a-b) $3-D$ Stokeslets-meshfree computations, (c-d) Derived $2-D$ theoretical solution. Results are given for wall contractions with phase lag $\theta_{12} = 0(deg.)$ during compression time $t = T/4$ and expansion time at $t = 3T/4$.

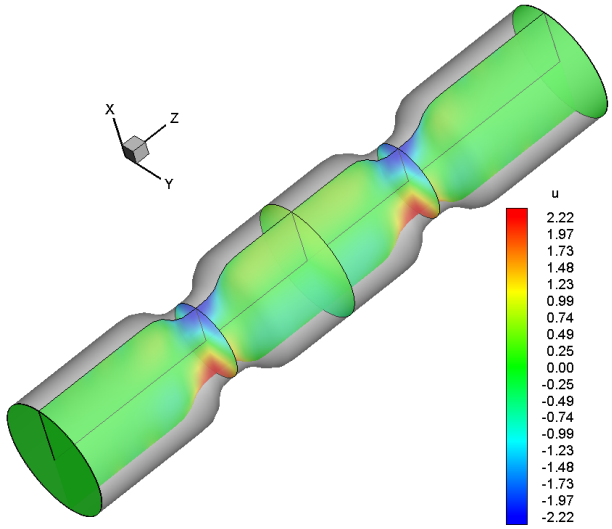

(a) 3-D Computations at $t = T/4$, $\theta_{12} = 0(deg.)$

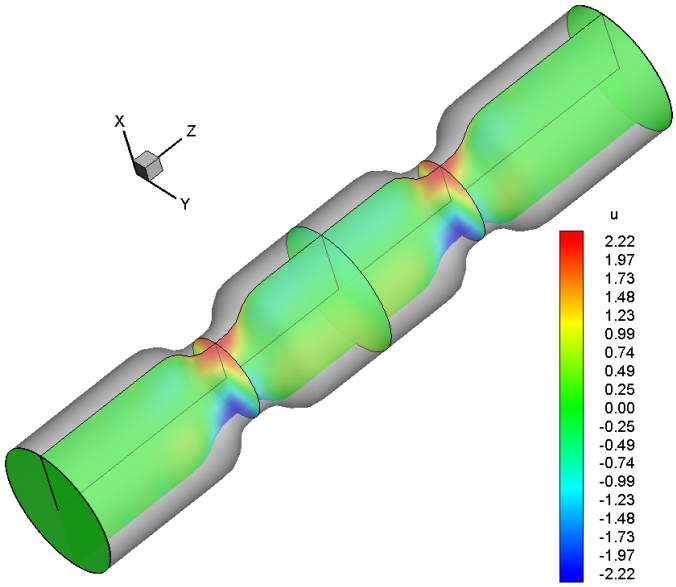

(b) 3-D Computations at $t = 3T/4$, $\theta_{12} = 0(deg.)$

Figure 6.6: u-velocity component contour lines using $3-D$ Stokeslets-meshfree computations: (a) compression time $t = T/4$, (b) expansion time at $t = 3T/4$. Results are given for wall contractions with phase lag $t = T/4$ and $\theta_{12} = 30(deg.)$.

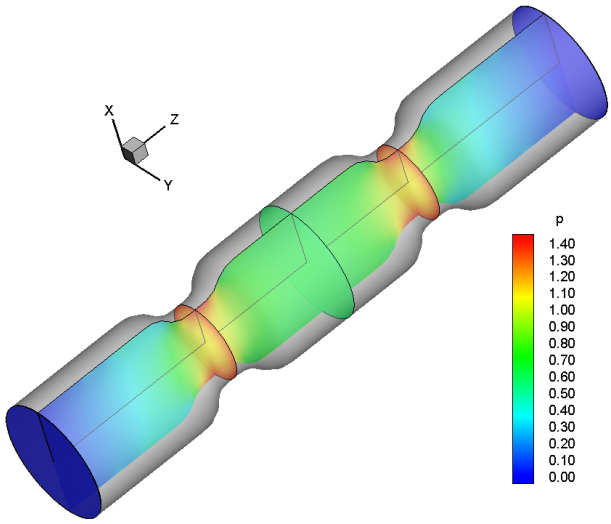

(a) 3-D Computations at $t = T/4$, $\theta_{12} = 0(deg.)$

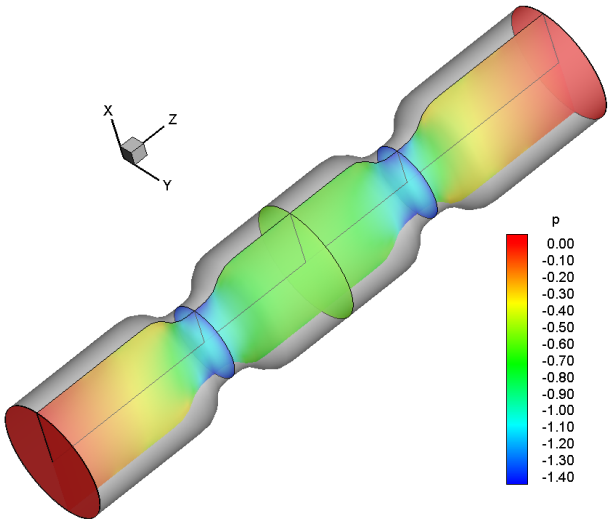

(b) 3-D Computations at $t = 3T/4$, $\theta_{12} = 0(deg.)$

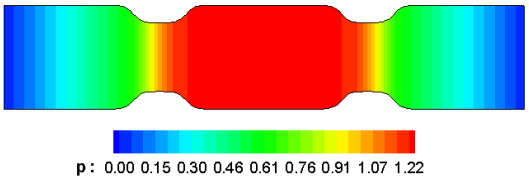

(c) 2-D Theory at $t = T/4$, $\theta_{12} = 0(deg.)$

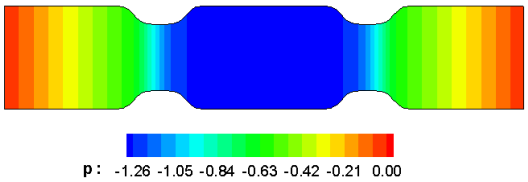

(d) 2-D Theory at $t = 3T/4$, $\theta_{12} = 0(deg.)$

Figure 6.7: Pressure contour lines: (a-b) $3-D$ Stokeslets-meshfree computations, (c-d) Derived $2-D$ theoretical solution. Results are given for wall contractions with phase lag $\theta_{12} = 0(deg.)$ during compression time $t = T/4$ and expansion time at $t = 3T/4$.

For instance, contour lines for velocity components are shown in Figs. (6.8-6.11). The pressure contours are shown in Fig. 6.12 at both compression and expansion times. Results have shown that, unlike the situation where $\theta_{12} = 0^\circ$ which is always characterized by having a stagnation zone of zero velocities between the two contractions and the flow is not allowed to transport between contraction zones. When $\theta_{12} = 30^\circ$, this stagnation zone is relaxed and there will be flow transport within the region between the two contractions as shown by the axial velocity contour lines calculated analytically and numerically as shown in Figs. 6.8 and confirmed by the axial velocity iso surfaces as shown in Fig. 6.9. Moreover, there is a pressure gradients in the region between the two contractions which indicates that, there is a flow transport in this region as shown in Fig. 6.10.

Finally, the effect using non-symmetric collapses on the velocity field and pressure distributions will be given in the next subsections.

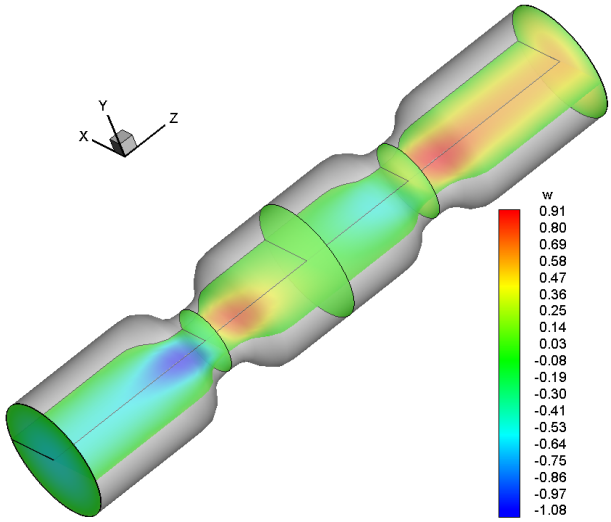

(a) 3-D Computations at $t = T/4$, $\theta_{12} = 30(deg.)$

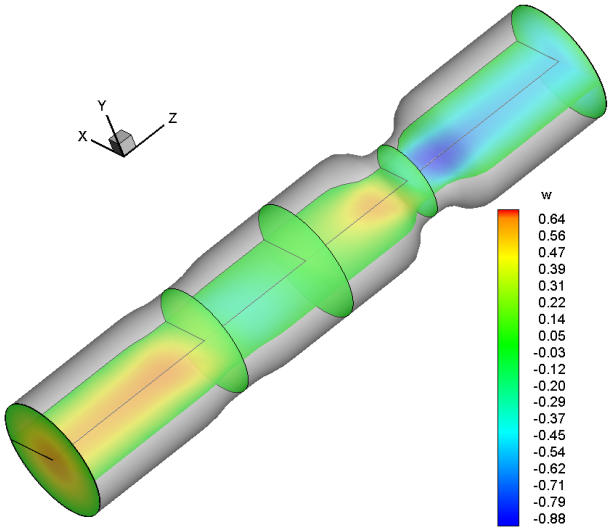

(b) 3-D Computations at $t = 3T/4$, $\theta_{12} = 30(deg.)$

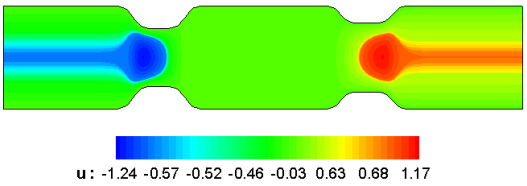

(c) 2-D Theory at $t = T/4$, $\theta_{12} = 30(deg.)$

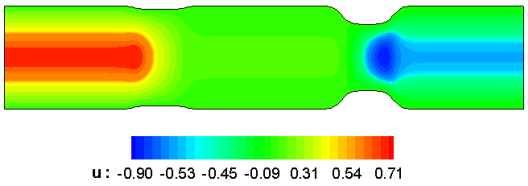

(d) 2-D Theory at $t = 3T/4$, $\theta_{12} = 30(deg.)$

Figure 6.8: Axial velocity contour lines: (a-b) $3-D$ Stokeslets-meshfree computations, (c-d) Derived $2-D$ theoretical solution. Results are given for wall contractions with phase lag $\theta_{12} = 30(deg.)$ during compression time $t = T/4$ and expansion time at $t = 3T/4$.

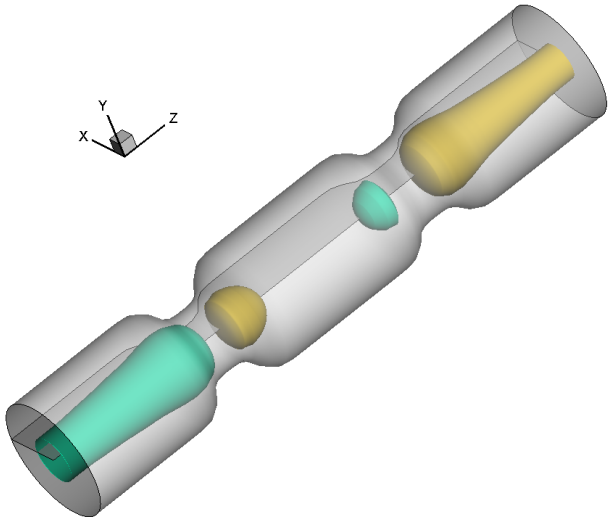

(a) 3-D Computations at $t = T/4$, $\theta_{12} = 30(deg.)$

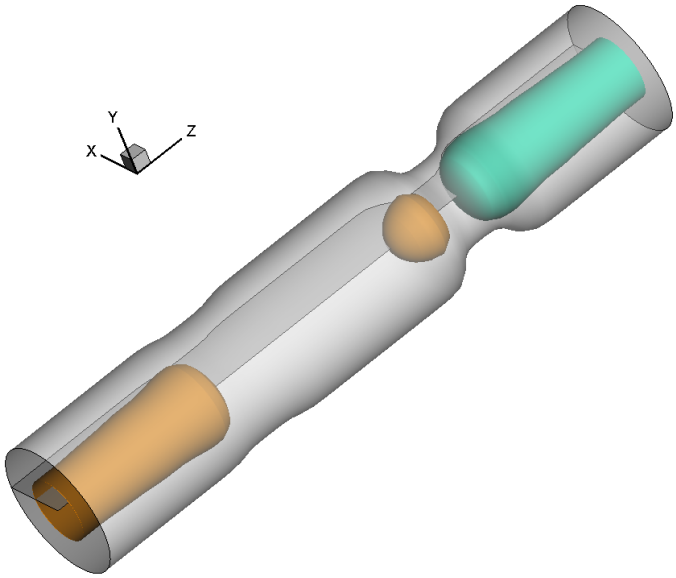

(b) 3-D Computations at $t = 3T/4$, $\theta_{12} = 30(deg.)$

Figure 6.9: Axial velocity iso-surfaces using $3 - D$ Stokeslets-meshfree computations: (a) compression time $t = T/4$, (b) expansion time at $t = 3T/4$. Results are given for wall contractions with phase lag $\theta_{12} = 30(deg.)$.

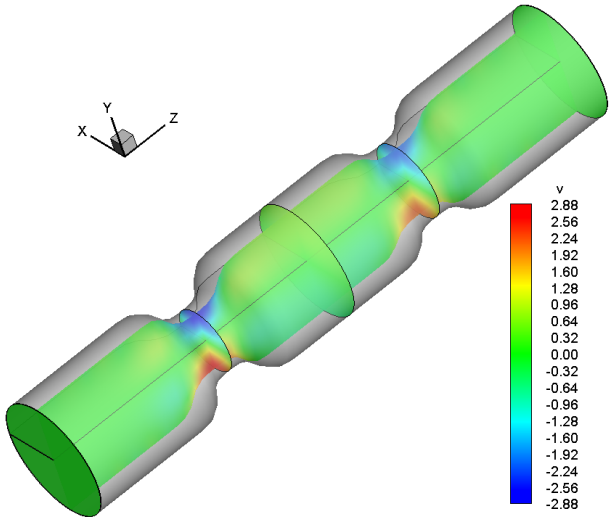

(a) 3-D Computations at $t = T/4$, $\theta_{12} = 30(deg.)$

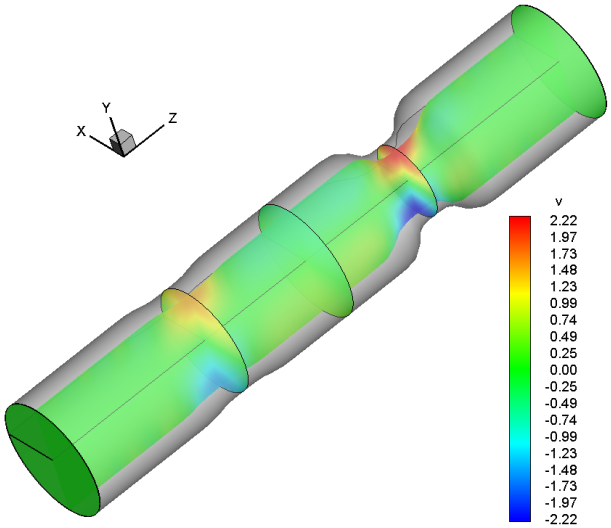

(b) 3-D Computations at $t = 3T/4$, $\theta_{12} = 30(deg.)$

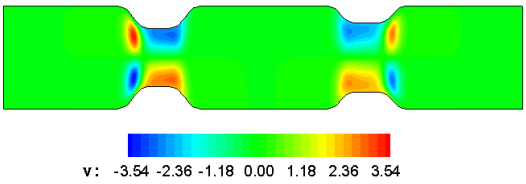

(c) 2-D Theory at $t = T/4$, $\theta_{12} = 30(deg.)$

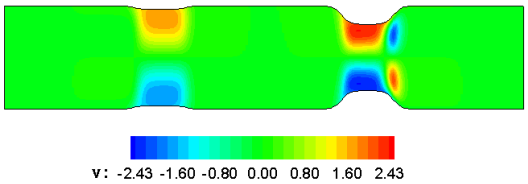

(d) 2-D Theory at $t = 3T/4$, $\theta_{12} = 0(deg.)$

Figure 6.10: Vertical velocity contour lines: (a-b) $3-D$ Stokeslets-meshfree computations, (c-d) Derived $2-D$ theoretical solution. Results are given for wall contractions with phase lag $\theta_{12} = 30(deg.)$ during compression time $t = T/4$ and expansion time at $t = 3T/4$.

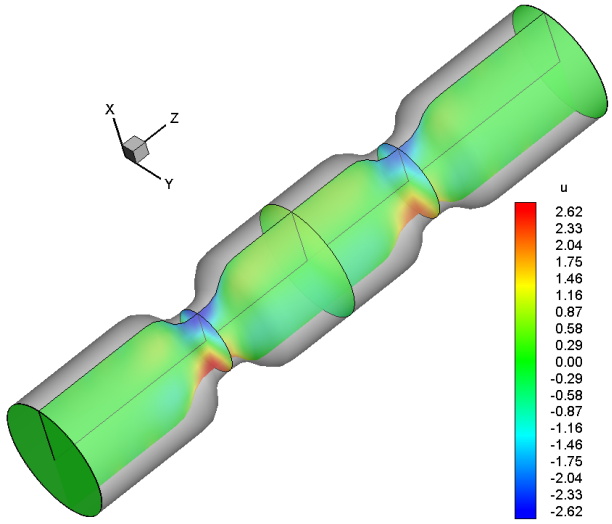

(a) 3-D Computations at $t = T/4$, $\theta_{12} = 30(deg.)$

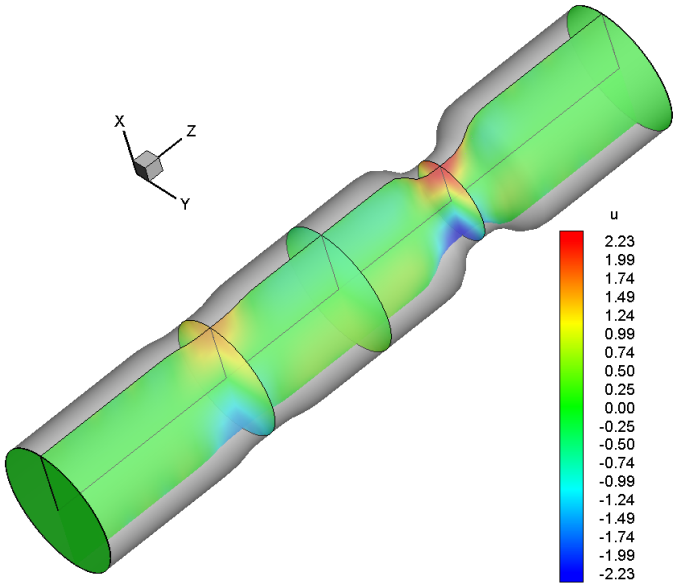

(b) 3-D Computations at $t = 3T/4$, $\theta_{12} = 30(deg.)$

Figure 6.11: u-velocity component contour lines using $3 - D$ Stokeslets-meshfree computations: (a) compression time $t = T/4$, (b) expansion time at $t = 3T/4$. Results are given for wall contractions with phase lag $t = T/4$ and $\theta_{12} = 30(deg.)$.

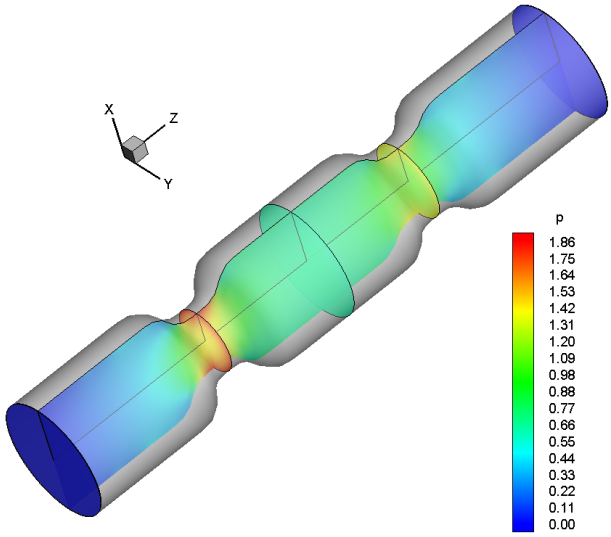

(a) 3-D Computations at $t = T/4$, $\theta_{12} = 30(deg.)$

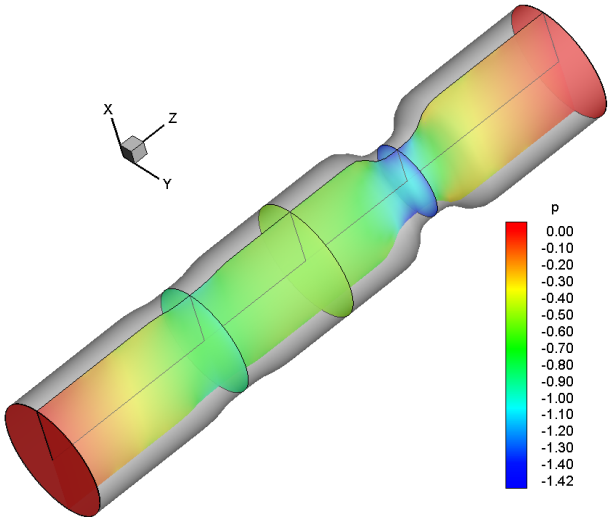

(b) 3-D Computations at $t = 3T/4$, $\theta_{12} = 30(deg.)$

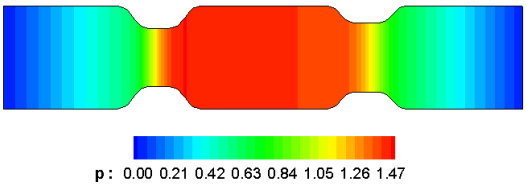

(c) 2-D Theory at $t = T/4$, $\theta_{12} = 30(deg.)$

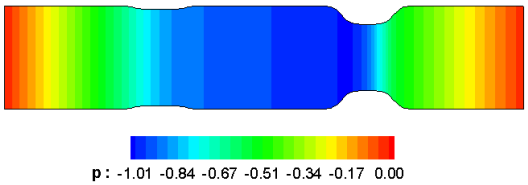

(d) 2-D Theory at $t = 3T/4$, $\theta_{12} = 30(deg.)$

Figure 6.12: Pressure contour lines: (a-b) $3-D$ Stokeslets-meshfree computations, (c-d) Derived $2-D$ theoretical solution. Results are given for wall contractions with phase lag $\theta_{12} = 30(deg.)$ during compression time $t = T/4$ and expansion time at $t = 3T/4$.

6.4 3-D of Non-Symmetric Tubes with Moving Two Contractions

In this part, the Stokeslets-meshfree numerical method Cortez (2001) is also used to solve for the induced flow motions in a three-dimensional tube with non-symmetric contractions. More specifically, the tube will have an elliptical cross-section in the collapse regions and a circular cross section away from contractions. The contractions are assigned to the tube in a non-symmetric manner in space and are set to move according to the wall profile identical to the one used previously in chapter 2, section 2.1.3.

The goal from this section is to perform 3-D meshfree simulations for tubes with non-symmetric contractions that are capable of predicting the induced flow by wall motions of a non-uniform cross-sectional tubes. Also, to study the effect of this non-symmetric wall contractions on the induced instantaneous flow parameters, and on time averaged net flow. Also, to compare the time averaged net flow induced in this case with the tube with axisymmetric contractions case of study.

Two simulation cases will be investigated in this part. Although, both cases consider a tube with elliptical cross-section in the contraction regions. However, in the first non-symmetric case of study we force the contraction only along the minor axis of the elliptical section and keeping the major axis fixed and equal to the tube original radius. In the second non-symmetric case of study, the contractions are forced to move from both sides i.e., along both the major and minor axes at the same time. It should be noted that, in order to make a fair comparison between these two cases, the volume of each tube used in the simulation has kept preserved. In other words, at any instant of time the volumes of both tube are forced to be equal. The results for both cases are organized in the following subsections,

6.4.1 Case 1: Elliptical Non-Symmetric Contractions along Minor Axis only

In this case of study, we considers a tube with two non-symmetric contractions along its length. These collapses take place along the minor axis only, while keeping the major axis fixed and equal to the tube original cross-section radius. A typical 3-D meshing that shows a pair of non-symmetric collapses of a tube with elliptical cross section subjected to wall contractions is shown in Fig. 6.13. As discussed before, once the strengths of the Stokeslets points are calculated, the MFS can be then applied to reconstruct the induced flow motions within the tube boundaries. The structure and development of the flow field induced by these cyclic compression and expansion contracting wall motions are given below,

In Fig. 6.14, we show the contour lines of w-velocity component when wall contractions are set to move with a zero phase lag i.e., $\theta_{12} = 0^\circ$ as well as when they move with non-zero phase lag $\theta_{12} = 30^\circ$. The w-velocity contour lines at different planes when $\theta_{12} = 0^\circ$ are given during the compression and expansion snapshot times $t = T/4\&3T/4$ as shown in Fig. 6.14 (a & b) respectively. Similarly, w-velocity contour lines at different planes at similar snapshots times $t = T/4\&3T/4$ for $\theta_{12} = 30^\circ$ are given in as shown in Fig. 6.14 (c & d) respectively.

Results have shown that, as the wall contractions undergo compression phase and start to move toward the tube centreline, the axial velocity component increases near the contraction regions and the flow is displaced, bifurcated, and exit the tube from both ends. moreover, when $\theta_{12} = 0^\circ$, there will be a stagnation region between the two contractions due to flow cancellation, since each collapse sends flow to both directions away from the contraction zone. This flow bifurcation is clearly shown by drawing the axial velocity iso-surfaces as shown in Fig. 6.15 (a & b). This stagnation zone will be smoothed out, when the tube collapse operate with non-zero phase lag $\theta_{12} = 30^\circ$, as shown in Fig. 6.15 (c & d). Similarly, the other velocity components namely v-velocity and u-velocity contour lines at different planes are also given during the compression and expansion times $t = T/4\&3T/4$ as shown in Fig. 6.16 and Fig. 6.17 respectively.

The pressure contours are shown in Fig. 6.18 (a & b) when wall contractions are set to move with a zero phase lag i.e., $\theta_{12} = 0^\circ$, and in Fig. 6.18 (c & d) when $\theta_{12} = 30^\circ$. The contour lines

during the compression time $t = T/4$ show that, as the wall contractions start to move toward the tube centreline, high pressure with adverse and favourable gradients are formed in and near the contraction regions. This induces flow motions away from the compression sites and forces the flow to exit from both ends as pointed out from the axial velocity contours. Moreover, the pressure is maximum or total in the stagnation zone between the two contractions. Similarly, data for pressure contours during the expansion phase at time $t = 3T/4$ are given. As expected, when the contraction regions expand back away from the centreline, an exactly similar contour lines and are developed but with opposite signs when compared with data at compression time $t = T/4$. However, when $\theta_{12} = 30°$, the pressure distributions during the expansion phase is different from the compression phase, which might be an indication of unidirectional flow production.

6.4.2 Case 2: Elliptical Non-Symmetric Contractions Through both Major and Minor Axes

In this case of study, the tube will have two non-symmetric contractions along its length. The collapses take place along both major and minor axes. A typical 3-D meshing that show a pair of non-symmetric collapses of a tube with elliptical cross section subjected to wall contractions is shown in Fig. 6.19. As discussed before, once the strengths of the Stokeslets points are calculated, the MFS can be then applied to reconstruct the induced flow motions inside the tube. The structure and development of the flow field induced by these contractions are given below in details.

Similar to case 1 of study, in Fig. 6.20, we show the w-velocity contour lines obtained numerically when contractions are set to move with a zero phase lag i.e., $\theta_{12} = 0°$ as well as when they move with non-zero phase lag $\theta_{12} = 30°$. The w-velocity contour lines at different planes are given during both compression and expansion snapshot times $t = T/4\&3T/4$ as shown in Fig. 6.20 (a & b) respectively for $\theta_{12} = 0°$. Similarly, w-velocity contour lines at different planes and at snapshots times $t = T/4\&3T/4$ for $\theta_{12} = 30°$ are also given in Fig. 6.20 (c & d) respectively. Results have shown that, as the wall contractions undergo compression phase and start to move toward the tube centreline, the axial velocity component increases near the contraction regions and the flow is displaced, bifurcated, and exits the tube from both directions. As discussed in the previous

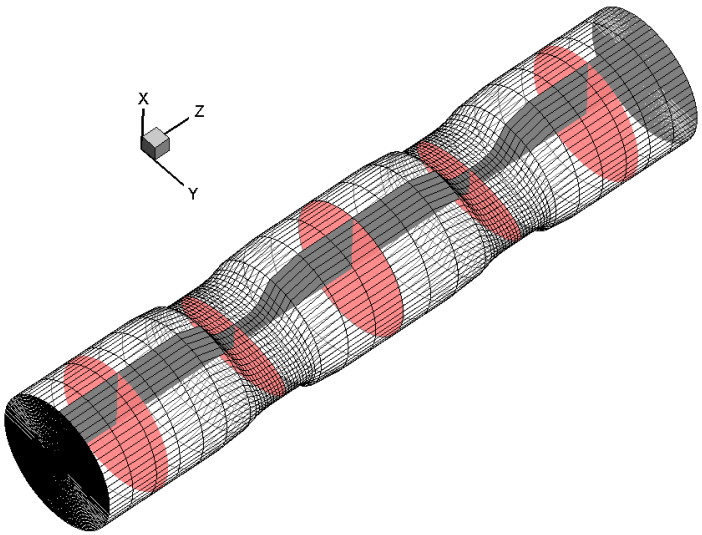

(a) 3-D view of non-symmetric contractions

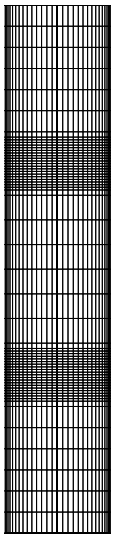

(b) (y-z) plane

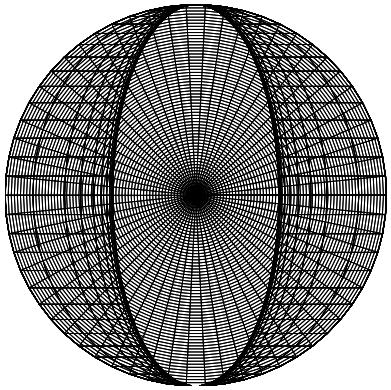

(c) (x-y) plane

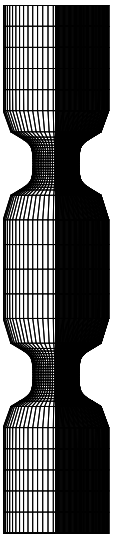

(d) (x-z) plane

Figure 6.13: Typical 3-D meshing: (a) Non-symmetric collapses of a $3-D$ tube with elliptical cross section subjected to two wall contractions. (b) $(y-z)$ plane of the tube that show the non-symmetric collapses and keeping major axis unchanged, $R_1 = R = 1$ constant. (c) $(x-y)$ plane to show the elliptical contractions. (d) $(x-z)$ plane of the tube that show the non-symmetric collapses by changing the minor axis with time,$R_2 = R_2(z,t)$.

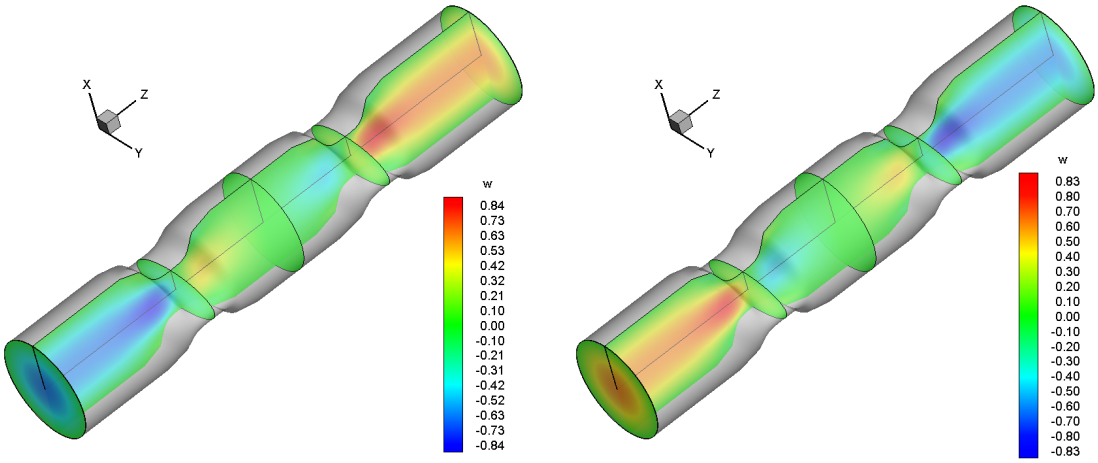

(a) $t = T/4$, $\theta_{12} = 0(deg.)$ (b) $t = 3T/4$, $\theta_{12} = 0(deg.)$

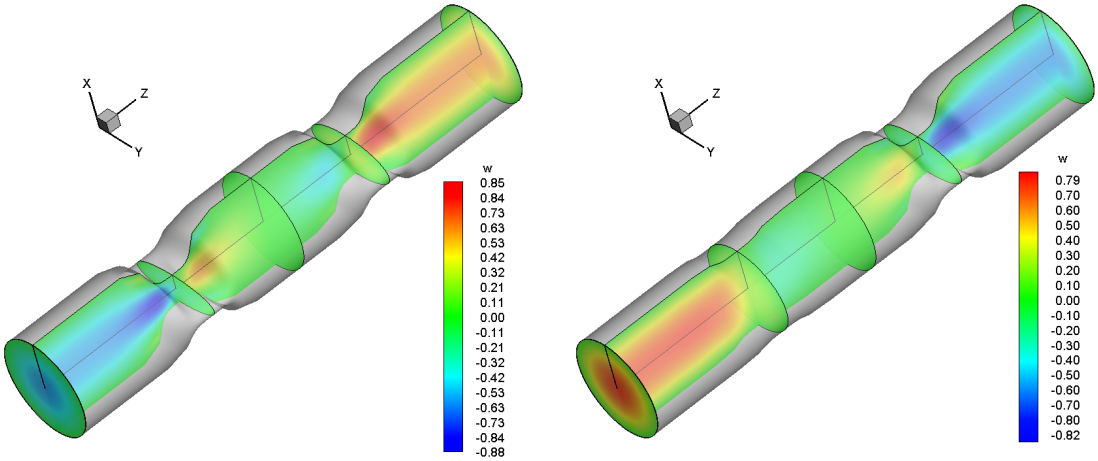

(c) $t = T/4$, $\theta_{12} = 30(deg.)$ (d) $t = 3T/4$, $\theta_{12} = 30(deg.)$

Figure 6.14: w-velocity contour lines using $3 - D$ Stokeslets-meshfree computations during compression time $t = T/4$ and expansion time at $t = 3T/4$: (a-b) phase lag $\theta_{12} = 0(deg.)$, (c-d) phase lag $\theta_{12} = 30(deg.)$

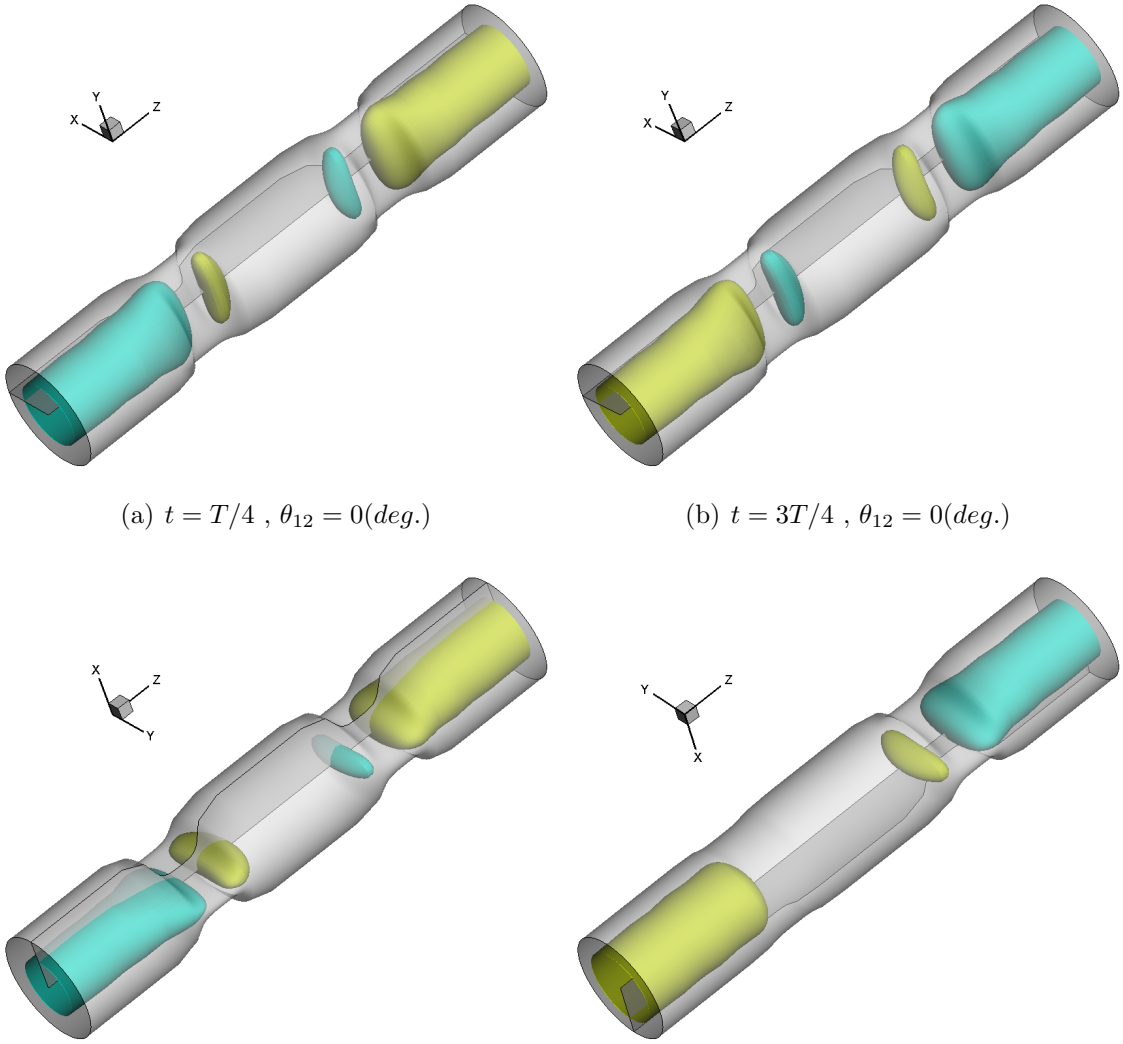

(a) $t = T/4$, $\theta_{12} = 0(deg.)$

(b) $t = 3T/4$, $\theta_{12} = 0(deg.)$

(c) $t = T/4$, $\theta_{12} = 30(deg.)$

(d) $t = 3T/4$, $\theta_{12} = 30(deg.)$

Figure 6.15: u-velocity iso-surfaces using $3 - D$ Stokeslets-meshfree computations during compression time $t = T/4$ and expansion time at $t = 3T/4$: (a-b) phase lag $\theta_{12} = 0(deg.)$, (c-d) phase lag $\theta_{12} = 30(deg.)$

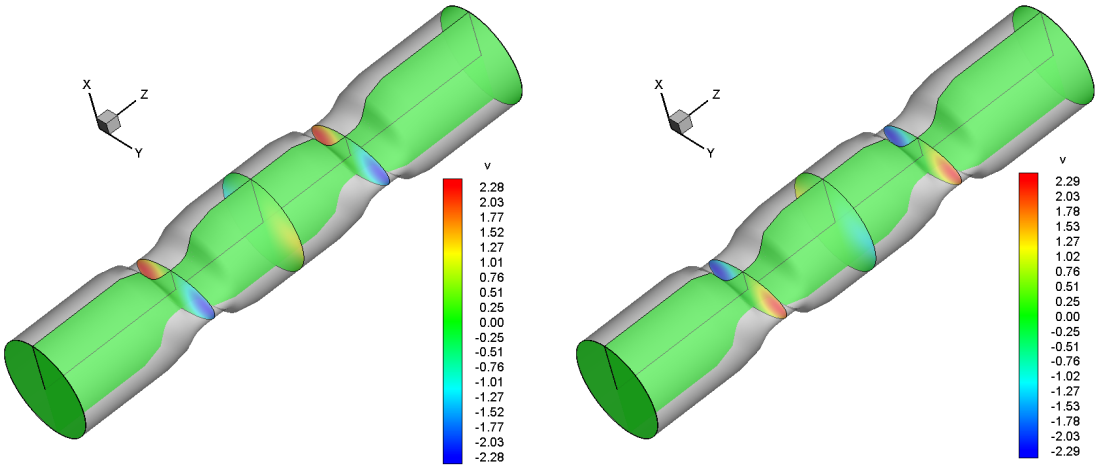

(a) $t = T/4$, $\theta_{12} = 0(deg.)$ (b) $t = 3T/4$, $\theta_{12} = 0(deg.)$

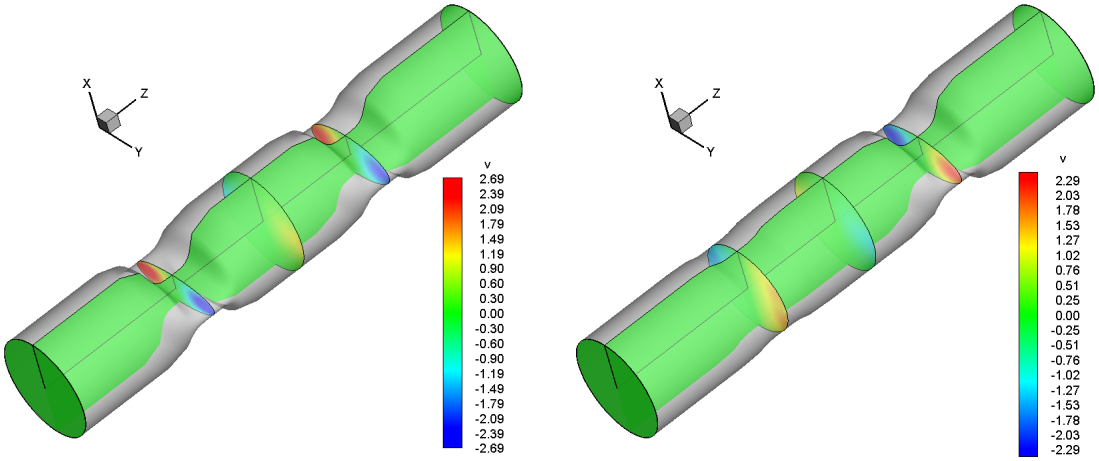

(c) $t = T/4$, $\theta_{12} = 30(deg.)$ (d) $t = 3T/4$, $\theta_{12} = 30(deg.)$

Figure 6.16: v-velocity contour lines using $3 - D$ Stokeslets-meshfree computations during compression time $t = T/4$ and expansion time at $t = 3T/4$: (a-b) phase lag $\theta_{12} = 0(deg.)$, (c-d) phase lag $\theta_{12} = 30(deg.)$

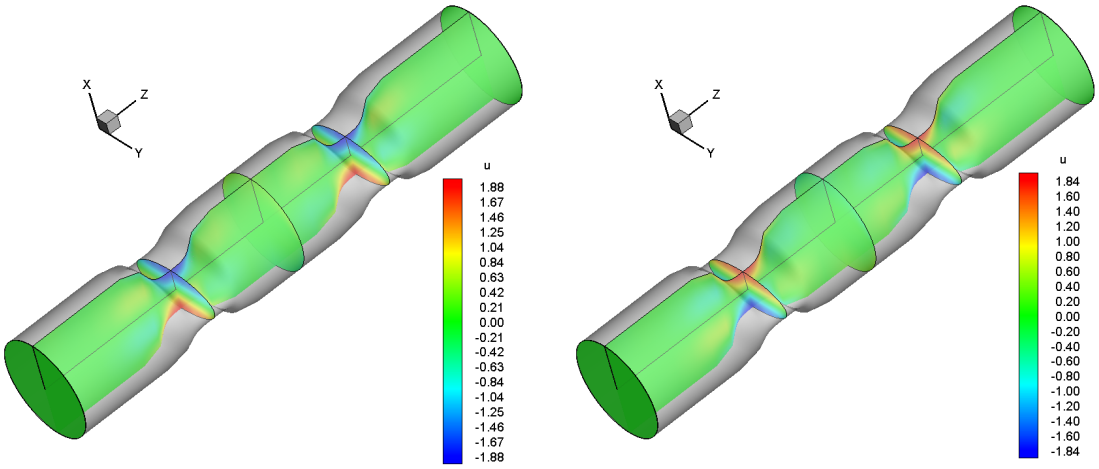

(a) $t = T/4$, $\theta_{12} = 0(deg.)$ (b) $t = 3T/4$, $\theta_{12} = 0(deg.)$

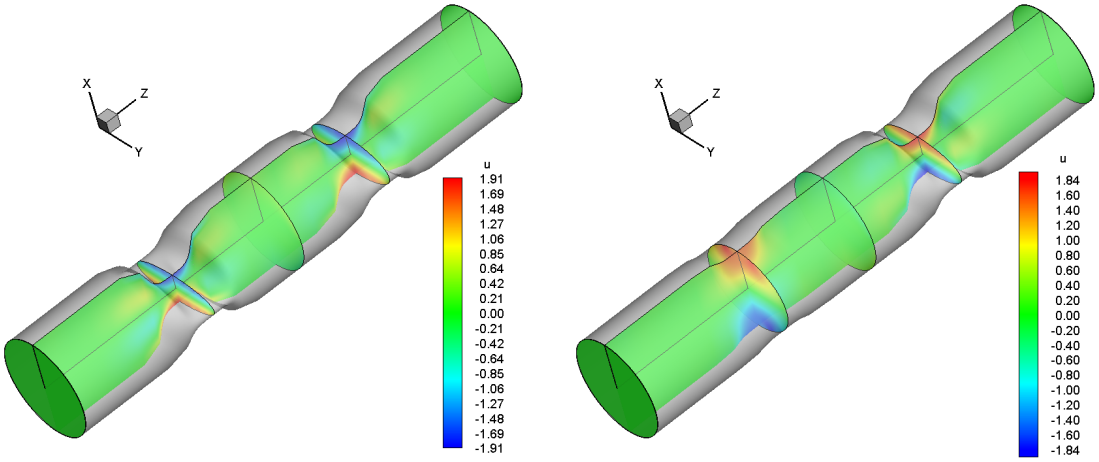

(c) $t = T/4$, $\theta_{12} = 30(deg.)$ (d) $t = 3T/4$, $\theta_{12} = 30(deg.)$

Figure 6.17: u-velocity contour lines using $3 - D$ Stokeslets-meshfree computations during compression time $t = T/4$ and expansion time at $t = 3T/4$: (a-b) phase lag $\theta_{12} = 0(deg.)$, (c-d) phase lag $\theta_{12} = 30(deg.)$

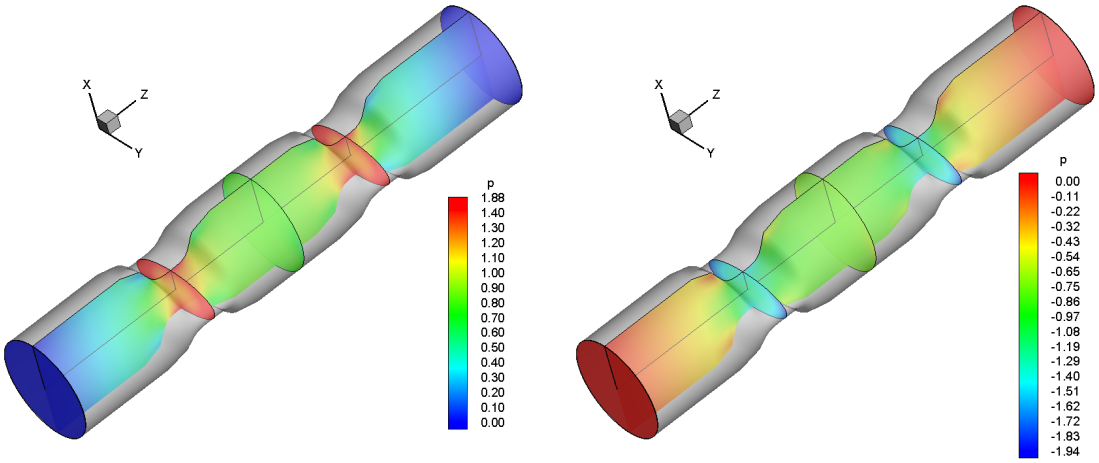

(a) $t = T/4$, $\theta_{12} = 0(deg.)$ (b) $t = 3T/4$, $\theta_{12} = 0(deg.)$

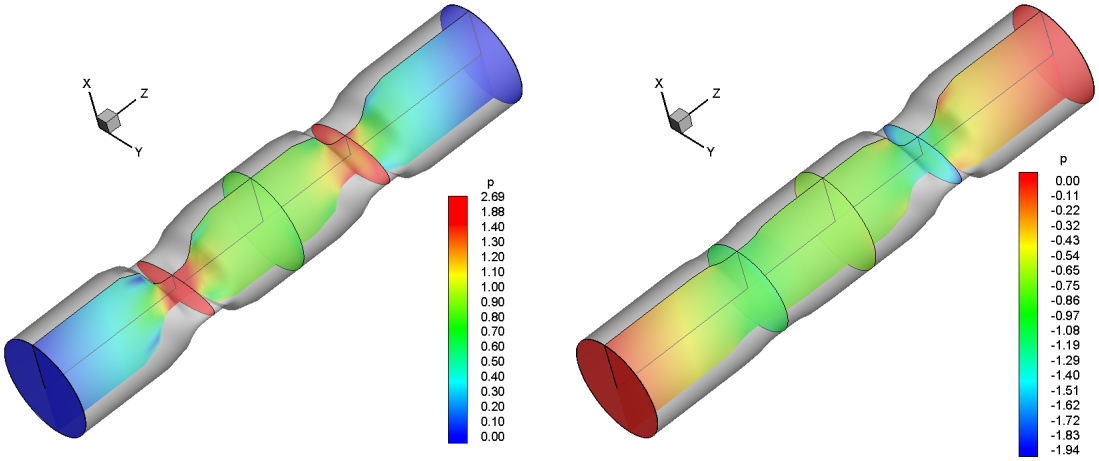

(c) $t = T/4$, $\theta_{12} = 30(deg.)$ (d) $t = 3T/4$, $\theta_{12} = 30(deg.)$

Figure 6.18: Pressure contour lines using $3 - D$ Stokeslets-meshfree computations during compression time $t = T/4$ and expansion time at $t = 3T/4$: (a-b) phase lag $\theta_{12} = 0(deg.)$, (c-d) phase lag $\theta_{12} = 30(deg.)$

cases, when $\theta_{12} = 0°$, there will be a stagnation region between the two contractions as a result of flow cancellation. This flow cancellation occurs due to the fact that each collapse sends flow to both directions away from the contraction zone. This is also clearly presented by drawing the axial velocity iso-surfaces as shown in Fig. 6.21 (a & b). This stagnation zone will be smoothed out, when the tube collapse operate with non-zero phase lag $\theta_{12} = 30°$, as shown in Fig. 6.21 (c & d). Moreover, the other velocity components namely v-velocity and u-velocity contour lines at different planes are given at similar compression and expansion snapshots times $t = T/4\&3T/4$ as shown in Fig. 6.22 and Fig. 6.23 respectively. Similar to the cases discussed previously, the pressure contours are also computed and shown in Fig. 6.24 (a & b) when contractions are set to move with a zero phase lag i.e., $\theta_{12} = 0°$, and in Fig. 6.24 (c & d) when $\theta_{12} = 30°$.

It is worthwhile to mention here that, As expected both case gives almost similar induced flow field patterns with slightly differences in magnitudes. However, these discrepancies in magnitudes might affect the time averaged quantities over a complete collapsing cycle. In section 6.6, we will show the time averaged net flow produced by each individual case of study and compare the output with the axisymmetric tube simulation case as will as with the 2D analytical tube solution.

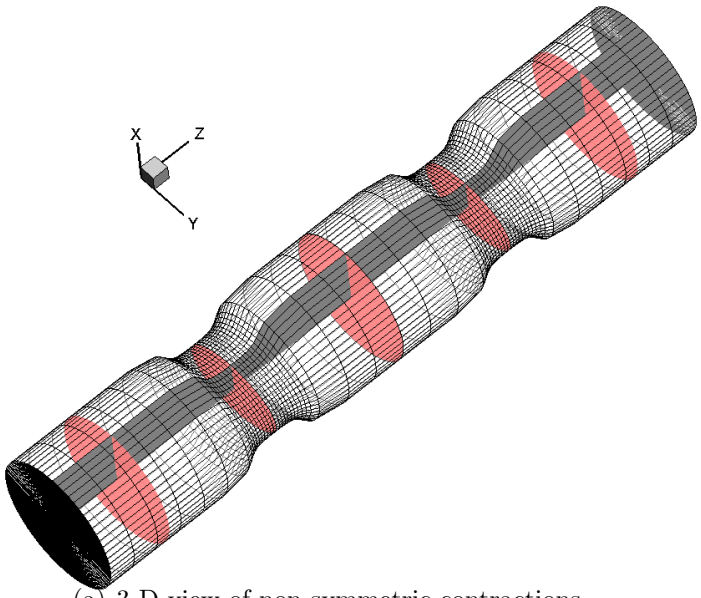

(a) 3-D view of non-symmetric contractions

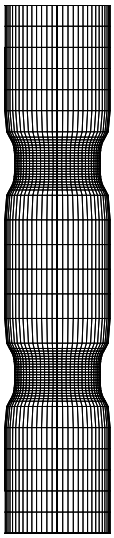

(b) (y-z) plane

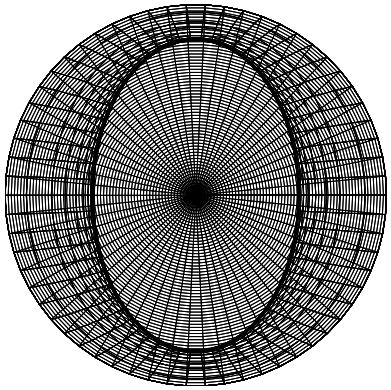

(c) (x-y) plane

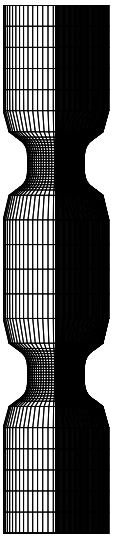

(d) (x-z) plane

Figure 6.19: Typical 3-D meshing: (a) Non-symmetric collapses of a $3-D$ tube with elliptical cross section subjected to two wall contractions. (b) $(y-z)$ plane of the tube that show the non-symmetric collapses by changing the major axis with time $R_1 = R_1(z,t)$. (c) $(x-y)$ plane to show the elliptical contractions. (d) $(x-z)$ plane of the tube that show the non-symmetric collapses by changing the minor axis with time, $R_2 = R_2(z,t)$.

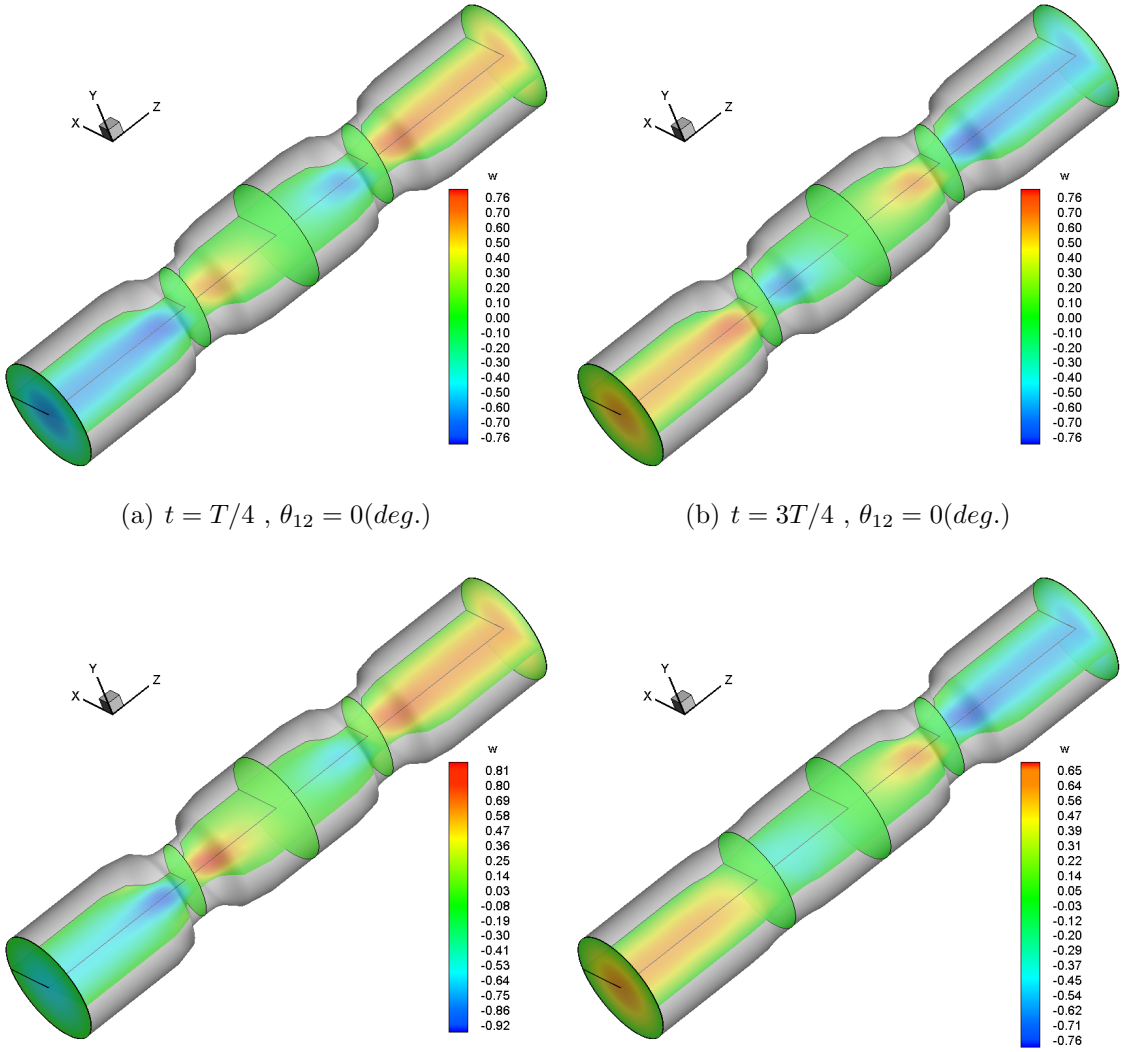

(a) $t = T/4$, $\theta_{12} = 0(deg.)$

(b) $t = 3T/4$, $\theta_{12} = 0(deg.)$

(c) $t = T/4$, $\theta_{12} = 30(deg.)$

(d) $t = 3T/4$, $\theta_{12} = 30(deg.)$

Figure 6.20: w-velocity contour lines using $3 - D$ Stokeslets-meshfree computations during compression time $t = T/4$ and expansion time at $t = 3T/4$: (a-b) phase lag $\theta_{12} = 0(deg.)$, (c-d) phase lag $\theta_{12} = 30(deg.)$

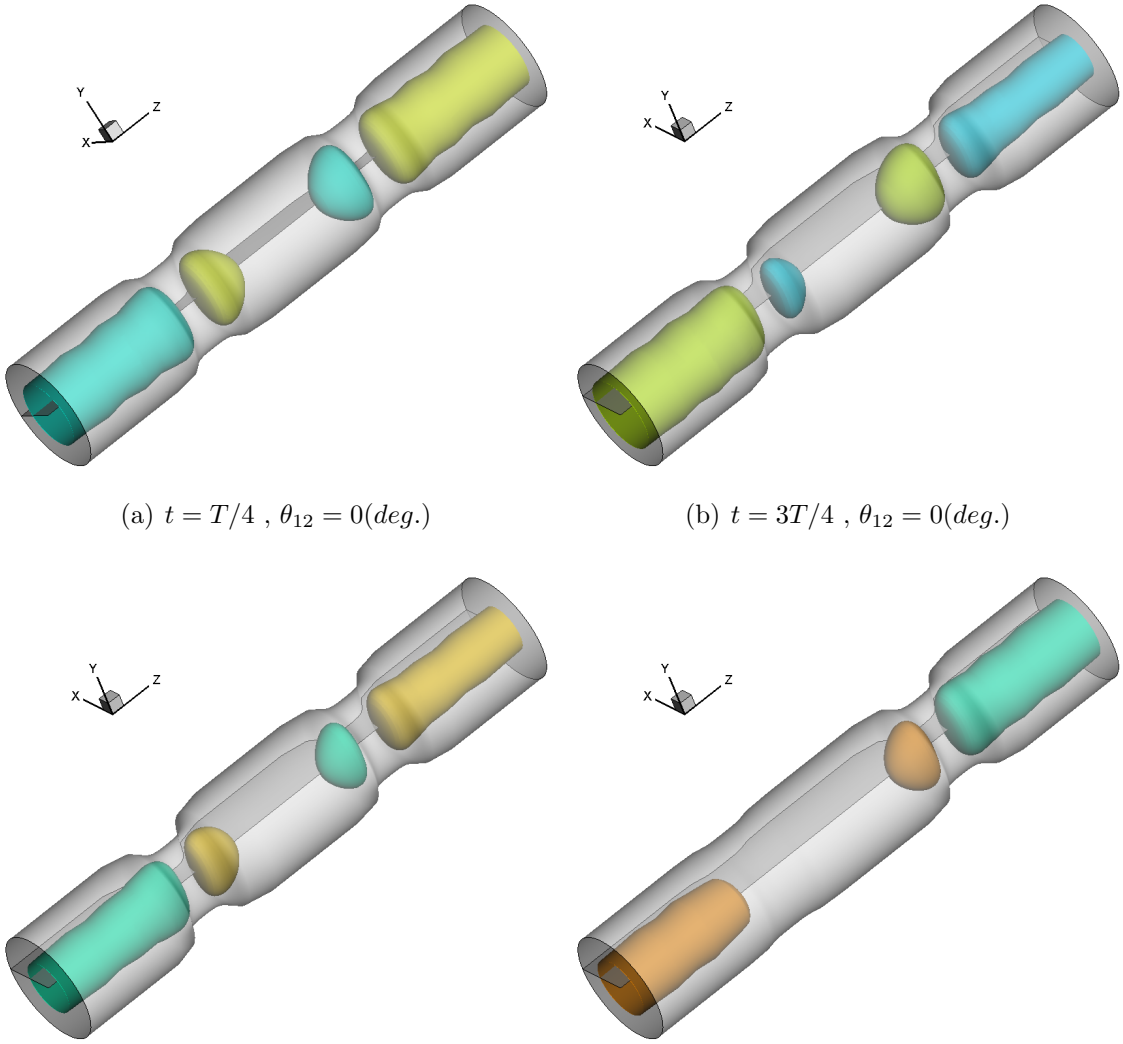

(a) $t = T/4$, $\theta_{12} = 0(deg.)$

(b) $t = 3T/4$, $\theta_{12} = 0(deg.)$

(c) $t = T/4$, $\theta_{12} = 30(deg.)$

(d) $t = 3T/4$, $\theta_{12} = 30(deg.)$

Figure 6.21: u-velocity iso-surfaces using $3 - D$ Stokeslets-meshfree computations during compression time $t = T/4$ and expansion time at $t = 3T/4$: (a-b) phase lag $\theta_{12} = 0(deg.)$, (c-d) phase lag $\theta_{12} = 30(deg.)$

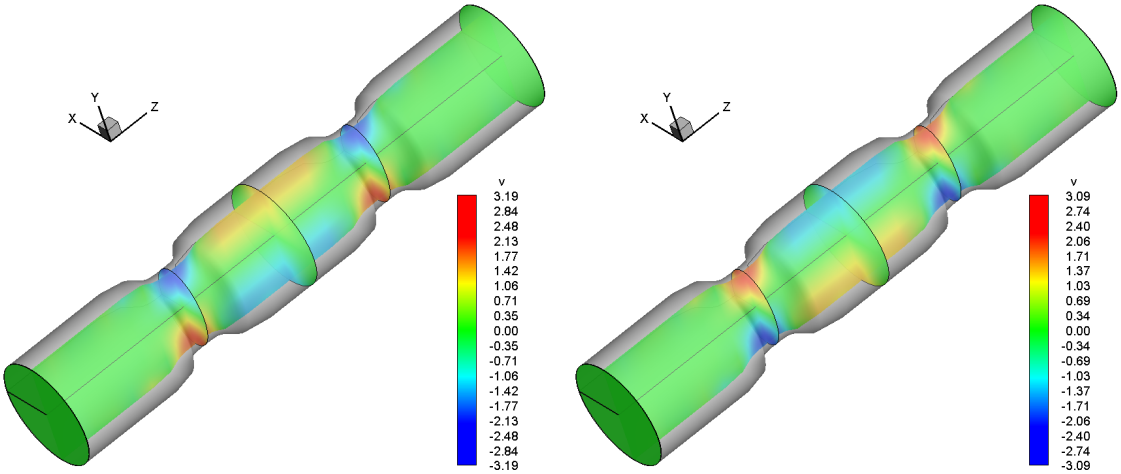

(a) $t = T/4$, $\theta_{12} = 0(deg.)$ (b) $t = 3T/4$, $\theta_{12} = 0(deg.)$

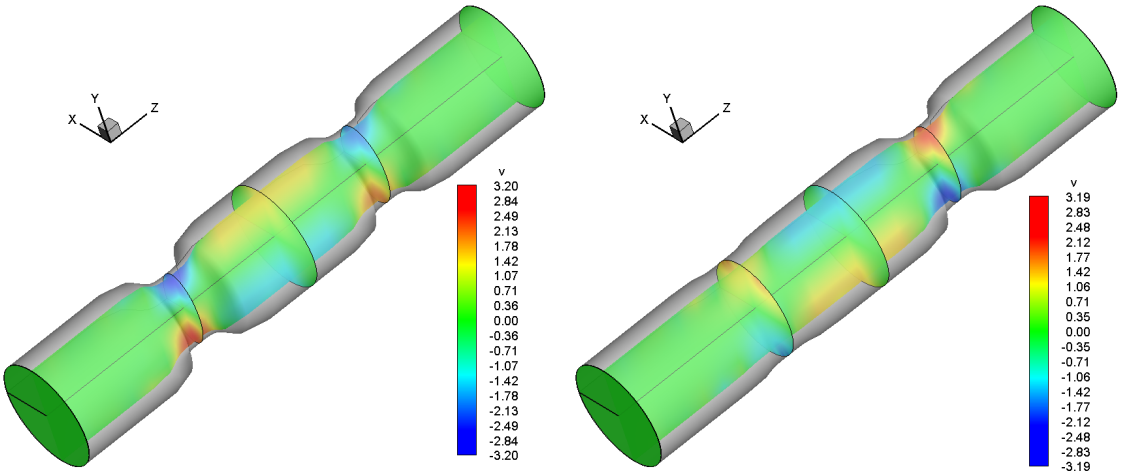

(c) $t = T/4$, $\theta_{12} = 30(deg.)$ (d) $t = 3T/4$, $\theta_{12} = 30(deg.)$

Figure 6.22: v-velocity contour lines using $3 - D$ Stokeslets-meshfree computations during compression time $t = T/4$ and expansion time at $t = 3T/4$: (a-b) phase lag $\theta_{12} = 0(deg.)$, (c-d) phase lag $\theta_{12} = 30(deg.)$

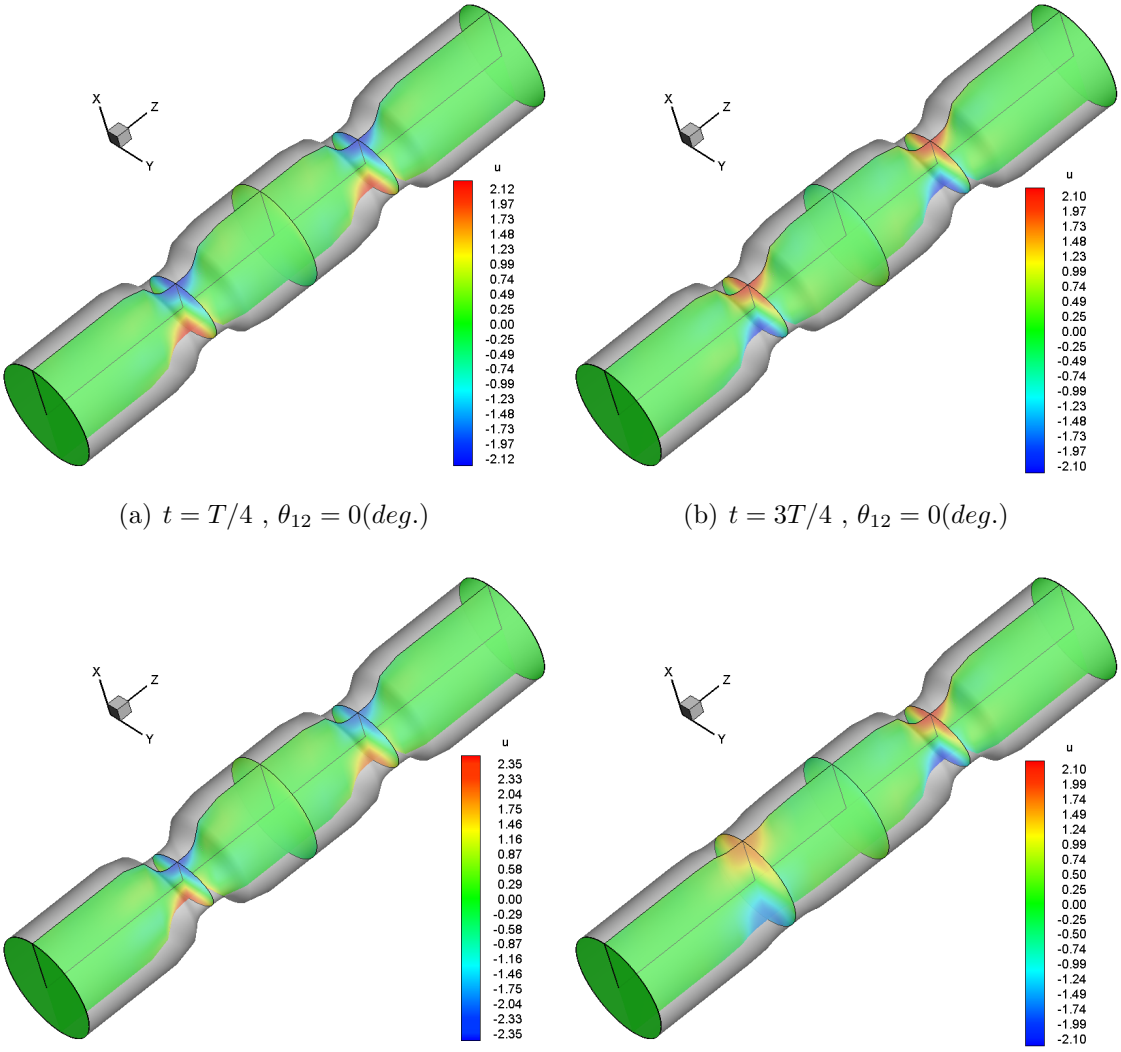

(a) $t = T/4$, $\theta_{12} = 0(deg.)$

(b) $t = 3T/4$, $\theta_{12} = 0(deg.)$

(c) $t = T/4$, $\theta_{12} = 30(deg.)$

(d) $t = 3T/4$, $\theta_{12} = 30(deg.)$

Figure 6.23: u-velocity contour lines using $3 - D$ Stokeslets-meshfree computations during compression time $t = T/4$ and expansion time at $t = 3T/4$: (a-b) phase lag $\theta_{12} = 0(deg.)$, (c-d) phase lag $\theta_{12} = 30(deg.)$

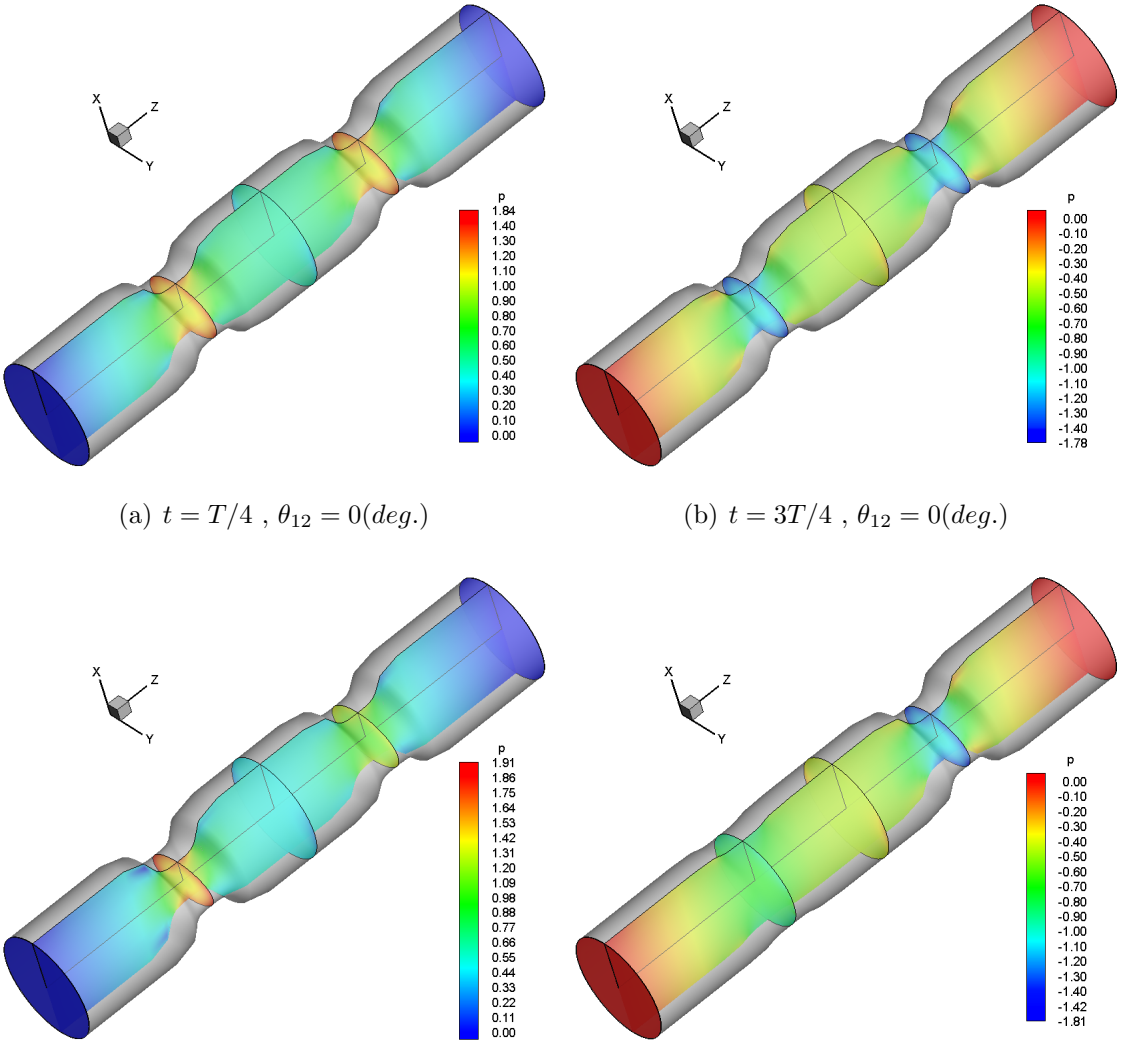

(a) $t = T/4$, $\theta_{12} = 0(deg.)$

(b) $t = 3T/4$, $\theta_{12} = 0(deg.)$

(c) $t = T/4$, $\theta_{12} = 30(deg.)$

(d) $t = 3T/4$, $\theta_{12} = 30(deg.)$

Figure 6.24: Pressure contour lines using $3 - D$ Stokeslets-meshfree computations during compression time $t = T/4$ and expansion time at $t = 3T/4$: (a-b) phase lag $\theta_{12} = 0(deg.)$, (c-d) phase lag $\theta_{12} = 30(deg.)$

6.5 3-D Channel with Moving Two Contractions

In this part, we use the similar numerical technique namely, the method of fundamental solutions MFS along with the regularized Stokeslets approach Cortez (2001) to solve for the induced flow field in a three-dimensional channel with two moving wall contractions. These contractions are attached to the top wall only and are set to move according to the wall profile identical to the one used previously in chapter 2, section 2.2.3. A schematic that shows the problem setting along with the distributions of the Stokeslets source points is given in Fig. 6.25 (a). The motion protocol profiles used in actuating the wall contractions are given in Fig. 6.25 (b). A typical 3-D meshing with no clustering that shows a non-symmetric collapses of a 3-D channel that have a square cross-sectional area and subjected to two wall contractions is shown in Fig. 6.26.

The goal of this section is to perform 3-D simulations and compare the flow field with our previously derived 2-D analytical channel model in chapter 2. Furthermore, to calculate the net flow induced by the 3-D simulations and compare it with the 2-D counter part. In other words, results from both the 3-D Stokeslets meshfree computations and the 2-D theoretical model are compared at different snapshot times. The comparison process will be given at two snapshots of times $t = T/4, 3T/4$ that represent compression and expansion collapsing phases. Moreover, two distinct phase lags $\theta_{12} = 0°\&30°$ are used in the comparison process. In other words, two main cases for situations where, the wall contractions are set to move with phase lags $\theta_{12} = 0°\&30°$ respectively. A detailed comparison between results computed by the 2-D analytical model and by the 3-D meshfree computations is given at the same geometric and flow conditions with values listed in Table 4.3. The details of the results for both cases are given in the following subsections.

6.5.1 Moving Two Contractions with $\theta_{12} = 0(deg.)$

In a similar procedure used in the tube simulation cases, once the strengths of the Stokeslets points are calculated, the MFS can be then applied to reconstruct the induced flow inside the channel. Here, a similar algorithm is used to obtain the Stokeslets strengths as given previously in subsection 4.5.2. The structure and development of the flow field induced by only using two wall contractions undergoes cyclic compression and expansion motions are shown. Results obtained by using both

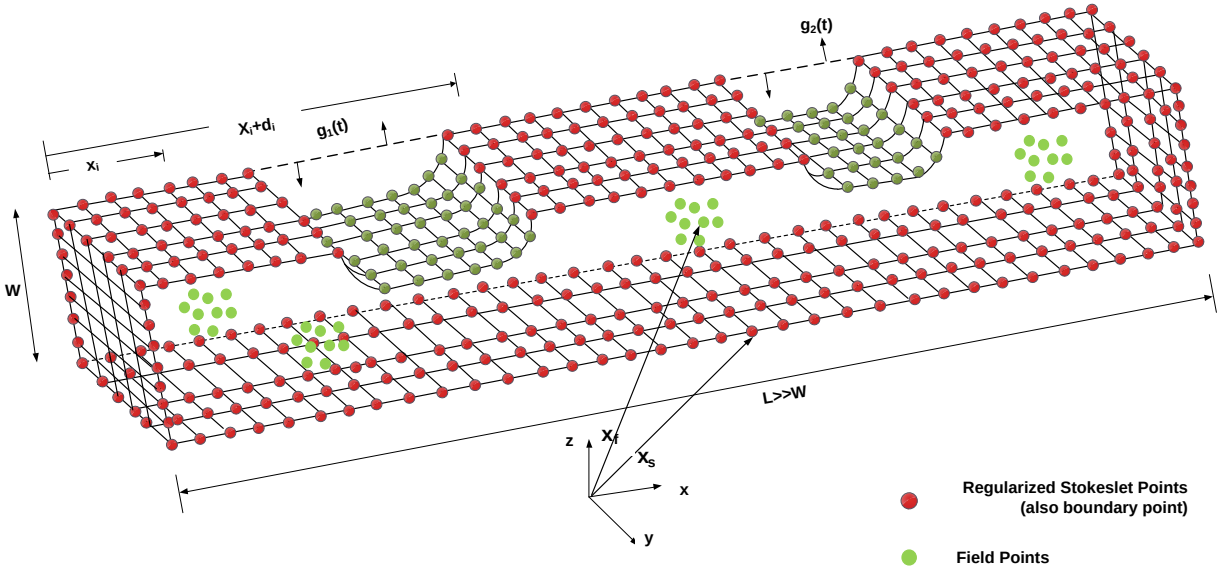

(a)

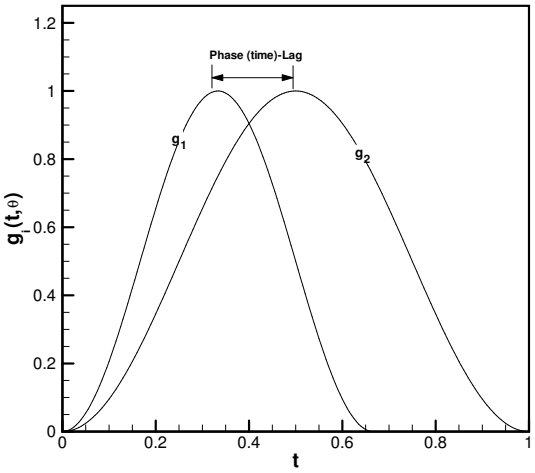

(b)

Figure 6.25: Problem Schematic: (a) $2D$ channel with moving upper wall contraction profile $H_2(x,t)$ and stationary lower wall profile $H_1(x)$ (b) $g_1(t)$ and $g_2(t)$, the motion protocols assigned to the first and second contractions, respectively.

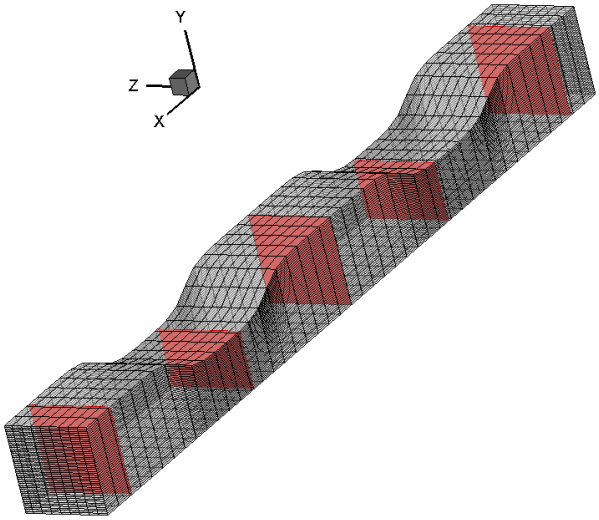

(a) 3-D view of non-symmetric contractions

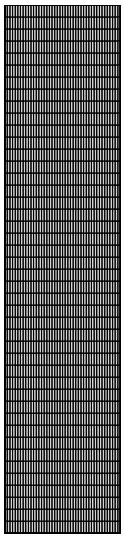

(b) (z-x) plane

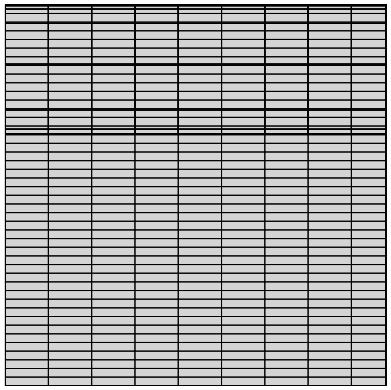

(c) (z-y) plane

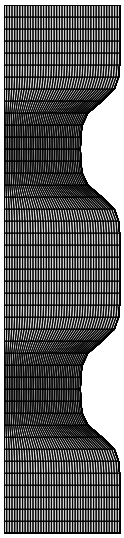

(d) (y-x) plane

Figure 6.26: Typical 3-D meshing with no clustering: (a) Non-symmetric collapses of a 3-D channel with square cross section subjected to two wall contractions. (b) $(z-x)$ plane that shows unchanged channel width unchanged, $W = 1$ constant. (c) $(z-y)$ plane to show the square-cross sectional. (d) $(z-x)$ plane of the channel that shows the non-symmetric collapses by changing the height axis with time,$H_2 = H_2(x,t)$.

the 3-D meshfree computations and are compared with the 2-D analytical counterpart as given below.

In Fig. 6.27, we show a comparison between the axial velocity contour lines obtained numerically and analytical when wall contractions are set to move with a zero phase lag $\theta_{12} = 0^{\circ}$. Contour lines that are obtained numerically for the u-velocity component are given at different planes during the compression and expansion snapshots times $t = T/4\&3T/4$ as shown in Fig. 6.27 (a & b) respectively. Moreover, the contour lines computed based on the 2-D analytical model at the same times are shown in Fig. 6.27 (c & d) respectively.

Results have shown that, as the wall contractions undergo compression phase and start to move toward the bottom wall, the axial velocity component increases near the contraction regions and the flow is displaced, bifurcated, and exit the channel from both directions. Since each collapse sends flow to both directions away from the contraction zone, there will be a stagnation region between the two contractions due to the flow cancellations. This stagnation region clearly shown by drawing the axial velocity iso-surfaces as shown in Fig. 6.28 (a & b). A reasonably good agreement has observed between the axial velocity obtained numerically ans theoretically.

Similarly, the vertical velocity contour lines at different planes during the compression and expansion snapshots defined by time $t = T/4\&3T/4$ are shown in Fig. 6.29 (a & b) respectively. The contour lines computed based on the 2-D analytical model at the same times are also shown in Fig. 6.29 (c & d). Results obtained analytically have shown to be characterized by two regions with opposite direction underneath each contraction zone as shown in Fig. 6.29 (c & d). Although, results have shown a fair agreement (same order of magnitudes are attained) between the flow contour lines obtained analytically and numerically using meshfree approach. Yet, these two observed regions could not been captured using the 3-D computations and the vertical velocity component computed numerically is more stretched.

A comparison between the pressure contours obtained numerically as shown in Fig. 6.29 (a & b) and the analytical counterpart as shown in Fig. 6.29 (c & d) is given here when wall contractions are set to move with a zero phase lag $\theta_{12} = 0^{\circ}$. The contour lines are given at similar compression and expansion snapshot times as mentioned before. For example, results at compression time $t = T/4$ show that, as the wall contractions start to move toward the bottom wall, high pressure

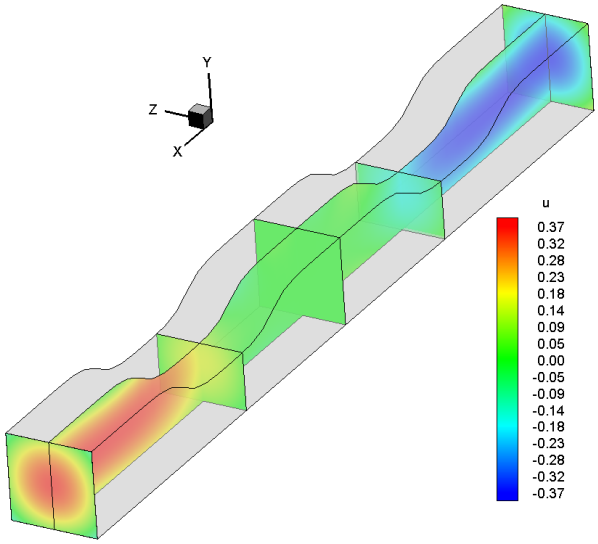

(a) 3-D Computations at $t = T/4$, $\theta_{12} = 0(deg.)$

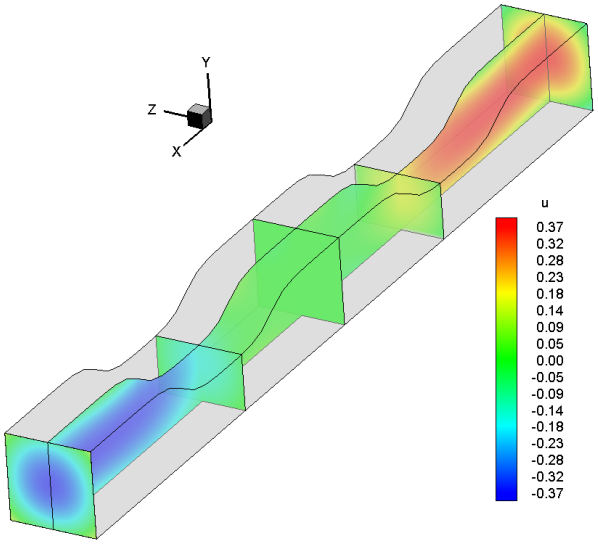

(b) 3-D Computations at $t = 3T/4$, $\theta_{12} = 0(deg.)$

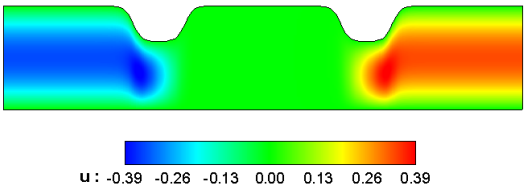

(c) 2-D Theory at $t = T/4$, $\theta_{12} = 0(deg.)$

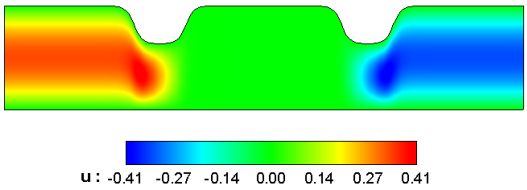

(d) 2-D Theory at $t = 3T/4$, $\theta_{12} = 0(deg.)$

Figure 6.27: Axial velocity contour lines: (a-b) $3-D$ Stokeslets-meshfree computations, (c-d) Derived $2-D$ theoretical solution. Results are given for wall contractions with phase lag $\theta_{12} = 0(deg.)$ during compression time $t = T/4$ and expansion time at $t = 3T/4$.

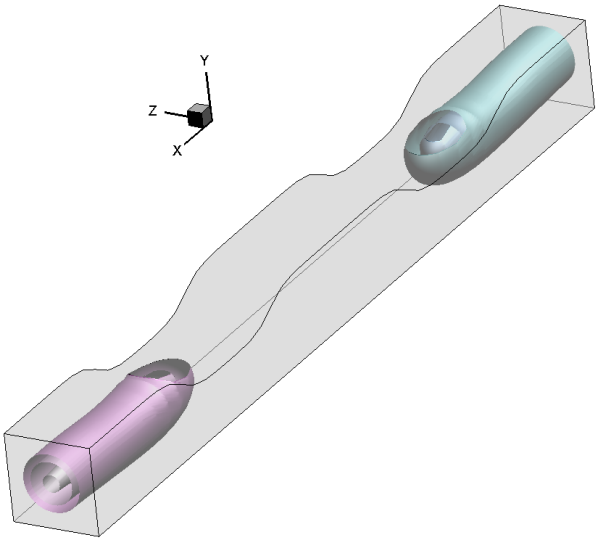

(a) 3-D Computations at $t = T/4$, $\theta_{12} = 0(deg.)$

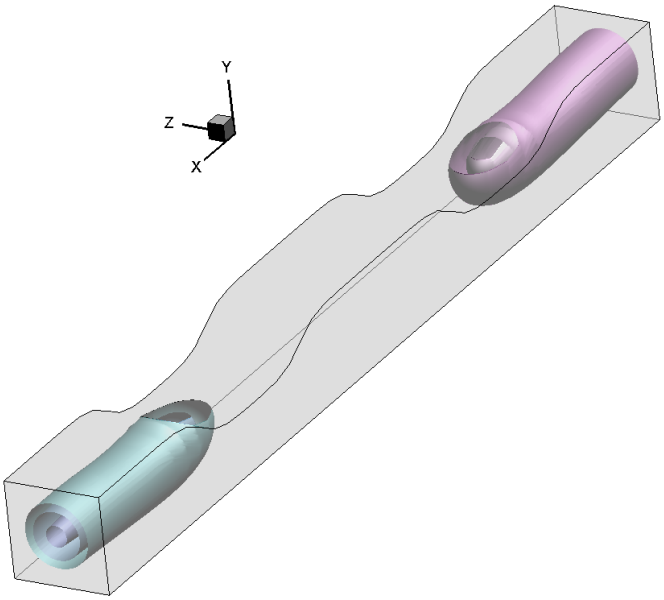

(b) 3-D Computations at $t = 3T/4$, $\theta_{12} = 0(deg.)$

Figure 6.28: Axial velocity iso-surfaces using $3-D$ Stokeslets-meshfree computations: (a) compression time $t = T/4$, (b) expansion time at $t = 3T/4$. Results are given for wall contractions with phase lag $\theta_{12} = 0(deg.)$.

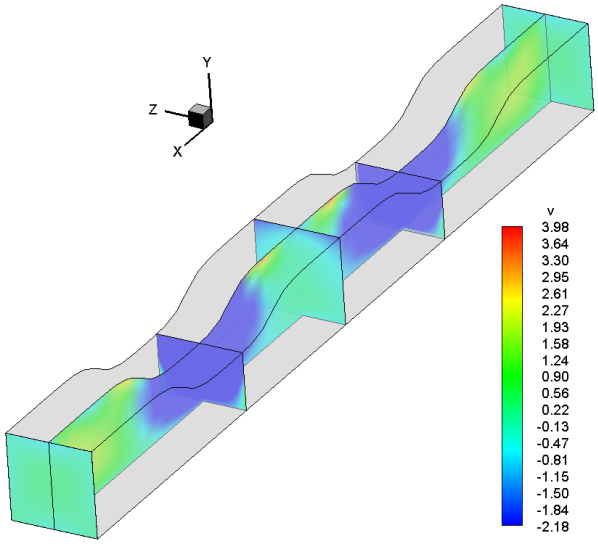

(a) 3-D Computations at $t = T/4$, $\theta_{12} = 0(deg.)$

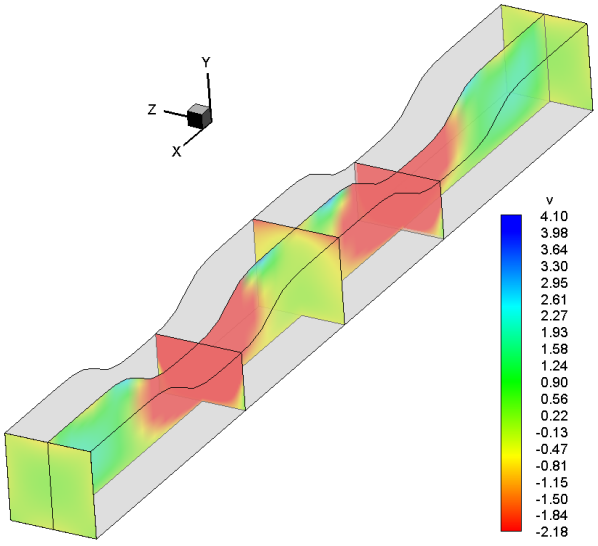

(b) 3-D Computations at $t = 3T/4$, $\theta_{12} = 0(deg.)$

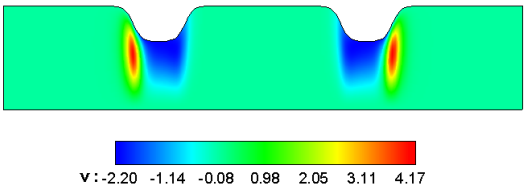

(c) 2-D Theory at $t = T/4$, $\theta_{12} = 0(deg.)$

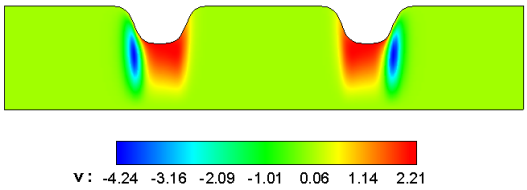

(d) 2-D Theory at $t = 3T/4$, $\theta_{12} = 0(deg.)$

Figure 6.29: Vertical velocity contour lines: (a-b) $3-D$ Stokeslets-meshfree computations, (c-d) Derived $2-D$ theoretical solution. Results are given for wall contractions with phase lag $\theta_{12} = 0(deg.)$ during compression time $t = T/4$ and expansion time at $t = 3T/4$.

with adverse and favourable gradients are formed in and near the contraction regions. This induces a flow away from the compression sites and forces the flow to exit the channel from both ends. This flow bifurcation is pointed out from the velocity contours. Moreover, the pressure has attained its maximum or total value in the stagnation zone between the two contractions. Similarly, data for pressure contours during the expansion phase at time $t = 3T/4$ are given. As expected, when the contraction regions expand back away from the bottom wall, an exactly similar contour lines and streamlines are developed but with opposite signs when compared with data at compression time $t = T/4$. Results have shown that, unlike the vertical velocity, the pressure contours obtained numerically have very good agreements with the 2-D analytical results.

6.5.2 Moving Two Contractions with $\theta_{12} = 30(deg.)$

In addition to results presented from the previous case study, where the two contractions move with no phase lag $\theta_{12} = 0°$, we also show similar plots for velocity and pressure contours at a situation where the wall contractions are set to move with a phase lag $\theta_{12} = 30°$. Results that are obtained by using the Stokeslets meshfree computational method and by the 2-D analytical model are compared at similar snapshot times that represent both compression $t = T/4$ and expansion $t = 4T/4$ phases.

For instance, contour lines for both velocity components are shown in Figs. (6.31-6.33). Similarly, the pressure contours are shown in Fig. 6.34 at both compression and expansion times as well. Results have shown that, unlike the situation where $\theta_{12} = 0°$ which is always characterized by having a stagnation zone of zero velocities between the two contractions and the flow is not allowed to transport. When $\theta_{12} = 30°$, this stagnation zone is relaxed and there will be flow transport within the region between the two contractions. This flow motion between the contraction regions are clearly shown by the axial velocity contour lines calculated analytically and numerically as given in Figs. 6.31 and is confirmed by plotting the axial velocity iso surfaces as shown in Fig. 6.32. Moreover, there is a pressure gradients in the region between the two contractions which indicate that, there is a flow transport in this region as shown in Fig. 6.34.

Finally, the effect of the phase lag protocol that have been assigned to the wall collapse motions

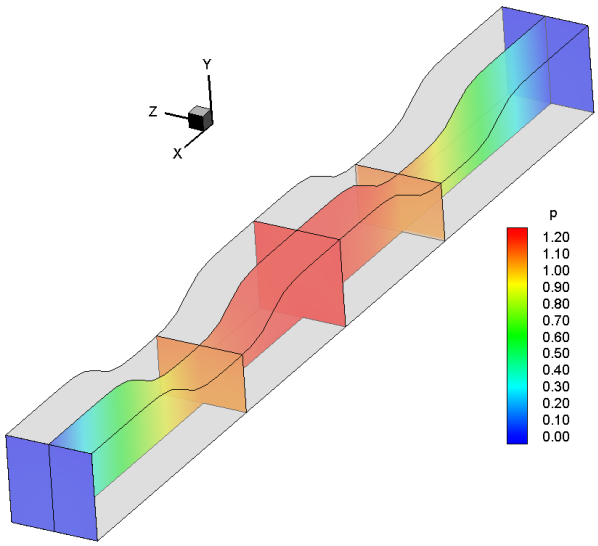

(a) 3-D Computations at $t = T/4$, $\theta_{12} = 0(deg.)$

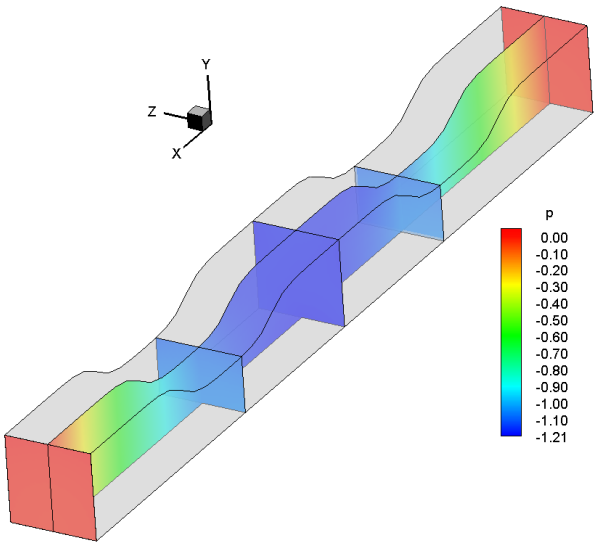

(b) 3-D Computations at $t = 3T/4$, $\theta_{12} = 0(deg.)$

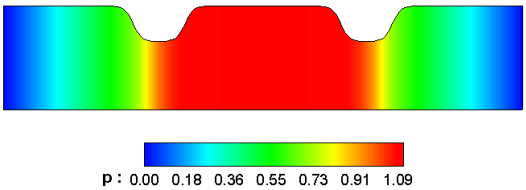

(c) 2-D Theory at $t = T/4$, $\theta_{12} = 0(deg.)$

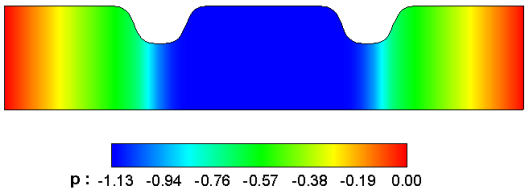

(d) 2-D Theory at $t = 3T/4$, $\theta_{12} = 0(deg.)$

Figure 6.30: Pressure contour lines: (a-b) $3-D$ Stokeslets-meshfree computations, (c-d) Derived $2-D$ theoretical solution. Results are given for wall contractions with phase lag $\theta_{12} = 0(deg.)$ during compression time $t = T/4$ and expansion time at $t = 3T/4$.

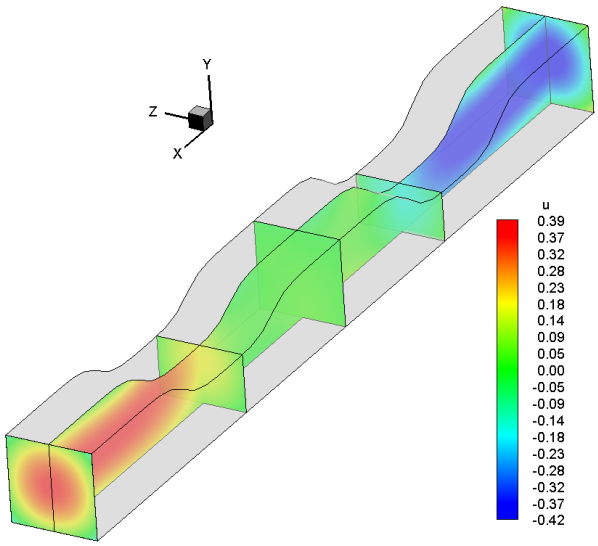

(a) 3-D Computations at $t = T/4$, $\theta_{12} = 30(deg.)$

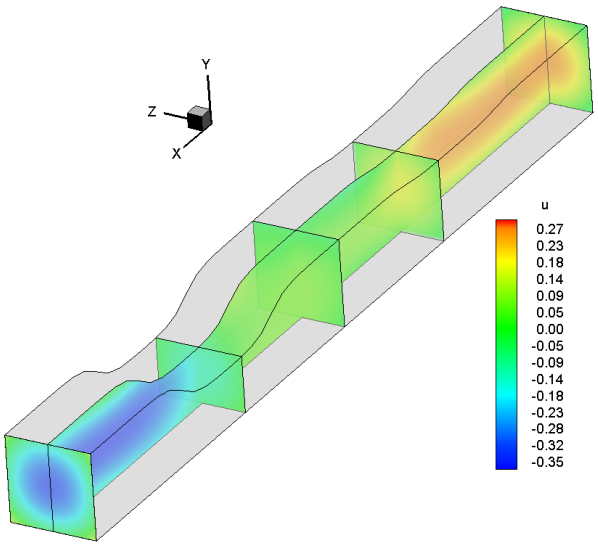

(b) 3-D Computations at $t = 3T/4$, $\theta_{12} = 30(deg.)$

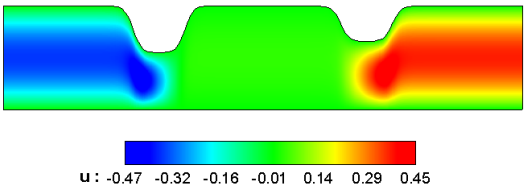

(c) 2-D Theory at $t = T/4$, $\theta_{12} = 30(deg.)$

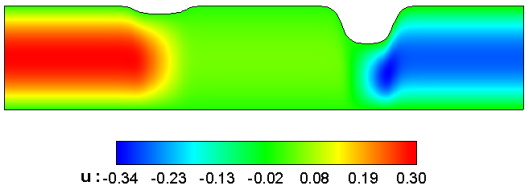

(d) 2-D Theory at $t = 3T/4$, $\theta_{12} = 30(deg.)$

Figure 6.31: Axial velocity contour lines: (a-b) $3-D$ Stokeslets-meshfree computations, (c-d) Derived $2-D$ theoretical solution. Results are given for wall contractions with phase lag $\theta_{12} = 30(deg.)$ during compression time $t = T/4$ and expansion time at $t = 3T/4$.

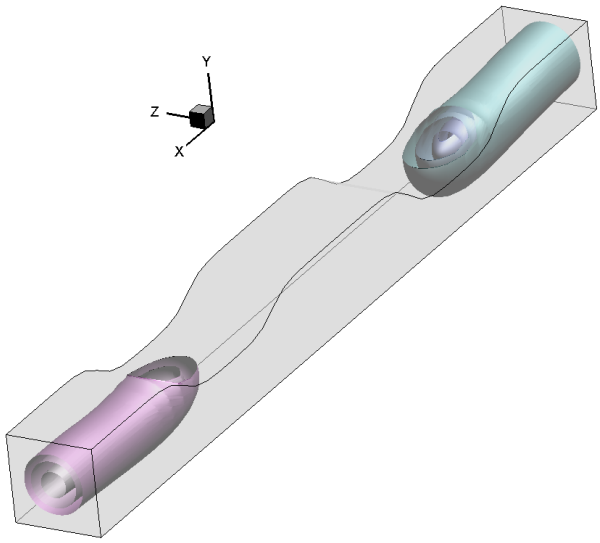

(a) 3-D Computations at $t = T/4$, $\theta_{12} = 30(deg.)$

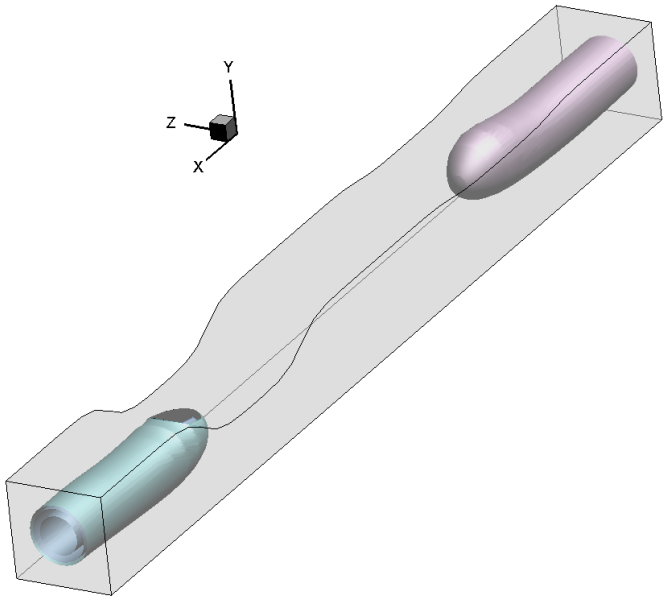

(b) 3-D Computations at $t = 3T/4$, $\theta_{12} = 30(deg.)$

Figure 6.32: Axial velocity iso-surfaces using $3-D$ Stokeslets-meshfree computations: (a) compression time $t = T/4$, (b) expansion time at $t = 3T/4$. Results are given for wall contractions with phase lag $\theta_{12} = 30(deg.)$.

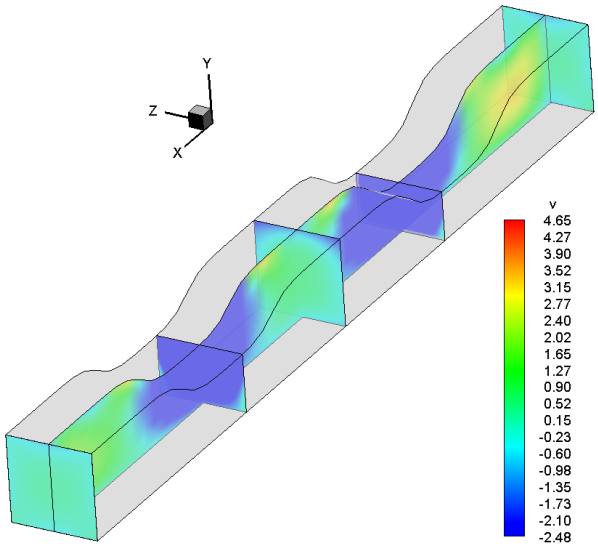

(a) 3-D Computations at $t = T/4$, $\theta_{12} = 30(deg.)$

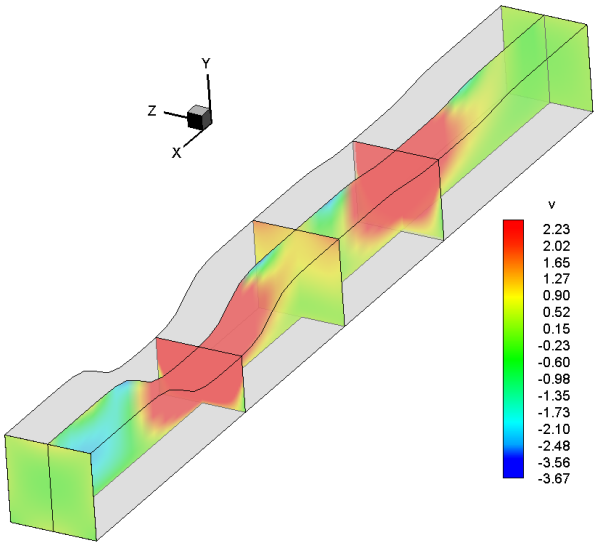

(b) 3-D Computations at $t = 3T/4$, $\theta_{12} = 30(deg.)$

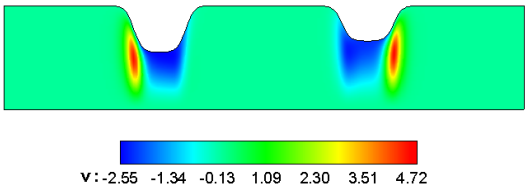

(c) 2-D Theory at $t = T/4$, $\theta_{12} = 30(deg.)$

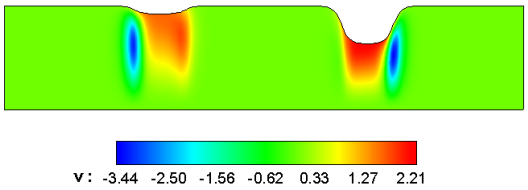

(d) 2-D Theory at $t = 3T/4$, $\theta_{12} = 30(deg.)$

Figure 6.33: Vertical velocity contour lines: (a-b) $3-D$ Stokeslets-meshfree computations, (c-d) Derived $2-D$ theoretical solution. Results are given for wall contractions with phase lag $\theta_{12} = 30(deg.)$ during compression time $t = T/4$ and expansion time at $t = 3T/4$.

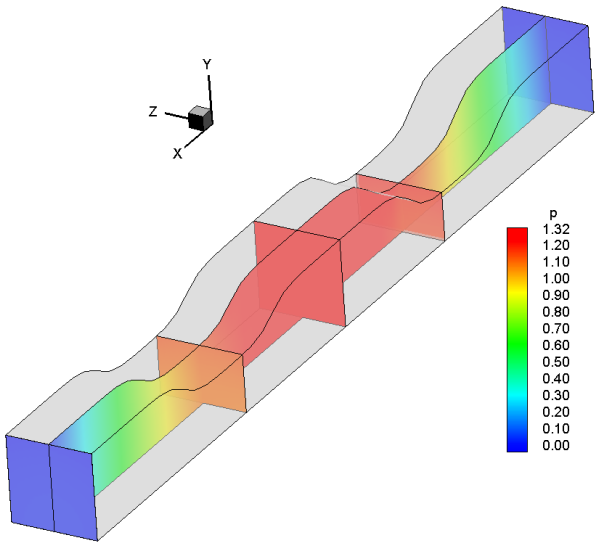

(a) 3-D Computations at $t = T/4$, $\theta_{12} = 30(deg.)$

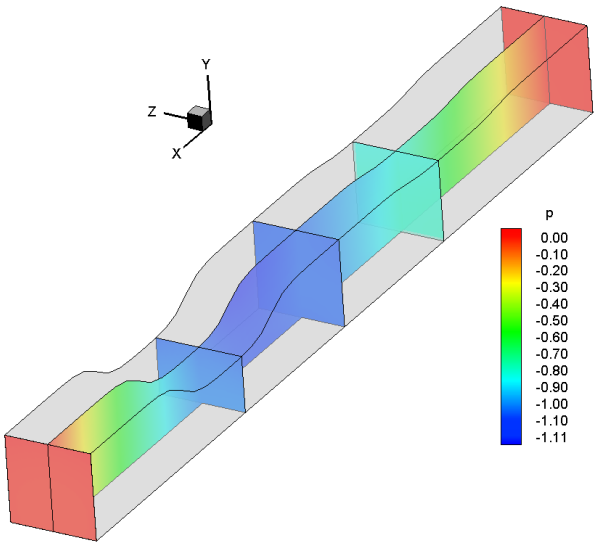

(b) 3-D Computations at $t = 3T/4$, $\theta_{12} = 30(deg.)$

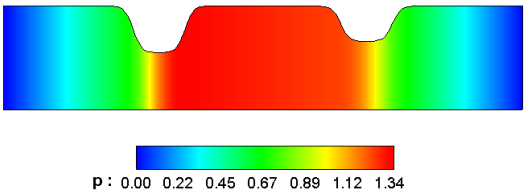

(c) 2-D Theory at $t = T/4$, $\theta_{12} = 30(deg.)$

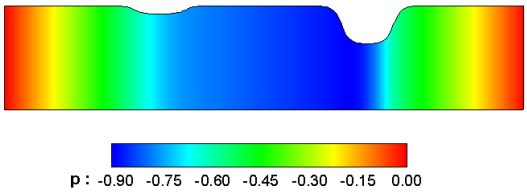

(d) 2-D Theory at $t = 3T/4$, $\theta_{12} = 30(deg.)$

Figure 6.34: Pressure contour lines: (a-b) $3-D$ Stokeslets-meshfree computations, (c-d) Derived $2-D$ theoretical solution. Results are given for wall contractions with phase lag $\theta_{12} = 30(deg.)$ during compression time $t = T/4$ and expansion time at $t = 3T/4$.

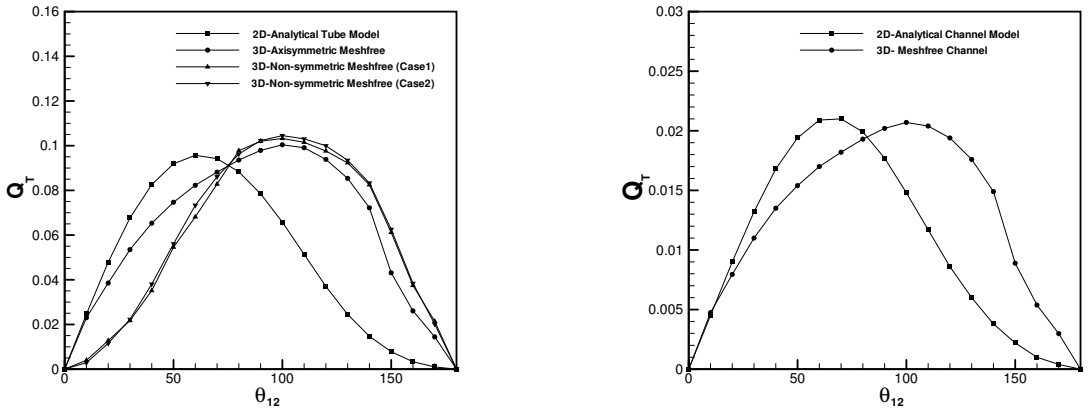

(a) Tube Pumping Model (b) Channel Pumping Model

Figure 6.35: Time averaged net flow rate comparisons between the $2D$ analytical solution and $3D$ Stokeslets-meshfree computations for both tube and channel pumping models

on the instantaneous and on the time averaged volumetric flow rate is investigated in section 6.6. Specifically, the time averaged volumetric flow rate over a complete contraction-expansion cycle for various phase lag values is studied to explore which contraction setting can be used to produce unidirectional net flows out of this system.

6.6 Computing the Net Flow Rate

Based on the 3-D Stokeslets-meshfree velocity field presented in the previous sections for both tubes and channels, we calculate the time averaged net flow rate Q_T as a function of the contraction movements phase lag θ_{12} parameter in this part. The goal is to compare the computed time averaged net flow based on the 3-D results and compare it with the time averaged net flow counterpart derived in our 2-D theoretical analysis given in chapter 2, for tube see section 2.1.3, and section 2.2.3 for channels.

In order to calculate the time averaged net flow rate, we first have to calculate the instantaneous net flow rate at desired areas along the axial directions. The details of calculating the time averaged

net flow rate can be also found in Aranda et al. (2011), which can be re-given briefly as

$$q(x,t) = \int_{A(x,t)} Q(x,y,z,t)dydz \tag{6.17}$$

where, $A(x,t)$ is the cross-sectional area along the tube/channel length x and time t. The above integration is approximated numerically using the standard trapezoidal rule. Once we have computed the instantaneous flow rate $q(x,t)$, we may average it over one period of time $T = 1/S_t$ or we may find the averaged flow rate per unit length. The time averaged net flow rate is simply computed by averaging computed values at discrete times since the flow rate is a periodic function in time. The time averaged net flow rate per unit length of the tube/channel is computed by

$$Q_T(x) = \frac{1}{T}\int_0^T q(x,t)dt \tag{6.18}$$

where, $T = 1/S_t$ is the time period. In the discrete form, the time averaged net flow rate can be computed using the quadrature trapezoidal rule,

$$Q_T(x) \approx \frac{1}{T}\sum_0^{n\Delta t} q(x,n\Delta t)\Delta t \tag{6.19}$$

where, $\Delta t = T/N_T$, N_T is the number of quadrature points in a time period $T = 1/S_t$.

In Fig. 6.35, we show the time averaged net flow rate as a function of the phase lag parameter. In the same figure, results obtained by the 2-D analytical solution are compared with the 3-D Stokeslets-meshfree computations for both tube and channel pumping models. The time averaged net flow for the tube model is given in Fig. 6.35 (a), where a comparison between the 3-D axisymmetric, asymmetric (case 1 and case 2) with the 2-D tube model derived previously in 2.1 is given.

Results have shown that, there is no a good agreement between 2-D axisymmetric and the 2-D tube model. However, the 3-D axisymmetric net flow rate have a similar trend as a function of the phase lag similar to 2-D analytical solution except the fact that, the maximum value occurs at $\theta_{12} = 110(deg.)$ rather than $\theta_{12} = 70(deg.)$ in the case of 2-D analytical counterpart. The net flow rate produced by 3-D axisymmetric and asymmetric cases are very close to each other and predict similar optimum values. This is because of, we have conserved the tube instantaneous volume at

each time step in all the simulated cases. In other words, at each simulated time step, we forced the axisymmetric and asymmetric tube volumes to be the same, so we can can have fair comparisons between the time averaged net flow rate for both cases.

Similarly, in Fig. 6.35 (b), the time averaged net flow rate as a function of the phase lag parameter for channel calculations is given. In particular, a comparison between the 3-D Stokeslets-messhfree channel results and the 2-D analytical model derived previously in 2.2 is also shown. Results have shown that, there is no a good agreement between 3-D channel and the 2-D channel analytical model. However, the 3-D channel net flow rate have a similar trend as a function of the phase lag similar to 2-D analytical solution except the fact that, the maximum values occurs at $\theta_{12} = 105(deg.)$ rather than $\theta_{12} = 65(deg.)$ which is predicted by the 2-D analytical model.

In summary, although the net flow rate distribution as a function of phase lag for both 3-D Stokeslets-meshfree computations and 2-D analytical results are different. They are still share similar physical interpretations about the pumping hypothesis we propose in this dissertation.

Chapter 7

Conclusions

In this dissertation we proposed two versions of a novel bioinspired pumping paradigm that is neither peristaltic nor belongs to impedance mismatch class of pumping mechanisms found in the literature. These insect-inspired pumping models presented here are expected to function efficiently in the microscale flow regime within simple channel/tube geometries and in a complex network of channels. The first pumping approach have shown the ability of inducing a unidirectional net flow by using an inelastic tube or channel with at least two moving contractions that move with non-zero phase(time) lags with respect to each other. Results have shown that, as a direct result of the wall contractions, a stagnation line/plane appears during wall compressions and disappears during expansion counterparts. The instantaneous motion of this stagnation line act as a "ghost-valve" and have a direct relation to the pumping mechanism claimed in this study. The second pumping approach presented; is a new concept for controlling the flow pumping directionality in a network of branching channels. The approach is termed as "selective pumping in a network."

Both theoretical analysis and Stokeslets-meshfree computational methods are used to solve for the 2D and 3D viscous flow transport in several micro-geometries such as, simple tubes and channels as well as complex network if channels with prescribed moving wall contractions. The derived theoretical analysis is based on both lubrication theory and quasi-steady approximations at low Reynolds number flow regime. The meshfree numerical method is based on the method of fundamental solutions MFS that uses a set of singularized force elements "Stokeslets" to induce the

flow motions. Moreover, the passive particle tracking simulation approach in the Lagrangian frame of reference is also used to strengthen and support our proposed pumping paradigm presented throughout research in this dissertation.

The results presented in this dissertation are expected to be helpful in mimicking features of physiological systems in insects and guide efforts to fabricate novel microfluidic devices and new generation of bioinspired hydraulic microsystems for flow control with improved efficiency. The details for the conclusions and findings out of this research are summarized in the subsequent sections.

7.1 Theoretical Findings

Inspired by the tracheal tube and rhythmic wall contractions found in the physiological system in insects, mathematical models that can solve for the induced flow transport in confined geometries with moving boundaries are derived in this dissertation. The mathematical analyses have shown to work as a novel pumping mechanism "ghost-valve pumping principle" at the microscales flow regime. The theoretical part of the analysis is based on the lubrication theory and the quasi-steady approximations, which are used to model flow motions and transport at low Reynolds numbers $Re \in [0, \delta]$ regime. Analytical expressions for the velocity field, static pressure, wall shear stress, and the volumetric flow rate are derived as a function of the prescribed wall motions.

The derived analysis has applied for flows in tubes, channels and networks with single or multiple of non-propagative class of wall contractions similar to the one that have been observed in the insect physiological system. The derived analysis has kept general to accommodate for any number of contractions, however we restricted our attention to only two collapses in case of tube/channel modelling, and a maximum of three contractions in each channel segment in the network simulation case of study. The kinematics and the geometry of these contractions is prescribed by a generic wall profile that allows for contractions to move with or without phase (time) lags with respect to each other.

The flow field developments and structures during both compression and expansion snapshot times that are imposed by wall contractions are calculated explicitly. The time averaged net flow rate over

a complete collapsing cycle is evaluated and has given as a function of phase lags and tube collapsing ratios. The present mathematical model is then optimized using the constrained optimization technique to find the design parameters that maximize the time averaged net flow. In addition, passive particle tracking simulations for both tube and channel with moving wall contractions are given to provide a qualitative support of the idea of using the setup under consideration here as a micropump and to show the ability of this setup to produce unidirectional flows. In additions, a quantified full numerical simulation based on the Stokeslets-method of fundamental solutions (MFS) were also given for validation purposes.

7.2 Meshfree Computational Findings

The main numerical and technical outcome of this study was the ability of performing a bi-validation process for both the analytical and numerical approaches used. The analytical results were used to validate the Stokeslet computational approach studied in this dissertation. Conversely, the numerical data were used to validate the assumptions made in the derivation of the theoretical model. Results show a good agreement between the analytical model and meshfree computations in the cases investigated. Furthermore, The numerical results show that, unlike grid-based CFD methods, the MFS require just a few singularity boundary points to approximate the type of flow under consideration here and produce accurate results. Other important features of the Stokeslets-based meshfree approach are, their robustness and adaptivity. Also, it was found that as the Stokeslets move according to the wall contraction protocol, the method adapts itself to accommodate the motions and accurate coefficients can be predicted, and the full flow complexity can be captured at every instant in time during the collapsing cycle. Furthermore, validation cases have been established by performing three-dimensional Stokeslets-meshfree simulations for both tubes and channels. Similarly, numerical results have shown to be in a good agreement between both analytical and meshfree computations in almost all of the cases that we considered. Therefore, can propose the following research claim/facts in a formal way as follows,

7.3 Dissertation Final Claims/Facts

Based on the theoretical analysis and meshfree computational results given in this dissertation, we claim the following pumping hypotheses:

- An inelastic tube or channel with non-peristaltic (non-propagative), and localized moving wall contractions can function as a pump, i.e., it can produce a unidirectional flow. According to the non-peristaltic wall collapse regime studied in this dissertation, the only requirement for producing unidirectional flow is the presence of at least two contraction sites that can move with a slight phase lag with respect to each other. Moreover, for a $2D$ analysis, a maximum net flow is produced when the contractions have the optimum phase lag value of about $\theta_{opt} \in [60 - 70]^{\circ}$. Moreover, the amount of the net flow produced has found to be a strong function of the collapse amplitude and motion phase lags. The amount of the induced net flow can be maximized by forcing the two contractions to move with an optimal phase lag value. Furthermore, the direction of the net flow can be altered according to the actuation collapse protocol.

- Transporting, manipulating and controlling flow directionality of a small amount of fluid in a complex network of channels can be done efficiently but using our proposed "selective-pumping-in-a-network" protocol. This can be achieved by actuating various contractions with different amplitudes and phase lags with respect to each other to induce the desired pressure drop across the network. The induced pressure gradient will force the fluid elements to chose a certain direction to go through a specific branch and avoids several possible routes or branches.

In summary, the present study can ideally provide some initial guidelines for the fabrication of novel bioinspired microfluidic devices and more specifically a new class of valveless pumping paradigm inspired by the motions of wall contractions observed in many of physiological systems. For instance, the rhythmic collapsing motions observed in insect respiratory systems are good candidates of these biomimetics micro devices. The results from this study could provide a basis for fabricating novel microfluidic devices inspired by physiological systems in insects.

Bibliography

Aboelkassem, Y., Staples, A. E., 2012a. Flow transport in a microchannel induced by moving wall contractions: a novel micropumping mechanism. Acta Mech. 223(3), 463–480.

Aboelkassem, Y., Staples, A. E., 2012b. Stokeslets-meshfree computations and theory for flow in a collapsible microchannel. Theor. Comput. Fluid Dyn. Published online, DOI 10.1007/s00162–012–0269–7.

Aboelkassem, Y., Staples, A. E., Socha, J., 2011. Microscale flow pumping inspired by rhythmic tracheal compressions in insects. Proceedings of the ASME Pressure Vessels and Piping. PVP2011, 57061.

Ainley, J., Durkin, S., Embid, R., Boindala, P., Cortez, R., 2008. The method of images for regularized stokeslets. J. of Comput. Phys. 227, 4600–4616.

Alves, C., Silvestre, A., 2004. Density results using stokeslets and a method of fundamental solutions for the stokes equations. Eng. Analysis with boundary Elements 28, 1245–1252.

Aranda, V., Cortez, R., Fauci, L., 2011. Stokesian peristaltic pumping in a three-dimensional tube with a phase-shift asymmetry. Phys. Fluids 23, 081901.

Batchelor, G. K., 1967. An introduction to fluid mechanics. Cambridge University Press.

Burmester, T., 2005. A welcome shortage of breath. Nature 433, 471–472.

Chen, C. W., Young, D. L., Tsai, C. C., Murugesan, K., 2005. The method of fundamental solutions for inverse 2d stokes problems. J. Comput. Mech. 37, 2–14.

Chu, A. K.-H., 2004. Transport control within a microtube. Physical review E 70, 061902.

Cortez, R., 2001. The method of regularized stokeslets. SIAM J. Sci. Comput. 23, 1204–1225.

Cortez, R., Fauci, L., Medovikov, A., 2005. The method of regularized stokeslets in three dimensions : analysis, validation, and applications to helical swimming. Phys. of Fluids 17, 031504.

Fairweather, G., Karageorghis, A., 1998. The method of fundamental solutions for elliptic boundary value problems. Adv. Comput. Math. 9, 69–95.

Feng, J., Josepf, D. D., 1995. The unsteady motion of solid bodies in creeping flows. J. Fluid Mech. 303, 83–102.

Fung, Y. G., Yih, C. S., 1968. Peristaltic transport. ASME: J. Appl. Mech. 35, 669–675.

Hariharan, P., Seshadri, V., Banerjee, R. K., 2008. Peristaltic transport of non-newtonian fluids in a diverging tube with different wave forms. Mathematical and Computer Modelling 48, 998–1017.

Harrison, J. F., 2003a. Respiratory Systems. Encyclopedia of Insects. Editors, V.H. Resh and R. Carde, Academic Press, San Diego.

Harrison, J. F., 2003b. Tracheal System. Encyclopedia of Insects. Editors, V.H. Resh and R. Carde, Academic Press, San Diego.

Hasimoto, H., Sano, O., 1980. Stokeslets and eddies in creeping flow. Ann. Rev. Fluid Mech. 12, 335–363.

Hayat, T., Saleem, N., Ali, N., 2009. Peristaltic flow of a carreau fluid in a channel with different wave forms. Numerical Methods for Paratial Diff. Eqs. 26, 519–534.

Hu, S. P., Fan, C. M., Chen, C. W., Young, D. L., 2005. Method of fundamental solutions for stokes' first and second problems. J. of Mechanics 21, 25–31.

Jaffrin, M. Y., Shapiro, A. H., 1971. Peristaltic pumping. Ann. Rev. Fluid Mech. 3, 13–36.

Kelley, C. T., 1999. Iterative Methods for Optimization. SIAM.

Li, M., Brasseur, J. G., 1993. Non-steady peristaltic transport in finite-length tubes. J. of Fluid Mechanics 248, 129–151.

Macagno, E., Christensen, J., 1980. Fluid mechanics of the duodenum. Ann. Rev. Fluid Mech. 12, 139–158.

Macagno, E., Christensen, J., Lee, L., 1982. Modeling the effect of wall movement on absorption in the intestine. Am. J. Physiol. 243, G541–G550.

Mahmood, T., Merkin, J., 1990. The flow in a narrow duct with an indentation or hump on one wall. Warme-und Stoffubertrangung 22, 69–76.

Nation, J. L., 2008. Insect Physiology and Biochemistry. CRC Press.

Neumaier, A., 1998. Solving ill-conditioned and singular linear systems : A tutorial on regularization. SIAM Rev. 40, 636–666.

Pandolfi, A., Ortiz, M., 2007. Improved design of low-pressure fluidic microvalves. J. Micromech. Microeng. 17, 1487–1493.

Pedley, T., Stephanoff, K. D., 1985. Flow along channel with a time-dependent indentation in one wall: The generation of vorticity waves. J. Fluid Mech. 160, 337–367.

Poullikkas, A., Karageorghis, A., Georgiou, G., Ascough, J., 1998. The method of fundamental solutions for stokes flows with a free surface. Numer Methods Partial. Diff. Eq. 14, 667–678.

Pozrikids, C., 1992. Boundary integral and singularity methods for linearized viscous flow. Cambridge University Press.

Ralph, M., Pedley, T. J., 1988. Flow in a channel with moving indentation. J. Fluid Mech. 190, 87–112.

Secomb, T., 1978. Flow in a channel with pulsating walls. J. Fluid Mech. 88, 273–288.

Shapiro, A. H., Jaffrin, M. Y., 1969. Peristaltic pumping with long wavelengths at low reynolds number. J. Fluid Mech. 37, 799–825.

Singh, P., Radhakrishnan, V., Narayan, K. A., 1990. Squeezing flow between parallel plates. Ingenieur-Archiv 60, 274–281.

Skalak, F., Wang, C. Y., 1978. On the unsteady squeezing of a viscous fluid from a tube. J. Austral. Math. Soc. 21 (Series B), 65–74.

Smyrlis, Y.-S., 2009. Applicability and applications of the method of fundamental solutions. J. Math. Comp. 78, 1399–1434.

Socha, J. J., Frster, T., Greenlee, K., 2010. Issues of convection in insects respiration : Insights from synchrotron x-ray imaging and beyond. Respiratory Physiology and Neurobiology 173S, S65–S73.

Socha, J. J., Lee, W.-K., Harrison, J. F., Waters, J. S., Fezzaa, K., Westneat, M. W., 2008. Correlated patterns of tracheal compression and convective gas exchange in a carabid beetle. J. Experimental Biology 211, 3409–3420.

Thien, N. P., Low, H. T., 1989. On the flow of a non-newtonian liquid induced by intestine-like contractions. J. of Biomechanical Eng. 111, 1–8.

Tsai, C. C., Young, D. L., Fan, C. M., Chen, C. W., 2006a. Mfs with time-dependent fundamental solutions for unsteady stokes equations. Eng. Analysis with Boundary Elements 30, 897–908.

Tsai, C. C., Young, D. L., Lo, D. C., Wong, T. K., 2006b. The method of fundamental solutions for three-dimensional stokes flow in exterior field. J. of Eng. Mech. 132, 317–326.

Uchida, S., Aoki, H., 1977. Unsteady flows in a semi-infinite contracting or expanding pipe. J. Fluid Mech. 82, 371–387.

Walker, S. W., Shelley, M. J., 2010. Shape optimization of peristaltic pumping. J. Computational Physics 229, 1260–1291.

Wang, C. Y., 1980. Arbitrary squeezing of fluid from a tube at low squeeze numbers. J. Appl. Math and Phys(ZAMP) 31, 620–627.

Wen, P. H., Wang, W., Liu, Y. W., 2009. Unsteady flows in a capillary lined with a thin porous surface layer by method of fundamental solutions. Int. J. Theoretical and applied Multiscale Mechanics 1, 86–106.

Westneat, M. W., , Socha, J., Lee, W.-K., 2008. Advances in biological structure, function and physiology using synchrotron x-ray imaging. Ann. Rev. of Physiology 70, 119–142.

Westneat, M. W., Betz, O., Blob, R. W., Fezzaa, K., Cooper, W. J., Lee, W.-K., 2003. Tracheal respiration in insects visualized with synchrotron x-ray imaging. Science 299, 558–560.

Young, D. L., Chen, C., Fan, C. M., Murugesan, K., Tsai, C. C., 2005. The method of fundamental solutions for stokes flow in a rectangular cavity with cylinders. J. Mech. B-Fluids 24, 703–716.

Young, D. L., Jane, S. J., Fan, C. M., Murugesan, K., Tsai, C. C., 2006. The method of fundamental solutions for 2d and 3d stokes problems. J. of Comput. Phys. 211, 1–8.

Zhao, S., Povitsky, A., 2009. Method of fundamental solutions for partial-slip fibrous filtration flows. Int. J. Numer. Meth. Fluids 61, 255–274.

Zhao, S., Povitsky, A., 2011. Three-dimentional boundary singularity method for partial-slip flows. Eng. Analysis with boundary Elements 35, 114–122.